CY CERGY PARIS UNIVERSITÉ

UNIVERSITY OF LJUBLJANA

THESIS

FOR OBTAINING THE TITLE OF: **DOCTOR**
DISCIPLINARY FIELD: **THEORETICAL PHYSICS**

AUTHOR: **ALEXIOS CHRISTOPOULOS**

THESIS DIRECTED BY **PROF. DMITRY L KOVRIZHIN, PROF. TOMAŽ PROSEN, DR. ANDREA DE LUCA**

Prepared at
Laboratory of Theoretical Physics and Modelling (LPTM)
Doctoral School No. 405: **Economics, Management, Mathematics, Physics and Computer Sciences**
Date: October 7, 2024

Emergence of chaos in classical and quantum many body dynamics

---

Members of the jury:
Prof. Dmitry L KOVRIZHIN (*Director*)
Prof. Tomaž PROSEN (*Co-Director*)
Dr. Andrea DE LUCA (*Supervisor*)
Dr. Jean AVAN (*Member*)
Prof. Austen LAMACRAFT (*Rapporteur*)
Dr. Jérôme DUBAIL (*Rapporteur*)
Dr. Laura FOINI (*Member*)
Jun-Prof. Jacopo DE NARDIS (Member)

"Imagination is more important than knowledge. For knowledge is limited, whereas imagination embraces the entire world, stimulating progress, giving birth to evolution. It is, strictly speaking, a real factor in scientific research."

Albert Einstein

Acknowledgements

I would like to acknowledge that the novel results, presented in this dissertation, are the fruits of collaboration with my supervisor A. De Luca and the directors of my thesis, D. L. Kovrizhin, and T. Prosen. I am grateful to my colleagues in LPTM and the Physics department of the University of Ljubljana, with whom I had scientifically intriguing discussions, which led to a deeper understanding of physics. Furthermore, I would like to thank my family, whose support has been and continues to be of utmost importance. Last but not least, I acknowledge the influence and contribution of the community of physicists, because we should never forget that science is a product of joint endeavour.

Abstract

This thesis investigates the emergence of chaos in classical and quantum many-body dynamics through three interconnected studies, yielding several novel results. The research initially explores correlations in dual-symplectic circuits, providing a thorough analysis of Hamiltonian flows and symplectic systems. A significant contribution is introducing the Ising-Swap model within dual-symplectic classical circuits, which reveals dynamical correlations using symplectic and dual-symplectic gates. A general method is proposed, which enables the exact computation of two-point dynamical correlation functions, which are shown to be non-vanishing only along the edges of light cones. These findings are validated through Monte Carlo simulations, displaying excellent agreement with theoretical predictions for various observables.

The subsequent study addresses chaos and unitary designs, starting with an examination of unitary designs, k-designs, and the Haar measure, progressing to the Porter-Thomas distribution. This research advances the understanding of universal distributions of overlaps from unitary dynamics by employing models like brick-wall circuits and the Random Phase Model. Notably, the study achieves the diagonalization of generalized Toeplitz matrices and analyses their spectrum, which provides an exact calculation of the Frame Potential, which is essential for understanding the universality of our theory.

The final segment of the thesis focuses on universal out-of-equilibrium dynamics of critical quantum systems, utilizing conformal field theory (CFT) to investigate fields and correlation functions. The study addresses the out-of-equilibrium dynamics of quantum systems perturbed by noise coupled to energy. Key results include detailed analyses of two-point correlations, entanglement entropy distributions, and energy density fluctuations, which are shown to be directly related to a set of stochastic differential equations (SDEs). It is shown, that one can study these SDEs, and analytically prove the existence of non-trivial stationary distributions with $-3/2$ tails. Benchmarking these findings with a free fermion model underscores the universality and robustness of the presented theoretical framework.

Overall, this thesis integrates theoretical models and mathematical frameworks to enhance the understanding of chaos in both classical and quantum systems. By

linking results from symplectic circuits, unitary designs, and out-of-equilibrium dynamics, it offers a comprehensive narrative that underscores the universal characteristics of chaotic behaviour in many-body dynamics.

Résumé

Cette thèse explore l'émergence du chaos dans la dynamique à plusieurs corps, à la fois classique et quantique, à travers trois études interconnectées, aboutissant à plusieurs résultats novateurs. La recherche commence par une exploration des corrélations dans les circuits symplectiques-duaux, offrant une analyse approfondie des flux hamiltoniens et des systèmes symplectiques. Une contribution significative est l'introduction du modèle Ising-Swap au sein des circuits classiques symplectiques-duaux, qui révèle des corrélations dynamiques à l'aide de portes symplectiques et duaux-symplectiques. Une méthode générale est proposée, permettant le calcul exact des fonctions de corrélation dynamique à deux points, qui se révèlent non nulles uniquement le long des bords des cônes de lumière. Ces résultats sont validés par des simulations Monte Carlo, montrant un excellent accord avec les prédictions théoriques pour diverses observables.

L'étude suivante aborde le chaos et les conceptions unitaires, en commençant par un examen des conceptions unitaires, des k-conceptions, et de la mesure de Haar, avant de progresser vers la distribution de Porter-Thomas. Cette recherche fait progresser la compréhension des distributions universelles des recouvrements issus des dynamiques unitaires en utilisant des modèles comme les circuits en briques et le Modèle à Phase Aléatoire. Notamment, l'étude réussit à diagonaliser des matrices de Toeplitz généralisées et à analyser leur spectre, ce qui permet un calcul exact du Potentiel de Frame, essentiel pour comprendre l'universalité de notre théorie.

La dernière partie de la thèse se concentre sur les dynamiques universelles hors d'équilibre des systèmes quantiques critiques, en utilisant la théorie des champs conformes (CFT) pour étudier les champs et les fonctions de corrélation. L'étude aborde les dynamiques hors d'équilibre des systèmes quantiques perturbés par un bruit couplé à l'énergie. Les résultats clés incluent des analyses détaillées des corrélations à deux points, des distributions d'entropie d'intrication, et des fluctuations de

densité d'énergie, qui sont démontrées comme étant directement liées à un ensemble d'équations différentielles stochastiques (SDEs). Il est montré qu'il est possible d'étudier ces SDEs et de prouver analytiquement l'existence de distributions stationnaires non triviales avec des queues en $-3/2$. Le benchmarking de ces résultats avec un modèle de fermions libres souligne l'universalité et la robustesse du cadre théorique présenté.

Dans l'ensemble, cette thèse intègre des modèles théoriques et des cadres mathématiques pour améliorer la compréhension du chaos dans les systèmes classiques et quantiques. En reliant les résultats des circuits symplectiques, des conceptions unitaires, et des dynamiques hors d'équilibre, elle offre un récit complet qui souligne les caractéristiques universelles du comportement chaotique dans la dynamique à plusieurs corps.

Contents

List of Abbreviations

CFT: *Conformal Field Theory*

CHSC: *Classical Heisenberg Spin Chain*

CUE: *Circular Unitary Ensemble*

c.s.t: *constant (quantity)*

DFT: *Discrete Fourier Transform*

FP: *Fokker-Planck*

GUE: *Gaussian Unitary Ensemble*

GinUE: *Ginibre unitary ensemble*

GOE: *Gaussian Orthogonal Ensemble*

jpdf: *joint probability distribution function*

KPZ: *Kardar-Parisi-Zhang*

LPTM: *Laboratory of Theoretical Physics and Modelling*

obc: *open boundary condition*

OTOC: *Out-of-Time-Order Correlator*

pbc: *periodic boundary condition*

pdf: *probability density function*

PT: *Porter-Thomas*

RMT: *Random Matrix Theory*

RPM: *Random Phase Model*

RUC: *Random Unitary Circuit*

SDE: *Stochastic Differential Equation*

Chapter 1

Introduction

Chaos is a critical concept that bridges classical and quantum physics, reflecting the complex and often unpredictable nature of dynamics in systems. In classical physics, chaos theory explores how deterministic systems, governed by precise dynamical laws, can exhibit behaviour that is highly sensitive to initial conditions, a phenomenon often illustrated by the "butterfly effect" [1]. This sensitivity leads to complex, seemingly random behaviour even in systems where the underlying rules are straightforward. Such chaotic behaviour has been observed in diverse contexts, from weather systems to planetary orbits, highlighting the inherent unpredictability of the natural world [2].

In contrast, quantum chaos extends this concept into the quantum realm, where systems are governed by the principles of quantum mechanics. Unlike classical systems, quantum systems do not exhibit sensitivity to the initial quantum state, making the study of chaos in this context historically challenging. Quantum chaos focuses on understanding how classical chaotic behaviour emerges in quantum systems, especially in the semi-classical limit, where quantum effects are still significant. This field explores the relationship between classical trajectories and quantum states, often using statistical methods to study the distribution of energy levels and the behaviour of wave functions in chaotic quantum systems [3].

This thesis aims to focus on the nature of chaos in both classical and quantum physics by the study of many body systems in three different frameworks: dual-symplectic circuits, k-designs in random unitary circuits and out-of-equilibrium dynamics in critical quantum systems. So let us start from the classical physics part of my thesis.

Dual-symplectic Circuits

Symplectic dynamics is central to the study of Hamiltonian systems, a subject deeply rooted in the work of Henri Poincaré, who established the foundations of dynamical systems and symplectic geometry [4]. At the heart of symplectic dynamics is the concept of symplectic form—a geometric structure that encodes the essential dynamical information of a system and is preserved under time evolution. A result of this is phase space volume conservation, known as Liouville's Theorem. If one imagines a "balloon", representing a volume in the phase space of a symplectic system, then the time evolution expands this balloon in certain directions and shrinks it into others, such that the total volume of the "balloon" is invariant.

This type of dynamics appears in many natural systems from celestial mechanics to fluid dynamics and thus a deeper understanding of such type of time evolutions is directly related to our understanding of nature. Symplectic systems can demonstrate a wide spectrum of behaviours, ranging from regular ones to chaotic ones. Regular dynamics involve periodicity or quasi-periodicity, meaning that the trajectories of the system in phase space either repeat after a certain period or cover a toroidal surface densely without filling the entire space. However, chaotic dynamics include mixing, meaning that any small volume of initial conditions will eventually spread out and fill a larger region of the phase space, leading to complex and irregular patterns. An indicator of mixing is sensitivity to initial conditions, which usually appears as an exponential divergence of trajectories and thus positive Lyapunov exponents [5]. In addition, it is possible that a system can demonstrate both regular and chaotic time evolution, with the phase space being a mixture of regular and chaotic regions. A well-known example of that is the Chirikov standard map [6]. However, the focus of this part is mostly on chaotic systems, especially classical spin chains.

What is the motivation behind the study of correlations in my thesis? In classical systems, the connection between chaos and correlations is a fundamental concept in understanding complex dynamical behaviour. The sensitive dependence on initial conditions in chaotic systems makes long-term prediction impossible, despite the system being deterministic, indicating that this type of time evolution leads to loss of information about the initial state. Correlations in chaotic systems describe how the state of one part of the system is related to the state of another part, in time. Since chaotic systems "forget" over time, it is expected that their correlations typically

decay over time. Consequently, correlations can be a significant tool for exploring chaos.

What is the motivation behind studying classical spin chains? The study of simple systems can be quite rich in physics since they can offer intuition and knowledge on the more fundamental mechanisms in nature. The aforementioned Chirikov map is a very good example of how much one can study and understand about chaos, especially for the transition between regular and chaotic behaviour, from a simple law for time evolution. Another example is classical spin chains. In recent years, classical spin chains have become a focal point in the study of symplectic dynamics. Integrability, ergodicity, and their breakdown in one-dimensional (1D) classical spin chain models, particularly in the classical Heisenberg spin chain (CHSC) [7, 8], have been extensively explored. The framework of fluctuating hydrodynamics [9], initially developed for classical anharmonic chains, has proven effective in studying correlations in these systems [10, 11, 12, 13], revealing universal scaling behaviours akin to those predicted by the Kardar-Parisi-Zhang (KPZ) equation. These studies have demonstrated that classical systems, under certain conditions, can exhibit behaviours closely resembling those of quantum systems, especially when investigating correlations and transport phenomena [14].

The concept of dual-symplectic dynamics represents an advancement in this field, and it would be one of the major subjects of discussion in this thesis. *However, what, do dual-symplectic dynamics contribute specifically in the study of chaos?*

Results and methods: Unlike traditional symplectic systems, where symplecticity governs only time evolution, dual-symplecticity extends this property to spatial direction. This idea has been observed in SO(3) invariant dynamics of classical spins [15], where correlation functions exhibit KPZ universality with a dynamical exponent of $3/2$. This thesis provides a comprehensive exploration of dual-symplectic dynamics and introduces an exact method for calculating dynamical correlation functions in dual-symplectic brick-wall 1D circuits.

In more detail, I consider a discrete in-space system consisting of N sites and a Floquet time evolution. The Floquet operator is constructed by a local symplectic gate Φ that couples two sites, e.g. $i, i+1$, in a brick-wall 1D geometry. The correlations of interest are of local observables on the points, $(y, 0)$ and $(y+x, t)$ of space-time, but the two-site invariance of the model, implies dependence only on x and the even, odd parity of y. The initial condition is considered to be the stationary

state of the system, which for chaotic systems (in the absence of conserved quantities) is the uniform measure over the phase space. The methodology begins by establishing a general diagrammatic formalism for symplectic dynamics on a finite measure phase space. Analytical expressions such as correlations are expressed via diagrams, mapping the mathematical framework, that would be needed otherwise, to transformations of these diagrams. This diagrammatic approach leads to a more practical and intuitive way to manage the analytics. The brick-wall geometry of the circuit leads to a coupling of the sites with a speed of $v_c = 2$, and thus no information can travel faster than that. It is an analogue to the speed of light in special relativity and, in the same way, one can define light cones in our discrete space-time circuit with a maximal velocity of v_c. Spacelike points are not causally connected, and correlations trivially vanish. However, this is not true for timelike points and in this case, an exact behaviour is not usually known for a generic symplectic circuit.

The diagrammatic formalism is then extended to dual-symplectic systems where Φ is dual-symplectic, where one derives exact expressions for the correlations of arbitrary local observables. A key finding of this thesis is that, in dual-symplectic circuits, the dynamical correlation functions vanish everywhere except along the light rays, $x = \pm v_c t$. Moreover, the behaviour of these functions along the light rays can be expressed in terms of a transfer operator $\mathcal{F}^{\pm}$. The $\pm$ sign represents the two different parities of y.

The thesis introduces a class of dual-symplectic systems called the Ising-Swap model [16], which is employed to validate the results via analytics and Monte Carlo simulations, and where the local gate Φ is a composition of rotations acting on classical spins. Specifically, I prove that, despite the infinite dimensionality of the local phase space, the transfer operator involved in the calculation of the correlation functions splits into finite-dimensional blocks, owing to the conservation of the total angular momentum. A significant advantage of this is that correlations depend on a finite number of angular momentum subspaces, and thus truncation is not required.

The scientific importance of a piece of research is not apparent, only on the specific subject it deals with but also on its influence on other subjects. Therefore, it is equally important for this thesis to answer the following question: *What other questions can the results of the thesis on dual-symplectic systems help answer?* My answer is the following.

The method introduced in the thesis is valid not only for dual-symplectic systems, as any local gate Φ which is volume-preserving and which also has a volume-preserving dual map $\tilde{\Phi}$ and satisfies Eq. (2.42), exhibits the same diagrammatic behaviour. Every symplectic map is volume and orientation-preserving, but the group of symplectic maps is significantly smaller than that of the volume-preserving ones (Non-squeezing theorem [17]). Consequently, there is a larger set of dynamical ergodic systems, which exhibit our diagrammatic representation, having correlations, which vanish everywhere except the edges of the light-cone.

The exploration of dual-symplectic dynamics in this thesis is deeply connected to works in both classical and quantum mechanics. The "surviving" of correlations only on the edges of the light cones, mirrors the phenomena observed in dual-unitary quantum circuits, where unitarity over space and time leads to simplifications in calculating dynamical quantities [18, 19, 20, 21]. The link between dual-symplecticity and dual unitarity implies feedback between the two, and discovery in one can help discover something original in the other. Especially, it can help answer questions such as: Is it possible to find a more general characterization or complete parametrization of the dual-symplectic circuits which may help in also, finding a parametrization of dual-unitary gates to larger than qubits [22] local spaces? Could one find exact results for different initial conditions, as has already been demonstrated in the dual unitary case [18]? The formalism showcased in this thesis can be a stepping stone to studying these types of questions.

We conclude this part by mentioning that classical circuits and correlations have been the main tools that were used in this thesis for studying chaos in many body classical systems. In the case of quantum many-body systems, quantum many-body circuits and especially random unitary circuits (RUCs) and their formation of $k-$designs can be fundamental for the study of quantum chaos. This is going to be another subject of discussion in this thesis, and it will be presented in more detail in the following parts.

Universal Distributions of overlaps in generic quantum many-body systems

The study of quantum many-body systems is at the forefront of contemporary physics, offering deep insights into complex phenomena that govern both theoretical and practical aspects of quantum mechanics [23, 24]. Among the myriad of topics within this field, quantum chaos and the scrambling of information stand out, due

to their profound implications for understanding the thermalization processes in quantum systems [25], the behaviour of quantum information [26], and even the nature of black holes [27]. An additional subject of exploration in this thesis is the intricate relationship between quantum chaos, random unitary circuits (RUCs), and unitary designs and how these concepts can lead to universal behaviours, when it comes to quantum states prepared by RUCs.

Quantum chaos, unlike its classical counterpart, does not arise from sensitivity to initial conditions. Classical chaos is characterized by the exponential divergence of trajectories in phase space, a phenomenon directly linked to the Lyapunov exponent. In contrast, quantum systems, governed by linear unitary evolution, do not exhibit such divergence. This can be understood by considering an initial condition $|\Psi_0\rangle$ and its small perturbation $\delta|\Psi_0\rangle$. If $U(t)$ is the unitary time evolution operator, then $\|U(t)\delta|\Psi_0\rangle\| = \|\delta|\Psi_0\rangle\|$, implying that the distances of nearby trajectories in Hilbert space do not diverge in time. Instead, quantum chaos is often identified by the statistical properties of energy levels and the distribution of eigenstate overlaps, which resemble those of random matrices [28]. If E_n are the ordered energy levels of the system, then in the study of energy spectra, classically integrable and ergodic Hamiltonian systems belong to two distinct universality classes. The energy spectrum of a classically integrable system is characterized by uncorrelated levels, with the energy gaps $S = E_{n+1} - E_n$ following Poissonian statistics, known as Berry-Tabor conjecture (1977) [29]. Conversely, for ergodic systems, it has been conjectured by Bohigas et al. (1984) [30] that the statistical properties of S align with those predicted by Random Matrix Theory (RMT), particularly the Gaussian Orthogonal Ensemble (GOE) for systems with time-reversal symmetry, or the Gaussian Unitary Ensemble (GUE) without such symmetry.

A critical aspect of quantum chaos is the process of quantum scrambling, where initially localized quantum information becomes distributed across the entire system, rendering it inaccessible to local measurements. Mathematically, this can be understood through out-of-time-order correlators (OTOCs), which measure how two initially local and commuting operators A and B evolve under the system's dynamics. An OTOC is defined as:

$$\mathrm{OTOC}(t) = \langle [A(t), B(0)]^\dagger [A(t), B(0)] \rangle \tag{1.1}$$

Here, $A(t) = U^\dagger(t)AU(t)$ represents the time-evolved operator under the unitary evolution $U(t)$. If the OTOC grows large, it indicates that the operators $A(t), B$ no longer commute, signalling that correlations and thus information from the region of B has spread (or scrambled) across the system.

Random quantum circuits (RQCs) have emerged as a powerful tool for studying these processes. RQCs consist of sequences of randomly chosen unitary gates applied to a quantum system, typically modelled as a chain of qubits or qudits.

Why should we study RUCs? One of the key applications of RQCs is their ability to efficiently approximate unitary t designs (also named unitary k design) [31], which can be useful for simulating random quantum states and operations. In principle, if one is interested in the application of random unitaries drawn from the Haar measure (which is practically a uniform distribution over the unitary group), then he is limited by the fact that they require exponential resources [32], in the sense that they require exponential many gates. Hence, it is more practical to consider less complex probability distributions over the unitary group that are sufficiently close to the Haar measure. The criterion for how closely the RUC reproduces the Haar ensemble is the unitary k-design [33]. When an RQC approaches a $k-$design, then the average of polynomials of degree k over RQCs is indistinguishable from the one coming from the Haar measure. This is similar to approaching the first k moments of a probability distribution. The approach to higher $k-$designs implies that, for all practical purposes, the RUC simulates more effectively the uniform ensemble of unitary matrices. Furthermore, RUCs have often been used to approximate chaotic dynamics, as discussed above in the context of RMT.

Scrambling is a by-product of strongly coupled chaotic dynamics [33], and consequently there should be a strong quantitative connection between quantum chaos and pseudorandomness. Pseudorandomness here refers to the capability of the chaotic unitary dynamics to effectively reproduce a distribution of random unitary matrices since in principle the unitary dynamics of a chaotic system create a deterministic flow over the unitary group. At large times the unitary evolution of a quantum chaotic system is expected to perform a "random walk" (time evolution is deterministic so it is a pseudorandom walk), over the unitary group and since there are no conserved charges, that implies that there is no preferred choice of basis and consequently one can effectively replace $U(t)$ in Eq. (1.1) with a unitary operator drawn from the Haar measure. Therefore, at large enough times, the pseudorandom

behaviour of the chaotic system leads to an ensemble of unitary gates, which approximates the Haar one and the k-design is a criterion of how close we are to Haar and thus how close the pseudorandom behaviour of the system, to being random.

What is the motivation for studying unitary k-designs and the overlaps of quantum states produced by RUCs ? Similarly to the case just described, if one constructs a RUC with some local Haar operators, then as the depth of a quantum circuit increases, the unitary operation it performs becomes increasingly more scrambling, eventually resembling those generated by a global Haar operator. The unitary k-designs significance lies in the fact that they act as a measure of convergence to the Haar measure of the whole system, likewise the moments of a distribution. Convergence of higher k-designs of the RUC to the Haar value is an indicator of a closer convergence to the Haar measure. Unitary designs are crucial for establishing lower bounds on the complexity of quantum circuits [34], in the sense of the minimum number of basic elementary gates necessary to generate the quantum state from a reference one. Another application is randomizing benchmarking [35], which involves applying sequences of randomly chosen quantum gates and is useful in ensuring that errors remain below the thresholds required for fault-tolerant quantum computing. An additional role of unitary designs has been the study of the distribution of overlaps between quantum states that were produced from RUCs. One can assume some two identical but statistically independent states, $|\Psi(t)\rangle = U(t)\,|\Psi_0\rangle\,, |\Psi'(t')\rangle = U'(t')\,|\Psi_0\rangle$ with the RUCs $U(t), U'(t')$ acting on some initial state $|\Psi_0\rangle$. The overlap $w = |\,\langle\Psi'(t')|\Psi(t)\rangle\,|^2$ between the two quantum states provides a measure of their similarity and is directly related to the statistics and complexity of the RUCs. Previous studies have shown that for random states drawn from the Haar measure, the distribution of overlaps follows the Porter-Thomas (PT) distribution [36], which describes the probability distribution of the overlap when $U(t), U'(t')$ are operations drawn from the Haar measure. PT distribution is a key indicator of Haar statistics and characterizes the behaviour of quantum systems under chaotic dynamics. The overlaps of quantum states are crucial for understanding how quantum circuits outperform classical simulations. By sampling random quantum circuits and measuring the overlaps between the generated quantum states, researchers can quantify the difference between quantum and classical computations via a quantity that is called cross-entropy [36], thereby checking for quantum supremacy. Furthermore, the theory produced on the distributions of the overlaps

can be used as a tool for verifying how close a real-life RUC, performs as expected via the comparison of the moments of w, with the theoretical results. Based on all the above, new research on the distributions of w can lead to significant discoveries due to their multi-faceted applications, and that is the main motivation behind the study of those distributions in this thesis.

Results and Methods: In this thesis, we present a detailed study of the statistical properties of quantum states evolved under RUCs with local Haar gates, with a particular focus on the distribution of overlaps between these states. The local Haar gates are chosen independently over space and time. We consider a scenario where the circuit acts on $d = 1$ dimensions, with L sites of local dimension q and evolves over a time t, resulting in a state that approximates a k-design, over time. Our research introduces a novel generalization of the PT distribution [37], extending it to a family of distributions which depend on a specific scaling limit (to be defined later). The PT distribution appears in the limit of $t \to \infty$, with, $t \gg L$, when the RUC has already approached the Haar measure up to large $k-$designs.

The methodology employed in this study involves several key steps, each contributing to a comprehensive understanding of the overlap distribution in chaotic quantum systems. I present them briefly here and the reader will find more details in the later sections of the thesis:

1. *Overlap Distribution in the Scaling Limit:* The core of our study focuses on the distribution of rescaled overlaps $w' = \mathcal{N}w$, $\mathcal{N} = q^L$ where both time t and the number of qudits L are large, for different types of periodic boundary conditions. We, specifically, target the regime, characterized by a single scaling parameter, $x = L/L_{\text{Th}}(t)$, where $L_{\text{Th}}(t)$ represents the volume scale at which complete scrambling occurs [38]. Our results demonstrate that the w' distribution converges to a family of universal distributions that depend on this scaling parameter, and we should mention that this is proven via analytical results for the moments of w'.

2. *Mapping to Statistical Models:* To derive the moments of w', we map the problem to a statistical model of dilute domain walls, via a transfer matrix method. This mapping allows us to express the moments as a partition function, which we solve using techniques from statistical mechanics. The average over the local

Haar gates of our RUC leads to local "spin" degrees of freedom of permutations and thus the resulting partition function corresponds to an effective one-dimensional model with ferromagnetic interactions over those "spins". The leading contributions to the partition function come from the ferromagnetic ground state and the excitations with fewer domain walls. Based on that, one can understand that the universality of the overlap distribution emerges from the density of dilute domain wall excitations.

3. *Random Phase Model and Toeplitz Matrices:* To further validate our results, we employ the Random Phase Model (RPM) [39] and analyse the transfer matrix associated with the overlap distribution in the limit of large local Hilbert space dimensions. This transfer matrix is shown to be a generalization of the Toeplitz matrix [40] and we provide an exact diagonalization technique of this matrix, demonstrating that the overlap distribution can be understood in terms of the eigenvalues of this matrix.

Can one use our results and methodology for different frameworks?. This part of the thesis contributes to the field by providing a comprehensive framework for understanding the universal properties of overlaps in chaotic quantum systems. Firstly, an interesting extension is Floquet circuits [41, 39], where the same random gates are being chosen over time, but not necessarily, over space. In this case, the local random Haar gates act like a strong spatial disorder that can lead to many-body localization (MBL) [42], where thermalization and scrambling are hindered [43], making our theory not valid (numerical proofs of that are presented in App. B.4). However, at weak disorder, the coupling of the degrees of freedom can be strong enough, to induce enough scrambling and one can still be in a thermalising phase and be able to apply our methodology but taking into account that now the average over the local Haar gates lead to local "spin" degrees of freedom which are permutations over the same Haar gates in time as well. Secondly, instead of considering the overlap between two different realizations of the circuit, we can consider the expansion of the state evolved by the circuit in the strings of the computational basis $w = |\langle a = a_1, \ldots, a_L|\Psi\rangle|^2, a_i = 0, 1$, which corresponds to taking $t' = 0$ and $|\Psi_0\rangle = |a = a_1, \ldots, a_L\rangle$. In this case, the distribution of w' on the various strings a will still be described by the universal distributions of our results. This result is important because of its relevance in concrete experiments. For example, in [44, 45], the

statistical distribution of the a-strings of a state evolved from a random circuit was used in an attempt to demonstrate quantum supremacy: a measure of the fidelity of the experiment was obtained precisely by assuming that w follows the PT distribution and in principle, one can do the same in the scaling regime by using our results. Finally, the analysis applied to the RPM suggests that the theory can be extended to $d > 1$, where the ferromagnetic statistical model is defined with the permutations being the local "spins" over a d-dimensional lattice. This will be better understood later when we present the details of our study.

Universal out of equilibrium dynamics

At this point, I present the third and last main subject of my thesis, which is related to out-of-equilibrium dynamics of critical quantum systems.

The study of quantum systems far from equilibrium has emerged as a vital area in modern physics, particularly in understanding the dynamics of critical systems subjected to external perturbations. This subject of the thesis dives into the universal out-of-equilibrium dynamics of one-dimensional critical quantum systems, focusing on how these systems respond to noise coupled to their energy density [46]. Our study uses Conformal Field Theory (CFT) as a foundational tool to explore these dynamics, providing universal results into the behaviour of quantum systems under such perturbations.

Critical phenomena in quantum systems, especially at second-order phase transitions, play a central role in condensed matter physics and statistical mechanics. From the renormalisation group theory, it is known that the 2nd-order critical point is associated with a fixed point where certain thermodynamic functions become singular [47]. A. Polyakov hypothesised [48] that the field theory at the critical point is invariant under the more general group of conformal transformations and not just scale changes. Such a theory is known as conformal field theory (CFT). These transformations stretch the lengths of vectors locally while preserving their relative angles, and are known as Conformal transformations. Consequently, the $d = 1 + 1$ CFT can be applied to the study of 1-D critical quantum systems (e.g., spin chains [49, 50]) and the classification of the fixed points of the renormalization group corresponds to identifying all possible quantum field theories with conformal symmetry. CFT has been instrumental in understanding the universal behaviour of critical systems in one dimension [46, 51, 52], such as the universality of finite-size correction in

the Free energy. The renormalization group theory complements this by explaining the universality observed in critical phenomena, where different physical systems can exhibit identical behaviour at large scales when they correspond to the same fixed point under the renormalization group flow.

What is the connection with the many body chaotic systems ? In order to understand this, we mention briefly the general intuition around thermalization for chaotic and integrable systems.

In chaotic quantum systems, the concept of thermalization is tightly linked to the Eigenstate Thermalization Hypothesis (ETH) [53]. Intuitively, thermalization in an isolated quantum system, where we consider the representation over the energy eigenstates $|E_\alpha\rangle$, implies that starting from a given initial physical state $|\Psi(0)\rangle = \sum_\alpha \sqrt{p_\alpha}\,|E_\alpha\rangle$, the system's observables eventually reach values described by the microcanonical (and Gibbs) ensembles after a sufficiently long time. The infinite-time average of a physical observable represented by the operator $\hat{O}$ (which typically consists of a linear combination of few-body operators) can be derived from :

$$\langle \hat{O} \rangle_\infty = \lim_{T\to\infty} \frac{1}{T} \int_0^T \langle \psi(t)|\hat{O}|\psi(t)\rangle dt = \sum_\alpha p_\alpha \langle E_\alpha|\hat{O}|E_\alpha\rangle$$

Thus, $\langle \hat{O} \rangle_\infty$ depends on the probabilities p_α along with the expectation values of the observable $\langle E_\alpha|\hat{O}|E_\alpha\rangle$, because the terms involving off-diagonal matrix elements of $\hat{O}$ oscillate at different frequencies and thus average out. Since p_α are determined by the initial state, the natural mechanism ensuring that an observable $\hat{O}$ reaches its thermal expectation value at long times for generic initial conditions is the assumption that the expectation values in individual eigenstates $\langle E_\alpha|\hat{O}|E_\alpha\rangle$ align with those of the microcanonical ensemble $\mathcal{O}_{\rm mc}(E_\alpha)$ defined by the probabilities p_α.

More specifically, the ETH proposes that in chaotic systems the fluctuations of matrix elements of local operators $\hat{O}$ in the energy eigenstate basis behave according to the ansatz:

$$\langle \alpha|\hat{O}|\beta\rangle = \mathcal{O}_{\rm mc}(\bar{E})\delta_{\alpha\beta} + g(\omega,\bar{E})R_{\alpha\beta},$$

where $\bar{E} = \left(E_\alpha + E_\beta\right)/2$ denotes the average eigenenergy, and $\omega = E_\alpha - E_\beta$ is the energy difference. Here, $R_{\alpha\beta}$ is a normally distributed random variable and $g(\omega,\bar{E})$

is a smooth function of ω and $\bar{E}$. The equation above suggests that individual many-body energy eigenstates have thermal local observables that are similar to the microcanonical ensemble values at the energy $E = E_\alpha$, so that $\langle E_\alpha|\hat{O}|E_\alpha\rangle \approx \mathcal{O}_{\rm mc}(E)$. Therefore, even if the entire system is initialized in an energy eigenstate, its subsystems perceive the rest of the system as an effective heat bath performing dynamics that are restricted only by the energy and implying that the reduced density matrix of the subsystem is thermal. Thus, the dependence on the initial condition is effectively lost from the point of view of time averages of local observables, indicating the loss of information and the intense scrambling of quantum chaotic dynamics.

On the contrary, in integrable systems, the dynamics of subsystems are restricted by the many conserved charges of the system. Instead, $\langle \hat{O} \rangle_\infty$ of local observables relax to a different value, described by a reduced density matrix known as Generalized Gibbs Ensemble (GGE):

$$\rho_{\rm GGE} = \frac{1}{Z_{\rm GGE}} \exp\left(-\sum_i \lambda_i I_i\right),$$

where I_i are the conserved quantities and λ_i are Lagrange multipliers. By definition, $\mathrm{Tr}\{(\rho_0 I_i)\} = \mathrm{Tr}\{(\rho_{\rm GGE} I_i)\}$, where ρ_0 is the initial state of the system. Thus, the coefficients λ_i depend on the initial condition, indicating that the dynamics retain information about the initial state, in contrast to chaotic systems.

Essentially, at large times the system equilibrates, and it can be a thermal equilibrium described by the Gibbs ensemble $\rho_{\rm Gibbs} = \exp\{-\beta H\}/Z_{\rm Gibbs}$ for isolated quantum many-body chaotic systems, or a different type given by the GGE in the case of integrable systems. However, for the dynamics towards equilibrium, the situation is much less clear, making the study of this type of dynamics very intriguing.

What is the motivation behind the study of out-of-equilibrium dynamics under the influence of noise ? Understanding out-of-equilibrium dynamics is crucial for several reasons. It sheds light on how quantum systems thermalize or fail to do so. The failing of thermalization can lead to more exotic phases described by phenomena, such as many-body localization (MBL) [54], equilibration toward generalized Gibbs ensembles due to integrability [55], quantum scars [56], and Hilbert space fragmentation [57]. Furthermore, understanding the non-equilibrium physics of interacting systems is not only fundamentally important but could contribute to future technological advancements. For example, quantum computers require the ability to

manipulate interacting quantum systems in real-time and the knowledge we can acquire on coherent dynamics from out-of-equilibrium ones, is a key area of focus for various experimental systems.

There are many ways to take a system out of equilibrium, such as applying a driving field pumping energy or particles in the system through external reservoirs, or a change in one of the system parameters, known as quantum quench. A particularly intriguing protocol is a noisy quench, especially when the noise is coupled to the system's energy density. That is, the subject of discussion of the third and last part of my thesis and the motivation behind it is encoded into its applications. Noise can induce complex dynamics such as heating, decoherence [58], and entanglement generation, all of which are critical for understanding the robustness of quantum systems in real-world conditions. The behaviour of quantum systems under noise has been investigated in various contexts, including the impact of $1/f$ noise [59, 60], which is common in physical systems, and the role of stochastic unitary dynamics, where it is possible of realizing it in concrete experiments, including cold-atom platforms [61] and trapped ions [62].

Results and Methods: The study performed in this part of my thesis aims to offer insights into answering two questions:

- Is there a universal feature in the dynamics of a system following a noisy quantum quench?
- What are the characteristics of the asymptotic, steady state reached after a quench?

In this part of the thesis, we explore the universal out-of-equilibrium dynamics of one-dimensional critical quantum systems perturbed by temporally white noise $\eta(x,t)$ coupled to their energy density. If $\hat{H}_0 = \int dx \hat{h}(x)$, is the unperturbed Hamiltonian then the total Hamiltonian is of the form:

$$\hat{H} = \hat{H}_0 + \hat{H}_1 = \int dx[1+\eta(x,t)]\hat{h}(x),$$

where $\hat{h}(x)$ is the Hamiltonian density, and the noise $\eta(x,t)$ is delta correlated in time with space correlations characterized by a smooth, function $f(x)$, which decreases fast enough at $x \gg 1$. The addition of the noise induces stochasticity over the unitary dynamics and thus the physical quantities of the system. This becomes clear, if we assume an initial condition $|\Psi(0)\rangle$ and evolve it under $\hat{H}$ up to time t for

example. At every time moment $\tau \leq t$ there is a temporal-spatial profile of the noise $\eta(x,\tau)$ which generates a specific trajectory in Hilbert space for $|\Psi(0)\rangle$. Then, if we repeat the process, one gets other spatial profiles of $\eta(x,\tau)$ and thus another trajectory for $|\Psi(0)\rangle$. In this manner, one collects samples of these trajectories as well as of the physical quantities, since they depend on the state of the system. This example gives a qualitative explanation of how the state and the physical quantities acquire a stochastic nature due to the noise.

The system is initially prepared in its critical ground state under a homogeneous and gapless Hamiltonian, ensuring scale invariance. The perturbation is introduced at $t > 0$, driving the system out of equilibrium. The main objective is to understand how this class of systems evolved over time and the nature of the stationary states they reach. The key result of this study is the demonstration that the system reaches a non-trivial and universal stationary distribution of states characterized by broad tails in the distributions of physical quantities. This finding is crucial because it indicates that the typical behaviour of the system cannot be fully captured by averaging over noise realizations; instead, one must consider the entire distribution of physical quantities.

Using CFT, we derive a universal description of the out-of-equilibrium dynamics. Specifically, we show that any two-point correlation is a function of a stochastic variable, which we denote $\kappa_\pm$ and as we will see in detail this stochastic variable is actually dependent on another variable named r. Thus, finding exactly the statistics over time boils down to solving the two coupled ordinary stochastic differential equations (SDEs) for $\kappa_\pm$ and r. These SDEs govern the evolution of two stochastic variables $\kappa_\pm$ and r. Solving these SDEs reveals that the system reaches a stationary state at long times, with the distribution of $\kappa_\pm$ taking a universal form with fat tails of $-3/2$. These fat tails result in the divergence of all the moments of the physical quantities of interest, such as the entanglement entropy and $\left\langle \hat{h}(x,t) \right\rangle$, where $\langle . \rangle$ indicates the expectation value over the initial state and $\hat{h}(x,t)$ is the time evolved energy density. The fat tails of $\left\langle \hat{h}(x,t) \right\rangle$ suggests that at large times the system demonstrates, locally intense fluctuations of the energy and on average it heats up to infinity but reaches a non-trivial steady state. These results are validated through a specific model—a chain of non-interacting spinless fermions with noisy hopping. This model provides a concrete example where the CFT predictions can be tested against numerical simulations.

Furthermore, the study examines the impact of the noise correlation length on the system's dynamics. By considering the scaling limit where the noise correlation length diverges, it is shown that the CFT predictions are precisely recovered, underscoring the universality of the results. Additionally, the timescales at which the CFT framework breaks down are estimated, offering a clear picture of the regime of validity of the approach.

The research also extends these results to systems initially prepared at finite temperatures. Notably, the initial temperature affects only the transient dynamics, while the stationary distribution remains unchanged. This robustness implies that the $-3/2$ tail observed in the energy density distribution is a universal feature of the system, independent of the initial conditions.

What further applications can our theory have? Several intriguing questions and future research directions remain open.

Firstly, it would be particularly exciting to observe the predictions of our theoretical framework in a specific experimental setup. The study of the statistics of quantum trajectories has recently gained significant attention, especially in the context of measurement-induced phase transitions [63, 64, 65]. Unlike other studies that require post-selection, our approach is free from this limitation, since stochasticity is induced by noise and not a measurement, making it a promising candidate for experimental verification. To enhance the feasibility of experimental observation, it is crucial to assess the robustness of the observed phenomena, such as by investigating the impact of thermal fluctuations. The study, in [46], indicates that a small initial temperature does not alter the fat tail behaviour of the energy density distribution. Secondly, our theory dealt with two-point correlation functions, however extending our methods to compute higher-order quantum correlation functions, such as four-point correlators, remains an important goal, as it would help provide insight into other physical aspects of the system. For example, the mutual information between two intervals is related to a four-point correlator of twist fields [66]. Lastly, the surprising emergence of a stationary distribution in our model raises fundamental questions about the conditions necessary to observe similar behaviour in other quantum stochastic systems. The stationary state identified in our continuous theory may correspond to a long-lived prethermal state in lattice systems, analogous to observations in many-body quantum scars [67].

In conclusion, this introduction exhibits the three main subjects of discussion in

this thesis and offers a brief overview of each field, the methods and results, and references to relevant literature. The thesis is organized into three chapters as follows:

- In Ch. 2, I present in detail the novel class of systems, of dual-symplectic classical circuits.
- In Ch. 3, I demonstrate in detail the theory and the novel results on the distribution of the overlaps w from RUCs.
- In Ch. 4, I showcase in detail the analytical approach and the results for universal out-of-equilibrium dynamics of critical quantum systems.

The reader will find a more detailed description of the structure of each part at the beginning of each chapter.

Chapter 2

Correlations in Dual-Symplectic Circuits

In this chapter we present the novel idea of dual-symplectic dynamics [16] according to which, symplecticity characterizes both time and space propagation. In this chapter, we demonstrate in detail the diagrammatic method that was utilised for representing the correlation functions and how dual-symplecticity, helps us simplify the diagrams. Furthermore, we introduce a family of dual-symplectic systems, called the Ising Swap Model, which is used to test our theory via numerical results.

This chapter is organised as follows:

- In Sec.2.1, we present some introduction to Hamiltonian flows.
- Sec. 2.2 we briefly introduce Symplectic systems.
  I would like to let the reader know that the theory presented in these first two sections can be found in different textbooks about dynamical systems, such as [3]. Those who already have a solid understanding of Hamiltonian flows and Symplectic dynamics may wish to continue directly to the next section.
- In Sec. 2.3, we showcase our novel results in dual-symplectic circuits and benchmark them with numerical results from the Ising Swap Model.

2.1 Hamiltonian flows

A stepping stone to understanding symplectic systems is Hamiltonian flows, and thus I chose to begin the theoretical inquiry with that. A Hamiltonian system is defined on a phase space M_N as the set of all the states $\boldsymbol{X} = (\boldsymbol{p}, \boldsymbol{q})$ and its flow described by a function $H(\boldsymbol{p}, \boldsymbol{q}, t)$, the Hamiltonian, and a set of differential equations,

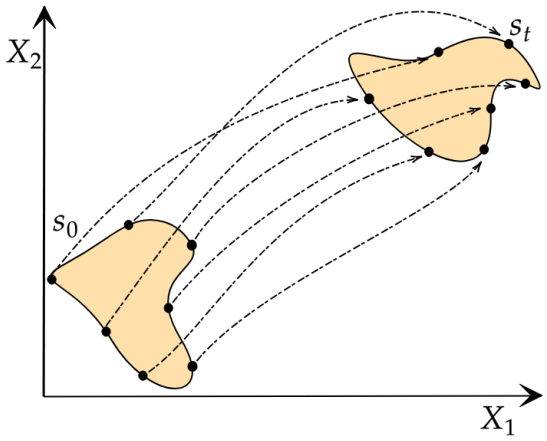

FIGURE 2.1: The conservation of volume in a phase space of $N = 1$ of a Hamiltonian system.

Hamilton's equations:

$$\dot{q}^i = \frac{\partial H}{\partial p^i}, \quad \dot{p}^i = -\frac{\partial H}{\partial q^i} \rightarrow \dot{\boldsymbol{X}} = \Omega \boldsymbol{\nabla}_{\boldsymbol{X}} H \tag{2.1}$$

Here the q^i are the generalised coordinates and p^i the generalised momenta, with $i = 1, 2, \ldots, N$ for a system with N degrees of freedom. The Poisson matrix Ω is the antisymmetric $2N \times 2N$ matrix:

$$\Omega = \begin{bmatrix} 0_N & \mathbb{1}_N \\ -\mathbb{1}_N & 0_N \end{bmatrix} \tag{2.2}$$

A typical example of a Hamiltonian is $H(\boldsymbol{p}, \boldsymbol{q}) = \boldsymbol{p}^2/2 + V(\boldsymbol{q})$, which represents the energy of a system of N particles interacting with a potential V, that depends only on their generalised coordinates. In the special case that the Hamiltonian has no explicit time dependence, $H = H(\mathbf{p}, \mathbf{q})$, we can use Hamilton's equations to show that, as $\mathbf{p}$ and $\mathbf{q}$ vary with time, the value of $H(\mathbf{p}(t), \mathbf{q}(t))$ remains a constant:

$$\frac{\mathrm{d}H}{\mathrm{d}t} = \frac{\mathrm{d}\mathbf{q}}{\mathrm{d}t} \cdot \frac{\partial H}{\partial \mathbf{q}} + \frac{\mathrm{d}\mathbf{p}}{\mathrm{d}t} \cdot \frac{\partial H}{\partial \mathbf{p}} = \frac{\partial H}{\partial \mathbf{p}} \cdot \frac{\partial H}{\partial \mathbf{q}} - \frac{\partial H}{\partial \mathbf{q}} \cdot \frac{\partial H}{\partial \mathbf{p}} = 0.$$

One of the basic properties of Hamilton's equations is that they preserve $2N$ dimensional volumes in the phase space M_N. This follows by taking the divergence of $\dot{\boldsymbol{X}}$, which gives

$$\boldsymbol{\nabla}_{\boldsymbol{X}} \cdot \dot{\boldsymbol{X}} = \frac{\partial}{\partial \mathbf{p}} \cdot \left(-\frac{\partial H}{\partial \mathbf{q}} \right) + \frac{\partial}{\partial \mathbf{q}} \cdot \left(\frac{\partial H}{\partial \mathbf{p}} \right) = 0.$$

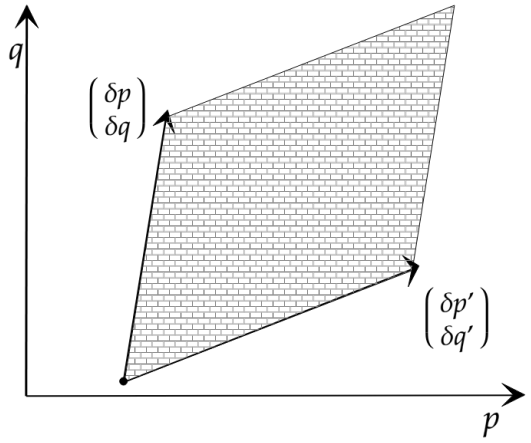

FIGURE 2.2: The differential symplectic area in the case of $N = 1$. In a two-dimensional phase space, it is equivalent to the area of the parallelogram formed by $\delta \boldsymbol{X}, \delta \boldsymbol{X}'$, but this is not true in higher dimensions.

where we used Eq. (2.1). Thus, if we consider an initial closed surface s_0 in the $2N$ dimensional phase space and evolve each point on the surface forward in time, we obtain at each instant of time t a new closed surface s_t (see Fig. 2.1) which contains within precisely the same $2N$ dimensional volume as does s_0. This follows from

$$\frac{\mathrm{d}}{\mathrm{d}t}\int_{V_t} d^{2N}\boldsymbol{X} = \oint_{s_t} \frac{\mathrm{d}\boldsymbol{X}}{\mathrm{d}t}\cdot \mathrm{d}\mathbf{s} = \oint_{s_t} \dot{\boldsymbol{X}}\cdot \mathrm{d}\mathbf{s} = \int_{V_t} \boldsymbol{\nabla}_{\boldsymbol{X}}\cdot \dot{\boldsymbol{X}}\mathrm{d}^{2N}\boldsymbol{X} = 0,$$

where $\int_{V_t}\cdots$ denotes integration over the volume enclosed by s_t, $\oint_{s_t}\cdots$ denotes a surface integral over the closed surface s_t, and the third equality is from the divergence theorem. As a consequence of this result, Hamiltonian systems do not have attractors in the usual sense, since the volume in phase space of initial conditions does not decrease. This incompressibility of phase space volumes for Hamiltonian systems is called Liouville's theorem.

One of the most fundamental structural properties of Hamilton's equations is their symplectic nature. In order to understand this better, let us consider three infinitesimally separated orbits, $\boldsymbol{X}(t) = (\mathbf{p}(t), \mathbf{q}(t))$, $\boldsymbol{X}(t) + \delta\boldsymbol{X} = (\mathbf{p}(t) + \delta\mathbf{p}(t), \mathbf{q}(t) + \delta\mathbf{q}(t))$, and $\boldsymbol{X}(t) + \delta\boldsymbol{X}' = (\mathbf{p}(t) + \delta\mathbf{p}'(t), \mathbf{q}(t) + \delta\mathbf{q}'(t))$, where $\delta\mathbf{p}$, $\delta\mathbf{q}$, $\delta\mathbf{p}'$, and $\delta\mathbf{q}'$ are infinitesimal vectors of dimension N. Then the quantity known as differential symplectic area is defined as:

$$\delta\mathbf{p}\cdot\delta\mathbf{q}' - \delta\mathbf{q}\cdot\delta\mathbf{p}', \tag{2.3}$$

An example of it is shown in Fig. 2.2 . Furthermore, the differential symplectic area

can be expressed as

$$\omega(\delta \boldsymbol{X}, \delta \boldsymbol{X}') = \delta \mathbf{p} \cdot \delta \mathbf{q}' - \delta \mathbf{q} \cdot \delta \mathbf{p}' = \delta \boldsymbol{X}^T \cdot \Omega \cdot \delta \boldsymbol{X}', \tag{2.4}$$

where T denotes transpose and the Hamiltonian flow has the characteristic of preserving ω:

$$\frac{\mathrm{d}}{\mathrm{d}t}\omega(\delta \boldsymbol{X}, \delta \boldsymbol{X}') = 0. \tag{2.5}$$

Actually, the symplectic area is known in differential geometry as symplectic form [68] and its invariance is a property of a more general class of dynamical systems which I am going to discuss later. We are now deriving Eq. (2.5). The time evolution of the differential symplectic area in Hamiltonian dynamics is given by:

$$\frac{\mathrm{d}}{\mathrm{d}t}\omega(\delta \boldsymbol{X}, \delta \boldsymbol{X}') = \frac{\mathrm{d}\delta \boldsymbol{X}^T}{\mathrm{d}t} \cdot \Omega \delta \boldsymbol{X}' + \delta \boldsymbol{X}^T \cdot \Omega \frac{\mathrm{d}\delta \boldsymbol{X}'}{\mathrm{d}t},$$

$$= \left(\frac{\partial \dot{\boldsymbol{X}}}{\partial \boldsymbol{X}} \cdot \delta \boldsymbol{X}\right)^T \cdot \Omega \delta \boldsymbol{X}' + \delta \boldsymbol{X}^T \Omega \left(\frac{\partial \dot{\boldsymbol{X}}}{\partial \boldsymbol{X}} \delta \boldsymbol{X}'\right),$$

$$\delta \boldsymbol{X}^T \left[\left(\frac{\partial \dot{\boldsymbol{X}}}{\partial \boldsymbol{X}}\right)^T \Omega + \Omega \frac{\partial \dot{\boldsymbol{X}}}{\partial \boldsymbol{X}}\right] \delta \boldsymbol{X}',$$

Now we are using Hamilton's equation:

$$= \delta \boldsymbol{X}^T \left[\left(\Omega \frac{\partial^2 H}{\partial \boldsymbol{X}^2}\right)^T \Omega + \Omega\Omega \frac{\partial^2 H}{\partial \boldsymbol{X}^2}\right] \delta \boldsymbol{X}',$$

$$= \delta \boldsymbol{X}^T \left[\left(\frac{\partial^2 H}{\partial \boldsymbol{X}^2}\right)^T \Omega^T \Omega + \Omega\Omega \frac{\partial^2 H}{\partial \boldsymbol{X}^2}\right] \delta \boldsymbol{X}' = 0,$$

where $\Omega\Omega = -\mathbb{1}_{2N}$, $\Omega^T = -\Omega$, and the matrix $\frac{\partial^2 H}{\partial \boldsymbol{X}^2}$ is symmetric. For systems with a single degree of freedom ($N = 1$), Eq. (2.5) establishes that infinitesimal areas, such as those defined by two infinitesimal vectors forming a parallelogram with area $\delta p' \delta q - \delta q' \delta p$ (see Fig. 2.2), are conserved under Hamiltonian flow, and thus by extension, finite areas are also preserved. Consequently, for $N = 1$, both Liouville's theorem and the symplectic condition articulate the same principle. However, for $N > 1$, the preservation of volume suggested by the symplectic condition extends beyond what is covered by Liouville's theorem alone. This underscores the symplectic condition as a more essential requirement in Hamiltonian mechanics, and as we will see later indeed, the preservation of the volume in M_N is a consequence of

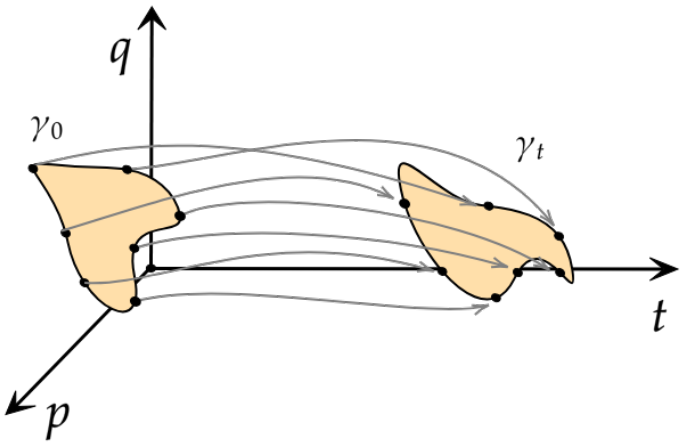

FIGURE 2.3: The conservation of the loop action under Hamiltonian dynamics.

the flow preserving ω.

The expression, $\delta\mathbf{p}\cdot\delta\mathbf{q}' - \delta\mathbf{q}\cdot\delta\mathbf{p}'$, represents the differential form of Poincaré's integral invariant [69]. This invariant is a fundamental concept in symplectic geometry and classical mechanics, capturing essential features of conservative dynamical systems. The invariant is defined as:

$$S_\gamma = \oint_\gamma \mathbf{p}\cdot\mathrm{d}\mathbf{q} = \sum_{i=1}^{N}\oint_\gamma p_i \mathrm{d}q_i, \tag{2.6}$$

where this integral is taken around a closed loop γ in the phase space spanned by coordinates $(\mathbf{p},\mathbf{q})$. We also refer to the integral, S_γ, as the symplectic area or the loop action. The invariance of this integral under time evolution, which is a cornerstone of Hamiltonian mechanics, implies that if γ evolves following the flow determined by Hamilton's equations, then $\gamma(t)$, the path at time t, is derived by evolving all points on $\gamma(0)$ forward in time. This property elucidates the conservation laws inherent in Hamiltonian systems and highlights the non-dissipative nature of such systems.

The previous results are related to energy-preserving flows. However, in the case of explicit dependence of the Hamiltonian in time $H(\boldsymbol{X},t)$ we need to generalise Eq. (2.6). Under dynamic flow, the loop action is described by the Poincaré-Cartan integral theorem [69]. The Poincaré-Cartan integral theorem extends the concept of conservation from classical Hamiltonian systems to more complex systems involving time as an explicit variable. In particular, consider the extended phase space of dimension $(2N+1)$, characterized by coordinates $(\boldsymbol{X},t)$. Within this framework,

assume γ_0 is a closed curve in this space, and the dynamics deform γ_0, as depicted in Fig. 2.3. According to the Poincaré-Cartan integral theorem, the generalised loop action I_{γ_0}:

$$I_{\gamma_0} \equiv \oint_{\gamma_0} (\mathbf{p} \cdot \mathrm{d}\mathbf{q} - H\mathrm{d}t), \tag{2.7}$$

in the extended phase space remains invariant in time $I_{\gamma_0} = I_{\gamma_t}$ This theorem broadens the classical notion of conservation in Hamiltonian mechanics by incorporating the dimension of time into the phase space, thereby enhancing the scope of the invariants under consideration. Furthermore, in scenarios where the Hamiltonian H does not explicitly depend on time, we end up back at the invariance of Eq. (2.6). This is true since the integrals of Hdt over the paths γ_0 and γ_t reside entirely on the $2N$ dimensional surface defined by the constant $H(\boldsymbol{X})$ and thus they vanish.

Hamiltonian Maps: The Hamiltonian flows already discussed are continuous in time, but in scenarios like Floquet dynamics that come from periodic in t Hamiltonians, or like for simplifying the analysis of the system, we need to deal with discrete flows. This raises the question: What happens in the case of discrete-time evolution? A simpler approach for exploring dynamics uses discrete maps that represent the Poincaré first-return map, also known as the Poincaré section and in our case as Hamiltonian maps at every time step τ. Consider a Hamiltonian system and define the 'time τ map' $\mathcal{F}_\tau$ for this system as follows:

$$\mathcal{F}_\tau(\boldsymbol{X}(t), t) = \boldsymbol{X}(t + \tau). \tag{2.8}$$

(Here, the second argument of $\mathcal{F}_\tau$ does not explicitly depend on t if the Hamiltonian is time-independent.) This map evolves the system by a time interval of τ. Hamiltonian maps $\mathcal{F}_\tau$ suggest another way of studying flows, where one ignores the continuous trajectory of the system in phase space and studies only the discrete points of the trajectory every time interval τ. The symplectic condition Eq. (2.5) for the discrete evolution becomes,

$$\omega(\delta\boldsymbol{X}, \delta\boldsymbol{X}')(t + \tau) = \omega(\delta\boldsymbol{X}, \delta\boldsymbol{X}')(t) \tag{2.9}$$

$$\delta\boldsymbol{X}^T(t + \tau) \cdot \Omega \cdot \delta\boldsymbol{X}'(t + T) = \delta\boldsymbol{X}(t)^T \cdot \Omega \cdot \delta\boldsymbol{X}'(t), \tag{2.10}$$

at this point upon differentiating Eq. (2.8) with respect to $\boldsymbol{X}$, we obtain:

$$\mathcal{J}_{\mathcal{F}_\tau}\, \delta\boldsymbol{X}(t) = \delta\boldsymbol{X}(t+T). \tag{2.11}$$

where $\mathcal{J}_{\mathcal{F}_\tau} = \frac{\partial \mathcal{F}_\tau}{\partial \boldsymbol{X}}$ is the Jacobian matrix of the map. We input this relation back to Eq. (2.10)

$$\left(\mathcal{J}_{\mathcal{F}_\tau} \cdot \delta\boldsymbol{X}(t)\right)^T \cdot \Omega \cdot \left(\mathcal{J}_{\mathcal{F}_\tau} \cdot \delta\boldsymbol{X}'(t)\right) = \delta\boldsymbol{X}^T(t) \cdot \Omega \cdot \delta\boldsymbol{X}'(t), \tag{2.12}$$

implying (since $\delta\boldsymbol{X}(t)$ and $\delta\boldsymbol{X}'(t)$ are arbitrary) that the matrix $\mathcal{J}_{\mathcal{F}_\tau}$ satisfies:

$$\Omega = \left(\mathcal{J}_{\mathcal{F}_\tau}\right)^T \cdot \Omega \cdot \left(\mathcal{J}_{\mathcal{F}_\tau}\right). \tag{2.13}$$

Hamiltonian maps inherently satisfy this condition and as we will see later this is a property of the larger class of symplectic maps. Eq. (2.13) is the differential expression of the preservation of ω and is related to the local behaviour of the map $\mathcal{F}_\tau$.

2.2 Symplectic systems

We have already seen that the Hamiltonian flows preserve the symplectic form Eq. (2.4) and consequently the Jacobian of the flow satisfies the symplectic condition Eq. (2.13). These properties have more consequences, than just the conservation of the volume in phase space and are characteristic of a larger class of systems, called symplectic systems.

By definition a symplectic system is a dynamical system, where the flow in M_N is generated by a symplectic map $\mathcal{F}$. In analogy to Hamiltonian systems, $\mathcal{F} : M_N \to M_N$ is a symplectic map if it preserves the symplectic form:

$$\mathcal{F} * \omega = \omega \to \omega(\delta\mathcal{F}(\boldsymbol{X}), \delta\mathcal{F}(\boldsymbol{X}')) = \omega(\delta\boldsymbol{X}, \delta\boldsymbol{X}') \tag{2.14}$$

where $\delta\boldsymbol{X}, \delta\boldsymbol{X}'$ are tangent vectors to M_N. Locally this condition becomes a restriction for the Jacobian of $\mathcal{F}$:

$$\Omega = \left(\mathcal{J}_{\mathcal{F}}\right)^T \cdot \Omega \cdot \left(\mathcal{J}_{\mathcal{F}}\right) \tag{2.15}$$

Any map whose Jacobian satisfies Eq. (2.15) everywhere is called locally symplectic.

If the phase space is not simply connected, then the conservation of ω for curves that cannot be deformed to a point is an additional requirement. Maps that are symplectic in this second sense are called exactly symplectic. The composition of symplectic maps is also symplectic. To see this, suppose that $\mathcal{F}$ and $\mathcal{G}$ are two symplectic maps. Then

$$(\mathcal{F}\circ\mathcal{G})*\omega \to \omega(\delta\mathcal{F}(\mathcal{G}(\boldsymbol{X})),\delta\mathcal{F}(\mathcal{G}(\boldsymbol{X}'))) = \omega(\delta(\mathcal{G}(\boldsymbol{X})),\delta(\mathcal{G}(\boldsymbol{X}'))) = \omega(\delta\boldsymbol{X},\delta\boldsymbol{X}') \to \omega$$

where we used Eq. (2.14) for each map. So $\mathcal{F}\circ\mathcal{G}$ is symplectic. In the case of linear maps, we obtain that the symplecticity is a property closed under matrix multiplication and that the maps form a Lie Group, called the symplectic group $Sp(2N)$ [70]. Its Lie Algebra is the set of Hamiltonian matrices [70]. Thus, every near identity symplectic matrix can be obtained as the exponential of a Hamiltonian matrix and corresponds to the time τ-map of a linear Hamiltonian flow. There are symplectic matrices, however, that are not the exponentials of Hamiltonian matrices, for example, $\begin{pmatrix} -1 & 1 \\ 0 & -1 \end{pmatrix}$.

A straightforward deduction from Eq. (2.15) is obtained by calculating its determinant for a symplectic map $\mathcal{F}$:

$$\mathrm{Det}(\mathcal{J}_{\mathcal{F}}^{T}\Omega\mathcal{J}_{\mathcal{F}}) = \mathrm{Det}(\Omega) \implies (\mathrm{Det}\,\mathcal{J}_{\mathcal{F}})^2 = 1,$$

given that $\mathrm{Det}(\Omega) = 1$. This result constrains $\mathrm{Det}(\mathcal{J}_{\mathcal{F}})$ to be either ± 1. Symplecticity is even more restrictive for the spectrum of the Jacobian matrix and it will be demonstrated that $\mathrm{Det}(\mathcal{J}_{\mathcal{F}}) = +1$, indicating that any symplectic map conserves both volume and orientation. This conservation is crucial for maintaining the fundamental properties of physical systems, such as invariance under symplectic transformations, which are essential in classical and quantum mechanics and are a consequence of the preservation of the symplectic form. Additionally, this inquiry into the determinant will also reveal a significant aspect of the eigenvalues of symplectic matrices, which are central to understanding stability and behaviour under dynamic transformations.

Let us examine the eigenvalue problem for $\mathcal{J}_{\mathcal{F}}$. The characteristic polynomial, which is a $2N$-order polynomial, is formulated as:

$$\mathrm{Det}(\mathcal{J}_{\mathcal{F}} - \lambda \mathbb{1}_{2N}) = 0. \tag{2.16}$$

This equation aids in determining the eigenvalues λ, which in turn describe the system's response to perturbations, pivotal in theoretical physics and applied mathematics. Given that the mapping is real, the characteristic polynomial associated with the matrix $\mathcal{J}_{\mathcal{F}}$ is also real. Therefore, if λ is an eigenvalue of M, then λ^*, its complex conjugate, must also be an eigenvalue of $\mathcal{J}_{\mathcal{F}}$.

Intriguingly, by applying Eq. (2.15), we can reformulate Eq. (2.16) as follows:

$$\begin{aligned} 0 &= \mathrm{Det}(\Omega)\,\mathrm{Det}(\mathcal{J}_{\mathcal{F}} - \lambda \mathbb{1}_{2N}) = \mathrm{Det}(\Omega \mathcal{J}_{\mathcal{F}} - \lambda \Omega) \\ &= \mathrm{Det}(\left((\mathcal{J}_{\mathcal{F}})^T\right)^{-1} \Omega - \lambda \Omega) = \mathrm{Det}(\left((\mathcal{J}_{\mathcal{F}})^T\right)^{-1} - \lambda \mathbb{1}_{2N})\,\mathrm{Det}(\Omega) \\ &= \mathrm{Det}((\mathcal{J}_{\mathcal{F}})^{-1} - \lambda \mathbb{1}_{2N}). \end{aligned} \tag{2.17}$$

This deduction confirms that if λ is an eigenvalue of $\mathcal{J}_{\mathcal{F}}$, then it must also be an eigenvalue of its inverse, or λ^{-1} is an eigenvalue as well of $\mathcal{J}_{\mathcal{F}}$. This property indicates that the characteristic polynomial is reflexive and can be expressed in the form:

$$\begin{aligned} &\lambda^N + C_1\lambda^{N-1} + C_2\lambda^{N-2} + \cdots + C_2\lambda^{2-N} \\ &+ C_1\lambda^{1-N} + \lambda^{-N} = 0. \end{aligned}$$

This automatically restricts the determinant to $\mathrm{Det}(\mathcal{J}_{\mathcal{F}}) = 1$, since it is the product of the eigenvalues λ. Thus, we have proven that the Jacobian matrix of a symplectic map $\mathcal{F}$ satisfies :

$$\mathrm{Det}(\mathcal{J}_{\mathcal{F}}) = 1. \tag{2.18}$$

and thus it conserves the phase space volume. This result is significant because it means two-dimensional symplectic maps preserve the oriented area element $dp_1 \wedge dq_1$. As we mentioned this is also the volume in $\mathcal{M}_1$ and this implies that the argument works both ways. Any two-dimensional map that conserves area and orientation is necessarily locally symplectic, but this is not in general true for $N > 1$.

According to Eq. (2.17) the eigenvalues of symplectic matrices occur in pairs or quadruplets. If λ is real, it pairs with λ^{-1}. If λ is complex, with only one partner under these equations, then $\lambda^* = \lambda^{-1} \rightarrow |\lambda| = 1$, positioning it on the unit circle.

Moreover, if $\lambda = 1$ is an eigenvalue, it must have even multiplicity, aligning with the even dimensionality of the phase space. Lastly, if λ is neither real nor of unit modulus, a quadruplet of eigenvalues forms:

$$\lambda, \lambda^{-1}, \lambda^{*}, \lambda^{-1*}. \tag{2.19}$$

Symplecticity imposes a strong restriction on the spectrum of $\mathcal{J}_{\mathcal{F}}$ and thus on the linear stability of the orbits as well. Symplectic maps inherently lack asymptotic stability due to their nature and in general, the dynamics of a symplectic map consist of a complicated mixture of regular and chaotic motion [71]. Numerical studies [72] indicate that the chaotic orbits have positive Lyapunov exponents and fill sets of positive measure that are fractal in nature .Generally, symplectic systems exhibit four primary stability types based on eigenvalue pairs (λ, λ^{-1}):

- **Hyperbolic:** Here, λ is a real number greater than one, indicating exponential divergence or convergence in the map's trajectory.
- **Hyperbolic with reflection:** This type occurs when λ is real and less than minus one, reflecting a trajectory inversion alongside exponential changes.
- **Elliptic:** Characterized by $\lambda = e^{2\pi i\phi}$ with a magnitude of one, this type indicates a stable, rotational motion around fixed points, typically seen in conservative systems.
- **Krein quartet:** Involves complex λ not on the unit circle, leading to a quartet of eigenvalues $(\lambda, \lambda^{-1}, \lambda^{*}, \lambda^{*-1})$, often signalling instability due to mixed magnitude and oscillatory components.

Hyperbolic stability type [73] is characterized by exponential behaviours—either divergence or convergence—depending on whether the eigenvalue is greater than one or less than minus one, respectively. Hyperbolic stability indicates sensitive dependence on initial conditions, a hallmark of chaotic systems where nearby trajectories diverge exponentially from each other over time. This makes predicting long-term behaviour challenging due to the rapid growth or decay of perturbations. The elliptic stability type [73], implies a periodic or quasi-periodic motion around fixed points, akin to rotational dynamics. This condition is associated with conservative systems where no energy is gained or lost over time, resulting in bounded and regular trajectories. The elliptic stability type is crucial for understanding the behaviour

of systems in which long-term behaviour tends to be predictable and non-chaotic, such as in many classical mechanics problems and celestial mechanics scenarios. Krein quartet stability [73] typically indicates mixed behaviours in the system's dynamics, potentially leading to instability. This is because the presence of complex eigenvalues of the unit circle can result in motions that combine rotation and exponential growth or decay, complicating the system's predictability and potentially leading to chaotic dynamics. After this discussion, one can observe that for a periodic orbit to maintain linear stability, all eigenvalues must be elliptic, resulting in rotational dynamics specified by the rotation numbers ϕ. This stability implies a predictable, non-expanding motion, crucial for applications in physics and engineering where steady-state behaviours are desired.

It is important to mention that, while symplectic maps on M_N maintain certain conservation properties, the set comprised by volume-preserving transformations (with only the restriction $\mathrm{Det}(\mathcal{J}_\mathcal{F}) = 1$) is bigger. This distinction was famously highlighted by Gromov through his "Symplectic camel" theorem [74]. He demonstrated that, while it is straightforward to design a volume-preserving map that embeds a closed ball with radius r in $\mathbb{R}^{2n}$ into a cylindrical space $C_1(R) = \{(q,p) : q_1^2 + p_1^2 \leq R^2\}$ regardless of their sizes, doing so symplectically is impossible if $r > R$. This foundational result has spurred the development of symplectic capacity and advanced the field of symplectic topology [75].

The restriction on the Jacobian matrix of the dynamics restricts the Lyapunov exponents [76] as well, and in particular the Lyapunov exponents h of a symplectic system come in pairs of $(h, -h)$. To understand this, we present a brief proof.

Lyapunov exponents are instrumental in understanding the chaotic and regular motion of a system. Suppose that initially, the system starts at $\boldsymbol{X}(0) \in M_N$ and we perturb $\boldsymbol{X}(0)$ slightly by the tangent vector $\delta\boldsymbol{X}(0)$. The change of the tangent vector under the action of the dynamics of the map $\mathcal{F}$ the evolution is governed by the Jacobian matrix. Upon a single application, we can write that:

$$\delta\mathcal{F}(\boldsymbol{X}(0)) = \mathcal{J}_\mathcal{F}(\boldsymbol{X}(0)) \cdot \delta\boldsymbol{X}(0). \tag{2.20}$$

Consequently after t applications of the map we obtain :

$$\delta\boldsymbol{X}(t) = \delta\mathcal{F}^t(\boldsymbol{X}(0)) = \mathcal{J}_{\mathcal{F}^t}(\boldsymbol{X}(0))\, \delta\boldsymbol{X}(0). \tag{2.21}$$

where $\mathcal{F}^t \equiv \underbrace{\mathcal{F} \circ \cdots \circ \mathcal{F}}_{t-\text{times}}$. Actually, Eq. (2.21) tracks the evolution of the small deviation $\delta \boldsymbol{X}(0)$ from the trajectory $\{\boldsymbol{X}(0), \boldsymbol{X}(1), \boldsymbol{X}(t) = \mathcal{F}^t(\boldsymbol{X}(0))\}$. It is straightforward to observe that by using the chain rule we can decompose the Jacobian matrix of $\mathcal{F}$ along the trajectory as follows:

$$\mathcal{J}_{\mathcal{F}^t}(\boldsymbol{X}(0)) = \mathcal{J}_{\mathcal{F}}(\boldsymbol{X}(t-1))\, \mathcal{J}_{\mathcal{F}}(\boldsymbol{X}(t-2)) \ldots \mathcal{J}_{\mathcal{F}}(\boldsymbol{X}(0)) \tag{2.22}$$

The Lyapunov exponent for the initial condition $\boldsymbol{X}(0)$ is defined as :

$$h(\boldsymbol{X}(0)) = \lim_{t\to\infty} \frac{1}{t} \ln \frac{\|\delta \boldsymbol{X}(t)\|}{\|\delta \boldsymbol{X}(0)\|}. \tag{2.23}$$

By definition we know that $\|\delta \boldsymbol{X}(t)\|^2 = \delta \boldsymbol{X}(t)^T \delta \boldsymbol{X}(t)$ and by using Eq. (2.21) we can also write :

$$h(\boldsymbol{X}(0)) = \lim_{t\to\infty} \frac{1}{2t} \ln \frac{\|\delta \boldsymbol{X}(t)\|^2}{\|\delta \boldsymbol{X}(0)\|^2} = \lim_{t\to\infty} \frac{1}{2t} \ln \left[\mathbf{u}_0^T A_t(\boldsymbol{X}(0)) \mathbf{u}_0\right] \tag{2.24}$$

where $A_t(\boldsymbol{X}(0)) = \left(\mathcal{J}_{\mathcal{F}^t}(\boldsymbol{X}(0))\right)^T \mathcal{J}_{\mathcal{F}^t}(\boldsymbol{X}(0))$ and $\mathbf{u}_0 = \delta \boldsymbol{X}(0)/\|\delta \boldsymbol{X}(0)\|$. At large times, we approximate the Lyapunov exponent $h(\boldsymbol{X}(0))$ as:

$$h(\boldsymbol{X}(0)) \approx \frac{1}{2t} \ln \left[\mathbf{u}_0^T A_t(\boldsymbol{X}(0)) \mathbf{u}_0\right] \tag{2.25}$$

The matrix $A_t(\boldsymbol{X}(0))$ is a real non-negative Hermitian $2N \times 2N$ matrix and thus possesses real, non-negative eigenvalues and real eigenvectors. When $\mathbf{u}_0$ aligns with one of its eigenvectors, it defines specific approximate values for the Lyapunov exponent. These values, $h_j(\boldsymbol{X}(0)) = \frac{1}{2t} \ln \lambda_j(t)$, where $\lambda_j(t)$ is an eigenvalue, are sorted such that $h_1(\boldsymbol{X}(0)) \geq h_2(\boldsymbol{X}(0)) \geq \ldots \geq h_{2N}(\boldsymbol{X}(0))$. Here, h_1 is the greatest, and h_{2N}, potentially the smallest or most negative. As t increases towards infinity, these approximate values $h_j(\boldsymbol{X}(0))$ tend towards the true Lyapunov exponents:

$$h_1(\boldsymbol{X}(0)) \geq h_2(\boldsymbol{X}(0)) \geq \cdots \geq h_{2N}(\boldsymbol{X}(0)). \tag{2.26}$$

As we already mentioned, the composition of symplectic maps such as $\mathcal{F}^t$ is also a symplectic map and thus its Jacobian matrix is a symplectic matrix satisfying Eq. (2.13). It is straightforward that the transpose of a symplectic matrix is also symplectic meaning that $A_t(\boldsymbol{X}(0))$ satisfies as well Eq. (2.13) at any time moment and

consequently, its eigenvalues come in pairs $\lambda_j(t), \lambda_j^{-1}(t)$. Then the Lyapunov exponents should come in pairs $\pm h_j(\boldsymbol{X}(0)) = \frac{1}{2t} \ln \lambda_j^{\pm 1}(t)$.

Importantly, the value of the Lyapunov exponent is not dependent on a specific trajectory of the system but rather on the general behaviour of trajectories in the vicinity of the initial conditions over time. This independence from specific trajectories arises because the Lyapunov exponent is defined as a limit to an infinite time, averaging the divergence rates of trajectories starting from infinitesimally close initial states. Thus, it reflects a global property of the dynamical system rather than the particulars of individual trajectories. Even if specific trajectories might exhibit unique or erratic behaviours due to specific local dynamics, the Lyapunov exponent captures the average exponential rate of divergence or convergence. We can then omit the initial condition $\boldsymbol{X}(0)$ in Eq. (2.26):

$$h_1 \geq h_2 \geq \cdots \geq h_{2N}. \tag{2.27}$$

The set of all the Lyapunov exponents is also called as Lyapunov spectrum. The Lyapunov exponent is crucial for analysing chaotic behaviour in systems. Generally, a positive Lyapunov exponent is associated with chaos [76], indicating that even minor differences in initial conditions can exponentially increase, resulting in vastly different outcomes as time progresses. In contrast, a negative exponent points to diminishing differences over time, which is characteristic of stable or periodic systems [76]. Therefore, by examining the collective behaviour of trajectories that start from closely situated initial points, rather than focusing on individual paths, the Lyapunov exponent acts as a powerful statistical tool for assessing whether a system is likely to exhibit stable or chaotic behaviour.

2.3 Dual-Symplectic Classical Circuits

Firstly, I would like to mention that this part presents the theory that was demonstrated in [16]. This section extends our discussion on symplectic models by introducing a new class called dual-symplectic systems. Here, we present a methodology for computing exactly, their dynamical correlation functions using symplecticity. We begin with introducing the model of our study in Sec. , then in Sec. 2.3.2 we introduce the diagrammatic approach in the density space and derive our analytic results,

and finally, in Sec. 2.3.3 we introduce the Ising Swap Model and use it to benchmark our results.

2.3.1 The Model

Consider a classical system with N variables $\{\vec{X}_i\}$, indexed by $i = 0, \ldots, N-1$. For simplicity, we assume N is even. These variables inhabit a finite measure space M, with the phase space formed by the Cartesian product of N instances of M, denoted M_N. Time is discrete, indexed by $t \in \mathbb{Z}$, with local interactions modelled by a symplectic map $\Phi : M \times M \to M \times M$ affecting pairs of adjacent sites. This forms part of a brick-wall circuit protocol under periodic boundary conditions, $\vec{X}_{i+N} \equiv \vec{X}_i$ (refer to Fig. 2.4).

Define $\Phi_{ij} : M_N \to M_N$ as a local gate applying Φ to variables $\vec{X}_i$ and $\vec{X}_j$, and acting idly on others. The operators $\mathcal{T}_{even} = \Phi_{0,1}\Phi_{2,3}\ldots\Phi_{N-2,N-1}$ and $\mathcal{T}_{odd} = \Sigma^{-1} \circ \mathcal{T}_{even} \circ \Sigma$ are introduced, where Σ is a shift operation. The *Floquet Operator* $\mathcal{T}$, which advances the system by one-time step, is defined as:

$$\mathcal{T} = \mathcal{T}_{odd} \circ \mathcal{T}_{even}, \tag{2.28}$$

and is symplectic, composed of local symplectic maps. The two-site translational symmetry of the system is captured by $\Sigma^{-2}\mathcal{T}\Sigma^2 = \mathcal{T}$. A point in M_N is represented by bold capital letters, e.g., $\boldsymbol{X}$, and a point in M by a vector, e.g., $\vec{X}$.

The local gate is graphically depicted as a blue rectangle with two inputs and outputs, each representing an instance of M:

$\Phi =$ 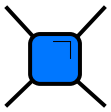 (2.29)

and based on this one can construct the diagrammatic representation of $\mathcal{T}$ as illustrated in Fig. 2.4.

2.3.2 Dynamical Correlations

2.3.2.1 Symplectic Gate

In this section, we explore 2-point correlation functions, and demonstrate how the property of symplecticity simplifies their calculation. Another way of studying a

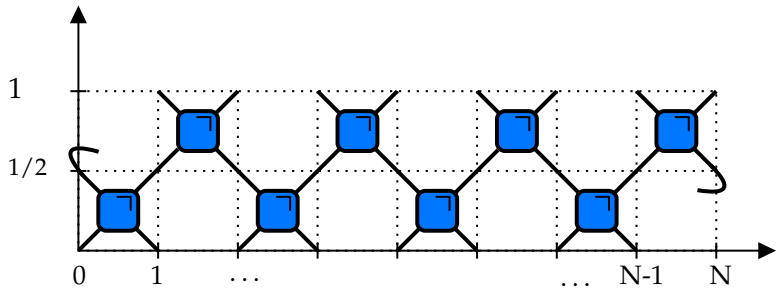

FIGURE 2.4: Graphical depiction of the symplectic brick-wall circuit's time evolution for one step. Figure taken from [16].

dynamical system is by its action on a density of initial conditions. The evolution of single trajectories defines the evolution of a density of "sprinkled" initial points on the phase space. To understand this better let us begin by defining the space of real functions over the phase space M_N:

$$D(M_N) = \{\rho | \rho : M_N \to \mathbb{R}\} \tag{2.30}$$

Phase-space distributions that fulfil the following conditions play a pivotal role:

$$\rho(\boldsymbol{X}) \in \mathbb{R}^+ , \quad \int d\boldsymbol{X} \rho(\boldsymbol{X}) = 1 . \tag{2.31}$$

It is advantageous for detailed analyses to consider the L^2 norm:

$$\|\rho\| = \left[\int d\boldsymbol{X} |\rho(\boldsymbol{X})|^2 \right]^{1/2} \tag{2.32}$$

Additionally, we introduce a Hermitian product:

$$\langle \rho_1 | \rho_2 \rangle = \int d\boldsymbol{X} \, \rho_1^*(\boldsymbol{X}) \rho_2(\boldsymbol{X}) , \quad \rho_1, \rho_2 \in L^2(M_N), \tag{2.33}$$

utilizing the braket notation $\langle \boldsymbol{X} | \rho | \boldsymbol{X} | \rho \rangle = \rho(\boldsymbol{X})$. Typically, any dynamical system defined by a map $\mathcal{F} : M_N \to M_N$ results in a dynamical transfer operator $\mathcal{P}_\mathcal{F} : D(M_N) \to D(M_N)$ known as the Frobenius-Perron operator with a Dirac delta kernel:

$$\mathcal{P}_h(\boldsymbol{X}, \boldsymbol{Y}) = \delta\big(\boldsymbol{X} - h(\boldsymbol{Y})\big) , \quad \boldsymbol{X}, \boldsymbol{Y} \in M_N, \tag{2.34}$$

which governs the dynamics based on initial conditions.

For the symplectic gate, which is reversible, the operator specifically acts on the phase-space distribution ρ as follows:

$$(\mathcal{P}_\Phi \circ \rho)(\boldsymbol{X}) = \int_{M_2} d\boldsymbol{Y}\, \delta\big(\boldsymbol{X} - \Phi(\boldsymbol{Y})\big)\rho(\boldsymbol{Y}) = \rho\big(\Phi^{-1}(\boldsymbol{X})\big)\,, \quad \boldsymbol{X} \in M_2 \tag{2.35}$$

This action is facilitated by the Jacobian of Φ, which is one since as explained in Sec.2.2 the symplectic property of Φ makes it a volume-preserving map, allowing $\mathcal{P}_\Phi$ to be modelled as an infinite-dimensional unitary matrix. The unitarity $\langle\rho_1|\mathcal{P}_\Phi^\dagger\mathcal{P}_\Phi|\rho_2\rangle = \langle\rho_1|\rho_2\rangle$ reflects the volume preservation in the phase space.

From Eq. (2.35), we can directly observe that a constant density ρ over M_2 is invariant under the action of $\mathcal{P}_\Phi$. An essential aspect of symplectic dynamics is the invariance of the uniform measure on the Hilbert space $L^2(M \times M)$ under the influence of the operator $\mathcal{P}_\Phi$. If we denote the measure of M as, $|M|$ then the local uniform measure is defined as $u = 1/|M| \to |u\rangle$. The uniform measure of two sites is then, $|u\rangle \otimes |u\rangle$ and one can construct the multi-site uniform measure in the same way. This operator's action preserves the existing structure and properties of the phase space, ensuring the constancy of the uniform measure:

$$\mathcal{P}_\Phi|u\rangle \otimes |u\rangle = |u\rangle \otimes |u\rangle;, \qquad \langle u| \otimes \langle u|\mathcal{P}_\Phi = \langle u| \otimes \langle u|, \tag{2.36}$$

In this setup, $\mathcal{P}_\Phi$ acts as a unitary operation in $L^2(M \times M)$, ensuring that left and right eigenvectors remain aligned. We typically use the normalized state $|\circ\rangle = \|u\|_2^{-1}|u\rangle$ for simplicity and clarity in our graphical representations, representing the state as: Eq. (2.36) is depicted as follows:

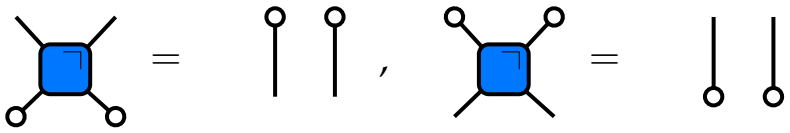

(2.37)

It is readily apparent that this characteristic ensures the Floquet transfer operator $\mathcal{T}$ maintains a stationary density represented by the uniform measure on M_N, symbolized as $|u_N\rangle = |u\rangle \otimes \ldots \otimes |u\rangle$. We also detail the L^2-normalized version $|\circ_N\rangle = \|u_N\|_2^{-1}|u_N\rangle$.

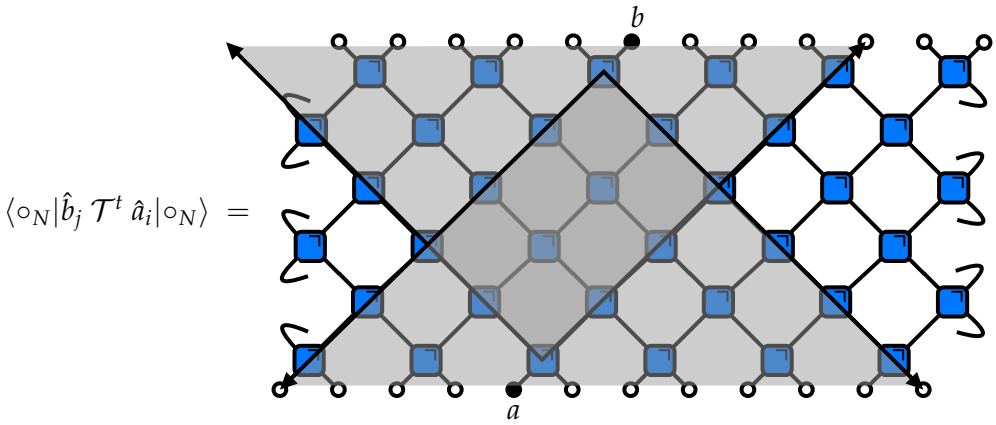

FIGURE 2.5: Graphical representations of the 2-point correlation function. The shaded grey areas and the black arrows delineate the causal cones attached to each local observable, with the "curly" edges denoting the periodic boundary conditions. The symplecticity of Φ simplifies this circuit to just the intersecting areas of the causal cones (double-shaded). Figure taken from [16].

Regarding any function defined on the phase space $a \in D(M_N)$ that represents a physical observable, its average across the phase-space density ρ is calculated by:

$$\int d\boldsymbol{X} \, a(\boldsymbol{X}) \rho(\boldsymbol{X}) = \langle 1_N | \hat{a} | \rho \rangle \tag{2.38}$$

The operation of $\hat{a}$ is specifically defined through $\langle \boldsymbol{X} | \hat{a} | \rho \rangle = a(\boldsymbol{X}) \rho(\boldsymbol{X})$, employing the unit scalar $|1_N\rangle \rightarrow 1_N(\boldsymbol{X}) = 1, \forall \boldsymbol{X} \in M_N$. The unit scalar $|1\rangle$ is equivalent to $\sqrt{|M|} |\circ\rangle$.

In general, for an ergodic symplectic system $|\circ_N\rangle$ is the unique invariant measure and thus at long times, any initial state will always converge to that. In our setting, we consider correlations of observables at long times and thus we focus on the invariant uniform measure. The connected dynamical correlation functions for the one-site observables are defined as:

$$C_{ab}(i,j;t) \equiv \langle 1_N | \hat{b}_j \mathcal{T}^t \hat{a}_i | u_N \rangle - \langle b_j \rangle \langle a_i \rangle = \langle \circ_N | \hat{b}_j \mathcal{T}^t \hat{a}_i | \circ_N \rangle - \langle \circ_N | \hat{b}_j | \circ_N \rangle \langle \circ_N | \hat{a}_i | \circ_N \rangle \tag{2.39}$$

where i, j range from 0 to $N-1$. Each local operator $\hat{a}_i$ acts exclusively on its corresponding site, formulated as $\hat{a}_i = \mathbb{1} \otimes \cdots \otimes \overset{\text{site } i}{\hat{a}} \otimes \cdots \otimes \mathbb{1}$. The second component represents the averages taken across the uniform measure, and for local observables, it is expressed as $\langle a_i \rangle = \langle 1_N | \hat{a}_i | u_N \rangle = \langle \circ | \hat{a} | \circ \rangle$.

Our primary focus is on the significant first term $\langle 1_N | \hat{b}_j \mathcal{T}^t \hat{a}_i | u_N \rangle$ within the correlation analysis, depicted in Fig. 2.5. Here, operations on single sites such as $\hat{a} | \circ \rangle$ or

$\hat{b}|\circ\rangle$ are marked with a bullet. The circuit's invariance under two-site shifts allows us to map the correlations from any index i to 0 or 1, depending on its even or odd status. This adjustment results in the correlations splitting into two distinct types:

$$C_{ab}(i,j;t) = \begin{cases} C^{+}_{ab}(j-i;t) & i = even \\ C^{-}_{ab}(j-i;t) & i = odd. \end{cases} \tag{2.40}$$

As illustrated in Fig. 2.5, by applying Eq. (2.37), all gates outside the light cone are removed. This light-cone spreads at a velocity of $v_c = 2$ from the operator's position $\hat{a}$ at the base. A similar logic is applied from the top, starting at the position j of the operator $\hat{b}$. This suggests that gates must only reside within the intersecting region of the forward and backward light-cones. Specifically, when $|i-j| > 2t$, these cones do not meet, resulting in trivially uncorrelated observables. Conversely, when $|i-j| \leq 2t$, the overlapping cones may produce non-vanishing correlations. Beyond $t > N/4$, light cones reach the boundary, introducing finite-size effects and complicating analytical predictions. Hence, we focus on times $t \leq N/4$ where the behaviour mimics that observed in the thermodynamic limit $N \to \infty$. The symplecticity of the gate $\mathcal{P}_\Phi$, as outlined in Eq. (2.37), helps eliminate any gates outside the intersection of these two cones. This leads to the following visual representation:

$\langle \circ_N | \hat{b}_j \, \mathcal{T}^t \, \hat{a}_i | \circ_N \rangle \; =$

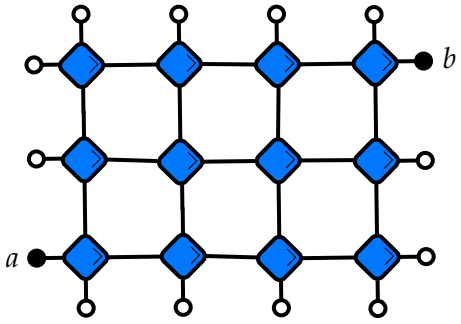

(2.41)

The diagram is rotated by 45° and we do not consider the case with the local observables on the same edge of the light-cone. The rectangle can be decomposed into rows or columns, which are represented as two different types of contracting transfer operators. This idea appears in the same manner in the folded picture of unitary circuits [77], and although it represents an important simplification, the calculation of 2-point correlation functions, remains challenging particularly, when $|i-j|$ does not scale with t, because the size of the involved transfer operators grows with time. We

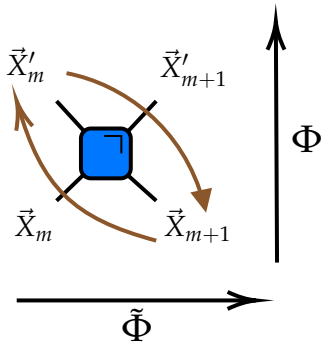

FIGURE 2.6: The local map Φ acting on two adjacent spins orchestrates their temporal dynamics. The innovative diagonal leg swapping transforms Φ into its dual map $\tilde{\Phi}$, which then governs spatial dynamics. This switch effectively transposes the time and space dimensions, propagating temporal changes spatially. Figure taken from [16]

will see in the following section that for dual symplectic gates additional simplifications are possible which allows one to calculate the correlation functions explicitly.

The discussion in this section established a diagrammatic method of dealing with classical symplectic circuits and as we shall see in the next section, this approach simplifies more in the case of dual-symplectic dynamics.

2.3.2.2 Dual-Symplectic Gates

To extract exact calculations, we introduce a specialized condition in the dynamics: the requirement for the gate Φ to be dual-symplectic. This means that the system's evolution remains symplectic when the roles of space and time are interchanged. To this end, we define a dual map $\tilde{\Phi}$, in the same way as in dual-unitary circuits [78]. Specifically, this map is defined by swapping the diagonal legs as illustrated in Fig. 2.6, resulting in the exchange of the axes of time and space. This leg swapping moves us from the dynamics in time direction to the ones in space, which is called the dual picture.

From Fig. 2.6, one can observe that in the dual picture, knowing the time evolution of a single site is enough to define the time evolution of its neighbour. This allows us to infer the entire system's time evolution from that of a single site. Diagrams like those shown in Fig 2.5 can be reinterpreted in the spatial direction, from left to right, by replacing Φ with $\tilde{\Phi}$. Such diagrams are more than visual aids; they represent integrals over the phase space M_N. Moving to the dual picture demands a change of integration variables, which is represented by the swapping of the aforementioned diagonal legs of Φ. However, there is an extra factor appearing, due to

the Jacobian of this transformation.

For the diagrammatic interpretations in both space and time directions, to remain consistent under this change of variables, the Jacobian must equal 1. This holds when the local gate Φ satisfies the following conditions:

$$\left|\det\left(\frac{\partial\Phi^1(\vec{X}_1,\vec{X}_2)}{\partial\vec{X}_2}\right)\right| = \left|\det\left(\frac{\partial\Phi^2(\vec{X}_1,\vec{X}_2)}{\partial\vec{X}_1}\right)\right| = 1 \quad ,\forall\vec{X}_1,\vec{X}_2 \in M\times M, \tag{2.42}$$

where $\Phi^{1,2}$ are the single-site outputs of the local gate defined as $\left(\Phi^1(\vec{X}_1,\vec{X}_2),\Phi^2(\vec{X}_1,\vec{X}_2)\right) = \Phi(\vec{X}_1,\vec{X}_2)$. One can move to the dual picture, by swapping the legs on either of the two diagonals of Φ, and that is why we get two conditions in Eq. (2.42). We present a detailed proof of Eq. (2.42) in Appendix A.1. Moreover, the dual map is an involution by definition, implying that the dual of the dual picture corresponds to the original one under Φ. Thus, our approach is consistent when $\tilde{\Phi}$ satisfies Eq. (2.42) as well. This condition is established in Appendix A.1. In the broader context, while an arbitrary symplectic map often possesses a non-unique or undefined dual one over $M\times M$, our focus is on a local gate Φ with a uniquely determined $\tilde{\Phi}$, satisfying Eq. (2.42).

Furthermore, with the additional property of dual-symplecticity, the set of graphical contraction rules specified by Eq. (2.37) expands to:

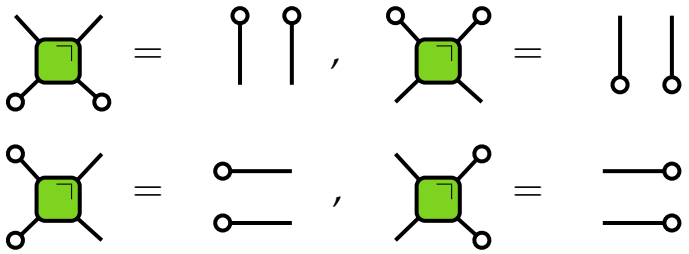

(2.43)

where a dual-symplectic gate is highlighted in green. This property ensures the preservation of the uniform measure in the spatial direction. Analogous to quantum systems, termed dual unitarity, this characteristic has led to the derivation of exact results in various systems. Similar results are anticipated for dual-symplectic dynamics. Indeed, herein, we demonstrate the utility of dual-symplecticity in precisely determining dynamical correlation functions. Notably, these correlations survive only along the edges of causal cones, with Eq. (2.40) assuming the form:

$$C_{ab}(i,j;t) = \begin{cases} \delta_{j-i,2t}\, C^{+}_{ab}(2t;t) & i = \text{even} \\ \delta_{j-i,-2t}\, C^{-}_{ab}(-2t;t) & i = \text{odd}. \end{cases} \tag{2.44}$$

We aim to demonstrate this using the established diagrammatic representation. To simplify the correlations outlined in Eq. (2.41), we utilize Eq. (2.43) at the corners of the rectangular area in Eq. (2.41), where the two adjacent $|\circ\rangle$, allow for further contraction of the diagram.

Repeating this procedure, we find that the diagram simplifies to the second term of Eq. (2.39), leading to the disappearance of connected correlations. As long as corners with two adjacent $|\circ\rangle$ exist, correlations vanish except in the cases where the surface area of the cross-section is zero and the parities of the local observables' sites match. This scenario implies that one side of the rectangle has a length of zero, reducing it to a line segment of length $2t$ with observables positioned at the edges.

From Fig. 2.5, it's apparent that depending on the parity of site i, one can have two different line segments:

$C^{+}_{a,b}(v_c t, t) =$ 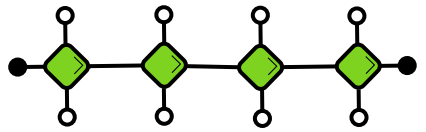 $i = \text{even}$

$C^{-}_{a,b}(-v_c t, t) =$ 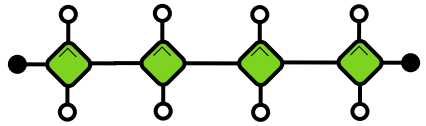 $i = \text{odd}$ (2.45)

For even i, correlations survive along the right-moving light edge, while for odd i, the same holds for the left-moving edge. Notably, analysing correlations of a single parity suffices, as correlations with opposite parity can be derived via a reflection of the circuit. In particular, if one performs a reflection across the axis passing between points $(N/2-1, N/2)$ in Fig. 2.5, then every site $i = 0, \ldots, N-1$ is mapped to $N-1-i$ and the two edges of the causal cone are being exchanged. Additionally, this reflection alters not only the parity of sites but also the spatial order of input and output states, transforming the local gate as $\mathcal{P}_\Phi \to P \circ \mathcal{P}_\Phi \circ P$, where P represents the Swap operation.

Expressing the correlations in terms of two distinct one-site transfer operators,

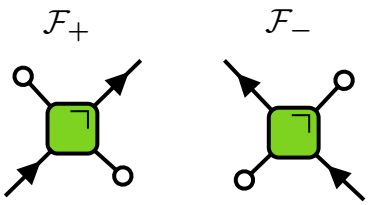

FIGURE 2.7: Graphical representation of two different types of transfer operators $\mathcal{F}_\pm$. The left (right) operator corresponds to the right (left) moving light edge in Eq. (2.45). Figure taken from [16].

denoted by $\mathcal{F}\pm$, we define the linear maps $\mathcal{F}\pm : L^2(M) \to L^2(M)$, where $\pm$ corresponds to even/odd parity, respectively. Graphically, these operators are depicted in Fig. 2.7.

Additionally, we observe the reflection property mentioned earlier, which maps the transfer operator of one parity to the other. Consequently, we'll omit the $\pm$ label, focusing solely on $\mathcal{F}+ \equiv \mathcal{F}$. As a result, according to Eq. (2.45), the correlations along the edges of the light cone take the form:

$$C_{a,b}(2t;t) = \langle\circ|\hat{b}\,\mathcal{F}^{2t}\,\hat{a}|\circ\rangle - \langle\circ|\hat{b}|\circ\rangle\langle\circ|\hat{a}|\circ\rangle \tag{2.46}$$

This is an important exact result, revealing that in dual-symplectic circuits, correlations are explicitly determined by transfer operators acting on a single site. Although the operator $\mathcal{F}$ is not generally Hermitian, as demonstrated in Appendix A.2, it is positive and a weak contraction. Assuming a pure point spectrum, as typically observed in the spin chain examples examined later, its spectral decomposition reads:

$$\mathcal{F} = \sum_{i=0}^{\infty} \mu_i \left|\mu_i^R\right\rangle \left\langle\mu_i^L\right|, \tag{2.47}$$

where we indicated the left and right eigenvectors as $|\mu_i^R\rangle$, $\langle\mu_i^L|$, and ordered the eigenvalues as $|\mu_0| \geq |\mu_1| \geq \ldots$. As it's a weak contraction, its spectrum lies within the unit disk, implying $|\mu_i| \leq 1$. Additionally, it is established in [79] that eigenvalues with $|\mu_i| = 1$ have equal algebraic and geometric multiplicities, resulting in trivial Jordan blocks. A direct implication of the dual-symplectic nature of $\mathcal{P}_\Phi$ is the invariance of the uniform measure under $\mathcal{F}$, guaranteeing the existence of the trivial eigenvalue $\mu_0 = 1$ with $\left|\mu_0^R\right\rangle = |\circ\rangle$ and $\left\langle\mu_0^L\right| = \langle\circ|$.

Substituting the spectral decomposition Eq. (2.47) into Eq. (2.46), we obtain:

$$C_{ab}(v_c t;t) = \sum_{i=1}^{\infty} \left\langle\circ\middle|\hat{b}\middle|\mu_i^R\right\rangle \left\langle\mu_i^L\middle|\hat{a}\middle|\circ\right\rangle \mu_i^{2t}, \tag{2.48}$$

where the $i = 0$ term in the sum cancels with the second term in Eq. (2.46).

It is worth noting that the spectrum of $\mathcal{F}$ can be used to analyse the level of ergodicity of our dual-symplectic system. Depending on the number of non-trivial eigenvalues equal to 1 or having a unit modulus, dual-symplectic circuits can exhibit various levels of ergodicity, as summarized in Table 2.8. For instance, in the non-interacting scenario, all eigenvalues are unimodular ($|\mu_i| = 1$), leading to correlations that either remain constant or oscillate around zero. Conversely, in the non-ergodic case, where more than one but not all eigenvalues are equal to 1, the correlations decay to a non-thermal value. When the system is ergodic and non-mixing, all non-trivial μ_i are not equal to 1, with at least one having a unit modulus, resulting in correlations oscillating around zero and their time averages vanishing at long times. Finally, for an ergodic and mixing system, all μ_i are within the unit disk, leading to correlations that decay to zero. A simple example of a non-interacting scenario is the dual-symplectic local gate $\mathcal{P}_\Phi = P \circ (\mathcal{P}_{\phi_1} \otimes \mathcal{P}_{\phi_2})$, where P represents the Swap gate and ϕ_1, ϕ_2 are single-site symplectic maps.

2.3.3 The Ising-Swap Model

Earlier, we investigated an abstract dual-symplectic circuit. To validate our general analytical findings, we now turn our attention to a 1D classical spin chain, where the local phase space is the unit sphere $M \equiv \mathcal{S}^2$. Here, we denote the coordinates by $\vec{X}_i \equiv \vec{S}_i$ with the constraint $|\vec{S}_i| = 1$. We introduce the 3-parameter family of dual-symplectic local gates, given by:

$$\Phi_{(\alpha,\beta,\gamma)} := \Big(R_x(\beta) \otimes R_x(\gamma)\Big) \circ I_\alpha \circ \Big(R_x(\gamma) \otimes R_x(\beta)\Big). \tag{2.49}$$

Here, $R_n(\theta), \theta \in [0, 2\pi)$ represents a single spin rotation (SO(3) rotation matrix) with respect to the axis $n \in \{x, y, z\}$ by an angle θ. I_α denotes the Ising Swap gate, defined

eigenvalues $\mu_i, \quad i \neq 0$	*non−interacting*	*non−ergodic*	*ergodic, non−mixing*	*ergodic, mixing*
$\mu_i = 1$		$\mu_1, \mu_2, \dots, \mu_{j<\infty}$		
$\lvert\mu_i\rvert = 1$	$\mu_1, \mu_2, \dots, \mu_\infty$	$\mu_{j+1}, \mu_{j+2}, \dots, \mu_{j+m<\infty}$	$\mu_1, \mu_2, \dots, \mu_{j<\infty}$	
$\lvert\mu_i\rvert < 1$		$\mu_{j+m+1}, \mu_{j+m+2}, \dots, \mu_\infty$	$\mu_{j+1}, \mu_{j+2}, \dots, \mu_\infty$	$\mu_1, \mu_2, \dots, \mu_\infty$

FIGURE 2.8: The table with all the different levels of ergodicity, concerning the non-trivial eigenvalues. Figure taken from [16].

as:

$$I_\alpha(\vec{S}_1, \vec{S}_2) = \left(R_z(\alpha S_1^z)\vec{S}_2, R_z(\alpha S_2^z)\vec{S}_1\right) \tag{2.50}$$

where α is the coupling constant of the interactions, $R_z(\theta)$ is a rotation around the z-axis, and S_i^z is the z-component of $\vec{S}_i$.

Assuming the SO(3) Poisson bracket on the unit sphere :

$$\{S_i^a, S_j^b\} = \delta_{ij}\epsilon_{abc}S_i^c \tag{2.51}$$

with ϵ_{abc} being the Levi–Civita symbol, Eq. (2.50) is easily recognized as the symplectic evolution of two sites under the Hamiltonian $H_{12} = \alpha S_1^z S_2^z$ for a time step $\delta t = 1$, followed by a Swap operation $(S_1^n, S_2^n) \to (S_2^n, S_1^n)$.

The spin variables, as implied by Eq. (2.51), are not the pairs (q, p) of conjugate variables, as typically expected in symplectic dynamics. However, a symplectic transformation can map from one set of conjugate variables to another. Here, we select the pairs φ_i, z_i with z_i being the Cartesian coordinate along the z-axis and φ_i representing the azimuthal angle of the i-th site. They satisfy :

$$\{\varphi_i, z_j\} = \delta_{ij} \quad , \quad \{\varphi_i, \varphi_j\} = \{z_i, z_j\} = 0 \tag{2.52}$$

The spin variables correspond to unit vectors on the sphere, expressed in terms of φ_i and z_i as:

$$S_i^x = \sqrt{1 - z_i^2}\cos(\varphi_i) \quad , \quad S_i^y = \sqrt{1 - z_i^2}\sin(\varphi_i) \quad , \quad S_i^z = z_i, \tag{2.53}$$

and it's easy to confirm that Eq. (2.53) satisfies the SO(3) Poisson bracket Eq. (2.51).

In Appendix A.3, we explicitly demonstrate that $\Phi(\alpha, \beta, \gamma)$ satisfies Eq. (2.42), enabling equivalent interpretations of the diagrams in both temporal and spatial directions. Employing the same method as in Appendix A.1, we derive the space-time dual of our model, defined as :

$$\tilde{\Phi}_{(\alpha,\beta,\gamma)} \equiv (\mathbb{1} \otimes (-\mathbb{1})) \circ \Phi_{(\alpha,-\beta,\gamma)} \circ ((-\mathbb{1}) \otimes \mathbb{1}), \tag{2.54}$$

where $\mathbb{1}$ represents the identity map and $-\mathbb{1}$ indicates a change of sign for all components $S_i^q \to -S_i^q$. Thus, the dual dynamics differs from the temporal one by a

simple sign transformation. As outlined in [15], our map $\Phi_{(\alpha,\beta,\gamma)}$ is space-time self-dual because flipping the spins in a checkerboard pattern is enough to move us to the dual picture. Dual-symplectic circuits with local gates Eq. (2.49) accommodate both ergodic and integrable cases depending on parameter choices. For instance, when $\alpha = 0$, the model becomes trivially non-interacting, signifying integrability. Another integrable scenario arises when both β and γ are either 0 or π, preserving the z-components of spins along their respective light rays and yielding conserved extensive quantities along lattice parity bipartitions. These local conserved quantities, termed gliders, have been examined in prior studies on dual-unitary quantum circuits [22]. Later, in Eq. (2.60), we provide analytical results for auto-correlation of z-components at integrable points where they do not decay to zero. Such models are also labelled super-integrable as they support an exponentially large number of extensive conserved quantities, obtainable by summing arbitrary products of z-components along the mentioned bipartitions, e.g., $\mathcal{Q} = \sum_i z_i z_{i+2} z_{i+4}$. At integrable points within the parameter space, phase space trajectories are confined to invariant tori, and the Lyapunov spectrum diminishes [80]. Conversely, away from these points, chaotic behaviour is anticipated. In Fig. 2.9, we depict examples of the Lyapunov spectrum at chaotic points in our Ising Swap model, where it exhibits a positive maximal Lyapunov exponent, indicating sensitivity to initial conditions, a characteristic feature of chaotic systems.

Having selected our family of local gates, we proceed with the computation of correlations. In Appendix A.4, we provide an analytical calculation of the transfer operator, both in phase space and density space:

$$f = R_x(\gamma) Q(\alpha) R_x(\gamma) \quad , \quad \mathcal{F} \equiv \mathcal{P}_f, \tag{2.55}$$

where $Q(\alpha) = \frac{1}{2}\int_{-1}^{1} dz' R_z(\alpha z')$ and $f : M \to M$. The transfer operator serves as the Frobenius-Perron operator of f, and its kernel is given in the same manner as in Eq. (2.34), for single-site phase space. Rotations maintain the total angular momentum, and since $\mathcal{F}$, per Eq. (2.55), is a composition of rotations, it shares this property. More precisely, denoting $J_i, i = x, y, z$ as the generators of single-site rotations, and $J^2 = \sum_i J_i^2$ as the angular momentum squared, it follows that $\mathcal{F}$ commutes with the total angular momentum operator and thus exhibits a block-diagonal form

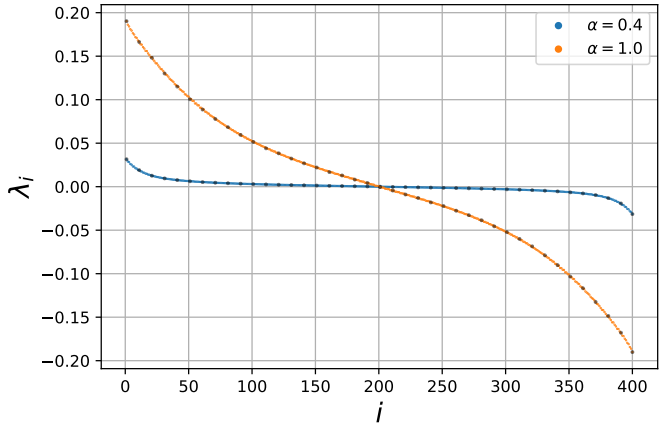

FIGURE 2.9: Lyapunov spectrum λ_i of the Ising Swap model, for two different coupling constants $\alpha = 0.4, 1$, angles $\beta = \sqrt{2}\pi, \gamma = \sqrt{3}\pi/2$, and system size $N = 200$. The figures were obtained for $t = 800$ and a sample size of $N_{sample} = 10^4$ initial states drawn from the uniform measure. The black circles represent the Lyapunov spectrum at every 10 exponents at time $t = 700$, showing excellent time convergence for λ_i. The spectrum is symmetric concerning the horizontal axis, as expected for a symplectic system, and has a positive maximal Lyapunov exponent indicating chaoticity for $\Phi_{\alpha,\beta,\gamma}$. Figure taken from [16].

in its eigenvalues. However, this characteristic doesn't stem from an underlying rotational symmetry but rather from the specific form of the local gate $\mathcal{P}_{\Phi_{\alpha,\beta,\gamma}}$. Indeed, the Ising swap gate in $\mathcal{P}_{\Phi_{\alpha,\beta,\gamma}}$ involves a *non-linear rotation*, i.e., a rotation whose angle depends on the z component of the neighbouring spin. Due to this nonlinearity, it doesn't exhibit a block-diagonal structure concerning the eigenvalues of J^2. Thus, the dynamics do not preserve J^2 and they do not demonstrate a rotational symmetry.

It's noteworthy that Eq. (2.55) is entirely independent of β. The correlation with the opposite parity is simply retrieved from the midpoint reflection $P \circ \mathcal{P}_{\Phi_{\alpha,\beta,\gamma}} \circ P = \mathcal{P}_{\Phi_{\alpha,\gamma,\beta}}$, which is equivalent to changing $\beta, \gamma \to \gamma, \beta$.

The Ising Swap model is defined via rotations, and that indicates the use of spherical harmonics as a convenient basis for the $L^2(\mathcal{S}^2)$ density space. In Appendices A.4 and A.5, we derive analytical expressions for the representations of $\mathcal{F}$ and $\mathcal{P}_{\Phi_{\alpha,\gamma,\beta}}$ in this basis for, which we parametrize $\mathcal{S}^2$ with z, φ. The spherical harmonics $|\ell, m\rangle$ correspond to $Y_{\ell,m}(z, \varphi)$ for $\ell = 0, 1, \ldots$, and $|m| \leq \ell$, forming a convenient orthonormal basis for $L^2(\mathcal{S}^2)$ functions.

Our strategy focuses on finding the representation of the transfer operator on this basis. Given that $\mathcal{F}$ preserves the total angular momentum, it assumes a block-diagonal form in ℓ, with each block of dimension $2\ell + 1$. Hence, the eigenvectors and eigenvalues in Eq. (2.47) can be indexed by a block index ℓ and an index $\tilde{m}$

within each block. Consequently, Eq. (2.48) takes the form:

$$C_{a,b}(2t,t) = \sum_{\ell=1}^{\infty} \sum_{\tilde{m}=-\ell}^{\ell} \left\langle \circ \middle| \hat{b} \middle| \mu^{R}_{\ell,\tilde{m}} \right\rangle \left\langle \mu^{L}_{\ell,\tilde{m}} \middle| \hat{a} \middle| \circ \right\rangle \mu^{2t}_{\ell,\tilde{m}}. \tag{2.56}$$

Considering the expression, we observe that if the local observables $|a_x\rangle, |b_y\rangle$ are confined within a finite number of total angular momentum subspaces, then the sum in Eq. (2.56) becomes finite. Specifically, only the shared values of ℓ between the two observables are relevant.

For instance, the observable $a(z,\phi) = z^2$ has non-zero overlaps only for $\ell = 0, 2$. Likewise, any polynomial in the variable z affects a finite number of blocks. This feature, as established in Appendix A.6, suggests that a limited set of exponentials in t suffices to capture the dynamics of the 2-point correlations when one of the observables a, b involves a finite number of ℓ blocks. In practical terms, one can determine the exact dynamical correlations by diagonalizing the common ℓ finite-dimensional blocks of $\mathcal{F}$. Additionally, observables lacking such overlapping subspaces yield vanishing correlations at all time steps.

Now, let's delve into some analytical findings for the selection of $a(z,\phi) = z^n$ and $b(z,\phi) = z$, where $n \in \mathbb{Z}^+$. In this scenario, a expands over $\ell = 0, 2, \ldots n$ when n is even, and $\ell = 1, 3, \ldots n$ when n is odd. Meanwhile, b expands only over $\ell = 1$. We can observe that when n is even, there are no overlapping subspaces shared between the two observables, resulting in correlations vanishing for all t. However, for odd n, the correlations solely depend on the $\ell = 1$ block of $\mathcal{F}$. Utilizing Eq. (2.55), we can explicitly derive the eigenvalues of this block:

$$\begin{aligned} \mu_{1,0} &= \frac{\sin(\alpha)}{\alpha} \\ \mu_{1,-1} &= \frac{(\alpha + \sin(\alpha))\cos(2\gamma) - \Delta(\alpha,\gamma)}{2\alpha} \\ \mu_{1,1} &= \frac{(\alpha + \sin(\alpha))\cos(2\gamma) + \Delta(\alpha,\gamma)}{2\alpha}, \end{aligned} \tag{2.57}$$

where $\Delta(\alpha,\gamma) = \sqrt{(\alpha + \sin\alpha)^2 \cos^2(2\gamma) - 4\alpha \sin(\alpha)}$. As only the $\ell = 1$ subspace contributes, we solely need to know the overlaps of the observables with this subspace:

$$\langle 1m | z^n \rangle = \frac{2\sqrt{3\pi}}{n+2} \delta_{m,0}. \tag{2.58}$$

The observable z^n is independent of the angle φ of $\mathcal{S}^2$, thus relying only on the spherical harmonics $|\ell m\rangle$ with $m = 0$. By diagonalizing the block of $\mathcal{F}$ corresponding to $\ell = 1$ and utilizing Eq. (2.57) and Eq. (2.58), we derive the exact expression for the correlations:

$$\begin{aligned} C_{a,b}(2t,t) &= \frac{1}{2^{2t+1}(n+2)}\left(\mathcal{E}^{+}(t)+\mathcal{E}^{-}(t)\right) \\ \mathcal{E}^{\pm}(t) &= \left(1 \pm \frac{\alpha-\sin\alpha}{\Delta}\right)\left(\frac{(\alpha+\sin\alpha)\cos(2\gamma)\pm\Delta}{\alpha}\right)^{2t}, \end{aligned} \tag{2.59}$$

where the opposite parity is obtained by substituting $\gamma \to \beta$. In the special integrable cases, we find:

$$\lim_{\alpha\to 0} C_{a,b}(2t,t) = \frac{\cos(4\gamma t)}{2+n} \quad , \quad \lim_{\gamma\to 0} C_{a,b}(2t,t) = \frac{1}{2+n}. \tag{2.60}$$

In Fig. 2.10, we present the results of the numerics, indicating that the correlations vanish everywhere except along the edges of the causal cone, thus confirming Eq. (2.59) for $n = 1$. It should be noted that we take advantage of the symmetries of our circuit for the numerical evaluation of the correlations. Specifically, in addition to the 2-site translation invariance, there exists a 1 time step translation invariance due to the correlations being evaluated over the invariant measure. Both of these symmetries allow us to average over a larger sample size, enhancing the accuracy of the numerical data.

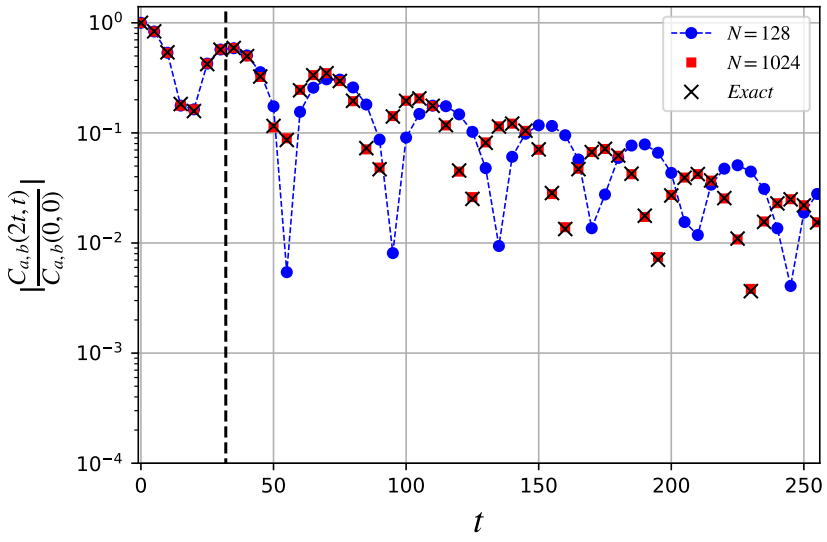

(A)

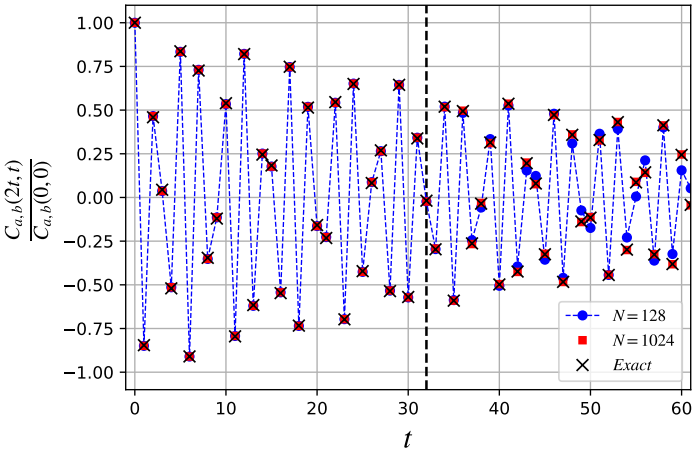

(B)

FIGURE 2.10: Normalized auto-correlations for the S^z spin component are presented, using the maximum value $C_{a,b}(0,0)$ for systems containing $N = 128, 1024$ spins. We use the parameters $\alpha = 0.3$, $\beta = \frac{\sqrt{2}}{4}\pi$, and $\gamma = \frac{\sqrt{2}}{2}\pi$, and the initial conditions are sampled $N_{\text{sample}} = 5 \times 10^4$ times. (A): The space-time correlation function $|C_{a,b}(x,t)/C_{a,b}(0,0)|$ for $N = 128$ shows that it diminishes outside the boundary ($x = v_c t$) of the causal cone. (B): This graph also contrasts the theoretical predictions for $C_{a,b}(x,t)/C_{a,b}(0,0)$ at the causal cone's right boundary, derived from Eq. (2.59), with results from exact diagonalization within the $\ell = 1$ subspace. A dashed line marks the time $t = N/4$ for $N = 128$, indicating the point beyond which the theory, suited to the thermodynamic limit, breaks apart. Post this time moment, the $N = 128$ system's results diverge from exact predictions, whereas the larger system size, $N = 1024$, continues to show robust agreement with theoretical expectations. Figure taken from [16].

Chapter 3

Chaos and Unitary designs

Although unitary designs are a well-studied subject, in this chapter we will study the overlaps between quantum states evolved under generic RUCs and demonstrate our novel results of a universal distribution that generalizes the PT distribution. These results contribute to the advancement of the field by providing, a comprehensive framework for understanding the statistical properties of overlaps in chaotic quantum systems and their implications for quantum state preparation and complexity.

The chapter is structured as follows:

- In Sec. 3.1 we provide an introduction to unitary designs, containing their definition and an introduction to Haar measure and Weingarten function. The reader may skip this section if he is already familiar with the subject.
- In Sec. 3.2, we present in detail the methodology we followed to recover the novel results on the distribution of the overlaps, as well as the theoretical and numerical benchmarking of our theory with the Random Phase Model [39]. We finally obtain the universal probability distribution of the overlaps from the moments, for the case of open boundary conditions(obc). In contrast, in the case of periodic boundary conditions(pbc), we obtain an in-law relation to another random variable, which is related to the exponentiation of a matrix drawn from the Gaussian Unitary Ensemble (GUE).

3.1 Unitary designs

3.1.1 k-designs

The interrelation between pseudorandomness and chaotic dynamics becomes evident when considering operator evolution. For example, let A be a local operator, acting on a single spin. Under a chaotic Hamiltonian H, the evolved operator

$A(t) = e^{iHt}Ae^{-iHt}$ is in general non-local operator due to the coupling terms in H and can be described by an expansion in terms of multiple local operators, each associated with a pseudorandom coefficient, written as follows:

$$A(t) = \sum_{j=0}^{\infty} \frac{(it)^j}{j!} \underbrace{[H, \ldots [H}_{j}, A \underbrace{]\ldots]}_{j}. \tag{3.1}$$

which is a special application of the Baker-Campbell-Hausdorff (BCH) formula. If H encompasses l-local interactions and is sufficiently "generic," the j-th term in this series consists of roughly $\sim (n/l)^{lj}$ terms, each with weights ranging from 1 to $\sim j(l-1)$, assuming a system of n spins with a Hilbert space dimension $d = 2^n$:

- At $j \sim n/(l-1)$, numerous terms of maximum weight n suggest delocalization across the system, indicative of fast-scrambling behaviour.
- When j approaches $2n/l \log(n/l)$, the sum of terms escalates to 2^{2n}, indicating complete engagement of the system because 2^{2n} is the total number of orthogonal linear operators acting on the Hilbert space.

These dynamics underscore the swift expansion and complexity typical of chaotic quantum systems, with the timescale for complete system coverage given by $t \sim O(\log n)$.

Over time, $A(t)$ is expected to span the entire unitary group. At sufficiently large times t, $A(t)$ might for many purposes resemble a random operator $\tilde{A} \equiv U^\dagger A(0)U$, where U is randomly selected from the unitary group. If this approximation holds, $A(t)$ would exhibit pseudorandom behaviour.

The expansion and complexity of $A(t)$ can be probed using a second local operator V. Specifically, the group commutator $A(t)^\dagger V^\dagger A(t)V$ serves as a measure of the butterfly effect and the strength of chaos in the system:

- If $A(t)$ remains of low weight with few terms, then $A(t)$ and V approximately commute, i.e., $[A(t), V] \approx 0$, making the operator $W(t)^\dagger V^\dagger A(t)V$ close to the identity.
- Conversely, if the dynamics are highly chaotic, $A(t)$ will eventually have significant commutators with virtually all other local operators in the system, rendering $A(t)^\dagger V^\dagger A(t)V$ nearly random and with a minimal expectation value in most states.

This leads to the decay of out-of-time-order correlator (OTOC), expressed as:

$$\left\langle A(t)^\dagger V^\dagger A(t) V \right\rangle = \left\langle U(t)^\dagger A^\dagger U(t) V^\dagger U(t)^\dagger A U(t) V \right\rangle \tag{3.2}$$

where $U(t) = e^{-iHt}$ is the unitary time evolution operator. This correlator, typically evaluated in a thermal state, acts as a straightforward diagnostic for quantum chaos [81], illustrating how quantum information becomes delocalized over time due to chaotic dynamics. The expectation value above is taken over the thermal state with density matrix $\rho = e^{-\beta H} / \operatorname{Tr}\{e^{-\beta H}\}$.

For chaotic systems and at sufficiently long timescales, the correlators described by Eq. (3.2) tend to minimise to a value, effectively represented by the transformation $A(t) \to U^\dagger A U$, with U being a randomly chosen unitary operator, drawn from the Haar measure. This behaviour aligns with the information-theoretic concept of scrambling, initially explored in [27].

However, the adequacy of OTOCs, as outlined in Eq. (3.2), as a definitive diagnostic for chaos remains an open question. The original analysis in [27] did not strictly require the dynamics to be represented by a uniformly random unitary of the Haar distribution, but a less complex ensemble, capable of replicating only certain moments of the Haar distribution, would suffice for many practical purposes. There may be other finer-grained properties of a system that are hidden at higher moments and would require a larger ensemble to replicate the statistics of the Haar random dynamics.

The extent to which a set of operators mimics the uniform distribution is effectively quantified by the concept of unitary k-designs, referenced in [82]. A unitary k-design is a probability distribution over a finite set of unitary matrices which cannot be distinguished from the uniform distribution over the entire unitary group (the Haar measure [83]), with respect to any test involving at most k copies of a unitary matrix from this distribution. This condition can be expressed in several ways, which we will explore in more detail later in this chapter.

If $U(d)$ is the d dimensional unitary group, then the set $\mathcal{E} = \{(p_i, U_i)\}_{i=1,\dots,N}$, $0 \geq p_i \leq 1, U_i \in U(d)$ is what we call an ensemble/distribution of unitary operators for the discrete case. The distribution should be normalised, thus $\sum_{i=1,N} p_i = 1$ In the case of continuous distribution, the definition becomes $\mathcal{E} = \{(dU, U)\}_{i=1,\dots,N}, U \in U(d)$ for some measure dU over $U(d)$.

Let f be a polynomial in $2d^2$ variables, considered as a function of an arbitrary $U \in U(d)$. Specifically, f is evaluated on the matrix elements of U and their complex conjugates $f(U) := f(U, U^*)$. We now provide a precise definition of the unitary k-design, keeping in mind that $\int_{\text{Haar}}$ refers to the integration over $U(d)$ with Haar measure:

Definition 1 *A probability distribution $\mathcal{E} = \{(p_i, U_i)\}_{i=1,\dots,N}$ over unitary matrices on $\mathcal{H} = \mathbb{C}^d$ is a unitary k-design if for any polynomial f in $2d^2$ variables, which is homogeneous of degree k in each variable:*

$$\int_{Haar} f(U)\, \mathrm{d}U = \sum_{U_i \in \mathcal{E}} p_i f(U_i)$$

Definition 2 *A probability distribution $\mathcal{E} = \{(p_i, U_i)\}_{i=1,\dots,N}$ over unitary matrices on $\mathcal{H} = \mathbb{C}^d$ is a unitary k-design if for all $\rho \in \mathcal{B}\left(\mathcal{H}^{\otimes k}\right)$:*

$$\int_{Haar} U^{\dagger \otimes k} \rho\, U^{\otimes k} \mathrm{d}U = \sum_{U_i \in \mathcal{E}} p_i U_i^{\dagger \otimes k} \rho\, U_i^{\otimes k}$$

(both of the definitions are straightforward to be extended to a continuous $\mathcal{E}$ as well.) where $\mathcal{B}(\mathcal{H}^{\otimes k})$ is the set of all linear operations on $\mathcal{H}^{\otimes k}$. Much of the research on unitary k-designs has been formulated according to Definition 2. The operation described in this definition is known as Twirl operation and plays an important role in many schemes for entanglement purification [84].

In both definitions, we observe that the left side of the equation, which deals with an infinite object and is challenging to compute, equals the expression on the right side which works with a finite object and is substantially easier to compute. The previously stated definitions of unitary k-designs are equivalent. To see this , rather than considering a general polynomial f, it is sufficient to focus on f as a monomial:

$$x_0^{b_0} x_1^{b_1} \dots x_{d^2-1}^{b_{d^2-1}} y_0^{c_0} y_1^{c_1} \dots y_{d^2-1}^{c_{d^2-1}} \tag{3.3}$$

where x_i, y_i are matrix elements of U, U^* respectively. If Definition 1 holds for all such monomials f, it will similarly apply to all polynomials f. By taking a specific element of the tensor in Definition 2, which is an operator in, $\mathcal{H}^{\otimes k}$ we end up with:

$$\int_{U(d)} dU \rho_{\alpha,\beta} (U^{\dagger \otimes k})_{m,\alpha} (U^{\otimes k})_{\beta,n} = \sum_{U_i \in \mathcal{E}, \alpha, \beta} p_i\, \rho_{\alpha\,\beta} (U_i^{\dagger \otimes k})_{m,\alpha} (U_i^{\otimes k})_{\beta,n} \tag{3.4}$$

where the bold indexes are defined like $\boldsymbol{\alpha} = (\alpha_1, \alpha_2, \ldots, \alpha_k)$, with $\alpha_i = 1, 2, \ldots, d$. And $(U^{\otimes k})_{\boldsymbol{m},\boldsymbol{\alpha}} = U_{m_1,\alpha_1} U_{m_2,\alpha_2} \ldots U_{m_k,\alpha_k}$ are monomials in the form of Eq. (3.3). This is just a compact way of indexing elements of an operator on $\mathcal{H}^{\otimes k}$. Consequently, Eq. (3.4) is a linear combination of such monomials f and the validity of Definition 1 is an adequate condition for Definition 2 to be satisfied. On the other way around, for the right choice of ρ ($\rho_{\boldsymbol{\alpha},\boldsymbol{\beta}} = \delta_{\boldsymbol{\alpha},\boldsymbol{m},\boldsymbol{\beta},\boldsymbol{n}}$) the summation in, Eq. (3.4) reduces to just a single monomial and according to the same logic, any polynomial f satisfies Definition 1, showing that one can prove the one definition from the other in both ways.

Usually in literature, definition 2 is expressed through the k-fold channel $\Phi_{\mathcal{E}}^{(k)}$ for a distribution $\mathcal{E}$. In particular, the action of the k-fold channel defined by the ensemble $\mathcal{E}$ is defined as:

$$\Phi_{\mathcal{E}}^{(k)}(\rho) := \sum_i p_i U_i^{\dagger \otimes k} \rho U_i^{\otimes k} \tag{3.5}$$

and for continuous distributions:

$$\Phi_{\mathcal{E}}^{(k)}(\rho) := \int_{\mathcal{E}} dU \; U_i^{\dagger \otimes k} \rho U^{\otimes k} \tag{3.6}$$

Thus one can rewrite Definition 2 as

Definition 3 *An ensemble $\mathcal{E}$ is considered a unitary k-design if*

$$\Phi_{\mathcal{E}}^{(k)}(\rho) = \Phi_{Haar}^{(k)}(\rho)$$

for any operator ρ.

Conceptually, a unitary k-design is as statistically random as the Haar ensemble up to the kth moment. This implies that a unitary k-design meets the criteria established by Definition 1, particularly when $f(U)$ includes terms up to the kth powers of U and U^* (including monomials of maximum degree k). Thus, if an ensemble is k-design, it also consists a $k-1$-design, although the reverse is not true in general. Moreover, it is straightforward to see that $\Phi_{\mathcal{E}}^{(k)}$ is linear operation since it satisfies $\Phi_{\mathcal{E}}^{(k)}(\lambda\rho + \lambda'\rho') = \lambda\Phi_{\mathcal{E}}^{(k)}(\rho) + \lambda'\Phi_{\mathcal{E}}^{(k)}(\rho')$ for any operators ρ, ρ' and $\lambda, \lambda' \in \mathbb{C}$.

3.1.2 Haar measure and Weingarten function

In this section, I present more details on the Haar measure and the calculation of integrals over Haar random unitary operators.

The focus is on the finite-dimensional Hilbert space $\mathcal{H}_k = \mathcal{H}^{\otimes k}$, which is practically k copies of $\mathcal{H}$. If I denote the basis of $\mathcal{H}_k$ as $\{|\alpha_1, \alpha_2, \ldots, \alpha_k\rangle\}, \quad \alpha_i = 1, 2, \ldots, d$ then the permutation operator P_σ, is defined by the action on the basis:

$$\begin{aligned} &P_\sigma \, |\alpha_1, \alpha_2, \ldots, \alpha_k\rangle = \left|\alpha_{\sigma(1)}, \alpha_{\sigma(2)}, \ldots, \alpha_{\sigma(k)}\right\rangle \\ &\text{or equivalently} \\ &\langle \beta_1, \beta_2, \ldots, \beta_k | P_\sigma | \alpha_1, \alpha_2, \ldots, \alpha_k \rangle = \delta_{\boldsymbol{\beta}, \sigma(\boldsymbol{\alpha})} \end{aligned} \tag{3.7}$$

where I compacted the index notation as $\boldsymbol{\alpha} = (\alpha_1, \alpha_2, \ldots, \alpha_k)$ and the permutation over the indices as $\sigma(\boldsymbol{\alpha}) = (\alpha_{\sigma(1)}, \alpha_{\sigma(2)}, \ldots, \alpha_{\sigma k})$.

This operation, essentially permutes the k-copies by the permutation $\sigma \in S_k$ and thus it implies that if ρ_i is an operation on a single copy $\mathcal{H}$ then

$$P_\sigma^{-1} (\rho_1 \otimes \cdots \otimes \rho_k) P_\sigma = \rho_{\sigma(1)} \otimes \cdots \otimes \rho_{\sigma(k)} \tag{3.8}$$

Using the definition Eq. (3.7) one can easily prove some properties of the permutation operator. Specifically,

- P_σ is a unitary operation
  Proof: $\langle \boldsymbol{\alpha} | P_\sigma^\dagger P_\sigma | \boldsymbol{\beta} \rangle = \sum_\gamma \langle \boldsymbol{\alpha} | P_\sigma^\dagger | \gamma \rangle \langle \gamma | P_\sigma | \boldsymbol{\beta} \rangle = \sum_\gamma \langle \gamma | P_\sigma | \boldsymbol{\alpha} \rangle \langle \gamma | P_\sigma | \boldsymbol{\beta} \rangle =$
  $= \sum_\gamma \delta_{\gamma, \sigma(\boldsymbol{\alpha})} \delta_{\gamma, \sigma(\boldsymbol{\beta})} = \delta_{\sigma(\boldsymbol{\alpha}), \sigma(\boldsymbol{\beta})} = \delta_{\boldsymbol{\alpha}, \boldsymbol{\beta}} \rightarrow P_\sigma^\dagger P_\sigma = \mathbb{1}$. In the same way, one can also prove that $P_\sigma P_\sigma^\dagger = \mathbb{1}$

- $P_\sigma P_{\sigma'} = P_{\sigma\sigma'}$ making P_σ a representation of the permutation S_k group of order k, over $\mathcal{H}_k$
  Proof: $\langle \boldsymbol{\alpha} | P_\sigma P_{\sigma'} | \boldsymbol{\beta} \rangle == \sum_\gamma \langle \boldsymbol{\alpha} | P_\sigma | \gamma \rangle \langle \gamma | P_{\sigma'} | \boldsymbol{\beta} \rangle = \sum_\gamma \delta_{\boldsymbol{\alpha}, \sigma(\gamma)} \delta_{\gamma, \sigma'(\boldsymbol{\beta})} = \delta_{\boldsymbol{\alpha}, \sigma\sigma'(\boldsymbol{\beta})} =$
  $\langle \boldsymbol{\alpha} | P_{\sigma\sigma'} | \boldsymbol{\beta} \rangle$

- From the two properties above, it is straightforward that $P_\sigma^{-1} = P_{\sigma^{-1}}$

Theorem 1 *Consider the algebra $L\left(\mathcal{H}^{\otimes k}\right)$ comprising all operators on the tensor space $\mathcal{H}^{\otimes k}$. Let $U(d)$ represent the unitary group on the Hilbert space $\mathcal{H}$. An operator ρ belongs to $L\left(\mathcal{H}^{\otimes k}\right)$ and commutes with every operator of the form $V^{\otimes k}$, where V is any element of*

$U(d)$, if and only if A can be expressed as a linear combination of permutation operators P_σ:

$$\left[\rho, V^{\otimes k}\right] = 0, \ \forall V \quad \Leftrightarrow \quad \rho = \sum_{\sigma \in S_k} c_\sigma P_\sigma. \tag{3.9}$$

From Eq. (3.8) is straightforward to see that the permutation of the copies of the same operator ($\rho_i = V$) does not make a difference and thus P_σ commits with $V^{\otimes k}$. Thus, when ρ is constructed as a linear combination of permutation operators, it naturally commutes with $V^{\otimes k}$. For more details on this theorem, you can refer to [85].

According to Eq. 3.6 if ρ being an operator in the tensor product space $\mathcal{H}^{\otimes k}$, then the k-fold channel of ρ with respect to the unitary group is:

$$\Phi^{(k)}_{\text{Haar}}(\rho) := \int_{\text{Haar}} U^{\dagger \otimes k} \rho U^{\otimes k} \, dU, \tag{3.10}$$

where the integration is over the unitary group with respect to the Haar measure [83], which is the unique, both left and right-invariant probability measure on the unitary group, satisfying:

$$\int_{\text{Haar}} dU = 1, \tag{3.11}$$

$$\int_{\text{Haar}} f(VU) \, dU = \int_{\text{Haar}} f(UV) \, dU = \int_{\text{Haar}} f(U) \, dU, \tag{3.12}$$

for any $V \in U(\mathcal{H})$ and for any function f. At this part, I am going to use the Haar measure properties to extract some properties of $\Phi^{(k)}_{\text{Haar}}$. Assuming $f(U) = U^{\dagger \otimes k} \rho U^{\otimes k}$, it follows that:

$$V^{\dagger \otimes k} \Phi^{(k)}_{\text{Haar}}(\rho) V^{\otimes k} = \Phi^{(k)}_{\text{Haar}} V^{\dagger \otimes k} \rho V^{\otimes k} = \int_{\text{Haar}} (V^\dagger U^\dagger)^{\otimes k} \rho (UV)^{\otimes k} = \\ = \int_{\text{Haar}} f(UV) \, dU = \Phi^{(k)}_{\text{Haar}}(\rho),$$

demonstrating that the k-fold channel is invariant under k-fold unitary conjugation of itself or its argument operator ρ:

$$\Phi^{(k)}_{\text{Haar}}(V^{\dagger \otimes k} \rho V^{\otimes k}) = V^{\dagger \otimes k} \Phi^{(k)}_{\text{Haar}}(\rho) V^{\otimes k} = \Phi^{(k)}_{\text{Haar}}(\rho), \tag{3.13}$$

where the properties Eq. (3.12) of right and left invariance of the Haar measure are used.

Eq. (3.13) asserts that $\Phi^{(k)}_{\text{Haar}}(\rho)$ commutes with all operators of the type $V^{\otimes k}$. Thus, we can apply Theorem 1 to express this as

$$\Phi^{(k)}_{\text{Haar}}(\rho) = \sum_{\sigma \in S_k} P_\sigma \cdot v_\sigma(\rho), \tag{3.14}$$

By taking advantage of the linearity of the $k-$fold channel, one can deduce that $v_\sigma(\lambda\rho + \lambda'\rho') = \lambda v_\sigma(\rho) + \lambda' v_\sigma(\rho')$ for any ρ, ρ' and $\lambda, \lambda' \in \mathbb{C}$, and thus $v_\sigma(\rho)$ is a linear function of ρ. The function $v_\sigma(\rho)$ can be represented as

$$v_\sigma(\rho) = \text{Tr}\left\{D_\sigma \rho\right\} \tag{3.15}$$

for some operators D_σ. The k-fold conjugation invariance Eq. (3.13) suggests that:

$$\Phi^{(k)}_{\text{Haar}}(V^{\dagger\otimes k}\rho V^{\otimes k}) = \Phi^{(k)}_{\text{Haar}}(\rho) \tag{3.16}$$

$$\sum_{\sigma \in S_k} P_\sigma v_\sigma(V^{\dagger\otimes k}\rho V^{\otimes k}) = \sum_{\sigma \in S_k} P_\sigma v_\sigma(\rho) \implies v_\sigma(V^{\dagger\otimes k}\rho V^{\otimes k}) = v_\sigma(\rho) \implies \tag{3.17}$$

$$\text{Tr}\Big\{D_\sigma V^{\dagger\otimes k}\rho V^{\otimes k}\Big\} = \text{Tr}\{D_\sigma \rho\} \tag{3.18}$$

Since this is true for any ρ, one can choose $\rho = |\boldsymbol{\alpha}\rangle\langle\boldsymbol{\alpha}'|$, for any $\boldsymbol{\alpha}, \boldsymbol{\alpha}'$ and finally obtain that:

$$V^{\otimes k} D_\sigma V^{\dagger\otimes k} D_\sigma = D_\sigma \tag{3.19}$$

So D_σ commutes with all operators $V^{\otimes k}$ and by reapplying Theorem 1, one can obtain:

$$\Phi^{(k)}_{\text{Haar}}(\rho) = \sum_{\sigma,\lambda \in S_k} W_{\sigma,\lambda} P_\sigma \,\text{Tr}\left\{P_\lambda \rho\right\}. \tag{3.20}$$

where the coefficients $W_{\sigma,\lambda}$ form a matrix over S_k, known as the Weingarten matrix. The action of the $k-$ fold Haar Channel depends explicitly on $\text{Tr}\{P_\lambda\rho\}$. Given Eq. (3.8) the permutation operator commutes with the $k-$copies of an operator of the form $U^{\otimes k}$ and thus $\Phi^{(k)}_{\text{Haar}}(P_\lambda) = P_\lambda$. According to this last relation, we derive that

$$P_\lambda = \sum_{\sigma,\lambda} W_{\sigma,\lambda} P_\sigma \,\text{tr}\left\{P_\lambda P_\sigma\right\}, \tag{3.21}$$

using that $\text{Tr}\left\{P_\sigma P_\lambda\right\} = d^{\#\text{cycles}(\sigma\lambda)}$, we end up with

$$\delta_{\sigma,\lambda} = \sum_{\sigma \in S_k} W_{\sigma,\lambda} C_{\sigma,\lambda}, \quad C_{\sigma,\lambda} := d^{\#\text{cycles}(\sigma\lambda)}, \tag{3.22}$$

where $\delta_{\sigma,\lambda}$ is the Kronecker delta, indicating the identity between permutations σ and λ in S_k. Eq. (3.22) can be expressed in a more compact way as the matrix multiplication $\mathbb{1} = WC$ and thus the Weingarten matrix is defined as:

$$W = C^{-1} \tag{3.23}$$

Here, it was assumed that the inverse C^{-1} exists, which is true for $k \leq d$. I should mention that the cycle decomposition is a common characteristic of the permutations belonging to the same conjugacy class, $\#\text{cycles}(p\lambda p^{-1}) = \#\text{cycles}(\lambda), \forall p, \lambda \in S_k$ making the $\#\text{cycles}(.)$ a class function. Applying this at Eq. (3.22), one deduces that $C_{p\sigma,\lambda p^{-1}} = C_{\sigma,\lambda}$. This can be, equivalently, written as:

$$B(p)CA(p) = C, \forall p \in S_k \tag{3.24}$$

where I define the matrices $A(p)_{\sigma_1,\sigma_2} = \delta_{\sigma_1,\sigma_2 p^{-1}}$ and $B(p)_{\sigma_1,\sigma_2} = \delta_{\sigma_1,p\sigma_2}$. Due to their definitions, it is straightforward to observe that $A^{-1}(p) = A(p^{-1})$ and $B^{-1}(p) = B(p^{-1})$. By inverting Eq. (3.24) I manage to recover the following property of the Weingarten function

$$A(p)WB(p) = W, \forall p \in S_k \tag{3.25}$$

where, I replaced p^{-1} with p.

In order to understand better how to calculate a k-fold Haar channel, I present the case of $k = 2$ copies. In this scenario, the symmetric group contains only two elements $S_2 = \{I = (1)(2), S = (12)\}$ and C is a 2×2 matrix. The identity permutation I is composed by 2 cycles and the transposition S by one, meaning that:

$$C = \begin{bmatrix} d^2 & d \\ d & d^2 \end{bmatrix} \tag{3.26}$$

and by inverting it, we can directly find the Weingarten matrix:

$$W = \frac{1}{d^2 - 1} \begin{bmatrix} 1 & -1/d \\ -1/d & 1 \end{bmatrix}$$

From Eq. (3.20) the Haar channel becomes explicitly:

$$\Phi^{(2)}_{\text{Haar}}(\rho) = \frac{1}{d^2 - 1} \left(I[\text{Tr}\{\rho\} - \frac{1}{d}\text{Tr}\{S\rho\}] + S[\text{Tr}\{S\rho\} - \frac{1}{d}\text{Tr}\{\rho\}] \right) \tag{3.27}$$

One can extend the previous considerations to the k-fold average of a Haar random state. One can define a random state by $|\psi\rangle = U|0\rangle$, where U is uniformly sampled from the unitary group $U(d)$ and $|0\rangle$ is a normalised state in $\mathcal{H}$. The integration over Haar measure of this state tensorized k times is given by Eq. (3.20)

$$\int_{\text{Haar}} (|\psi\rangle\langle\psi|)^{\otimes k} d\psi := \Phi^{(k)}_{\text{Haar}}\left((|0\rangle\langle 0|)^{\otimes k}\right) = \sum_{\sigma,\lambda\in S_k} W_{\sigma,\lambda} P_\sigma \,\text{Tr}\left\{P_\lambda |0\rangle\langle 0|)^{\otimes k}\right\} = \tag{3.28}$$

$$= \sum_{\sigma,\lambda\in S_k} W_{\sigma,\lambda} P_\sigma = \sum_{\sigma\in S_k} c_\sigma P_\sigma \tag{3.29}$$

where the k copies of $|0\rangle$ are invariant under any permutation, $P_\lambda \,|0\rangle^{\otimes k} = |0\rangle^{\otimes k}$ and the normalisation leads to $\text{Tr}\left\{|0\rangle\langle 0|^{\otimes k}\right\} = \langle 0|0\rangle^k = 1$. The last thing one needs to calculate is the expression $c_\sigma = \sum_{\lambda\in S_k} W_{\sigma,\lambda}$. In matrix representation, it can be written as $\vec{v}_\sigma^T W \vec{v}_1$ with $(\vec{v}_\sigma)'_\sigma = \delta_{\sigma,\sigma'}$ being one of the vectors of the basic and $\vec{v}_1 = (1, 1, \dots)$. By the definitions of, $A(p), B(p)$ one can directly deduce the following:

$$A(p)\vec{v}_1 = B(p)\vec{v}_1 = \vec{v}_1 \quad , \quad A(p)\vec{v}_\sigma = \vec{v}_{\sigma p^{-1}},\ B(p)\vec{v}_\sigma = \vec{v}_{p\sigma} \forall p \in S_k \tag{3.30}$$

Finally, I use these equations as well as Eq. 3.25:

$$\vec{v}_\sigma^T A(p) W B(p) \vec{v}_1 = \vec{v}_\sigma^T W \vec{v}_1 \implies \vec{v}^T_{\sigma p^{-1}} W \vec{v}_1 = \vec{v}_\sigma^T W \vec{v}_1 \implies c_{\sigma p^{-1}} = c_\sigma \forall p \in S_k \tag{3.31}$$

The quantity $c_\sigma = c \forall \sigma \in S_k$ is common for every permutation and the $k-$fold average becomes

$$\int_{\text{Haar}} (|\psi\rangle\langle\psi|)^{\otimes k} d\psi = c \sum_{\sigma\in S_k} P_\sigma \tag{3.32}$$

. At this point, I am taking advantage of the normalisation of $|\psi\rangle$ and by tracing Eq. (3.32)

$$c_\sigma = c = \frac{1}{\sum_{\lambda\in S_k} d^{\#\,\text{cycles}(\lambda)}} = \frac{1}{k!\binom{k+d-1}{k}}. \tag{3.33}$$

Finally, one arrives at the relationship

$$\int_{\text{Haar}} (|\psi\rangle\langle\psi|)^{\otimes k} d\psi = \frac{1}{k!\binom{k+d-1}{k}} \sum_{\sigma\in S_k} P_\sigma. \tag{3.34}$$

Before ending this section, we should mention a useful mathematical trick that

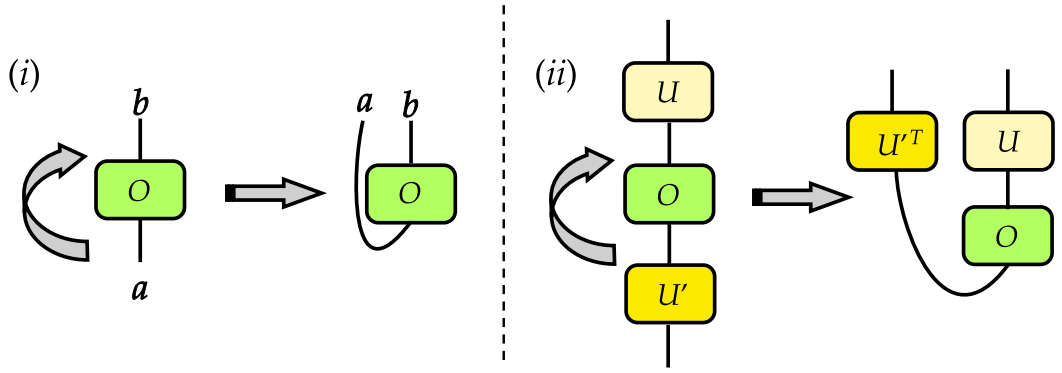

FIGURE 3.1: (i) The folded picture of an operator over $\mathcal{H}_k$, with each leg representing the degrees of freedom of $\mathcal{H}_k$. (ii) The product UOU' of operators, which in the folded picture becomes $U'^T \otimes U \,|O\rangle\rangle$

we are going to need later. This trick is called the "folded" picture and is used to map an operator over $\mathcal{H}_k$, to a state in $\mathcal{H}_{2k}$ and thus the "folding" transfers us from a $k-$copies Hilbert space to a $2k$-copies one. For example, an arbitrary operator O over $\mathcal{H}_k$ with elements, $O_{\boldsymbol{a},\boldsymbol{b}}$ will be mapped to the state $|O\rangle\rangle \in \mathcal{H}_{2k}$ with components $\langle \boldsymbol{a},\boldsymbol{b}|O\rangle\rangle = O_{\boldsymbol{a},\boldsymbol{b}}$. This is graphically represented in Fig. 3.1. In the same figure, there is as well the demonstration of a product of operators. Another example that we are going to use later is the "folded" picture of the permutation operator defined in Eq. (3.7), which is symbolised as $|\sigma\rangle\rangle$, has elements $\langle \boldsymbol{a},\boldsymbol{b}|\sigma\rangle\rangle = \delta_{\boldsymbol{a},\sigma(\boldsymbol{b})}$ and is graphically depicted as

$$|\sigma\rangle\rangle \;\rightarrow$$

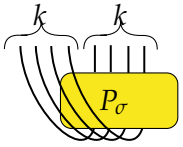

(3.35)

where each leg represents the degrees of freedom of $\mathcal{H}$. The state $|\sigma\rangle\rangle$ is known as the permutation state. A final important example that we are going to need later is the $k-$fold Haar channel, which according to Eq. (3.20), its folded picture will be

$$\Phi^{(k)}_{\text{Haar}}(.) \rightarrow \sum_{\sigma,\lambda\in S_k} W_{\sigma,\lambda} \langle\langle \lambda|.\rangle\rangle \;|\sigma\rangle\rangle \tag{3.36}$$

which is represented diagrammatically as

$$\Phi^{(k)}_{\text{Haar}} \rightarrow \sum_{\sigma,\lambda \in S_k} W_{\sigma,\lambda}$$

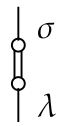

(3.37)

where each open leg represents the degrees of freedom of $\mathcal{H}_{2k}$ and each permutation "bond", depicted with the double lines has a weight given by the Weingarten matrix.

3.2 Universal distributions of overlaps from unitary dynamics

I would like to, firstly, inform the reader that this part showcases the theory and results presented in [37]. The authors in [36] have already proved the Porter-Thomas distribution, which is, practically, the distribution that one recovers for overlaps $w' = \mathcal{N} \langle \Psi_1 | \Psi_2 \rangle$ of quantum states $|\Psi_1\rangle, |\Psi_2\rangle$ when they are being sampled from the Haar ensemble and $\mathcal{N}$ is the dimension of the Hilbert space. However, in this section, we emphasize on something more general and in particular, on the distribution of these overlaps when $|\Psi_1\rangle, |\Psi_2\rangle$ come from a random circuit that forms a k-design. Particularly, in our study, we focus on the scaling limit where both time t and space L are large. The regime is characterized by the parameter $x = L/L_{\text{Th}}(t)$, with $L_{\text{Th}}(t)$ representing the volume scale at which complete scrambling occurs. We find exact results for a family of universal distributions $p(w'; x)$, largely independent of microscopic details and for two different types of boundary conditions: periodic ones (pbc) and open (obc). This scaling regime is mapped to a statistical model where the moments of the overlaps are expressed as a partition function, via a transfer matrix. This leads to an effective statistical one-dimensional model with ferromagnetic interactions in permutation space, where universality emerges from the density of dilute domain wall excitations governed by x.

The methodology followed is extensive, and for this purpose, I organise this section as follows:

- In Sec. 3.2.1, we set up the problem by defining the generic type of RQCs that we are going to study, as well as the random variable of the overlaps. Afterwards, we focus on the moments of this random variable, which is going to be the main object of our study.

- In Sec. 3.2.2, we use a coarse-grained picture to express the moments of the overlaps via a transfer matrix, where the transfer matrix is drawn from the Ginibre unitary ensemble (GinUE). Our problem is established for two types

of boundary conditions: periodic and open. Then we show how in the scaling limit, the moments admit a universal form that does not depend on the microscopic details of the model, but on just a single parameter named x.

- In Sec. 3.2.3, we explicitly show that the moments of the overlaps are related to a partition function of a statistical model with domain walls. We explicitly define the Hamiltonian of this model and then analytically calculate the partition function. Finally, we demonstrate that our statistical model leads to the same scaling limit for the moments.

- In Sec. 3.2.4, we introduce the Random Phase Model(RPM) and then explicitly find the transfer matrix related to the moments of the overlaps in the limit of large local Hilbert space with the help of many-body diagrams. This transfer matrix is what we will see later as a generalisation of the Toeplitz matrix.

- In Sec. 3.2.5, we introduce a methodology to diagonalise a generalised Toeplitz matrix, we showcase analytically, that in the limit of a large local Hilbert space for the model, one recovers the same scaling limit for the moments, validating our theory.

- In Sec. 3.2.6, we finally obtain the universal probability distribution of the overlaps from the moments, for the case of open boundary conditions (obc), whereas in the case of periodic boundary conditions (pbc), we obtain an in-law relation to another random variable, which is related to the exponentiation of a matrix drawn from Gaussian Unitary Ensemble (GUE).

3.2.1 Setting up the problem

We begin by establishing the specifics of the type of model that we are interested in. We consider a circuit that acts on N qdits with a total depth of t. Each qdit corresponds to a $q-$dimensional local Hilbert space $\mathbb{C}^q$ and thus the total Hilbert space is $\mathcal{H} = \mathbb{C}^{q^N}$. For the moment, we consider the system to start from an arbitrary initial state $|\psi_0\rangle$ and evolve to a depth t in time as $|\psi(t)\rangle = W(t)\,|\psi_0\rangle$. The operator $W(t)$ denotes a random unitary operation, which implements a RUC of depth t. Now we consider two independent realizations $W(t_1), W'(t_2)$ of the circuit, with different depth t_1, t_2 and create the two random states $|\psi(t_1)\rangle = W(t_1)\,|\psi_0\rangle\,, |\psi'(t_2)\rangle = W'(t_2)\,|\psi_0\rangle$. We are interested into investigating the distribution of the overlap,

which is given by the random variable

$$w' = \mathcal{N}\left|\langle\psi'(t_2)|\psi(t_1)\rangle\right|^2 = \mathcal{N}\left|\left\langle\psi_0\left|W'^{\dagger}(t_2)W(t_1)\right|\psi_0\right\rangle\right|^2, \tag{3.38}$$

where $\mathcal{N} = q^N$ represents the dimension of $\mathcal{H}$. As either or both (what matters is the total depth $t = t_1 + t_2$) of the depths t_1, t_2 becomes large, the unitary matrix $W'^{\dagger}(t_2)W(t_1)$ behaves more and more like a Haar random unitary operation on $U(\mathcal{N})$ and the RUC is anticipated to serve as a k-design for increasingly large values of k. Consequently, the distribution $p(w')$ of the overlap w' approaches the Porter-Thomas distribution $p_{PT}(w') = e^{-w'}, w' \geq 0$ [36], which is typically associated with the overlap between two uniformly selected pure states.

A RUC forms ensembles of pure states, which are defined as distributions of states obtained by acting on a reference state $|\psi_0\rangle$ with unitary operators W, drawn according to a specific measure, $\mathcal{E} := \{|\psi\rangle = W|\psi_0\rangle, W \sim d\mu(W) \text{ or } |\psi\rangle \sim d\mu_{\mathcal{E}}(\psi)\}$. For any given ensemble $\mathcal{E}$, the overlap distribution is defined as

$$p_{\mathcal{E}}(w') = \int d\mu_{\mathcal{E}}(\psi)d\mu_{\mathcal{E}}(\psi')\delta\left(w' - \mathcal{N}\left|\langle\psi' \mid \psi\rangle\right|^2\right) = \mathbb{E}\left[\delta\left(w' - \mathcal{N}\left|\langle\psi' \mid \psi\rangle\right|^2\right)\right]_{\mathcal{E}} \tag{3.39}$$

It is important to mention that actually, the ensemble $\mathcal{E}$ has a dependence in the depth t of the RUC, but for practical reasons we omit it. Given an ensemble of states $\mathcal{E}$, one can define the object

$$\rho^{(k)}[\mathcal{E}] = \int d\mu_{\mathcal{E}}(\psi)\,|\psi\rangle\langle\psi|^{\otimes k}, \quad \|\psi\| = 1 \implies \mathrm{Tr}\left\{\rho^{(k)}[\mathcal{E}]\right\} = 1 \tag{3.40}$$

This is the average over the ensemble $\mathcal{E}$ of the k-replicated density matrix, and it is an operator acting on $\mathcal{H}^{\otimes k}$. To understand its significance, we can examine a specific element of it

$$\left(\rho^{(k)}[\mathcal{E}]\right)_{\alpha_1,\alpha_2,\ldots\alpha_k,\alpha'_1,\alpha'_2,\ldots\alpha'_k} = \int d\mu_{\mathcal{E}}(\psi)\psi_{\alpha_1}\psi^*_{\alpha'_1}\psi_{\alpha_2}\psi^*_{\alpha'_2}\ldots\psi_{\alpha_k}\psi^*_{\alpha'_k} \tag{3.41}$$

with $\alpha_i = 1, 2, \ldots, \mathcal{N}$. Knowing that $\psi_\alpha\psi^*_{\alpha'}$ are elements of the density matrix $|\psi\rangle\langle\psi|$, Eq. (3.41) represents the moments of the density matrix, related to the ensemble $\mathcal{E}$. These moments are characteristic of the specific ensemble of states, and thus can be used to define a notion of how similar or how close two ensembles are. In particular,

we define the notion of distance between two ensembles $\mathcal{E}, \mathcal{E}'$ as

$$\Delta_2^{(k)}[\mathcal{E}, \mathcal{E}'] = \left\| \rho^{(k)}[\mathcal{E}] - \rho^{(k)}[\mathcal{E}'] \right\|_2 \tag{3.42}$$

where we used the $\|O\|_2 = \sqrt{\mathrm{Tr}\{O^\dagger O\}}$ Frobenius norm. When $\Delta_2^{(k)}[\mathcal{E}, \mathcal{E}'] = 0$ by definition $\rho^{(k)}[\mathcal{E}] = \rho^{(k)}[\mathcal{E}']$ and thus the k-moments of the distributions are the same. If this is true for every, k then the ensembles $\mathcal{E}, \mathcal{E}'$ are the same. Another, more familiar way of denoting Eq. (3.40) is by writing down the explicit dependence in $W, W^\dagger$, and from Eq. (3.28) we can see that the k-fold density matrix satisfies $\rho^{(k)}[\mathcal{E}] = \Phi_{\mathcal{E}}^{(k)}(\rho_0^{(k)})$ and is actually a k-fold channel acting on $\rho_0^{(k)} = |\psi_0\rangle\langle\psi_0|^{\otimes k}$ where the expectation is taken over $|\psi\rangle, |\psi'\rangle$, both sampled independently of $\mathcal{E}$.

To quantitatively study the approach of one ensemble to the other, we define the Frame Potential

$$F^{(k)}[\mathcal{E}] = \left\| \rho^{(k)} \right\|_2^2 = \mathrm{Tr}\left[\left(\rho^{(k)} \right)^2 \right] = \int d\mu_{\mathcal{E}}(\psi) d\mu_{\mathcal{E}}\left(\psi'\right) \left| \langle \psi' \mid \psi \rangle \right|^{2k} \tag{3.43}$$

another expression of the Frame Potential comes from using the explicit dependence on W, according to which Eq. (3.43) becomes

$$F^{(k)}[\mathcal{E}] = \int d\mu(W) d\mu\left(W'\right) \left| \langle \psi_0 \mid W'^\dagger W \mid \psi_0 \rangle \right|^{2k} = \int d\mu(W) d\mu\left(W'\right) \langle \psi_0 \mid^{\otimes 2k} \left(W^\dagger W'\right)^{\otimes k} \otimes \left(W'^\dagger W\right)^{\otimes k} \mid \psi_0 \rangle^{\otimes 2k} \tag{3.44}$$

we set $U = W'^\dagger W$ and by denoting the measure of U as $d\mu'(U)$. The random matrix U generally follows a different ensemble than W, which we denote as $\mathcal{E}'$. Thus, the measure $d\mu'$ is not the same as $d\mu$. Then Eq. (3.44) becomes

$$F^{(k)}[\mathcal{E}] = \int d\mu'(U) \langle \psi_0 \mid^{\otimes k} U^{\dagger \otimes k} (|\psi_0\rangle\langle\psi_0|)^{\otimes k} U^{\otimes k} \mid \psi_0 \rangle^{\otimes k} = \langle \psi_0 \mid^{\otimes k} \Phi_{\mathcal{E}'}^{(k)}(|\psi_0\rangle\langle\psi_0|) \mid \psi_0 \rangle^{\otimes k} \tag{3.45}$$

This equation expresses a direct relation of the Frame potential with the $k-$fold channel. There is an average over the $k-$copies of U and $k-$copies of $U^\dagger$, which can be graphically seen in Fig.3.2, where we used the "folded" picture introduced in Sec. 3.22. A special case that is interesting for our problem is the Haar RUC, when the pure states are drawn from the Haar ensemble $\mathcal{E} = \mathrm{Haar}$. We can explicitly calculate the Frame Potential of the Haar ensemble over $U(\mathcal{N})$ by using Eq. (3.34), according

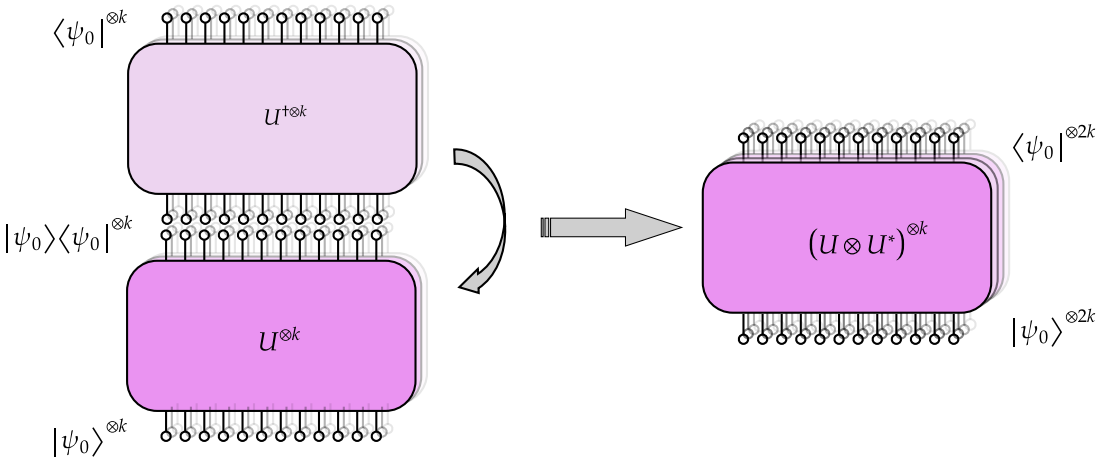

FIGURE 3.2: The Frame potential $F^{(k)}[\mathcal{E}]$ for an ensemble $\mathcal{E}$ in the folded picture. Each operator is represented by N incoming and N outgoing legs, and the quantum state by N input legs. The folding of k copies of $U^\dagger$ leads to $2k$ copies of U, U^*.

to which the k-fold density matrix becomes

$$\rho^{(k)}[\text{Haar}] = \frac{1}{k!\binom{k+d-1}{k}} \sum_{\sigma\in S_k} P_\sigma. \tag{3.46}$$

and from the definition Eq. (3.43)

$$F^{(k)}_{\text{Haar}} = \frac{1}{k!\binom{k+\mathcal{N}-1}{k}} \sum_{\sigma\in S_k} \text{Tr}\Big\{P_\sigma \rho^{(k)}[\text{Haar}]\Big\} = \frac{1}{k!\binom{k+\mathcal{N}-1}{k}} \sum_{\sigma\in S_k} \text{Tr}\Big\{\rho^{(k)}[\text{Haar}]\Big\} \tag{3.47}$$

The permutation operator of the $k-$copies, by definition leaves the $k-$copies of the same state invariant $P_\sigma |\psi\rangle^{\otimes k} = |\psi\rangle^{\otimes k}$ and thus it is true in general that

$$P_\sigma \rho^{(k)}[\mathcal{E}] = \rho^{(k)}[\mathcal{E}] \quad \text{for any } \mathcal{E} \text{ and } \sigma \in S_k \tag{3.48}$$

Since k-fold density matrix has a unit trace, we finally deduce the Frame Potential for the Haar ensemble

$$F^{(k)}_{\text{Haar}} = \frac{1}{\binom{k+\mathcal{N}-1}{k}} \overset{\mathcal{N}\gg 1}{\to} \frac{k!}{\mathcal{N}^k} \tag{3.49}$$

At this point, we present a theorem that we are going to need for our study.

Theorem 2 *For any ensemble of pure states $\mathcal{E}$ produced by unitary operations, it is true that*

$$F^{(k)}_{\mathcal{E}} \geq F^{(k)}_{Haar}$$

Proof

By the definition in Eq. (3.42) and of the Frame Potential, we obtain

$$(\Delta_2^{(k)}[\mathcal{E},\text{Haar}])^2 = \text{Tr}\left\{\left(\rho^{(k)}[\mathcal{E}]\right)^2\right\} + \text{Tr}\left\{\left(\rho^{(k)}[\text{Haar}]\right)^2\right\} - 2\,\text{Tr}\left\{\rho^{(k)}[\mathcal{E}]\rho^{(k)}[\text{Haar}]\right\} = \\ = F_{\mathcal{E}}^{(k)} + F_{\text{Haar}}^{(k)} - 2\,\text{Tr}\left\{\rho^{(k)}[\mathcal{E}]\rho^{(k)}[\text{Haar}]\right\} \quad (3.50)$$

The third term can be simplified by using Eq. (3.48) and the result in Eq. (3.49), which lead to $\text{Tr}\left\{\rho^{(k)}[\mathcal{E}]\rho^{(k)}[\text{Haar}]\right\} = F_{\text{Haar}}^{(k)}$. So finally, we end up with

$$(\Delta_2^{(k)}[\mathcal{E},\text{Haar}])^2 = F_{\mathcal{E}}^{(k)} - F_{\text{Haar}}^{(k)} \quad (3.51)$$

and consequently, $F_{\mathcal{E}}^{(k)} - F_{\text{Haar}}^{(k)} \geq 0$. This is valid for any $\mathcal{E}$ ensemble, and the Haar ensemble is the ensemble of pure states that minimises $F_{\mathcal{E}}^{(k)}$. We can also write that

$$\Delta_2^{(k)}[\mathcal{E},\text{Haar}] = \sqrt{F_{\mathcal{E}}^{(k)} - F_{\text{Haar}}^{(k)}} \quad (3.52)$$

showcasing, that the approach to a k-design can be quantified by the approach of the Frame Potential to its Haar value. Another, important property of the Frame Potential is that it is directly connected to the probability distribution of overlaps, which we denote as $p(w')$. In particular, based on the definitions Eqs. (3.38),(3.43) it is straightforward to observe that

$$F_{\mathcal{E}}^{(k)} = \mathcal{N}^{-k}\mathbb{E}\left[w'^k\right]_{\mathcal{E}} \quad (3.53)$$

The frame potential defines the moments of w' and thus the distribution of the overlaps for a RUC. At large depths the ensemble $\mathcal{E}$ approaches the Haar one and from Eq. (3.49) we can find that the moments become $\mathbb{E}[w']_{\text{Haar}} = \mathcal{N}^k/\binom{k+\mathcal{N}-1}{k} \overset{\mathcal{N}\gg 1}{\to} k!$, for $t \gg 1$, which as expected are the moments of the PT distribution [36].

3.2.2 Ginibre Ensemble and transfer matrix

In our investigation, we analyse a one-dimensional lattice with L q-dimensional sites. Although our argument is more broadly applicable to different geometries of RUC with local interactions, we choose to consider a brick-wall RUC. Each local gate $u_{i,i+1}(t)$ that acts on adjacent sites i and $i+1$ at time t is random and selected independently of some ensemble $\mathcal{E}$. Each time step, $\Delta t = 1$, consists of both an even

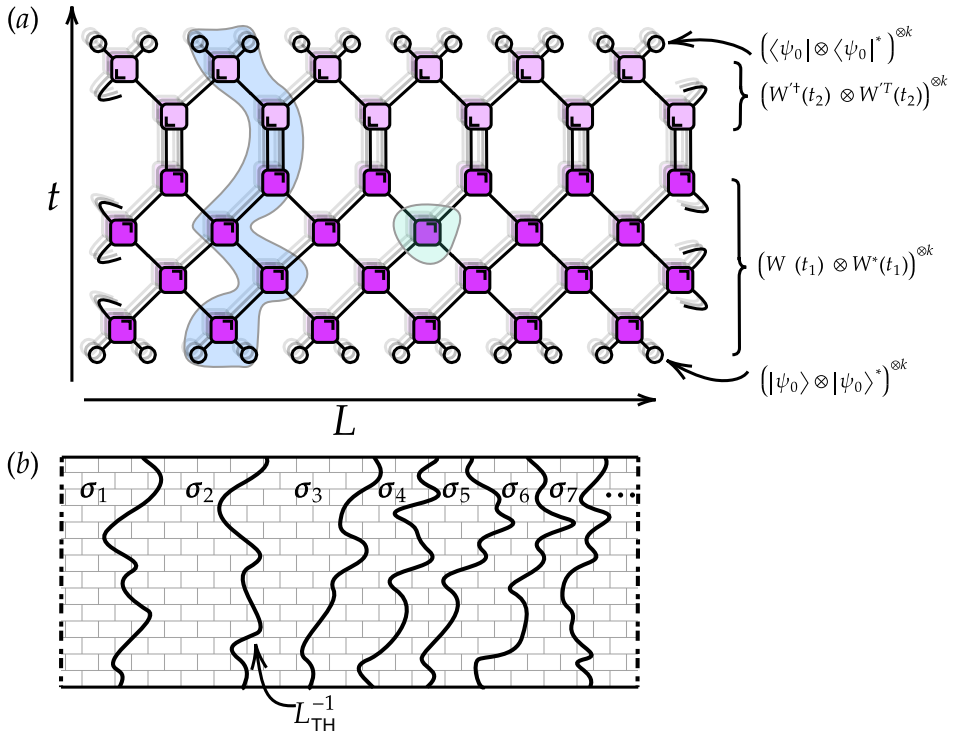

FIGURE 3.3: (a) A representation of the overlap $w'^k = \langle\psi_0|W'^{\dagger}(t_2 = 1)W(t_1 = 2)|\psi_0\rangle$ with $k = 3$ for depth 3 and system size L, with 6 in total copies. The transfer matrix is highlighted in light blue for a single copy. The tensor product of the local gate , $u \otimes u^* \otimes \cdots \otimes u \otimes u^*$, is highlighted in light green. (b) In the Thouless scaling limit, the overlap $\mathbb{E}[w^k]$ can be interpreted as the grand canonical partition function of a dilute gas of domain walls, corresponding to transpositions connecting two permutations and each carrying a fugacity L_{Th}^{-1}. Correspondingly, the size of each domain is $\sim L_{\mathrm{Th}}(t)$.

and an odd layer, relatively shifted to each other by a single site as shown in Fig. 3.3(a).

At this point, it is important to mention an alternative way of representing w'. Mathematically, one can use the properties of the tensor product and express the $k-$power of the overlap as

$$w'^k = \mathcal{N}^k \left(\langle\psi_0|\otimes\langle\psi_0|^*\right)^{\otimes k} \left(W'^{\dagger}(t_2)\otimes W'^{T}(t_2)\right)^{\otimes k} \left(W(t_1)\otimes W^*(t_1)\right)^{\otimes k} \left(|\psi_0\rangle\otimes|\psi_0\rangle^*\right)^{\otimes k} \tag{3.54}$$

This expression, admits k copies of the RUC and k copies of its complex conjugate, leading to a graphical representation of $2k$ copies as shown in Fig. 3.3. The space of $2k$ copies or else $\mathcal{H}_{2k}$ will be where we establish our theory, as we demonstrate later.

Within this setup, the overlap w' is depicted as in Fig. 3.3(a). When averaged over the ensemble, determining w' simplifies to computing an appropriate partition function. This becomes clear by examining the overlaps in the spatial direction. In

particular, the local interactions of the circuit allow us to define a spatial transfer matrix G_i, which includes all gates (and initial states) acting temporally on the i-th qudit. An example of this is shown in Fig. 3.3(a) for a brick-wall circuit. We represent the product of these transfer matrices by,

$$G = G_1 G_2 \cdots G_L.$$

with G_i representing the transfer matrix of the i-th site and of a single replica. The overlap w' is directly related to the transfer matrix G, and its explicit form depends on the boundary conditions. For periodic boundary conditions (pbc), w' is expressed as $w'_{\text{pbc}} = |\operatorname{Tr}[G]|^2$, and for open boundary conditions (obc), it is $w'_{\text{obc}} = |l^\dagger G r|^2$ where l, r are boundary vectors whose specific forms depend on the details of the boundary conditions and are not important here. The statistical independence of the local gates implies that the matrices G_i are statistically independent as well between different indices. At total depth, $t = t_1 + t_2$ G_i "cuts off" an increase in t number of legs, with each leg representing q degrees of freedom. Thus G_i are of size $M(t) \times M(t)$ matrices where $M(t) = q^{f(t)}$, where $f(.)$ is a non-decreasing function, and its exact form depends on the geometry of the circuit. In our case of a brick-wall geometry, every single time step cuts off 2 legs and the boundary conditions in the time direction, induced by, $|\psi_0\rangle$ reduces the number of legs by 2, leading to $f(t) = 2t - 2$. The exponential growth in time of matrix size is a general feature, and we omit the time dependence of M unless necessary.

We focus on RUCs, that represent chaotic quantum systems. In this scenario, if we imagine a system of specific size L then at sufficiently large times the unitary dynamics, having no conserved quantities are going to be described by the Haar measure over $U(q^L)$ and the circuit will form a k-design for increasing values of k in time. As the unitary dynamics in the time direction approach higher moments of the Haar ensemble, the non-unitary "dynamics" in the space direction [86, 87] demonstrate an emergence of non-Hermitian Ginibre Unitary Ensemble (GinUE) [38]. This is a complex matrix ensemble, where the matrix elements are iid complex Gaussian variables. When both t and L are large, there can be cells of smaller subsystems for which the spatial dynamics have converged to GinUE, and we denote the cell's size as ℓ, which in general is time-dependent $\ell = \ell(t)$. The system is then described by the product of many large random matrices, indicating a domain where universality

could emerge, as suggested in references [38, 88, 89, 90] and this is what we are going to prove later. More precisely, in a coarse-grained view, we organise these matrices into groups of size ℓ an indicated below

$$\tilde{G}_a := G_{a\ell+1} G_{a\ell+1} \cdots G_{(a+1)\ell}, \tag{3.55}$$

with

$$G = \prod_{a=1}^{L/\ell} \tilde{G}_a \tag{3.56}$$

For sufficiently large ℓ, we assume the absence of a privileged basis due to the chaotic nature of the system. Since the dynamics in the spatial direction of generic many-body chaotic systems is non-Hermitian, the matrices $\tilde{G}_a$ are appropriately sampled from the simplest non-Hermitian random matrices, the GinUE, where each matrix element is independently drawn as a complex Gaussian variable with zero mean and variance, which we denote as ν^2. We are interested in the moments of the overlaps and thus in th behaviour of w'^k, which also can be written as

$$w'^k = \begin{cases} \mathrm{Tr}[G \otimes \cdots \otimes G \otimes G^* \otimes \cdots \otimes G^*], & \text{for pbc} \\ (l^{\dagger \otimes k} \otimes r^{\dagger \otimes k}) G \otimes \cdots \otimes G \otimes G^* \otimes \cdots \otimes G^* (r^{\otimes k} \otimes l^{\otimes k}), & \text{for obc} \end{cases} \tag{3.57}$$

with $k-$ copies of G, G^*. The object, $G \otimes \cdots \otimes G \otimes G^* \otimes \cdots \otimes G^*$ represents the $k-$moments of the ensemble of the transfer matrix. In the coarse-grained picture, Eq. (3.57) becomes

$$w'^k = \begin{cases} \mathrm{Tr}\left[\prod_{\alpha=1}^{L/\ell} (\tilde{G}_\alpha \otimes \cdots \otimes \tilde{G}_\alpha \otimes \tilde{G}_\alpha^* \otimes \cdots \otimes \tilde{G}_\alpha^*)\right], & \text{for pbc} \\ (l^{\dagger \otimes k} \otimes r^{\dagger \otimes k}) \left(\prod_{\alpha=1}^{L/\ell} \tilde{G}_\alpha \otimes \cdots \otimes \tilde{G}_\alpha \otimes \tilde{G}_\alpha^* \otimes \cdots \otimes \tilde{G}_\alpha^*\right) (r^{\otimes k} \otimes l^{\otimes k}), & \text{for obc} \end{cases} \tag{3.58}$$

When $\tilde{G}_\alpha$ approach the GinUe then $\tilde{G}_\alpha \otimes \cdots \otimes \tilde{G}_\alpha \otimes \tilde{G}_\alpha^* \otimes \cdots \otimes \tilde{G}_\alpha^*$ represent the $k-$moments of this ensemble and as calculated in App. B.1, they are exactly:

$$\mathbb{E}_{\mathrm{GinUe}} \left[\tilde{G}_\alpha \otimes \cdots \otimes \tilde{G}_\alpha \otimes \tilde{G}_\alpha^* \otimes \cdots \otimes \tilde{G}_\alpha^*\right] = \nu^{2k} \sum_{\sigma \in S_k} |\sigma\rangle\rangle\langle\langle\sigma|, \tag{3.59}$$

The average over GinUE leads to the average over products of Gaussian random variables, which can be computed by Isserlis' theorem This theorem allows one to compute higher-order moments in terms of the second-order ones, which in our case are $\mathbb{E}[(\tilde{G}_\alpha)_{b,c} (\tilde{G}_\alpha^*)_{b',c'}] = \nu^2 \delta_{b,b'} \delta_{c,c'}$ and $\mathbb{E}[(\tilde{G}_\alpha)_{b,c} (\tilde{G}_\alpha)_{b',c'}] = \mathbb{E}[(\tilde{G}_\alpha)^*_{b,c} (\tilde{G}_\alpha)^*_{b',c'}] = 0$.

Isserlis' theorem imposes that the only non-vanishing components of the tensor in Eq. (3.59) are the ones related to the permutation of each copy of $\tilde{G}_\alpha$ with the copies of $\tilde{G}_\alpha$. That is why there is the appearance of the permutation states $|\sigma\rangle\rangle \in \mathbb{C}^{M^{2k}}$ via $\langle\langle \boldsymbol{\beta}, \bar{\boldsymbol{\beta}} \mid \sigma\rangle\rangle = \delta_{\boldsymbol{\beta},\sigma(\bar{\boldsymbol{\beta}})}$, where $\boldsymbol{\beta}, \bar{\boldsymbol{\beta}}$ represent the indices corresponding to the $k-$copies of the M dimensional Hilbert space of $\tilde{G}_\alpha$. Here we used the formalism of the "folded" picture that was established. in Sec. 3.1.2. We continue with defining another matrix over the permutation space S_k with elements

$$T_{\sigma,\sigma'} = \nu^{2k} \langle\langle \sigma \mid \sigma' \rangle\rangle \tag{3.60}$$

. Then, with the help of Eq. (3.60) the coarse-grained picture of the moments leads to

$$\mathbb{E}[G \otimes \cdots \otimes G \otimes G^* \otimes \cdots \otimes G^*] = \nu^{2k} \sum_{\sigma,\sigma'} \left[T^{L/\ell - 1}\right]_{\sigma,\sigma'} |\sigma\rangle\rangle\langle\langle\sigma'| \tag{3.61}$$

So it is straightforward, to observe that T acts like another transfer matrix but this time over S_k and that we get as many T as cells of the system that have converged to GinUE. A direct application of Eq. (3.61) to Eq. (3.57), helps us derive the moments of the overlaps as a function of this transfer matrix, written exactly as

$$\mathbb{E}[w'^k] = \begin{cases} Tr[T^{L/\ell}], & \text{for pbc} \\ |l^\dagger r|^{2k} \sum_{\sigma,\sigma'} (T^{L/\ell - 1})_{\sigma,\sigma'} & \text{for obc} \end{cases} \tag{3.62}$$

This expression is going to be useful later for the mapping to the statistical model and the emergence of universality of our problem. We proceed with calculating exactly the values of $T_{\sigma,\sigma'}$. First, we should remind to the reader that $|\sigma\rangle\rangle$ is a state over the $2k$ copies of a M dimensional Hilbert space, permuting by σ the $k-$copies of them to the rest $k-$copies. This is actually the representation of the permutation operator P_σ in Eq. (3.7) in the folded picture, or as a state in the $M^k \otimes M^k$ space. In this picture, then $P_\sigma \to |\sigma\rangle\rangle$, we directly get $\langle\langle \sigma \mid \sigma' \rangle\rangle = \mathrm{Tr}\{P_\sigma^\dagger P'_\sigma\} = M^{\#\text{cycles}(\sigma^{-1}\sigma')} = M^{\#\text{cycles}(\sigma\sigma'^{-1})}$, where we used the properties of P_σ from Sec. 3.1.2 and the fact that #cycles(.) is a class function. Thus, the transfer matrix's elements are exactly

$$T_{\sigma,\sigma'} = \nu^{2k} M^{\#\text{cycles}(\sigma\sigma'^{-1})} \tag{3.63}$$

Another way of writing this equation is through the minimum number of transpositions needed to decompose a permutation, e.g. $(123) = (12)(23)$. As proven in [91], if $\sigma \in S_k$ can be decomposed in #cycles(σ) disjoint cycles, then it can be decomposed to a minimum number of $D(\sigma) = k - \#\text{cyclyes}(\sigma)$ transpositions. Following this logic, for the composition $\sigma\sigma'$ of permutations, one can interpret $D(\sigma\sigma'^{-1}) = k - \#\text{cyclyes}(\sigma\sigma'^{-1})$ as the minimal number of transpositions that σ differs by σ' and Eq. (3.63) can be then expressed as

$$T_{\sigma,\sigma'} = (v^2 M)^k M^{-D(\sigma\sigma'^{-1})} \tag{3.64}$$

On can also express $M^{-D(\sigma\sigma'^{-1})}$ as

$$M^{-D(\sigma\sigma')} = \delta_{D(\sigma\sigma'^{-1}),0} + \frac{\delta_{D(\sigma\sigma'^{-1}),1}}{M} + \frac{\delta_{D(\sigma\sigma'^{-1}),2}}{M^2} + \cdots + \frac{\delta_{D(\sigma\sigma'),k-1}}{M^{k-1}} \tag{3.65}$$

where one gets an expansion over the different number of minimal transpositions that σ, σ' can differ. As we already mention M is increasing in time, so at large times or equivalently at $M \to \infty$, with the help of Eq. (3.65), Eq. (3.64) one can see that T admits the expansion

$$T(\sigma,\sigma') = (v^2 M)^k \left(\delta_{D(\sigma\sigma'^{-1}),0} + \frac{\delta_{D(\sigma\sigma'^{-1}),1}}{M} + O\left(M^{-2}\right) \right) \tag{3.66}$$

When $D(\sigma\sigma'^{-1}) = 0$ then $\sigma = \sigma'$ since they do not differ by any transposition and this corresponds to the diagonal elements of T and when $D(\sigma\sigma'^{-1}) = 1$ then $\sigma = \tau\sigma'$ for some transposition τ, which corresponds to the elements of T that differ by a single transposition. Thus, we define over S_k the matrices $\mathbb{1}_{\sigma,\sigma'} = \delta_{\sigma,\sigma'}$ and $A_{\sigma,\sigma'} = \delta_{D(\sigma\sigma'^{-1}),1}$ and then we can write Eq. (3.66) in the matrix from

$$T = (v^2 M)^k \left(\mathbb{1} + \frac{1}{M} A + O(M^{-2}) \right) \tag{3.67}$$

The matrix A denotes the adjacency matrix of the transposition graph and practically indicates which pairs of permutations differ minimally by a single transposition, by having unity elements for those pairs and zero otherwise. The higher order adjacency matrices defined similarly by $\delta_{D(\sigma\sigma'^{-1}),i}$, $i = 2,3,4,\ldots$ are related to A and they can be defined by, A as we prove in App. B.2. The important information that we can extract from Eq. (3.67) is that at large M, the leading contributions to T and

thus of Eq. (3.61), are the terms coming from identical pairs of permutations $\sigma = \sigma'$ and the ones that differ by a single transposition, meaning that $D(\sigma\sigma'^{-1}) = 1$.

For practical purposes, we do not want to carry factors that enter the moments Eq. (3.62) from Eq. (3.64), or the l, r vectors of obc, since the factors do not alter the physical context of our results. To achieve this, we normalise the first moment by demanding $\mathbb{E}[w'] = 1$ and then absorb the remaining coefficient to ν^2. For $k = 1$ the symmetric group S_1 and Eq. (3.62), becomes

$$\mathbb{E}[w'] = \begin{cases} (\nu^2 M)^{L/\ell} \to \nu^2 = 1/M, & \text{for pbc} \\ (\nu^2 M)^{L/\ell} |l^\dagger r|^2 \to \nu^2 = |l^\dagger r|^{-2\ell/L}/M, & \text{for obc} \end{cases} \tag{3.68}$$

The variance ν^2 of the GinUE absorbs the extra factors coming from the boundary conditions, so from now on we can ignore them. We proceed with studying a specific scaling limit of our model. We firstly define the Thouless length as $L_{\text{Th}}(t) = M(t)\ell(t)$ and based on this we define the scaled length $x = L/L_{\text{Th}}$ so we can restrict our study to the limit where t, L approaches infinity such that x is constant. In this limit, we can write Eq. (3.82) as

$$\lim_{\substack{t,L\to\infty \\ x=L/L_{\text{Th}}(t)}} T^{L/\ell} = \left(\mathbb{1} + \frac{xA}{Mx}\right)^{Mx} = e^{xA} \tag{3.69}$$

and the moments of the overlap have the following asymptotic behaviour.

$$\lim_{\substack{t,L\to\infty \\ x=L/L_{\text{Th}}(t)}} \mathbb{E}\left[w'^k\right] = \begin{cases} \text{Tr}\{e^{xA}\}, & \text{for pbc} \\ \sum_{\sigma,\sigma'} \left(e^{xA}\right)_{\sigma,\sigma'}, & \text{for obc} \end{cases} \tag{3.70}$$

The definition of $L_{\text{Th}}(t) = M(t)\ell(t)$ contains an important physical interpretation for our problem. The specifics of $M(t)$ and $\ell(t)$ are characteristic of the microscopic details of the system, making L_{Th} the parameter of our problem, which in the scaling limit, encodes the details about the specific choice of the system of interest. Thus, we can say that the fine details of the circuit's microstructure, such as the level locality and the coupling strength, influence the scaling limit by determining the characteristic length scale $L_{\text{Th}}(t)$. However, the asymptotic behaviour of the moments in Eq. (3.70) directly depends on x and does not capture the fine details of the system, but rather showcases a universal behaviour. They rely solely on the eigenvalues of the

adjacency matrix A.

3.2.3 The statistical model of domain walls

At this point, we have all the tools we need to establish our statistical model, to which we can map our problem. We start with the definition of the state space. We are focussing on a statistical model with the state of $\Omega = \{\sigma_1, \sigma_2, \ldots, \sigma_{L/\ell+1}\}, \sigma_i \in S_k$ for $i = 1, 2, \ldots, L/\ell + 1$. Each microstate is represented by a chain $L/\ell + 1$ sites, with a local spin variable σ_i as a permutation of S_k. The Hamiltonian defined on Ω has the exact form:

$$H(\sigma_1, \sigma_2, \ldots, \sigma_{L/\ell+1}) = \sum_{i=1}^{L/\ell} D(\sigma_i \sigma_{i+1}^{-1}) \tag{3.71}$$

and the effective inverse temperature is defined as $\beta = \log M$. This Hamiltonian represents effectively a spin chain with nearest neighbour ferromagnetic interactions and with a two-site energy bond of $D(\sigma_i \sigma_{i+1}^{-1})$. The boundary conditions of the spin chain are defined by the choice of pbc or obc in the original problem, and they do not affect the Hamiltonian H. Thus, for a statistical model like this, we define the partition function for each boundary condition:

$$\mathcal{Z}_{\text{b.c}}(\beta) = \begin{cases} \sum_{\substack{\{\sigma_i\}\in\Omega \\ \sigma_i = \sigma_{L/\ell+1}}} e^{-\beta H(\{\sigma_i\})} = \sum_{\substack{\{\sigma_i\}\in\Omega \\ \sigma_i = \sigma_{L/\ell+1}}} \prod_{i=1}^{L/\ell} M^{-D(\sigma_i \sigma_{i+1}^{-1})} & \text{for pbc} \\ \sum_{\{\sigma_i\}\in\Omega} L_{\sigma_1} R_{\sigma_{L/\ell+1}} e^{-\beta H(\{\sigma_i\})} = \sum_{\{\sigma_i\}\in\Omega} L_{\sigma_1} R_{\sigma_{L/\ell+1}} \prod_{i=1}^{L/\ell} M^{-D(\sigma_i \sigma_{i+1}^{-1})} & \text{for obc} \end{cases} \tag{3.72}$$

where in the case of periodic boundary conditions the spin on the edges of the chain $\sigma_1 = \sigma_{L/\ell+1}$ are bound to be the same, whereas the open boundary conditions introduce some extra vectors over the S_k space, whose components depend on the spin variables on the left and right edge $L_{\sigma_1}, R_{\sigma_{L/\ell+1}}$. For our purpose, these vectors are defined to be

$$L_\sigma = \langle\langle L \mid \sigma \rangle\rangle = (l^\dagger r)^k, \quad R_\sigma = \langle\langle \sigma \mid R \rangle\rangle = (r^\dagger l)^k \tag{3.73}$$

We continue, by using (3.72)(3.63) and Eq. (3.62) to derive:

$$\mathbb{E}[w'^k] = (\nu^2 M)^{kL/\ell} \mathcal{Z}_{\text{b.c}}(\beta), \quad \text{for b.c=pbc or obc} \tag{3.74}$$

We now see the direct connection of the moments of the overlap distribution with our statistical model of the spin chain. The calculation of these moments is mapped

to the calculation of the partition function $\mathcal{Z}_{\text{b.c}}$. It is important to mention that we chose not to focus on the general expansion of Eq. (3.66), but only up to orders up to the adjacency matrix A, since the rest are sub-leading in the scaling limit. This is equivalent to restricting the energy bonds up to, 1 and to achieve that we have to introduce a new term on the Hamiltonian that imposes the condition $D(\sigma_i\sigma_{i+1}^{-1}) \leq 1$. So we write H as follows:

$$H(\sigma_1, \sigma_2, \ldots, \sigma_{L/\ell+1}) = \sum_{i=1}^{L/\ell} D(\sigma_i\sigma_{i+1}^{-1}) + \sum_{i=1}^{L/\ell} V\left(D(\sigma_i\sigma_{i+1}^{-1})\right) \tag{3.75}$$

where

$$V(x) = \begin{cases} 0, \text{when } x \leq 1 \\ \infty, \text{otherwise} \end{cases} \tag{3.76}$$

The second term in the Hamiltonian is a potential on the spin chain that diverges when an energy bond contributes more than 1, leading to zero contribution of these microstates for the partition function. This is a way of "filtering out" these microstates from our problem. The potential $V(x)$ can be chosen to diverge at some other integer, e.g. $x = 2, 3, \ldots$, meaning that we consider the case of higher order terms e.g. $O(M^{-2}), O(M^{-3}), \ldots$ in Eq. (3.66), and thus contributions from permutations that have $D(\sigma\sigma'^{-1}) > 1$, but this leads to a more complicated statistical model, which is out of our scope of interest. From now on, we focus on the model described by Eq. (3.75).

A trivial way of expressing a partition function is as a function of the energy levels of H. In particular, the state space partitions into sectors of microstates and each one of them corresponds to a specific energy level E_i of the Hamiltonian, which is written as $\Omega = \Omega_0 \cup \Omega_1 \cup, \ldots$. For example, if E_0 is the ground state, then $\Omega_0 = \{\{\sigma_i\} \in \Omega \text{ s.t } H(\{\sigma_i\}) = E_0\}$. In the same way, we can define the other sectors $\Omega_1, \Omega_2, \ldots$ for the first, second excited state e.t.c. The cardinality $|\Omega_i| = \#(E_i)$ is what we call the degeneracy of the energy level E_i. Thus, we can now write the partition function as

$$\mathcal{Z}_{\text{pbc}}(\beta) = \sum_i \#(E_i) e^{-\beta E_i} \tag{3.77}$$

We demonstrate analytically the calculation of the partition function only for pbc,

since the methodology can be directly extended to the case of obc. Eq. (3.77) expresses that the partition function is completely defined by knowing the energy levels E_i and their degeneracy $\#(E_i)$. So let's try to find these numbers for our specific model of spin chain.

We start with the ground state. The Hamiltonian H in Eq. (3.71) is frustration-free, meaning that its ground state energy is the ground state of each local term $D(\sigma_i\sigma_{i+1}^{-1})$. There is no energy wise, competition between the local terms of the spin chain when it reaches the ground state and thus $E_0 = 0$, where each bond $D(\sigma_i\sigma_{i+1}^{-1}) = 0$. This implies that the microstate that minimises the energy is the one where all spins have the same value $H(\sigma,\sigma,\ldots,\sigma) = 0$. There are $|S_k| = k!$ of such possible microstates, which means that $\#(E_0) = k!$. We call these common spin-valued regions as domains. The first excited state can be easily found by Eq. (3.71). If we just change one of the zero energy bonds in the microstate, to the unit value, $D(\sigma_i\sigma_{i+1}^{-1}) = 1$ then this would imply that there should be another bond of unit value because of pbc and thus the first excited energy level is $E_1 = 2$. This change is equivalent to creating two different domains of spins and thus two domain walls, between them, but the two different values of spin should differ only by a single transposition, as a result of the unity that $\tau_1\tau_2 = \mathbb{1}$. The number of configurations that satisfy this is, actually $\mathrm{Tr}\{A^2\}$, based on the definition of the adjacency matrix A. Since the two walls can be distributed in L/ℓ different bonds, we get a degeneracy of $\#(E_1) = \mathrm{Tr}\{A^2\}\binom{L/\ell}{2}$. The second excited state requires three energy bonds as 1 and the rest zero, leading to $E_2 = 3$. The microstates that have this property should have three domain walls of cost 1. One example of this is a microstate like $\{\sigma_1 = \sigma,\sigma_2 = \sigma,\ldots,\sigma_i = \sigma',\sigma_{i+1} = \sigma',\ldots,\sigma_j = \sigma'',\sigma_{j+1} = \sigma'',\ldots,\sigma_{L/\ell+1} = \sigma\}$ for pbc, where $\sigma = \tau_1\sigma'$, $\sigma' = \tau_2\sigma''$, $\sigma'' = \tau_3\sigma$ and where we have three domain walls of cost 1. Again, the transpositions that the spin values differ should satisfy $\tau_1\tau_2\tau_3 = \mathbb{1}$. By counting again in the same manner as for the previous case and taking into account, we can find that the degeneracy of E_2 of these types of states is $\#(E_2) = \binom{L/\ell}{3}\mathrm{Tr}\{A^3\}$. The factor $\binom{L/\ell}{3}$ represents the number of possible configurations of 3 domain walls among L/ℓ bonds. There is a pattern in the degeneracy, that starts to appear. To generalise it, the N-th excited state is, $E_N = N + 1$ and the microstates that correspond to this energy level should have $N + 1$ domain walls.

By the same counting scheme as before, one can find that

$$\#(E_N) = \binom{L/\ell}{N+1} \mathrm{Tr}\Big\{A^{N+1}\Big\} \tag{3.78}$$

At this point, we can write explicitly the partition function for the periodic boundary conditions by using Eq. (3.77) and Eq. (3.78):

$$\mathcal{Z}_{\mathrm{pbc}}(\log M) = k! + \sum_{N=1}^{L/\ell-1} M^{-(N+1)} \binom{L/\ell}{N+1} \mathrm{Tr}\Big\{A^{N+1}\Big\} \tag{3.79}$$

The pbc is what makes the trace operation over A appear and $\mathrm{Tr}\{A\} = 0$ represents that the single domain-wall configurations are not allowed under these specific boundary conditions.

The previous formalism on the study of the energy levels of the statistical model was done for pbc however, it can be used to describe the obc case as well. There are a few minor changes that need to be made. Specifically, assume that in the framework of obc, the spins on the edges of the chain are fixed to the values $\sigma_1, \sigma_{L/\ell+1}$. The ground state of the system, then, will be the same as before, so zero domain walls. The absence of domain walls is true only for $\sigma_1 = \sigma_{L/\ell+1}$ with a degeneracy of 1 and zero otherwise. In the absence of pbc, it is not necessary that $\sigma_1 = \sigma_{L/\ell+1}$ and thus we can have microstates of a single domain wall of energy $E_1 = 1$. As we pass from domain walls, we accumulate transpositions, meaning that at a single domain wall configuration, the spin edges should satisfy $\sigma_1 = \tau\sigma_{L/\ell+1}$. So, if $\sigma_1 = \tau\sigma_{L/\ell+1}$, then the degeneracy $\#(E_1) = L/\ell$ and zero otherwise. For the level $E_2 = 2$ we should have 2 domain walls and thus $\sigma_1 = \tau_1\tau_2\sigma_{L/\ell+1}$. There are $(A^2)_{\sigma_1,\sigma_{L/\ell+1}}$ ways to choose such τ_1, τ_2 degeneracy of these microstates. In the same manner, we can study the higher excited states and get the following energy levels and degeneracies:

$$E_N = N, \quad \#(E_N) = \binom{L/\ell}{N} (A^N)_{\sigma_1,\sigma_{L/\ell+1}} \tag{3.80}$$

and the partition function for the obc would be according to Eq. (3.72)

$$\mathcal{Z}_{\mathrm{obc}}(\log M) = \sum_{N=0}^{L/\ell} M^{-N} \binom{L/\ell}{N} \mathrm{Tr}\Big\{LR^T A^N\Big\} \tag{3.81}$$

where R^T is the transpose of the vector R over the S_k space. By replacing the matrix LR^T with $\mathbb{1}$, we get back the pbc partition function.

We made all the previous discussion so that we can explain and understand our statistical model of the spin chain and finally find the partition function that is related to the moments $\mathbb{E}[w'^k]$. This statistical model was just a trick to help us digest the mathematics behind it. But now let us have a look at what exactly these mathematics are.

The main object of interest is the transfer matrix T, which is directly connected to the moments in Eq. (3.62) and specifically its power $T^{L/\ell}$. At this point, we use Eq. (3.66) and recover that

$$T^{L/\ell} = (\nu^2 M)^{KL/\ell}(\mathbb{1} + \frac{1}{M}A)^{L/\ell} \tag{3.82}$$

The matrices $A, \mathbb{1}$ commute and thus we can employ the binomial expansion to further deduce:

$$T^{L/\ell} = (\nu^2 M)^{kL/\ell} \sum_{N=0}^{L/\ell} M^{-N} A^N \binom{L/\ell}{N} \tag{3.83}$$

It is then straightforward to get the same expressions as with the statistical model when we apply Eq. (3.83) in Eq. (3.62). The binomial expansion, practically, demonstrates that what the statistical model was calculating was the choices of N terms A/M out of the L/ℓ terms of $\mathbb{1} + A/M$. The specific choices of A/M representing the domain walls' microstates and the possible such choices, the degeneracy of their energy level E_N. Every time we stumble upon A, this creates a domain wall. Finally, by fixing the parameter ν as indicated in Eq. (3.68), one observes that the statistical model leads to the same expressions for the moments as in Eq. (3.70).

3.2.4 Random Phase Model

In this section, we study a specific model and substantiate the universality of the moments of w' established previously by analytically extracting the Frame potential for this specific model.

The model of interest is the random Phase Model (RPM) and it was initially introduced in [39]. RPM is a random quantum circuit model, for which the time evolution is a matrix product

$$\mathcal{T}(t) = \prod_{t'=1}^{t} \mathcal{U}(t') \tag{3.84}$$

where $\mathcal{U}(t)$ is a $q^L \times q^L$ operator, with L the number of sites and q the local Hilbert space dimension of each site. $\mathcal{T}(t)$ represents the time evolution up to t, whereas

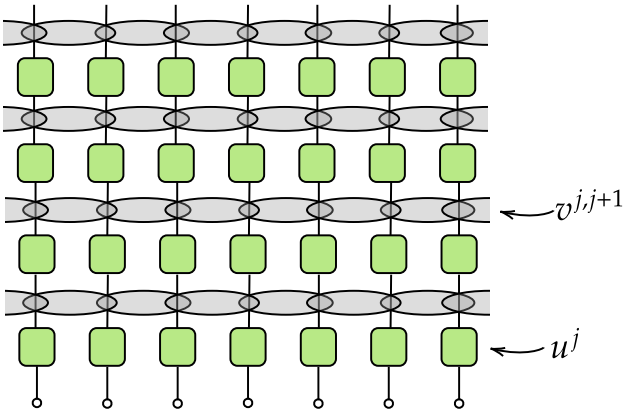

FIGURE 3.4: Circuit representation of the RPM model. Rectangles represent single-site unitaries drawn from the Haar ensemble; ellipses represent the two site coupling gates $v^{(j,j+1)}$. The layer of rectangles represents the $\mathcal{U}_1(t)$ layer of single site gates, whereas the ellipses represent the layer $\mathcal{U}_2(t)$ of coupling phase gates. The circles at the bottom represent the initial, factorised, state.

$\mathcal{U}(t)$ represents the single time step evolution operation at the time moment t. Here we focus on a $1D$ lattice with L sites and open boundary conditions. The evolution at each time step is obtained by two types of gates with $\mathcal{U}(t) = \mathcal{U}_2(t)\mathcal{U}_1(t)$, where $\mathcal{U}_1(t)$ contains only single-site operations and $\mathcal{U}_2(t)$ couples neighbouring sites. More specifically,

$$\mathcal{U}_1(t) = \bigotimes_{j=1}^{L} u^{(j)}(t) \tag{3.85}$$

generates transformations at each site, with the $q \times q$ unitary matrices $u^{(j)}(t)$ being drawn from the Haar ensemble over $U(q)$. $\mathcal{U}_2(t)$ couples neighbouring sites and is diagonal in the basis of site orbitals with matrix elements

$$[\mathcal{U}_2(t)]_{a_1,\dots a_L;a_1,\dots a_L} = \exp\left[\imath \sum_{j=1}^{L} \varphi^{(j)}_{a_j,a_{j+1}}(t)\right] \tag{3.86}$$

where $a_j \in \{1,\dots,q\}$ are the degrees of freedom for the $i-$th site. We take each coefficient $\varphi^{(j)}_{a_j,a_{j+1}}(t)$ to be a Gaussian random variable with mean zero and variance ϵ. The standard deviation $\sqrt{\epsilon}$ defines the typical scale of the fluctuations that the phases can have, and thus by increasing it we increase the mixing that $\mathcal{U}_2$ causes upon the L sites. This indicates that ϵ effectively controls the coupling between neighbouring spins. a trivial case is when there is zero coupling, with $\epsilon = 0$ and $\mathcal{U}_2 = \mathbb{1}$. A diagrammatic representation of the RPM circuit is shown in Fig. 3.4.

Constraining the gates $u^{(j)}(t)$ and $\phi^{(j)}(t)$ to be site or time-independent (or both),

this model gives access to translational invariant and Floquet models, as explored in [92]. Here, in contrast, we shall consider the case where all gates are drawn independently in space and time. The coupling gate in Eq. (3.86) admits nearest neighbouring interactions, making it possible to be expressed by a two-site coupling gate. In particular, if we define the two-site gates:

$$v^{(j,j+1)}(t)_{a_j,a_{j+1},a'_j,a'_{j+1}} = \delta_{a_j,a'_j}\delta_{a_{j+1},a'_{j+1}} \exp\left\{i\varphi^{(j)}_{a_j,a_j+1}(t)\right\} \tag{3.87}$$

then Eq. (3.86) becomes,

$$\mathcal{U}_2(t) = \bigotimes_{i=1}^{L} v^{(j,j+1)}(t) \tag{3.88}$$

making it straightforward that $v^{(j,j+1)}$ represents a two site coupling gate for our model. So the local random gates $u^j, v^{(j,j+1)}$ generate an ensemble of random circuits of the RPM, which is denoted as $\mathcal{E}_{\text{RPM}}$.

3.2.4.1 Many-body Diagrams in the RPM

We now consider the diagrammatic calculation of $\rho_k[\mathcal{E}_{\text{RPM}}(t)]$. The time-evolved wave function $|\psi(t)\rangle = \mathcal{T}(t)\,|\psi_0\rangle$ is constructed by acting the circuit, represented as in Fig. 3.4, to an arbitrary initial state $|\psi_0\rangle$. By drawing the random local gates from the ensembles described in Sec. 3.2.4 we construct an ensemble of time evolution operators $\mathcal{T}(t)$ and thus an ensemble of states described by the following $k-$fold density matrix

$$\rho^{(k)}[\mathcal{E}_{\text{RPM}}(t)] = \int d\mu_{\mathcal{E}_{\text{RPM}}}(\psi)\,|\psi(t)\rangle\langle\psi(t)|^{\otimes k} = \int d\mu_{\mathcal{E}_{\text{RPM}}}(t)\mathcal{T}(t)^{\otimes k}(|\psi_0\rangle\langle\psi_0|)^{\otimes k}\mathcal{T}(t)^{\dagger\otimes k} \tag{3.89}$$

To represent $\rho_k[\mathcal{E}_{\text{RPM}}(t)]$, we need to consider k copies of the bra and k copies of the ket. A first observation that we can make from $\rho^{(k)}[\mathcal{E}_{\text{RPM}}(t)]$ is that there is freedom of choice for the initial state $|\psi_0\rangle$, up to single site unitary operations. This is the result of the single-site Haar random matrices in RPM. If we consider the initial state $|\psi'_0\rangle = \bigotimes_{i=1}^{L} u'^{(i)}\,|\psi_0\rangle$, with $u'^{(i)}$ being single site unitary matrices from $U(q)$.

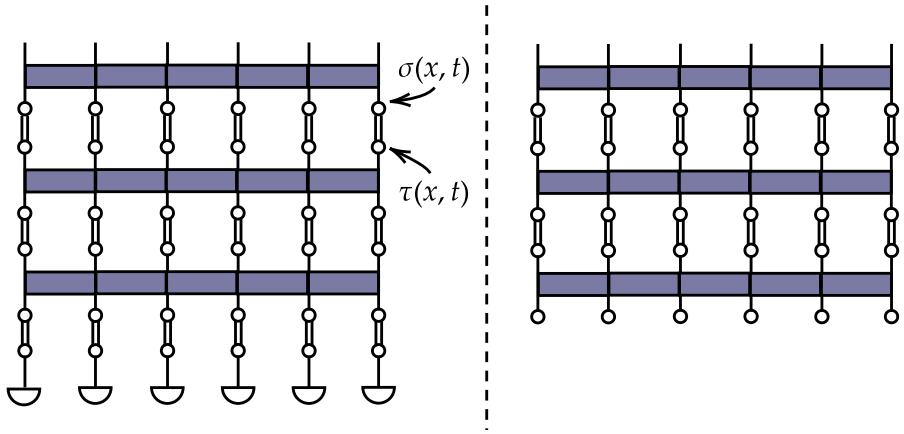

FIGURE 3.5: The $\rho^{(k)}[\mathcal{E}_{\text{RPM}}(t)]$ as the $2k$ copies of RPM averaged over the local one site gates u^j and the two site coupling ones $v^{(j,j+1)}$. The Haar average on the single site gates introduces the pairs of local "spin" variables $\sigma(x,t), \tau(x,t)$ at every space-time point of the circuit. On the left, it is the circuit with the initial state, $|\psi_0\rangle^{\otimes 2k}$. On the right, the independence of the initial state since $\langle\langle\sigma|\,(|\psi_0\rangle^{\otimes 2k}) = 1 \forall \sigma \in S_k$. A more detailed explanation of the diagram is presented in the main text.

Then the $k-$fold density matrix for that initial condition would be

$$\rho^{(k)}[\mathcal{E}_{\text{RPM}}(t)] = \int d\mu_{\mathcal{E}_{\text{RPM}}}(t) \left(\mathcal{T}(t)\bigotimes_{i=1}^{L} u'^{(i)}\right)^{\otimes k} (|\psi_0\rangle\langle\psi_0|)^{\otimes k} \left(\mathcal{T}(t)\bigotimes_{i=1}^{L} u'^{(i)}\right)^{\dagger\otimes k} =$$
$$= \int d\mu_{\mathcal{E}_{\text{RPM}}}(t)\mathcal{T}(t)^{\otimes k}(|\psi_0\rangle\langle\psi_0|)^{\otimes k}\mathcal{T}(t)^{\dagger\otimes k} \tag{3.90}$$

where we used the property of the Haar measure for the single site operations of $\mathcal{U}_1$ layer, of being invariant under left and right multiplication by unitary operations Eq. (3.12). As a result, the average over $\mathcal{E}_{\text{RPM}}$ absorbs local operations such as $u'^{(i)}$. All initial states $|\psi_0'\rangle$ lead to an ensemble of states with the same statistics. This can be generalised to the level of the locality of the Haar random unitary gates. For example, if $\mathcal{U}_1$ incudes Haar random unitary gates that couple m sites, then the same result holds for initial states like $|\psi_0'\rangle = \bigotimes_{i=1}^{L/m} u'^{(i)}|\psi_0\rangle$, that differ by unitary operations $u'^{(i)}$ on m sites. Thus, in this section, we choose the initial state as $|\psi_0\rangle = \bigotimes_{i=1}^{L}|0\rangle$, where each site is on the same orbital, and perform our calculations without loss of generality. The calculations can be understood better through a diagrammatic approach, and that is the technique we will use from now on, for the estimation of $\rho^{(k)}[\mathcal{E}_{\text{RPM}}(t)]$. The local gates $u^{(j)}(t), v^{(j,j+1)}(t)$ in the two layers in Eq. (3.85),(3.88) are being drawn independently meaning that the measure $d\mu_{\mathcal{E}_{\text{RPM}}(t)}$ is factorizing into the single site Haar measures of each $u^{(j)}$ at each time moment and site of the

circuit $\mathcal{T}(t)$, as well as the measure of the coupling gates $v^{(j,j+1)}$ for each pair of coupled sites and time moment. Thus $\rho^{(k)}[\mathcal{E}_{\text{RPM}}(t)]$ represented in Fig. 3.5, is a $2k$ copy of the circuit $\mathcal{T}(t)$, where one has to perform the average over these local gates.

At this point, we will explain the diagram we just mentioned in more detail, so that we can clarify the different parts of it more clearly. The result is a circuit with the same geometry as $\mathcal{T}(t)$ and the local gates being replaced by their average. So it is important to find the result of these local averages. We start with the Haar gates for one site $u^{(j)}$. When one averages over $u^{(j)}$, one obtains a $k-$fold Haar channel, which admits the graphical representation shown in Eq. 3.37, according to which the Haar average replaces the copies of $u^{(j)}$ with two local "spin" degrees of freedom. Moreover, the Haar average introduces, "spin" variables $\sigma(x,t), \tau(x,t) \in \mathcal{S}_k$ indicated as $\circ$ in Fig. 3.5. Each specific choice of these permutations represents a permutation "bond" and contributes with a weight given by the Weingarten matrix. We use the notation introduced in Eq. (3.37), where the Weingarten matrix $W_{\sigma,\tau}$ is represented, with double lines. The coloured rectangles, on the other hand, indicate the average over the $2k$ copies of the phase gate $v^{(j,j+1)}$, depicted as

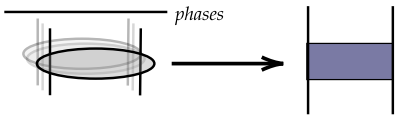

(3.91)

where the average is being performed over the phases $\varphi^{(j)}$,drawn from $\mathcal{N}(0,\epsilon)$. Finally, $|\psi_0\rangle^{\otimes 2k}$, are depicted as  . Then, based on the diagrammatics just explained, one can interpret Fig. 3.5 as tensor products and products of the local averages.

Now, looking back at Fig. 3.5, it is clear that a transfer matrix representation is possible. The transfer matrix can be built using the building block

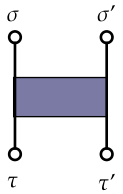

(3.92)

which depends on the local "spin" degrees of freedom of nearest neighbours. The transfer matrix is then represented as a single site column of Fig. 3.5, and it is a matrix in S_k. This is explained in more detail in the next section. Finally, $\rho^{(k)}[\mathcal{E}_{\text{RPM}}(t)]$

can be slightly simplified by, noting that, the term with the initial states, on the bottom of Fig. 3.5, can be evaluated explicitly as $\langle\langle\sigma|0\rangle\rangle = \mathrm{Tr}\{P_{\sigma^{-1}}(|0\rangle\langle 0|)^{\otimes k}\} = \langle 0|0\rangle^k = 1$. Consequently, they are trivially one for every $\sigma \in S_k$, since k copies of a state are invariant under any permutation. From now on we can ignore these terms, meaning that there is no dependence on $|\psi_0\rangle$ and we can focus on the rest part of the diagram as indicated in Fig. 3.5

This shows that for any k the density matrix is reduced to a sum over permutations σ and τ that can appear at every space-time position, weighted by the cost or coming from the average over the random phases.

However, the number of terms in this calculation grows rather quickly: there are $k!$ permutations for each $\sigma(x,t), \tau(x,t)$ at each spacetime point (x,t); this leads to $(k!)^{2Lt_{\max}}$ diagrams, for a circuit of L sites and evolved up to a maximum time moment $t_{\max}$. Since $\rho_k[\mathcal{E}_{\mathrm{RPM}}]$ is being expressed as a sum of these $(k!)^{2Lt_{\max}}$ diagrams, the fast growth of the number of terms makes the analytic calculations very intricate, if not feasible at all. That is why, we focus on the limit of $q \to \infty$, where the number of diagrams reduces to $(k!)^L$ since, as we will see later, the leading contributions in this limit come from common local spins over the same site. The next section is devoted to showcasing the details of the analytic results in this limit.

3.2.4.2 Large-q calculation

To make the calculation feasible in practice, we consider the limit $q \to \infty$. In this limit, one can use the expansion

$$W_{\sigma,\tau} \overset{q\to\infty}{\sim} q^{-k-D(\sigma\tau^{-1})} \prod_i (-1)^{\mathcal{C}_i(\sigma\tau^{-1})-1} c_{\mathcal{C}_i(\sigma\tau^{-1})-1}\,, \tag{3.93}$$

where $\mathcal{C}_i(\sigma)$ is the length of the i-th cycle in the cycle-decomposition of σ, and $c_m = (2m)!/m!(m+1)!$ is the Catalan number. Finally, $D(\sigma)$ is the minimal number of transpositions that σ can be decomposed into. It becomes thus obvious from Eq. (3.93) that in the limit, $q \to \infty$ the leading terms are the ones that minimise, $D(\sigma\tau^{-1})$ and this is true when $\sigma = \tau$. At this limit the leading contribution comes when $\sigma = \tau$ in $W_{\sigma,\tau}$ and thus $\sigma(x,t) = \tau(x,t)$ at every space-time position in Fig. 3.5. Additionally, contractions between loops at different time steps force $\sigma(x,t) = \sigma(x,t+1)$. The average over the diagonal matrices of the phase gates $v^{(j,j+1)}$ leads to a diagonal matrix in the $2k$ copies space. When $\sigma(x,t) \neq \sigma(x,t+1)$ then we end up

with a non-diagonal element of the $2k$ rank tensor and thus only configurations with $\sigma(x,t) = \sigma(x,t+1)$ have non-vanishing contributions. This can be understood by using the "folded space" formalism presented in Sec. 3.22, which can help us interpret the diagrams as mathematical objects. With this discussion, we established that the leading order in $1/q$ configurations of $\rho^{(k)}[\mathcal{E}_{\mathrm{RPM}}(t)]$ are the ones, where the permutations over a single site x are common at every time step. These type of configurations of the k replicated density matrix leads to the following expression,

$$\rho^{(k)}_{\mathrm{RPM}}(t) = q^{-kL} \sum_{\sigma_1,\ldots,\sigma_L} \left[\prod_{i=1}^{L} M^{(k)}_{\sigma_i,\sigma_{i+1}} \right] P_{\sigma_1} \otimes \ldots \otimes P_{\sigma_L} \,, \tag{3.94}$$

where P_σ labels the permutation operator over the k copies on each site. The coefficient $M^{(k)}_{\sigma,\sigma'}$ comes from the average over the random phases. This expression is well understood through Fig. 3.5, where at each site j, we get t layers of the circuit with each layer represented as

$\overline{m^{(k)}_{\sigma,\sigma'}} =$ 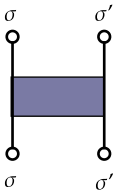

(3.95)

Thus, for each site, there is a product of t factors coming from the gates $v^{(j,j+1)}$ and in the last time step the state $|\sigma_j\rangle\rangle$ or the permutation operator P_{σ_j} is left. Each site is characterised by a specific permutation σ_j, which, as already explained, is common for every time moment of this specific site.

In order to find the analytic expression of $M^{(k)}_{\sigma,\sigma'}$, we first need to calculate exactly the diagram Eq. (3.95) This diagram is interpreted as

$$\overline{m^{(k)}_{\sigma,\sigma'}} \quad \text{where} \, , m^{(k)}_{\sigma,\sigma'} = q^{-2k} \langle\langle \sigma,\sigma' | v^{(j,j+1)\otimes k} \otimes v^{*(j,j+1)\otimes k} | \sigma,\sigma' \rangle\rangle \tag{3.96}$$

where $\overline{(.)}$ indicates the average over the Gaussian phases of the matrix representation of $v^{(j,j+1)}$ and $|\sigma,\sigma'\rangle\rangle = |\sigma\rangle\rangle \otimes |\sigma'\rangle\rangle$. The factor q^{-2k} comes from the asymptotic limit of the Weingarten function. Then the factor $M^{(k)}_{\sigma,\sigma'}$ is a product of t of these building blocks,

$$M^{(k)}_{\sigma,\sigma'} = \overline{(m^{(k)}_{\sigma,\sigma'})^t} = \overline{m^{(k)}_{\sigma,\sigma'}}^t \tag{3.97}$$

where we took advantage of the statistical independence of the local phase gates

$v^{(j,j+1)}$ at different time steps. For an exact calculation of $\rho^{(k)}[\mathcal{E}_{\mathrm{RPM}}(t)]$ is thus mandatory to find $\overline{m^{(k)}_{\sigma,\sigma'}}$. In order to evaluate this expression, we need to employ the definition of $|\sigma\rangle\rangle$, demonstrated in Sec. 3.1.2 and Eq. (3.87), according to which we obtain

$$
\begin{aligned}
&m^{(k)}_{\sigma,\sigma'} = q^{-2k} \sum_{\boldsymbol{i},\boldsymbol{j},\boldsymbol{i}',\boldsymbol{j}'} \left\langle \boldsymbol{i},\sigma(\boldsymbol{i}),\boldsymbol{j},\sigma'(\boldsymbol{j})\middle|v^{\otimes k}\otimes v^{*\otimes k}\middle|\boldsymbol{i}',\sigma(\boldsymbol{i}'),\boldsymbol{j}',\sigma'(\boldsymbol{j}')\right\rangle = \\
&q^{-2k} \sum_{\boldsymbol{i},\boldsymbol{j},\boldsymbol{i}',\boldsymbol{j}'} \left\langle \boldsymbol{i},\boldsymbol{j}\middle|v^{\otimes k}\middle|\boldsymbol{i}',\boldsymbol{j}'\right\rangle \left\langle \sigma(\boldsymbol{i}),\sigma'(\boldsymbol{j})\middle|v^{*\otimes k}\middle|\sigma(\boldsymbol{i}'),\sigma'(\boldsymbol{j}')\right\rangle = \\
&q^{-2k} \sum_{\boldsymbol{i},\boldsymbol{j},\boldsymbol{i}',\boldsymbol{j}'} \prod_{n=1}^{k} \delta^{\boldsymbol{i}',\boldsymbol{j}',\sigma(\boldsymbol{i}'),\sigma'(\boldsymbol{j}')}_{\boldsymbol{i},\boldsymbol{j},\sigma(\boldsymbol{i}),\sigma'(\boldsymbol{j})} e^{i\sum_{n=1}^{k}(\phi_{i_n,j_n}-\phi_{i_{\sigma(n)},j_{\sigma'(n)}})} = q^{-2k}\sum_{\boldsymbol{i},\boldsymbol{j}} e^{i\sum_{n=1}^{k}[\phi_{i_n,j_n}-\phi_{i_{\sigma(n)},j_{\sigma'(n)}}]} = \\
&q^{-2k}\sum_{\boldsymbol{i},\boldsymbol{j}} e^{i\sum_{n=1}^{k}[\phi_{i_n,j_n}-\phi_{i_{\sigma\sigma'^{-1}(n)},j_n}]}
\end{aligned}
\tag{3.98}
$$

where the site indices $j, j+1$ were omitted for this calculation and in the last step we change the summation variables such that $\boldsymbol{i} \to \sigma'^{-1}(\boldsymbol{i}), \quad \boldsymbol{j} \to \sigma'^{-1}(\boldsymbol{j})$. For practical purposes, we compactify all the Kronecker δ to a single one, which is defined as follows $\delta^{a_1,a_2,\dots}_{b_1,b_2,\dots} = \prod_i \delta_{a_i,b_i}$. Now that we have found $m^{(k)}_{\sigma,\sigma'}$ as an explicit expression of the Gaussian phases, we can also find its average. To understand, how to do that, we demonstrate the simpler case of $k = 3$ and then generalise it to any k.

- $k = 3$ ***case of*** $m^{(k)}_{\sigma,\sigma'}$

When we are dealing with three copies for example one gets that

$$
\overline{m^{(3)}_{\sigma,\sigma'}} = q^{-2k} \sum_{\boldsymbol{i},\boldsymbol{j}} \overline{e^{ix_{\sigma\sigma'^{-1}}}} \tag{3.99}
$$

where the exponent is denoted as

$$
x_{\sigma\sigma'^{-1}} = \phi_{i_1,j_1} + \phi_{i_2,j_2} + \phi_{i_3,j_3} - \phi_{i_{\sigma\sigma'^{-1}(1)},j_1} - \phi_{i_{\sigma\sigma'^{-1}(2)},j_2} - \phi_{i_{\sigma\sigma'^{-1}(3)},j_3} \tag{3.100}
$$

This exponent is a sum of Gaussian random variables making it a Gaussian random variable itself. Depending on the values of $\boldsymbol{i},\boldsymbol{j}$ and $\sigma\sigma'^{-1}$, the phases ϕ_{i_n,j_n} and $\phi_{i_{\sigma\sigma'^{-1}(n)},j_n}$ can be different or the same to each other, and this is what defines the exact Gaussian distribution of $x_{\sigma\sigma'^{-1}}$. As a result, terms in the sum which have an exponent $x_{\sigma\sigma'^{-1}}$, with the same number of independent phases $\phi_{i,j}$ and identical ones, lead to

the same contribution. We define $n_f(\sigma), \quad \sigma \in S_k$ as the number of fixed points of the permutation σ. A fixed point is the index which is unchanged by the permutation, e.g. $\sigma = (12)$ has the property that $\sigma(3) = 3$ in the case of three copies. The index 3 remains unchanged. Assume that we are interested in a permutation with no fixed points such as $\sigma\sigma'^{-1} = (123)$ for Eq. (3.99) then the same equation becomes

$$\overline{m^{(3)}_{\sigma,\sigma'}} = q^{-6}\overline{\sum_{i,j} e^{i[\phi_{i_1,j_1}+\phi_{i_2,j_2}+\phi_{i_3,j_3}-\phi_{i_2,j_1}-\phi_{i_3,j_2}-\phi_{i_1,j_3}]}} \tag{3.101}$$

The terms of the sum with $i_1 = i_2 = i_3$ have an exponent of $x_{(123)} = 0$, leading to a contribution of 1 for all these $q^{3+1} = q^4$ terms. The same is valid for the terms with $j_1 = j_2 = j_3$. For terms of, $i_1 = i_2 \neq i_3, j_1 = j_2 \neq j_3$ the exponent becomes $x_{(123)} = \phi_{i_2,j_2} + \phi_{i_3,j_3} - \phi_{i_3,j_2} - \phi_{i_1,j_3}$. That makes $x_{(123)}$ a sum of 4 Gaussian random variables $\mathcal{N}(0,\epsilon)$ and thus $x_{(123)} \sim 2\mathcal{N}(0,\epsilon)$. Using the well-known Gaussian integrals, one can calculate that in this case $\overline{e^{ix_{(123)}}} = e^{-2\epsilon}$. The number of such terms, according to simple combinatorics, is $(q(q-1))^2$. In the case of $i_1 \neq i_2 \neq i_3, j_1 \neq j_2 \neq j_3$, there is no cancellation of the phases and the exponent is a sum of 6 Gaussian random variables making $x_{(123)} \sim \sqrt{6}\mathcal{N}(0,\epsilon)$ and $\overline{e^{ix_{(123)}}} = e^{-3\epsilon}$. Again, one can find that there are $(q(q-1)(q-2))^2 = \binom{q}{3}^2$ such terms. Now we bring back to our memory that the calculations are being performed in the $q \to \infty$ limit and consequently, out of all these cases, the leading contributions come from the one with the leading number in q terms and the rest of the cases are subheading in q. In this limit, thus we can write:

$$\overline{\sum_{i,j} e^{i[\phi_{i_1,j_1}+\phi_{i_2,j_2}+\phi_{i_3,j_3}-\phi_{i_2,j_1}-\phi_{i_3,j_2}-\phi_{i_1,j_3}]}} \underset{q\to\infty}{\approx} q^6 e^{-3\epsilon} + O(q^5) \tag{3.102}$$

or equivalently,

$$\overline{m^{(3)}_{\sigma,\sigma'}} \underset{q\to\infty}{\approx} e^{-3\epsilon} + O(q^{-1}) \tag{3.103}$$

This example makes clear that the leading contribution comes from the terms of $i_1 \neq i_2 \neq i_3, j_1 \neq j_2 \neq j_3$, and that each of these terms has a contribution, which depends on how many independent phases exist at $x_{\sigma\sigma'^{-1}}$. In the previous example, we studied the situation when, $\sigma\sigma'^{-1}$ has no fixed points. Assume now, that we are interested in a permutation with a single fixed point e.g. $\sigma\sigma'^{-1} = (12)$. Then we get an exponent of $x_{(12)} = \phi_{i_1,j_1} + \phi_{i_2,j_2} - \phi_{i_2,j_1} - \phi_{i_1,j_2}$. In the same manner as before, the leading contribution comes from the $\binom{q}{3}^2$ terms of $i_1 \neq i_2 \neq i_3, j_1 \neq j_2 \neq j_3$, with the only difference that $x_{(12)} \sim 2\mathcal{N}(0,\epsilon)$ and $\overline{e^{ix_{(12)}}} = e^{-2\epsilon}$. Every single fixed point of

the permutation reduces the number of independent phases by 2. The large q limit would then be

$$\overline{m^{(3)}_{\sigma,\sigma'}} \underset{q\to\infty}{\approx} e^{-2\epsilon} + O(q^{-1}) \tag{3.104}$$

• ***Arbitrary*** k ***case of*** $m^{(k)}_{\sigma,\sigma'}$

Now it is simple to generalize this logic to arbitrary k and σ, σ'. Under this most general scenario, the leading contribution at large q comes from the $\binom{q}{k}^2$ terms of $i_1 \neq i_2 \neq \ldots \neq i_k, j_1 \neq j_2 \neq \ldots \neq j_k$ and the exponent is a sum of $2(k - n_f(\sigma\sigma'^{-1}))$ independent phases and thus $x_{\sigma\sigma'^{-1}} \sim \sqrt{2(k - n_f(\sigma\sigma'^{-1}))}\mathcal{N}(0,\epsilon)$ leading to a contribution of $\overline{e^{ix_{\sigma\sigma'^{-1}}}} = e^{-\epsilon(k-n_f(\sigma\sigma'^{-1}))}$ for each of these terms in the sum. Finally, one recovers that in the most general case

$$\overline{m^{(k)}_{\sigma,\sigma'}} \underset{q\to\infty}{\approx} e^{-\epsilon(k-n_f(\sigma\sigma'^{-1}))} + O(q^{-1}) \tag{3.105}$$

This implies that at the leading order in q Eq. (3.97) becomes

$$M^{(k)}_{\sigma,\sigma'} \underset{q\to\infty}{\approx} e^{-t\epsilon(k-n_f(\sigma\sigma'^{-1}))} + O(q^{-1}) \tag{3.106}$$

This calculation gives access to an exact form of $\rho^{(k)}_{\text{RPM}}(t)$ and with this knowledge on our hands we can now find the exact form of the Frame Potential for the RPM. By going back to Eq. (3.43) we can now evaluate the frame potential. We have

$$F^{(k)}[\mathcal{E}_{RPM}(t)] = \text{Tr}\left[\rho^{(k)}_{\text{RPM}}(t)^2\right] = q^{-2kL} \sum_{\{\sigma\},\{\sigma'\}} \prod_{i=1}^{L} M^{(k)}_{\sigma_i,\sigma_{i+1}} M^{(k)}_{\sigma'_i,\sigma'_{i+1}} \text{Tr}\left[P_{\sigma_i} P_{\sigma'_i}\right] \tag{3.107}$$

with $\text{Tr}\left[P_{\sigma_i} P_{\sigma'_i}\right] = q^{\#\text{cycles}(\sigma_i\sigma'_i)}$. At the leading order in large q, is the identity permutation with the leading contribution, and thus we take $\sigma'_i = \sigma_i^{-1}$. Moreover, the number of fixed points is a class function and a permutation and its inverse has the same number of fixed points, meaning that $n_f(\sigma) = n_f(\sigma^{-1})$. It is straightforward that the use of these properties of n_f in (3.106) imply that $M^{(k)}_{\sigma,\sigma'} = M^{(k)}_{\sigma^{-1},\sigma'^{-1}}$. This

leads to

$$F^{(k)}_{\text{RPM}}(t) = q^{-kL} \sum_{\{\sigma\}} \prod_{i=1}^{L} [M^{(k)}_{\sigma_i,\sigma_{i+1}}]^2 = q^{-kL} \sum_{\{\sigma\}} \prod_{i=1}^{L} e^{-2\epsilon t(k-n_f(\sigma\sigma'^{-1}))} = q^{-kL} \operatorname{Tr}\left[T(\alpha)^L\right] \tag{3.108}$$

where we introduced the matrix $T(\alpha)$ of size $k! \times k!$ defined over S_k.

$$T(\alpha)_{\sigma,\sigma'} = \alpha^{(k-n_f(\sigma\sigma'^{-1}))}, \quad \alpha = e^{-2\epsilon t} \tag{3.109}$$

The trace is a result of the periodic boundary conditions of our problem. The matrix T is the spatial transfer matrix for our problem, and it encodes the information about the behaviour of the Frame potential and consequently of the overlaps, as we will demonstrate later. The diagonal elements are $T(\alpha)_{\sigma,\sigma} = 1$ and the symmetry of n_f under inversion of the permutation means that $T(\alpha)_{\sigma,\sigma'} = T(\alpha)_{\sigma',\sigma}$ and the transfer matrix is being symmetric. Quantum chaotic systems such as RPM are expected to demonstrate at larger t, time evolution operators, which can be mirrored by the statistical properties of Random Haar matrices. This can be seen, via Eqs. (3.108),(3.2.2) in the limit of $t \to \infty$ the parameter $\alpha \to 0$ and the sum is dominated by the situation where all permutations are the same $\sigma_i = \sigma$ independently of i, leading to $\lim_{t\to\infty} F^{(k)}_{\text{RPM}}(t) = k!/q^{kL}$. This is the value of the Frame potential for the Haar measure Eq. (3.49) proving the convergence to Haar at large times.

Another interesting limit, as a benchmark for the theory, is the non-interacting one. As we already mentioned, this is the limit $\epsilon \to 0$, of vanishing effective coupling, where the nearest neighbouring sites do not interact and thus the system decouples to L independent local systems. Let us see if our current results, for the RPM, comply with the previous logic. In the limit $\epsilon \to 0$, $\alpha = 1$ and from (3.109) we observe that $T(\alpha)_{\sigma,\sigma'} = 1$. It is easy to prove that for a matrix with only $+1$ entries one gets $\left(T(\alpha)^L\right)_{\sigma,\sigma'} = (k!)^{L-1}$, and Eq. (3.108) leads to $\lim_{\epsilon\to 0} F^k_{\text{RPM}}(t) = \left(\frac{k!}{q^k}\right)^L$ in large q, with $\frac{k!}{q^k}$ being the value of the Frame potential for a single-site system that converged to the Haar measure. In general, in the uncoupled case, the local Haar unitaries $u^{(j)}$, make each site converge to Haar measure, and thus we end up with L copies of the Haar distribution, which agrees with our expectations. Moreover, the action of the local Haar gates $u^{(j)}$ at every time step makes the site converge to Haar after just a single time step, explaining the time dependence of the frame potential in $\epsilon \to 0$.

In Sec. 3.2.2, we mentioned how the overlaps and the Frame potential omit a universal description based on the spatial transfer matrix formalism that was developed in that section. In addition, the expansion of the transfer matrix Eq. (3.67) up to permutations that differ by a single transposition leads to the use of the Thouless length L_{Th}, which depends on the microscopic details of the model. We can use the definition of the spatial transfer matrix $T(\alpha)$, in order to find L_{Th} for RPM. More specifically, we expand Eq. (3.109) in α, up to permutations $\sigma\sigma'^{-1} = \tau$, where τ is a transposition.

$$T(\alpha) = \mathbb{1} + \alpha^2 A + O(\alpha^3) \tag{3.110}$$

where A is the adjacency matrix transpositions. The maximum number of fixed points is k, and comes uniquely from the identity permutation $n_f(\mathbb{1}) = k$. So the diagonal elements $\sigma = \sigma$ have the leading contribution. The next order term, comes from permutations that have $k-2$ fixed points since it is not possible to have $k-1$ fixed points. These permutations are the ones that satisfy $\sigma\sigma'^{-1} = \tau$. So now we compare Eq. (3.110) with

$$T(\alpha) = \mathbb{1} + \frac{1}{L_{\text{Th}}(t)} A + O(L_{\text{Th}}(t)^{-3/2}) \tag{3.111}$$

and we recover that $L_{\text{Th}}(t) = \alpha^{-2} = e^{4\epsilon t}$. This is consistent with the scaling limit of $x = L/L_{\text{Th}}(t)$ defined in Sec. 3.2.2, and gives the same result

$$\lim_{\substack{t,L\to\infty \\ x=L/L_{\text{Th}}(t)}} T(\alpha)^L = \left(\mathbb{1} + \frac{xA}{xL_{\text{Th}}(t)}\right)^{xL_{\text{Th}}(t)} = e^{xA} \tag{3.112}$$

and consequently

$$\lim_{\substack{t,L\to\infty \\ x=L/L_{\text{Th}}(t)}} F^{(k)}_{\text{RPM}}(t) = q^{-kL} \operatorname{Tr}\left[e^{xA}\right] \tag{3.113}$$

At this point, we have expressed the Frame potential of the RPM, through the transfer matrix $T(\alpha)$, and found its scaling limit. The relation between the frame potential and the moments of overlaps $F^{(k)}_{\text{RPM}}(t) = \mathcal{N}^k \mathbb{E}\left[w'^k\right]$ (for pbc), lead to the same result demonstrated in Sec. 3.2.2. In general, the transfer matrix of the RPM model demonstrates the same scaling limit as the universal transfer matrix in Sec. 3.2.2, indicating already the validity of the universality of the theory. However, in the next section, we will show in detail how to diagonalise the matrix $T(\alpha)$, by exploiting the Toeplitz matrix formalism, and find exact results for $F^{(k)}_{\text{RPM}}(t)$. One can

also use the same formalism to directly find the spectrum of the adjacency matrix of transpositions A and thus obtain the exact forms of the moments Eq. (3.70).

3.2.5 Diagonalisation of $T(\alpha)$

To find the trace of $T(\alpha)^L$ it is enough to know the spectrum of the transfer matrix. Here we demonstrate a general formalism that makes it possible to find the full spectrum $\{\lambda_1, \lambda_2, \ldots, \lambda_{k!}\}$ of the matrix $T(\alpha)$, where we ordered $\lambda_i > \lambda_{i+1}$. The formalism that we are going to use is based on the generalisation of the concept of Toeplitz matrix [40] as well as the application of the Fourier transform on finite groups [93].

3.2.5.1 Generalised Toeplitz matrices

A Toeplitz matrix is a special type of matrix in which each descending diagonal from left to right is constant. In other words, all the elements along any given diagonal are the same.

A Toeplitz matrix F of size $n \times n$ can be represented as

$$F = \begin{pmatrix} f_0 & f_{-1} & f_{-2} & \cdots & f_{-(n-1)} \\ f_1 & f_0 & f_{-1} & \cdots & f_{-(n-2)} \\ f_2 & f_1 & f_0 & \cdots & f_{-(n-3)} \\ \vdots & \vdots & \vdots & \ddots & \vdots \\ f_{n-1} & f_{n-2} & f_{n-3} & \cdots & f_0 \end{pmatrix}, \quad F_{i,j} = f_{i-j}$$

Here, f_i are the elements of the matrix, and each element f_{i-j} depends only on the difference $i - j$, not on the individual indices i and j. Due to the finer structure, a $n \times n$ Toeplitz matrix has only $2n - 1$ degrees of freedom instead of n^2.

A circulant matrix is a special type of Toeplitz matrix where each row vector is shifted by one element to the right relative to the preceding row vector. Formally, a circulant matrix C of size $n \times n$ can be represented as:

$$C = \begin{pmatrix} c_0 & c_1 & c_2 & \cdots & c_{n-1} \\ c_{n-1} & c_0 & c_1 & \cdots & c_{n-2} \\ c_{n-2} & c_{n-1} & c_0 & \cdots & c_{n-3} \\ \vdots & \vdots & \vdots & \ddots & \vdots \\ c_1 & c_2 & c_3 & \cdots & c_0 \end{pmatrix}, \quad C_{i,j} = c_{(i-j) \mod n}$$

Here, the first row defines the entire matrix, making the total degrees of the matrix n. The set of indices in a circulant matrix can be associated with the elements of the cyclic group $\mathbb{Z}_n$. The cyclic group $\mathbb{Z}_n$ is the group of integers $0, 1, \ldots, n-1$, equipped with modulo n addition. In this context, the element c_i in the first row of the circulant matrix corresponds to the element $i \in \mathbb{Z}_n$.

The structure of a circulant matrix is inherently related to the group operation in $\mathbb{Z}_n$. Specifically, the (i, j)-th entry of a circulant matrix depends only on the difference $(i-j) \mod n$, reflecting the group operation of $\mathbb{Z}_n$ and that property is the key one, which makes circulant matrices diagonalizable by Discrete Fourier Transform (DFT) [40].

Now we will generalize this concept to an arbitrary finite group G. Given any function $f : G \to \mathbb{C}$, we can generalise this notion to an arbitrary group G introducing a $|G| \times |G|$ (with $|G|$ the order of the group G) matrix

$$F_{\sigma,\sigma'} = f(\sigma\sigma'^{-1}) , \qquad \forall \sigma, \sigma' \in G \tag{3.114}$$

The matrix $T(\alpha)$ defined in Eq. (3.109) has exactly this form with $G = S_k$, but here we will keep the discussion general. Similarly to the case of standard Toeplitz matrices, the spectrum can be investigated using the Fourier transform. However, the DFT is not useful for groups, which have different structures than $\mathbb{Z}_n$; therefore, we will generalize this concept as well.

For Given a finite group G, the group's representations $\rho : G \to \mathrm{GL}(d_\rho, \mathbb{C})$ with dimension d_ρ, and a function $f : G \to \mathbb{C}$, we define its Fourier transform $\hat{f}(\rho)$ as a function over the space of representations of G which reads

$$\hat{f}(\rho) = \sum_{\sigma \in G} f(\sigma)\rho(\sigma) . \tag{3.115}$$

The inverse of this relation can be shown [93] to be given by

$$f(g) = \frac{1}{|G|} \sum_{\rho \in \mathrm{Irr}(G)} \dim(\rho) \, \mathrm{Tr}\left[\rho(g^{-1})\hat{f}(\rho)\right] \tag{3.116}$$

where the sum is restricted to the irreducible representations $\mathrm{Irr}(G)$ [94]. The nice property about this Fourier transform is that it converts convolutions into a product

of Fourier Transforms [93]. In other words, if $h, g : G \to \mathbb{C}$

$$h(\sigma) = \sum_{\sigma' \in G} f(\sigma\sigma'^{-1}) g(\sigma') \quad \Rightarrow \quad \hat{h}(\rho) = \hat{f}(\rho)\hat{g}(\rho) \tag{3.117}$$

•***Proof***

We start from the definition Eq. (3.115) for the scalar h, where we insert the convolution Eq. (3.117)

$$\hat{h}(\rho) = \sum_{\sigma \in G} h(\sigma)\rho(\sigma) = \sum_{\sigma, \sigma' \in G} f(\sigma\sigma'^{-1}) g(\sigma')\rho(\sigma) \tag{3.118}$$

Afterwards, we take advantage of the group structure and change summation variables as $\sigma = \sigma''\sigma'$.

$$\hat{h}(\rho) = \sum_{\sigma', \sigma'' \in G} f(\sigma'') g(\sigma')\rho(\sigma''\sigma') \tag{3.119}$$

By definition a representation ρ is a homomorphism meaning that $\rho(\sigma''\sigma') = \rho(\sigma'')\rho(\sigma')$. So finally, we recover

$$\hat{h}(\rho) = \left(\sum_{\sigma'' \in G} f(\sigma'')\rho(\sigma'') \right) \left(\sum_{\sigma' \in G} g(\sigma')\rho(\sigma') \right) = \hat{f}(\rho)\hat{g}(\rho) \tag{3.120}$$

Now let's consider an eigenvector of the matrix F in Eq. (3.114). Labelling its components as $c(\sigma)$ for any $\sigma \in G$, it must satisfy

$$\sum_{\sigma' \in G} f(\sigma\sigma'^{-1}) c(\sigma') = \lambda c(\sigma) \tag{3.121}$$

This is a convolution and thus taking the Fourier transform of both sides, this implies

$$\hat{f}(\rho)\hat{c}(\rho) = \lambda \hat{c}(\rho)\,, \qquad \forall \rho \in \mathrm{Irr}(G) \tag{3.122}$$

Note that each side of this equation is matrices of size $\dim(\rho) \times \dim(\rho)$. To solve this equation, let's write the spectral decomposition of the matrix $\hat{f}(\rho)$ in bracket notation:

$$\hat{f}(\rho) = \sum_{j=1}^{\dim(\rho)} \lambda_j(\rho) \, |j\rangle \langle j| \tag{3.123}$$

Then, we see that for any $\tilde{\rho} \in \mathrm{Irr}(G)$ and any pair $i, j \in \{1, \ldots, \dim(\rho)\}$, the following choice of $\hat{c}(\rho)$ provides a solution of Eq. (3.122)

$$\hat{c}(\rho) \equiv \hat{c}^{(i,j,\tilde{\rho})}(\rho) = \begin{cases} 0 & \rho \neq \tilde{\rho} \\ |i\rangle \langle j| & \rho = \tilde{\rho} \end{cases} \tag{3.124}$$

where $|i\rangle$ and $\langle j|$ refer respectively to the right and left eigenvectors of $\hat{f}(\rho)$. Once plugged in Eq. (3.122), it leads to,

$$\hat{f}(\rho)\hat{c}^{(i,j,\tilde{\rho})}(\rho) = \lambda_i(\tilde{\rho})\hat{c}^{(i,j,\tilde{\rho})}(\rho) \; . \tag{3.125}$$

This shows that the spectrum of the matrix F is given by the $\lambda_i(\rho)$ for $\rho \in \mathrm{Irr}(G)$ and $i = 1, \ldots, \dim(\rho)$. In Eq. (3.125) we can fix the index i, while j is "running" all over its $\dim(\rho)$ values and thus each $\lambda_i(\rho)$ has a degeneracy $\dim(\rho)$. This provides a full spectral decomposition since one has the known equality [93]

$$\sum_{\rho \in \mathrm{Irr}(G)} \dim(\rho)^2 = |G| \tag{3.126}$$

Now let us consider the case where the function f is a class function, i.e. it is invariant under the group conjugation

$$f(\omega\sigma\omega^{-1}) = f(\sigma) \; . \quad \forall \omega, \sigma \in G \tag{3.127}$$

A conjugacy class of an element in G is defined as the set of elements of G, that differ by a conjugacy transformation $\mathrm{cl}(\sigma) = \{g\sigma g^{-1}, \forall g \in G\}$. Consequently, a class function f has the same value all over $\mathrm{cl}(g)$ and in general if we define $\mathrm{Cl}(G) = \{\mathrm{cl}(g), \forall g \in G\}$, then f has, at most, as many values as conjugacy classes exist. Moreover, conjugacy is an equivalence relation, making $\mathrm{Cl}(G)$ a partition of G. This property implies that the generalised Toeplitz matrix, has a finer structure, when f is a class function and this as we will see later is reflected upon its spectrum, by increasing the degeneracy of the eigenvalues.

In the case where f is a class function, one can see that

$$[\hat{f}(\rho), \rho(\sigma)] = 0 \; , \qquad \forall \sigma \in G \tag{3.128}$$

•***Proof***

Indeed, by definition we have

$$\hat{f}(\rho)\rho(\sigma) = \sum_{\sigma' \in G} f(\sigma')\rho(\sigma')\rho(\sigma) \sum_{\sigma' \in G} f(\sigma')\rho(\sigma'\sigma) = \sum_{\sigma'' \in G} f(\sigma''\sigma^{-1})\rho(\sigma'')$$

where we used the fact that ρ is a homomorphism on G and changed summation variables as $\sigma'' = \sigma'\sigma$. Then we use the property of a class function to obtain $f(\sigma^{-1}\sigma'') = f(\sigma''\sigma^{-1})$.

$$\hat{f}(\rho)\rho(\sigma) = \sum_{\sigma'' \in G} f(\sigma^{-1}\sigma'')\rho(\sigma'') = \sum_{\sigma''' \in G} f(\sigma''')\rho(\sigma\sigma''') = \rho(\sigma) \sum_{\sigma''' \in G} f(\sigma''')\rho(\sigma''') = \rho(\sigma)\hat{f}(\rho) \quad (3.129)$$

Due to Schur's lemma [93], if $\rho \in \mathrm{Irr}(G)$, $\hat{f}(\rho)$ must be a multiple of the identity.

$$\hat{f}(\rho) = \lambda(\rho)\mathbb{1} \quad (3.130)$$

where thus in the spectral decomposition Eq. (3.123), $\lambda_j(\rho) = \lambda(\rho)$ for all j's. For generalised Toeplitz matrices obtained by class functions, the eigenvalues are labelled by the irreducible representations ρ and since every $\lambda_j(\rho)$ has already a degeneracy $\dim(\rho)$, each $\lambda(\rho \in \mathrm{Irr}(G)$ each has a degeneracy given by $\dim(\rho)^2$. From now on we are working with the irreps of G, so ρ indicates an irrep. We can finally obtain an equation for $\lambda(\rho)$ by taking the trace of both sides in Eq. (3.115) and using (3.130)

$$\mathrm{Tr}\left[\hat{f}(\rho)\right] = \dim(\rho)\lambda(\rho) = \sum_{\sigma \in G} f(\sigma)\chi_\rho(\sigma) \quad (3.131)$$

where $\chi_\rho(\sigma) = \mathrm{Tr}[\rho(\sigma)]$ is the character of the representation ρ and thus, by definition $\chi_\rho(1) = \dim(\rho)$, with 1 indicating the neutral element of G and $\rho(1) = \mathbb{1}$. Since both the function f and the character are class functions, we can rewrite the sum as a sum over conjugacy classes $\mathrm{Cl}(G)$

$$\lambda(\rho) = \sum_{\sigma \in G} \frac{f(\sigma)\chi_\rho(\sigma)}{\chi_\rho(1)} = \sum_{\mu \in \mathrm{Cl}(G)} \frac{f(\mu)\chi_\rho(\mu)|\mu|}{\chi_\rho(1)} \quad (3.132)$$

where we used that $\chi_\rho(1) = \dim(\rho)$, we denote as $|\mu|$ the size of the conjugacy class μ and $f(\mu)$ is the common value of the scalar over μ. Eq. (3.132) demonstrates a direct connection of the eigenvalues of the generalized Toeplitz matrices with the group structure of G. In particular, knowing the characters over the irreps and the conjugacy classes $\mathrm{Cl}(G)$, is enough to determine the eigenvalues. As an example, we can look at the case where $f(\mu) = 1$ irrespectively of μ. In this case, from Eq. (3.132), we have

$$\lambda(\rho) = \sum_{\sigma\in G} \frac{\chi_\rho(\sigma)}{\chi_\rho(1)} = \delta_{\rho,1_\mathrm{r}}|G| \tag{3.133}$$

where, 1_r is the trivial irrep. The trivial irreducible representation of G is a homomorphism $1_\mathrm{r} : G \to \mathrm{GL}(1,\mathbb{C})$, to 1-dimensional complex vector spaces. Formally, it maps every element $\sigma \in G$ to 1, $\rho(\sigma) = 1 \quad \forall\sigma \in G$ and thus its character is trivially $\chi_{1_\mathrm{r}}(\sigma) = 1, \quad \forall\sigma \in G$. Eq. (3.133) is derived by using the orthogonality of the characters over irreps ρ, ρ'

$$\frac{1}{|G|}\sum_{\sigma\in G} \chi_\rho(\sigma)\chi^*_{\rho'}(\sigma) = \delta_{\rho,\rho'} \tag{3.134}$$

by making the choice of $\rho' = 1_\mathrm{r}$. Eq. (3.133) is of course consistent with the fact that for $f = 1$, the matrix F reduces to a matrix made of 1's, which thus has only one non-vanishing eigenvalue, which equals the size of the matrix itself, i.e. $|G|$. The non-vanishing eigenvalue is characterized by 1_r, and has a degeneracy of $\dim(1_\mathrm{r}) = 1$, making it unique. A matrix composed just of ones satisfies, $F^2 = k!F$ and that makes this operation a scalar multiple of a projection.

3.2.5.2 Spectrum of $T(\alpha)$ and scaling functions

We now use the formalism developed in the previous part and specialise the discussion to the case, where we diagonalise the matrix $T(\alpha)$. In this case, $G = S_k$ and $f(\sigma) = \alpha^{k-n_f(\sigma)}$. We can expand Eq. (3.108) as

$$F^{(k)}_{\mathrm{RPM}}(t) = q^{-kL} \sum_{\rho\in\mathrm{Irr}(S_k)} \dim(\rho)^2\lambda(\rho)^L \tag{3.135}$$

In the case of S_k, the irreducible representations and the conjugacy classes are labelled by partitions (or Young diagram) of size k [95]. Unfortunately, the explicit expression of $\chi_\rho(\lambda)$ is not simple (see for instance [95]). There are two simple cases: $t = 0$, where $\alpha = 1$ making $T(\alpha)$ a matrix of ones and thus one can apply (3.133); the

case $t \to \infty$, where $\alpha = e^{-4\epsilon t} \to 0$. In this case, $f(\sigma) = \delta_{\sigma,1}$ and from Eq. (3.132) we can observe, that only the conjugacy class of the identity survives (as all points are fixed) and $\lambda(\rho) = 1, \forall \rho \in \mathrm{Irr}(S_k)$. Consequently, Eq. (3.135), becomes:

$$\lim_{t\to\infty} F^{(k)}_{\mathrm{RPM}}(t) = q^{-kL} \sum_{\rho\in \mathrm{Irr}(S_k)} \dim(\rho)^2 = k!/q^{-kL} = F^{(k)}_{\mathrm{Haar}} \tag{3.136}$$

where we used the identity given in Eq. (3.126) and taken into consideration the large q limit for $F^{(k)}_{\mathrm{Haar}}$.

The largest eigenvalue corresponds to the case of the trivial irreducible representation 1_{r}, where all elements of S_k are sent to 1. We shall provide a brief proof of this.

•***Proof***

In [96] it was already proven that the characters of S_k have the following upper bound

$$\left|\frac{\chi_\rho(\sigma)}{\chi_\rho(1)}\right| \leq \chi(1)^{\beta-1+\varepsilon} \to \left|\frac{\chi_\rho(\sigma)}{\chi_\rho(1)}\right| \leq 1 \forall \sigma \in S_k \tag{3.137}$$

for some $\beta \in (0, 1-\varepsilon)$ and $\varepsilon > 0$ and $\rho \in \mathrm{Irr}(S_k)$. If we apply Eq. (3.137) to Eq. (3.132) then we get

$$|\lambda(\rho)| \leq \sum_{\mu\in \mathrm{Cl}(G)} \left|\frac{f(\mu)\chi_\rho(\mu)|\mu|}{\chi_\rho(1)}\right| \leq \sum_{\mu\in \mathrm{Cl}(G)} f(\mu)|\mu| = \lambda(1_{\mathrm{r}}) \tag{3.138}$$

with $f(\mu)$ being a real, non-negative scalar. Therefore, the trivial representation is the one characterizing the maximal eigenvalue. This gives the maximal eigenvalue,

$$\lambda(1_{\mathrm{r}}) = \sum_{\substack{a_j, \\ \sum_j j a_j = k}} \frac{k!\alpha^{k-a_1}}{\prod_j (a_j)! j^{a_j}} \tag{3.139}$$

where we rewrote the sum over partitions μ as a sum over the integers a_j counting the number of j's in the partition (as explained in the following paragraph). We also used the explicit formula for the size of the conjugacy class [96], μ as

$$|\mu| = \frac{k!}{\prod_j (a_j)! j^{a_j}} \tag{3.140}$$

A conjugacy class μ of S_k is characterised by an integer partition which is denoted as

$(1^{a_1}2^{a_2}\dots k^{a_k})$ and denotes the conjugacy class of permutations with cycle type as a_1-cycles of length 1, a_2 cycles of length 2, etc. For, example, all transpositions belong to the class, with cycle type $(1^{k-2}2^1)$. The permutations arrange k points meaning that the lengths should add up to k, and thus $\sum_j ja_j = k$. The value of the class function is $f(\mu) = \alpha^{k-a_1}$ since the fix points are indicated by cycles of length 1. In the same approach, as for $\lambda(1_r)$ one can find that an expression for all the eigenvalues

$$\lambda(\rho \in \mathrm{Irr}(S_k)) = \sum_{\substack{a_j, \\ \sum_j ja_j = k}} \frac{k!\alpha^{k-a_1}}{\prod_j (a_j)! j^{a_j}} \frac{\chi_\rho((1^{a_1}\dots k^{a_k}))}{\chi_\rho((1^k))} \tag{3.141}$$

with the identity element represented as the k fixed point partition (1^k) In addition, the unique maximal eigenvalue has an eigenspace spanned by the vector $|1_s\rangle$, which is just a column of ones.

•***Proof***

We apply the transfer matrix $T(\alpha)$ to the vector, $|1_s\rangle$

$$T(\alpha)\,|1_s\rangle \overset{\sigma \text{ component}}{\to} \sum_{\sigma' \in S_k} f(\sigma\sigma'^{-1}) = \sum_{\sigma'' \in S_k} f(\sigma'') \tag{3.142}$$

where we used the group structure to change the summation variable $\sigma'' = \sigma\sigma'^{-1}$. Since f is a class function we can write the sum over $\mathrm{Cl}(S_k)$ and finally get that

$$\sum_{\sigma'' \in S_k} f(\sigma'') = \sum_{\mu \in \mathrm{Cl}(S_k)} |\mu| f(\mu) = \lambda(1_r) \to T(\alpha)\,|1_s\rangle = \lambda(1_r)\,|1_s\rangle \tag{3.143}$$

This result is valid for any generalised Toeplitz matrix of a class function and by replacing $f(\sigma) = \alpha^{k-n_f(\sigma)}$, in our case, we get Eq. (3.139). The maximal eigenvalue has the leading contribution in the trace appearing in the Frame Potential in Eq. (3.108), making it a good way to extract the time scales at which RPM approaches a $k-$design. In particular, if we perform an expansion over α at Eq. (3.139), up to order α^2, one gets

$$\lambda(1_r) = 1 + \binom{k}{2}\alpha^2 + O(\alpha^3) \tag{3.144}$$

where we kept the partitions with k and $k-2$ fixed points, which correspond to the identity and the $\binom{k}{2}$ transpositions, respectively. So the Frame Potential of RPM

depends on $\lambda(1_r)^L$ and has approached the Haar one at times for which the maximal eigenvalue is close at one and thus $\binom{k}{2}L\alpha^2 \ll 1$, or equivalently

$$t \gg t_k \equiv \frac{1}{4\epsilon}\log\left(\frac{Lk(k-1)}{2}\right) \tag{3.145}$$

with t_k indicating the time scales at which the system approaches a $k-$design and as we can see it is of the order of $\sim \log(Lk^2)$. It is interesting to also note that, the time scales t_k agree also with our intuitive expectations. In the non-interactive limit $\epsilon \to 0$, RPM never approaches a L site Haar measure and thus t_k diverges, and the larger the effective coupling, the more mixing the local phase gates $v^{(j,j+1)}$ cause and thus the system approaches the Haar ensemble faster. As a final part of this section, we will find the exact form for the Frame potential in the scaling limit.

In order to investigate this limit, we assume large L and t, such that $x = L\alpha^2 = L/L_{\text{Th}}(t)$ is constant. The asymptotic behaviour of the Frame potential would then be

$$\tilde{F}^{(k)}_{\text{RPM}} = \lim_{\substack{t\to\infty \\ L\to\infty \\ L/L_{\text{Th}}(t)=x}} \frac{F^{(k)}_{\text{RPM}}(t)}{F^{(k)}_{\text{Haar}}} = \frac{1}{k!}\sum_{\rho\in\text{Irr}(S_k)} \dim(\rho)^2 e^{x\nu(\rho)} \tag{3.146}$$

To obtain this expression, we performed again an expansion up to the second order in α for Eq. (3.141) and obtained that

$$\lim_{\substack{t\to\infty \\ L\to\infty \\ \alpha^2 L=x}} \lambda(\rho)^L = \lim_{\substack{t\to\infty \\ L\to\infty \\ L/L_{\text{Th}}(t)=x}} (1+\alpha^2\nu(\rho)+O(\alpha^3))^L = e^{x\nu(\rho)}\,, \quad \nu(\rho) = \binom{k}{2}\frac{\chi_\rho((1^{k-2}2^1))}{\chi_\rho((1^k))} \tag{3.147}$$

The coefficient $\nu(\rho)$ is obtained by the conjugacy class of transpositions, which is responsible for the order α^2 term in the eigenvalues. Moreover, according to Eq. (3.137) the coefficient satisfies $|\nu(\rho)| \leq \nu(1_r) = \binom{k}{2}$, meaning that the trivial representation is the irrep with the leading exponential in Eq. (3.146) and thus, at large x, one obtains

$$\tilde{F}^{(k)}_{\text{RPM}} \overset{x\to\infty}{=} \frac{1}{k!}e^{xk(k-1)/2} \tag{3.148}$$

At small x instead, we have the expansion

$$\tilde{F}^{(k)}_{\text{RPM}} \overset{x\to 0}{=} \left(1+\frac{k(k-1)x^2}{4}+O(x^3)\right) \tag{3.149}$$

•***Proof***

This limit can be calculated by expanding the exponential $e^{x\nu(\rho)} = 1 + x\nu(\rho) + x^2\nu(\rho)^2/2 + O(x^3)$ up to second order in Eq. (3.146) and then using Eq. (3.147), which leads to

$$\tilde{F}^{(k)}_{\text{RPM}} = \frac{1}{k!}\sum_{\rho\in\text{Irr}(S_k)} \dim(\rho)^2 + x\binom{k}{2}\chi_\rho(1^{k-2}2^1)\chi_\rho((1^k)) + \frac{x^2}{2}\binom{k}{2}^2\chi_\rho((1^{k-2}2^1))^2 \tag{3.150}$$

where we used that $\chi_\rho((1^k)) = \dim(\rho)$.At this point, we will need the second orthogonality relation of the characters, according to which

$$\sum_{\rho\in\text{Irr}(G)} \chi_\rho(\sigma)\chi^*_\rho(\sigma') = \begin{cases} |C_G(\sigma)|\,, & \text{if } \sigma,\sigma' \text{ belong to the same conjugacy class} \\ 0 & \text{otherwise.} \end{cases} \tag{3.151}$$

for an arbitrary finite group G. $C_G(\sigma)$ is called the centralizer and is defined as $C_G(\sigma) = \{\sigma' \in G \text{ such that } \sigma'\sigma\sigma'^{-1} = \sigma\}$. Henceforth, $C_G(\sigma)$ contains all the elements of the group that commute with σ. We can directly see that by choosing σ' as the identity element we get for S_k that,

$$\sum_{\rho\in\text{Irr}(S_k)} \chi_\rho(1^{k-2}2^1)\chi_\rho((1^k)) = 0 \tag{3.152}$$

So the order x term in Eq. (3.150) vanishes. For the third term of the same equation, we need to notice that a transposition is the same as its inverse. Then by using that $\chi_\rho(\sigma^{-1}) = \chi^*_\rho(\sigma)$, we can deduce from the orthogonality relation that

$$\sum_{\rho\in\text{Irr}(S_k)} \chi_\rho((1^{k-2}2^1))^2 = \left|C_{S_k}((1^{k-2}2^1))\right| \tag{3.153}$$

For a cycle type $(1^{a_1}2^{a_2}\dots k^{a_k})$ its centralizer is found [95] to have an order of

$$|C_{S_k}((1^{a_1}2^{a_2}\dots k^{a_k}))| = \prod_{i=1}^{k} i^{a_i}\cdot a_i! \tag{3.154}$$

Then we can deduce for the cycle type of the transpositions that,

$$\left|C_{S_k}((1^{k-2}2^1))\right| = 2\cdot(k-2)! \tag{3.155}$$

Finally we replace Eqs. (3.152),(3.153) into the expansion Eq. (3.150) to recover

$$\tilde{F}^{(k)}_{\text{RPM}} \overset{x\to 0}{=} \left(1+\frac{k(k-1)x^2}{4}+O(x^3)\right) \tag{3.156}$$

The previous discussion in this section was made for the RPM with pbc, however, it can be used to study as well the case of open boundary conditions. Specifically, for obc there is no coupling between the sites $L, 1$ from the layer $U_2(t)$, implying that there is no transfer matrix coupling these sites and thus (3.108) becomes:

$$F^{(k)}_{\text{RPM,obc}}(t) = q^{-kL}\sum_{\{\sigma\}}\prod_{i=1}^{L-1}[M^{(k)}_{\sigma_i,\sigma_{i+1}}]^2 = q^{-kL}\sum_{\{\sigma\}}\prod_{i=1}^{L-1} e^{-2\epsilon t(k-n_f(\sigma\sigma'^{-1}))} = q^{-kL}\sum_{\sigma_1,\sigma_L}\left(T(\alpha)^{L-1}\right)_{\sigma_1,\sigma_L} \tag{3.157}$$

One can validate again by Eq. (3.112), that $F^{(k)}_{\text{RPM,obc}}(t)$ leads again to the same moments of the overlaps as in Sec. 3.2.2. We now use the vector $|1_s\rangle$ that was introduced before and deduce

$$F^{(k)}_{\text{RPM,obc}}(t) = q^{-kL}\langle 1_s|T(\alpha)^{L-1}|1_s\rangle = q^{-kL}k!\lambda(1_r)^{L-1} \tag{3.158}$$

where we used t that $|1_s\rangle$ is an eigenvector of the maximal eigenvalue. In the scaling limit that was established before, one finally recovers the scaled Frame potential for obc

$$\tilde{F}^{(k)}_{\text{RPM,obc}} = e^{x\frac{k(k-1)}{2}} \tag{3.159}$$

which is the same as the $x\to\infty$ limit of the pbc case.

3.2.6 Probability distribution of overlaps

We now explore the probability distribution $p(w';x)$ of the overlaps. We are going to use the results of the previous section to find the universal exact expression of the moments of, w', and then reverse engineer our way from the moments to the exact form of the probability distribution. Our method is based on expressing w' as a product of two independent random variables, for which we find the probability distributions.

The moments and Frame potential are related via the equation $F^{(k)}_{\text{RPM}}(t) = \mathcal{N}\mathbb{E}\left[w'^k\right]$, with $\mathcal{N}$ being the dimension of Hilbert space. Now the results in Eqs. (3.146),(3.159),

lead to the following exact results

$$\lim_{\substack{t,L\to\infty \\ x=L/L_{\mathrm{Th}}(t)}} \mathbb{E}\left[w'^k\right] = \begin{cases} \sum_{\rho\in \mathrm{Irre}(S_k)} \dim(\rho)^2 e^{x\nu(\rho)}, & \text{for pbc} \\ k! e^{xk(k-1)/2}, & \text{for obc} \end{cases} \tag{3.160}$$

We start with finding the probability distribution $p_{\mathrm{obc}}(w';x)$ in the case of obc. Using the information from the moments in the equation above, we can now derive the overlap distribution. It is practical to view $k!e^{xk(k-1)/2}$ as a product of the moments of two independent random variables. We express $w' \overset{\text{in law}}{=} w_0 g$ as the product of the random variables w_0, g. Here, w_0 is the variable with moments $\mathbb{E}_{\mathrm{obc}}[w_0^k] = k!$, whereas the variable g represents the residual $\mathbb{E}_{\mathrm{obc}}[g^k] = e^{xk(k-1)/2}$. The distribution that leads to the moments of w_0 is already known and is the Porter-Thomas distribution. Consequently, the distribution of w_0, which we denote as $P_1(w_0)$, is exactly

$$P_1(w_0) = \Theta(w_0) e^{-w_0} \tag{3.161}$$

On the other hand, $e^{xk(k-1)/2}$ are the moments of the Log-normal distribution with parameters $\mu = -x/2$ and $\sigma = x$ (the mean value and variance of the normal distribution, where the log-normal comes from), meaning that g follows the distribution

$$P_2(g) = \Theta(g) \frac{1}{g\sqrt{x}\sqrt{2\pi}} \exp\left(-\frac{(\ln g + x/2)^2}{2x}\right) \tag{3.162}$$

Afterwards, we can find the distribution of the overlaps since

$$p_{\mathrm{obc}}(w';x) = \int_{-\infty}^{+\infty} dw_0 dg P_1(w_0) P_2(g) \delta(w' - w_0 g) = \int_{-\infty}^{+\infty} dg P_1(w'/g) P_2(g) \tag{3.163}$$

We use the expressions given for P_1, P_2 and by performing the change of variables $y = (\ln g + x/2)/\sqrt{2x}$, we finally recover

$$p_{\mathrm{obc}}(w';x) = \Theta(w') \int_{-\infty}^{+\infty} \frac{dy\, e^{-y^2}}{\sqrt{\pi}} \exp\left\{-w' e^{y\sqrt{2x} - x/2}\right\} \tag{3.164}$$

For the case of pbc, the procedure is the same but in this case, the moments of g take a more complicated form, whereas we choose to keep the same moments for w_0

$$\mathbb{E}_{\mathrm{pbc}}[w_0^k] = k!, \quad \mathbb{E}_{\mathrm{pbc}}[g^k] = \frac{1}{k!} \sum_{\rho\in \mathrm{Irre}(S_k)} \dim(\rho)^2 e^{x\nu(\rho)} \tag{3.165}$$

For periodic boundary conditions, the distribution of g is more complex. As discussed in various studies [97, 98], its generating function can be expressed as

$$g_{\text{pbc}} \overset{\text{in law}}{=} \lim_{n\to\infty} \frac{1}{n} \text{tr}\left[e^{\sqrt{xn}H+xB}\right] \tag{3.166}$$

where H is a $n \times n$ matrix drawn from the Gaussian Unitary Ensemble (GUE), $P(H) \propto \exp\{-n\,\text{Tr}\{H^2\}/2\}$, [99]. B is a diagonal matrix with and its diagonal entries are $(-1/2, -3/2, \ldots, -(2n-1)/2)$. Eq. (3.166) is being proven in detail in App. B.3.

The random variable g represents the crucial random fluctuations that cause the system to diverge from the Porter-Thomas distribution (an indication of the approach to Haar statistics). To see that, let us assume the limit of large time and fixed system size, or else the limit $x \to 0$. From the expressions derived above (for both obc and pbc), it is straightforward to observe that the fluctuations of g vanish in this limit, and its distribution converges to $P(g) \to \delta(g-1)$. Thus, $g = 1$ and the overlaps follow the same distribution as the random variable w_0, which is the Porter-Thomas one. Conversely, on the limit where the system size is increasing sufficiently, such that $x > 0$ is increasing, then the typical value of g is increasing as well, with respect to the value 1, indicating an increase in the fluctuations of w' from w_0, which have a typical size of $\mathbb{E}[w' - w_0] = \mathbb{E}[g] - 1$.

We conclude by demonstrating the agreement of the numerics with our theory for the distributions of w', in Fig. 3.6, where we present numerical results for two different models: RPM and brick-wall-model (BWM), verifying the universality of our theory. The reader can refer to App. B.4 for more details about the numerical simulations as well as additional numerics on our theory.

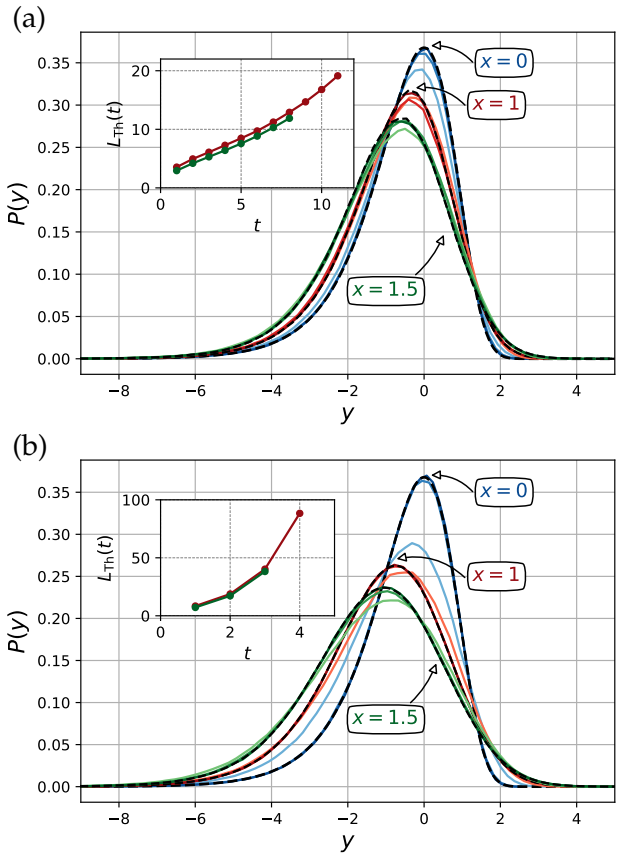

FIGURE 3.6: Comparison of the distribution of $y = \log w'$ between numerical simulation and the theoretical prediction (black dashed line) for different values of x and increasing value of the depth t, which is indicated with darker shades of the same colour. For each t, the value of $L \sim L_{\mathrm{Th}}(t)$ (shown in the insets) is chosen so that $\mathbb{E}[y]$ matches the theoretical prediction. (a): The pbc, numerical simulation of the RPM at $q = 2, \epsilon = 1$. For $x = 0$, we show the pairs $(t, L) \in \{(7,8), (11,8), (15,8)\}$; for $x = 1$, $(t, L) \in \{(3,6), (5,9), (10,17)\}$; for $x = 1.5$, $(t, L) \in \{(3,8), (5,11), (8,18)\}$. The theoretical distribution of y was generated for $w = w_0\, g$ using (3.166) and for a sample size $N_{\mathrm{sample}} = 10^6$ at $n = 300$. (b): The obc, numerical simulation for a brick-wall model (BWM) where the local 2-site gate is chosen independently of the Haar distribution at $q = 2$. We show data for $x = 0$, $(t, L) \in \{(1,6), (3,6), (4,6)\}$; for $x = 1$, $(t, L) \in \{(1,8), (3,40), (4,88)\}$; for $x = 1.5$, $(t, L) \in \{(1,11), (2,26), (3,57)\}$. The theoretical distribution $P(y)$ was created by the use of (3.164). All numerical distributions were obtained from a sample size $N_{\mathrm{sample}} = 1.5 \times 10^6$. Figure taken from [37].

Chapter 4

Universal out-of-equilibrium dynamics of critical quantum systems

This chapter examines critical one-dimensional quantum systems initially prepared in their ground state. Practically, the starting Hamiltonian is homogeneous and gapless, ensuring scale invariance. Under these conditions, the low-energy spectrum is independent of the microscopic details and can be accurately described by a CFT. Here, we introduce a spatially smooth, temporally white noise, coupled to the energy density for $t > 0$, which drives the system out-of-equilibrium through the resulting unitary dynamics. Using conformal field theory, we derive a universal description of the out-of-equilibrium dynamics. We demonstrate that the complete distribution of correlation functions reaches a non-trivial stationary limit, which is not apparent at the level of noise averages but instead shows apparent heating. This chapter is organized as follows:

- In Sec. 4.1, we present a brief introduction to CFT and focus mainly on notions from this theory that are going to be useful. In more detail, we first present how primary fields and their $N-$point functions transform under conformal transformations, as well as in the special case of $d = 2$. Secondly, we present the stress-energy tensor and its relation with conserved charges such as energy and momentum. Finally, we demonstrate how the replica trick can relate the entanglement entropy with the $N-$point function of specific primary fields, called twist fields.

- In Sec. 4.2 we showcase our original results on the out-of-equilibrium dynamics of $d = 1 + 1$ critical systems. In particular:
  - In Sec. 4.2.1 we introduce the model and give a brief review of the main results. The theory is established for a one-dimensional model, that undergoes a second-order quantum phase transition and that is quenched by noise coupled to the energy density with spatial correlation given by a smooth function $f(x)$.
  - In Sec. 4.2.2, we take advantage that the time evolution under our set-up, of a primary field, is a conformal transformation and relate the dynamical $N-$ point functions of primary fields, with N stochastic backward trajectories. Our description appears with two chiralities due to the CFT in $d = 1 + 1$. In addition, we derive the Fokker-Planck (FP) equation that governs the statistics of these backward trajectories.
  - In Sec. 4.2.3, we focus on the case of two-point correlations and thus two stochastic trajectories and obtain the exact relation between the two-point correlations and the backward trajectories via two stochastic variables $\kappa^{\pm} \equiv \kappa, r$ for each chirality. r is related to the initial distance ℓ of the backward trajectories.
  - In Sec. 4.2.4, we use the 4-point FP equation of the backward trajectories in order to find the FP equation of the jpdf $P_t(r, \kappa)$(for either chiralities). This new FP equation is then employed to extract the stochastic differential equations (SDEs) of κ, r.
  - In Sec. 4.2.5, we study the SDEs at both the cases of $\ell \ll 1$ and $\ell \gg 1$ by keeping only the leading terms in these limits. We prove that in the case of $\ell \ll 1$ we obtain a Bougerol SDE, which admits a stationary distribution of $-3/2$ tails for κ, whereas for $\ell \gg 1$ at small times κ follows a rescaled Brownian motion.
  - In Sec. 4.2.6, we use the characteristic function of κ and derive its stationary equation, which takes the form of a Schrödinger equation. By analysing it, we prove the "fat" $-3/2$ tails of the distribution of κ for arbitrary ℓ and in the case of $\ell \gg 1$, we exhibit that a Levy distribution appears.

- In Sec. 4.2.7, we employ the replica trick and the Schwarzian derivative to find the exact relation between the entanglement entropy and the energy density respectively, with κ and thus obtain their distributions.
- In Sec. 4.2.8, we provide a brief description of the Wigner function formalism used to extract the energy density for a spinless, free fermion model. In the scaling limit, the theory approaches our CFT result, and we conclude with some numerical benchmarking for the entanglement entropy and energy density as well.

4.1 Introduction to Conformal Field Theory

To begin with, I would like to inform the reader that this section includes theories that can be found in Chaps. 4,5 from [100], and [101], with more details.

4.1.1 Primary Fields and Correlation Functions

Consider $g_{\mu\nu}$ the metric tensor in a space-time of dimension d. A conformal transformation of the coordinates is an invertible mapping $\boldsymbol{x} \to \boldsymbol{x}'$, which leaves the metric tensor invariant up to a scale:

$$g'_{\mu\nu}\left(x'\right) = \Omega(x) g_{\mu\nu}(x) \tag{4.1}$$

In other words, a conformal transformation is locally equivalent to a (pseudo) rotation and a dilation. This set of transformations forms the conformal group and their different types can be (translation) $x'^{\mu} = x^{\mu} + a^{\mu}$, (dilation) $x'^{\mu} = \alpha x^{\mu}$, (rotation),$x'^{\mu} = R^{\mu}{}_{\nu} x^{\nu}$ with the R being a symmetric tensor and (special conformal transformations) $x'^{\mu} = \frac{x^{\mu} - b^{\mu} x^2}{1 - 2b\cdot x + b^2 x^2}$, where b is a constant vector. Consequently, the infinitesimal transformation ϵ^{μ} of the coordinates $x^{\mu} \to x^{\mu} + \epsilon^{\mu}$, can be $\epsilon^{\mu} = a^{\mu}, \alpha x^{\mu}, R^{\mu}{}_{\nu} x^{\nu}, b^{\mu} x^2 - 2x^{\mu} b \cdot x$ and have at most quadratic dependence on x. It is important to mention, that even though $g_{\mu,\nu}$ can be arbitrary, from now on we focus on a Euclidean metric $g_{\mu,\nu} = \delta_{\mu,\nu}$.

An important feature of CFT is the effect of conformal transformations on specific fields called quasi-primary fields. In particular, CFT satisfies the following:

1. There is a set of fields $\{\Phi_i\}$ that is generally infinite and contains all the derivatives of these fields as well.

2. There is a subset of fields $\{\phi_j\}$ which are called quasi-primary and under a finite conformal mapping $x \to x'$ transform by definition as:

$$\phi_i(x) \to \left|\frac{\partial x'}{\partial x}\right|^{\Delta_i/d} \phi_i(x') \quad \text{where}$$
$$\left|\frac{\partial x'}{\partial x}\right| = \frac{1}{\sqrt{\det(g')}} = \Omega^{-d/2} \tag{4.2}$$

with Δ_i is a parameter that characterises change of the respective field ϕ_i under a conformal transformation, known as scaling dimension. The Jacobian of the transformation is indicated, as $\left|\partial x'/\partial x\right|$. Due to this, the N-point correlation functions satisfy:

$$\langle \phi_1(x_1) \dots \phi_N(x_N) \rangle = \Big(\prod_{i=1}^{N} \left|\frac{\partial x'}{\partial x}\right|_{x=x_i}^{\Delta_i/d} \Big) \langle \phi_1(x_1') \dots \phi_N(x_N') \rangle \tag{4.3}$$

under a finite conformal mapping $x \to x'$.

3. The rest of the fields can be expanded as linear combinations of quasi-primary ones and their derivatives.

4. There is a vacuum $|0\rangle$ that is invariant under finite conformal transformations.

The discussion in this part is done in an arbitrary dimension d and not just $d = 2$. The change of the N-point function Eq. (4.3) under conformal transformations, can impose restrictions on it, especially in the case of $N = 2, 3$. We illustrate this with the following examples.

As mentioned earlier, ordinary translations and rotations are part of the conformal group, and it is easy to check that $\Omega = 1$ for them. According to Eq. (4.3):

$$\langle \phi_1(x_1) \dots \phi_N(x_N) \rangle = \langle \phi_1(x_1') \dots \phi_N(x_N') \rangle \tag{4.4}$$

Translations imply that the correlation function depends only on the relative positions $\{x_i - x_j\}$ of the coordinates, while rotations restrict the dependence to just the distances $r_{ij} = |x_i - x_j|$. Invariance under dilatations ($\Omega = \lambda^{-2}$) implies dependence only on ratios r_{ij}/r_{mn}, and special conformal transformation symmetry implies dependence only on specific cross ratios of the form $(r_{ij}r_{mn})/(r_{im}r_{jn})$. Therefore, invariance under the full conformal group tells us that the correlation function is a

function of only these cross-ratios, with $N(N-3)/2$ such cross-ratios [102].

Next, we will demonstrate the calculation of a 2-point function of two quasi-primary fields, which according to our conformal field theory $\langle\phi_1(x_1)\phi_2(x_2)\rangle = f(r_{12})$, is just a function of the relative distance r_{12}. For a dilation $x' = \lambda x$, from Eq. (4.3):

$$\begin{aligned}&\langle\phi_1(x_1)\phi_2(x_2)\rangle = \left|\frac{\partial x'}{\partial x}\right|^{\Delta_1/d}_{x=x_1}\left|\frac{\partial x'}{\partial x}\right|^{\Delta_2/d}_{x=x_2}\langle\phi_1(x_1')\phi_2(x_2')\rangle \rightarrow \\ &f(r_{12}) = \lambda^{(\Delta_1+\Delta_2)}f(\lambda r_{12})\end{aligned} \tag{4.5}$$

With a differentiation with respect to λ, we end up with the first-order ordinary differential equation:

$$yf'(y) + (\Delta_1+\Delta_2)f(y) = 0 \tag{4.6}$$

where $y = \lambda r_{12}$. This is a first-order linear differential equation and is straightforward to observe that it admits the solution:

$$\langle\phi_1(x_1)\phi_2(x_2)\rangle = \frac{A_{12}}{r_{12}^{(\Delta_1+\Delta_2)}} \tag{4.7}$$

where A_{12} is an integration constant. As a last step, we exploit the special conformal invariance with $\Omega = (1+2b\cdot x + b^2x^2)^2$ and the known analytic expression Eq. (4.7) of the correlation function. By substituting these quantities into Eq. (4.5), one finds the following relation:

$$A_{12}\left[1 - \left(\frac{1+2b\cdot x_1 + b^2x_1^2}{1+2b\cdot x_2 + b^2x_2^2}\right)^{(\Delta_2-\Delta_1)/2}\right] = 0 \tag{4.8}$$

Therefore the above equation, requires $\Delta_1 = \Delta_2 = \Delta$ if $A_{12} \neq 0$ or $\Delta_1 \neq \Delta$ if $A_{12} = 0$. The 2-point correlations of fields with the same Δ_i survive, whereas the ones that transform differently under conformal transformations have trivially vanishing 2-point functions. This is expressed by the following equation:

$$\langle\phi_1(x_1)\phi_2(x_2)\rangle = \frac{A_{12}}{r_{12}^{2\Delta}}\delta_{\Delta_1,\Delta_2} \tag{4.9}$$

The 3-point function can also be exactly calculated, in a similar approach [103]:

$$\langle\phi_1(x_1)\phi_2(x_2)\phi_3(x_3)\rangle = \frac{A_{123}}{r_{12}^{\Delta_1+\Delta_2-\Delta_3}r_{23}^{\Delta_2+\Delta_3-\Delta_1}r_{31}^{\Delta_3+\Delta_1-\Delta_2}} \tag{4.10}$$

Conformal invariance allows us to determine the exact expressions of the two- and

three-point correlation functions of the quasi-primary operators. The same is not true for higher-point correlation functions. For $N \geq 4$ point functions, the constraints due to conformal invariance, which we used before, are not enough to determine $\langle \phi_1(x_1)\phi_2(x_2)\dots\phi_N(x_N)\rangle$ explicitly. In this case, the N-point correlation functions can have an arbitrary dependence on the $N(N-3)/2$ cross ratios. An explicit expression would require additional information related to the specific type of problem in the study, except in two dimensions ($d = 2$), where the local conformal group can provide more constraints.

The systems of interest in this chapter are of 1 spatial and 1 temporal dimension. Consequently, we now focus on CFT of $d = 2$ with the temporal coordinate x^0 and the spatial x^1. In two dimensions, CFT has a spatial property. It can be described by a pair of complex coordinates $z = x^0 + ix^1, \bar{z} = x^0 - ix^1$ on $\mathbb{C}^2$. We will call the analytic functions of just z(or $\bar{z}$) dependence holomorphic (or just antiholomorphic) ones. The infinitesimal form of the Conformal transformations $z \to z + \epsilon(z), \bar{z} \to \bar{z} + \bar{\epsilon}(\bar{z})$ have a holomorphic $\epsilon(z)$ and an anti-holomorphic part, $\bar{\epsilon}(\bar{z})$ and each part can have at most quadratic dependence on $z, \bar{z}$ respectively. Specifically, the zero-order is associated with translations, the first order with dilatations and rotations, and the second order with special conformal transformations. Under these complex variables, we define the primary fields $\phi_i(z, \bar{z})$ as those that transform as:

$$\phi_i(z, \bar{z}) \to \left(\frac{\partial F}{\partial z}\right)^{a_i} \left(\frac{\partial \bar{F}}{\partial \bar{z}}\right)^{\bar{a}_i} \phi_i(z', \bar{z}') \tag{4.11}$$

under an arbitrary conformal transformation $z \to z' = F(z)$, $\bar{z} \to \bar{z}' = \bar{F}(\bar{z})$. The conformal transformation is defined by two parts: the holomorphic $F(z)$ and the anti-holomorphic $\bar{F}(\bar{z})$. As we can see in Eq. (4.11), one gets a Jacobian term for each holomorphic/anti-holomorphic dependence. The two real quantities a_i and $\bar{a}_i$ are known as the conformal weights of the primary field. The primary fields can be seen as a generalization in $\mathbb{C}^2$ of the quasi-primary fields mentioned in the previous section. As a consequence of Eq. (4.11), their correlation function satisfies:

$$\langle \phi_1(z_1)\dots\phi_N(z_N)\rangle = \Big[\prod_{i=1}^{N} \left(\frac{\partial F(z_i)}{\partial z}\right)^{a} \left(\frac{\partial \bar{F}(z_i)}{\partial \bar{z}}\right)^{\bar{a}_i}\Big] \langle \phi_1(z_1')\dots\phi_N(z_N')\rangle \tag{4.12}$$

with $(a_i, \bar{a}_i)$ being the conformal weights of each primary field. For example, given a field with scaling dimension Δ dimension and spin s, its conformal weights would then be $\alpha = (\Delta + s)/2$, $\bar{\alpha} = (\Delta - s)/2$.

A primary field is also a quasi-primary field, but the reverse is untrue. A primary field satisfies Eq. (4.11) for an arbitrary conformal transformation; however, for the case of a quasi-primary field transform similarly, only under finite conformal transformations (the Möbius mappings [102] in two dimensions). The primary fields constitute a subset of the theory's $\{\Phi_i\}$. The remaining fields are called secondary fields and may be quasi-primary or not.

4.1.2 Stress-Energy Tensor and Radial Quantization in $d = 2$

Due to the locality of the theory, there exists a local field $\mathrm{T}_{\mu\nu}$ [104], called the stress-energy tensor, defined by the variation of the local action $S[\phi]$ under the infinitesimal transformation ϵ^{ν}:

$$\delta S = \frac{1}{(2\pi)^{d-1}} \int dx^d \mathrm{T}_{\mu\nu} \partial^{\mu} \epsilon^{\nu}(x) \tag{4.13}$$

According to Polyakov's theorem [105], translational invariance implies the conservation law:

$$\partial_{\mu} \mathrm{T}^{\mu\nu} = 0 \tag{4.14}$$

Rotational invariance implies that the stress-energy tensor is symmetric with respect to its indices:

$$\mathrm{T}^{\mu\nu} = \mathrm{T}^{\nu\mu} \tag{4.15}$$

Finally, invariance under dilatations leads to the zero trace condition:

$$\mathrm{T}^{\mu}_{\mu} = 0 \tag{4.16}$$

In two dimensions, the line element for the Euclidean metric is $ds^2 = dzd\bar{z}$. Thus, the components of the metric in the complex coordinates are:

$$g_{zz} = g_{\bar{z}\bar{z}} = 0 \quad , \quad g_{z\bar{z}} = g_{\bar{z}z} = \frac{1}{2} \tag{4.17}$$

and its inverse is therefore:

$$g^{zz} = g^{\bar{z}\bar{z}} = 0 \quad , \quad g^{z\bar{z}} = g^{\bar{z}z} = 2 \tag{4.18}$$

Considering the covariance transformation of the stress-energy tensor for the $x \to x'$ coordinate change:

$$\mathrm{T}^{\mu'\nu'} = \frac{\partial x'^{\mu}}{\partial x^{\alpha}} \frac{\partial x'^{\nu}}{\partial x^{\beta}} \mathrm{T}^{\alpha\beta} \tag{4.19}$$

one can calculate the relations connecting the components in (x^0, x^1) and in $(z, \bar{z})$:

$$\begin{aligned} \mathrm{T}_{zz} &= \frac{1}{4}\Big(\mathrm{T}_{00} - \mathrm{T}_{11} - 2i\mathrm{T}_{10}\Big) \\ \mathrm{T}_{\bar{z}\bar{z}} &= \frac{1}{4}\Big(\mathrm{T}_{00} - \mathrm{T}_{11} + 2i\mathrm{T}_{10}\Big) \\ \mathrm{T}_{z\bar{z}} &= \mathrm{T}_{\bar{z}z} = \frac{1}{4}\mathrm{T}^{\mu}_{\mu} = \frac{1}{4}(\mathrm{T}_{00} + \mathrm{T}_{11}) \end{aligned} \tag{4.20}$$

Due to the traceless condition from Polyakov's theorem, the crossing components vanish $\mathrm{T}_{z\bar{z}} = \mathrm{T}_{\bar{z}z} = 0$. Additionally, the conservation Eq. (4.14) leads to:

$$\begin{aligned} \bar{\partial}\mathrm{T}_{zz} + \partial\mathrm{T}_{\bar{z}z} = 0 \to \bar{\partial}\mathrm{T}_{zz} = 0 \\ \partial\mathrm{T}_{\bar{z}\bar{z}} + \bar{\partial}\mathrm{T}_{z\bar{z}} = 0 \to \partial\mathrm{T}_{\bar{z}\bar{z}} = 0 \end{aligned} \tag{4.21}$$

where we used Eq. (4.18) and $T^{\mu\nu}$ in the complex plane coordinates. In two-dimensional conformal field theories, there is a natural splitting in the variables $(z, \bar{z})$. The two non-vanishing components depend only on z or only on $\bar{z}$: the former has a holomorphic dependence, while the latter has an anti-holomorphic dependence:

$$\mathrm{T}(z) = \mathrm{T}_{zz} \quad , \quad \bar{\mathrm{T}}(\bar{z}) = \mathrm{T}_{\bar{z}\bar{z}} \tag{4.22}$$

These properties will be important in the sequel.

Why do we need to discuss the stress-energy tensor? The reason lies within Noether's theorem [106], which states that a quantum theory with symmetry is associated with a conserved current j^{μ} that satisfies the conservation law $\partial_{\mu} j^{\mu} = 0$. Through this current, one can construct the conserved charge $Q_j = \int dx^{d-1} j_0(x)$, which gives us the symmetry variation of a field Φ:

$$\Phi \to \delta\Phi = \epsilon[Q_j, \Phi] \tag{4.23}$$

for an infinitesimal transformation ϵ. The charges related to a conformal invariant theory can be generated by the stress-energy tensor, defining the transformation laws of the fields. For example, the current related to an infinitesimal conformal

transformation is $j_\mu = \mathrm{T}_{\mu\nu}\epsilon^\nu$ with a conserved charge:

$$Q_j = \frac{1}{2\pi i}\oint \left(dz\mathrm{T}(z)\epsilon(z) + d\bar{z}\bar{\mathrm{T}}(\bar{z})\bar{\epsilon}(\bar{z})\right) \tag{4.24}$$

where the integration is performed over a circle with a fixed radius in the complex plane. From Eq. (4.23):

$$\delta\Phi(w,\bar{w}) = \frac{1}{2\pi i}\oint \left(dz\epsilon(z)[\mathrm{T}(z),\Phi(w,\bar{w})] + d\bar{z}\bar{\epsilon}(\bar{z})[\bar{\mathrm{T}}(\bar{z}),\Phi(w,\bar{w})]\right) \tag{4.25}$$

At this stage, it is beneficial to introduce the procedure of radial quantization for a more practical approach to our formulation. We begin with the two-dimensional space-time $d = 2 \to (x^0, x^1)$, which we already know maps to the complex coordinates $Z, \bar{Z} = x^0 \pm ix^1$ (the notation for $z, \bar{z}$ changed to capital letters). Next, we compactify the space coordinate $x^1 \equiv 2\pi + x^1$. This allows us to define the space-time on a cylinder, where x^0 determines the height and x^1 its circumference. Now, we consider a conformal mapping of this cylinder to the complex plane of z:

$$(x^0, x^1) \to z = e^{x^0 + ix^1} \tag{4.26}$$

The infinite past and future $x^0 = \pm\infty$ are mapped to the origin and infinity, respectively $z = 0, \infty$, while the equal-time circles (for fixed x^0) of the cylinder become circles of constant radius in the complex plane (fixed $|z| = \exp(x^0)$). Considering this, we can understand how the conformal mappings can be implemented in the z-plane. For example, a time translation $x^0 \to x^0 + \Delta t$ in the cylinder is a dilation $z \to e^{\Delta t}z$ in the complex plane. We know that the conserved charge of time translations is the Hamiltonian H [107] of the system, thus H is the generator of dilatations in the z-plane. Moreover, since we already know that for the infinitesimal time translation $x^0 \to x^0 + c.s.t$ the change of $Z, \bar{Z}$ is $\epsilon(Z) = \bar{\epsilon}(\bar{Z}) = 1$. Therefore, from Eq. (4.24), the Hamiltonian is constructed via $\mathrm{T}_{\mu\nu}$ as:

$$H = \frac{1}{2\pi i}\oint \left(dZ\ \mathrm{T}(Z) + d\bar{Z}\ \bar{\mathrm{T}}(\bar{Z})\right) \tag{4.27}$$

In the same approach, by employing that momentum P is the charge related to space translations $x^1 \to x^1 + c.s.t$ with $\epsilon(Z) = -\bar{\epsilon}(\bar{\bar{Z}}) = i$ one recovers:

$$P = \frac{1}{2\pi}\oint \left(dZ\ \mathrm{T}(Z) - d\bar{Z}\ \bar{\mathrm{T}}(\bar{Z})\right) \tag{4.28}$$

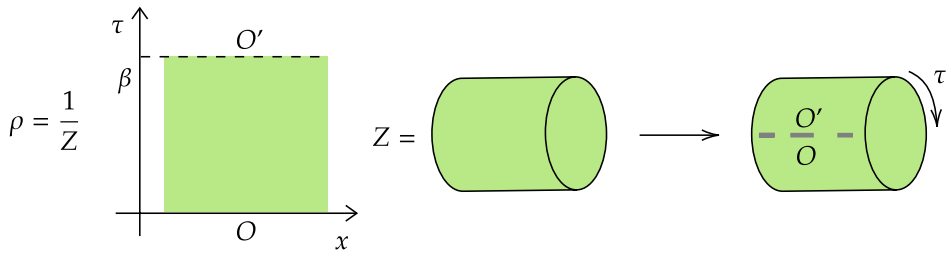

FIGURE 4.1: From density matrix to reduced density matrix. Left: path integral representation of $\rho\Big(\{O_x\}\big|\{O'_{x'}\}\Big)$. Centre: the partition function is obtained by sewing together the edges along $\tau = 0$ and $\tau = \beta$ to form a cylinder of circumference β. Right: the reduced density matrix ρ_A is obtained by sewing together only those points which are not in A. This is a consequence of $\mathrm{Tr}_{\bar{A}}$.

4.1.3 Entanglement Entropy and the Replica Trick

The entanglement entropy S_A of a subsystem A is given by the von Neumann entropy $S_A = -\mathrm{Tr}_A\, \rho_A \ln \rho_A$, where $\rho_A = \mathrm{Tr}_{\bar{A}}\ \rho$ is the reduced density matrix of this subsystem. For instance, A could represent a block or multiple disjoint blocks of spins in an infinite Ising chain. When the density matrix ρ of the entire system $\Sigma \equiv A \cup \bar{A}$ is in a pure state, then $S_A = S_{\bar{A}}$. Furthermore, we utilise the concept of Rényi entropies, defined as:

$$S_A^{(n)} = \frac{1}{1-n} \ln \mathrm{Tr}\, \rho_A^n, \tag{4.29}$$

which satisfies the limit $S_A = \lim_{n\to 1} S_A^{(n)}$. Entanglement entropy is a critical indicator of the properties of an extended quantum system when A and $\bar{A}$ correspond to a spatial bipartition of the system [108]. However, for a system Σ in a mixed state, entanglement entropy is no longer an effective measure of entanglement as it combines quantum and classical correlations. Consequently, in high-temperature mixed states, it must reflect the extensive thermal entropy unrelated to entanglement, necessitating the definition of a new quantity [109].

In models with a finite number of degrees of freedom, the entanglement entropy is most practically computed through the diagonalisation of the reduced density matrix ρ_A. Once its eigenvalues $\{\varrho_i\}$ are obtained, one can calculate the entanglement entropy as $S_A = -\sum_i \varrho_i \ln \varrho_i$. However, for a generic interacting quantum field theory, obtaining the full matrix ρ_A is a complex task. Therefore, we adopt the replica trick as an alternative approach [108, 110].

A concise description of the replica trick is as follows: By definition, $\sum_i \varrho_i = 1$

with $\varrho_i \in [0,1]$. Hence, $\mathrm{Tr}\,\rho_A^n = \sum_i \varrho_i^n$ converges for $n \geqslant 1$ and is analytic for $\mathrm{Re}(n) \geqslant 1$. The same applies to the derivative with respect to n in this region. Therefore, if $\mathrm{Tr}\,\rho_A^n$ is known for any $n \geq 0$, the limit $S_A = \lim_{n\to 1} S_A^{(n)}$ can also be determined. The replica trick is applied for positive integers and reduces the computation of $\mathrm{Tr}\,\rho_A^n$ to that of a partition function on a composed Riemann surface [101, 111].

In this report, we study a system in a $d = 1+1$ dimensional space. We start with a (discrete space) lattice quantum theory with lattice spacing a_s, where x is the discrete space coordinate and $\{\hat{O}_x\}$ represents a complete set of local commuting observables. Their eigenstates $\{|O_x\rangle\}$ form a complete basis $|\{O_x\}\rangle = \bigotimes_x |O_x\rangle$. Given the Hamiltonian H of the system, the elements of the density matrix are:

$$\rho\Big(\{O_x\}\big|\{O'_{x'}\}\Big) = Z^{-1}\langle\{O_x\}|e^{-\beta H}|\{O'_{x'}\}\rangle \tag{4.30}$$

The normalization factor is the partition function $Z = \mathrm{Tr}\exp(-\beta H)$, ensuring $Tr\,\rho = 1$. In the path integral formulation [112], the density matrix is expressed as:

$$\rho\Big(\{O_x\}\big|\{O'_{x'}\}\Big) = Z^{-1}\int D[O(y,\tau)]\prod_{x,x'}\delta(O(y,0)-O_{x'})\delta(O(y,\beta)-O_x)e^{-S_E}, \tag{4.31}$$

where $S_E = \int_0^\beta d\tau L$ is the Euclidean action and L the Euclidean Lagrangian. Integration is performed over the imaginary time $\tau = -it$ on the $x-\tau$ plane. A graphical representation of the path integral introduced in Eq. (4.31) is presented in Fig. 4.1.

The trace restricts our interest to the diagonal elements of ρ and thus the partition function is determined by setting $\{O_x\} = \{O'_{x'}\}$, equivalent to sewing the edges at $\tau = 0$ and $\tau = \beta$, forming a cylinder of circumference β (see Fig. 4.1).

We focus on the case of a single subinterval $[u,v]$, with length denoted as $l = |u-v|$. Thus, the subsystem A consists of the points in $[u,v]$. To obtain ρ_A, we trace over $\bar{A}$, which in Eq. (4.31) translates into sewing only points not belonging to A. This results in open cuts on the cylinder along (u,v) at $\tau = 0$. By making n copies (each labelled by j) of this cylinder and sewing them along the cut, we obtain a n sheet structure $\mathbb{R}_{n,1}$ (see Fig. 4.2) to find $\mathrm{Tr}\,\rho_A^n$. Denoting $Z_n(A)$ as the partition function on this surface, we have:

$$\mathrm{Tr}\,\rho_A^n = \frac{Z_n(A)}{Z^n}. \tag{4.32}$$

In the continuous space limit $a_s \to 0$, the coordinate x takes real values and the

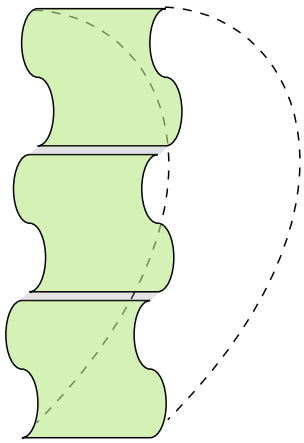

FIGURE 4.2: A representation of the Riemann surface $\mathbb{R}_{3,1}$. Each sheet represents the open cylinder of a single copy of ρ_A and $\mathrm{Tr}\,\rho_A^3$ is represented by sewing together 3 sheets with periodic boundary conditions.

equality in Eq. (4.32) changes to proportionality[113]. This is due to the divergences that appear in the $a_s \to 0$, where one multiplies by a renormalisation constant so that we can eventually get something finite. We also introduce the Lagrangian density $\mathcal{L}$ through $L = \int dx\mathcal{L}$.

Another crucial feature is the locality of the Lagrangian density, implying no explicit dependence on $\mathbb{R}_{n,1}$. This allows expressing and calculating the partition function from a different model. Specifically, it is a model of n independent copies (labelled by i) of the complex plane $\mathbb{C}$ ($z = x + i\tau$), implementing suitable boundary conditions near the boundaries of $A \to u, v$. As detailed in [113], the partition function on $\mathbb{R}_{n,1}$ becomes a path integral in the complex plane:

$$Z_n(A) = \int D[\mathcal{T}_1]\dots D[\mathcal{T}_n] \exp\Big(-\int_{\mathbb{C}} dxd\tau\mathcal{L}^{(n)}[\{\mathcal{T}_i\}](x,\tau)\Big), \tag{4.33}$$

where:

$$\mathcal{L}^n[\{\mathcal{T}_i\}](x,\tau) = \mathcal{L}[\mathcal{T}_1](x,\tau) + \dots \mathcal{L}[\mathcal{T}_n](x,\tau) \tag{4.34}$$

with conditions $\mathcal{T}_i(x,0^+) = \mathcal{T}_{i+1}(x,0^-)$, $x \in [u,v]$ and $n+i \equiv i$.

The local fields $\mathcal{T}_i$ are termed twist fields and arise whenever there is a global symmetry $\sigma \to \int dxd\tau\mathcal{L}[\sigma\mathcal{T}](x,\tau) = \int dxd\tau\mathcal{L}[\mathcal{T}](x,\tau)$. By global symmetry, we mean a symmetry that acts the same way everywhere in space, and that does not change the positions of fields. In the model described by Eq. (4.34) we have the appearance of twist fields that are associated with two cyclic permutation symmetries

$i \to i+1$, $i \to i-1$ under the exchange of copies (where $i = 1, \ldots, n+1 \equiv 1$). We denote them respectively as $\mathcal{T}_n$, $\tilde{\mathcal{T}}_n$. For a single subinterval $[u, v]$ subsystem A in $\mathbb{R}_{n,1}$, we have the following formulation:

$$\langle B(x, \tau; j\text{-sheet})\rangle_{\mathcal{L},\mathbb{R}_{n,1}} = \frac{\langle \mathcal{T}_n(u,0)\tilde{\mathcal{T}}_n(v,0)B_j(w)\rangle_{\mathcal{L}^{(n)},\mathbb{C}}}{\langle \mathcal{T}(u,0)\tilde{\mathcal{T}}(v,0)\rangle_{\mathcal{L}^{(n)},\mathbb{C}}}, \tag{4.35}$$

where B_j is the field in the $\mathcal{L}^{(n)}$ model ($n-$copies of $\mathbb{C}$) of the $j-$copy, and the denominator is the partition function:

$$Z_n(A) \propto \langle \mathcal{T}_n(u,0)\tilde{\mathcal{T}}_n(v,0)\rangle_{\mathcal{L}^{(n)},\mathbb{C}} \tag{4.36}$$

Eq. (4.35) is valid because the ratio accounts for all proportionality constants that we get in the continuous limit.

For two or more ($N \geqslant 2$) disjoint subintervals [114] with $[u_1, v_1], \ldots, [u_N, v_N]$, these results generalise to the boundary points $\{u_i, v_i\}$ (also called branch points) by adding the twist fields on them and denoting $\mathbb{R}_{n,N}$ for the $n-$ sheet structure with N branch cuts. For example, Eq. (4.35) becomes:

$$\langle B(x, \tau; j\text{-sheet})\rangle_{\mathcal{L},\mathbb{R}_{n,1}} = \frac{\langle \mathcal{T}_n(u_1,0)\tilde{\mathcal{T}}_n(v_1,0)\ldots\mathcal{T}_n(u_N,0)\tilde{\mathcal{T}}_n(v_N,0)B_j(w)\rangle_{\mathcal{L}^{(n)},\mathbb{C}}}{\langle \mathcal{T}_n(u_1,0)\tilde{\mathcal{T}}_n(v_1,0)\ldots\mathcal{T}_n(u_N,0)\tilde{\mathcal{T}}_n(v_N,0)\rangle_{\mathcal{L}^{(n)},\mathbb{C}}}, \tag{4.37}$$

and the partition function is:

$$Z_n(A) \propto \langle \mathcal{T}_n(u_1,0)\tilde{\mathcal{T}}_n(v_1,0)\ldots\mathcal{T}_n(u_N,0)\tilde{\mathcal{T}}_n(v_N,0)\rangle_{\mathcal{L}^{(n)},\mathbb{C}} \tag{4.38}$$

Therefore, the $N-$point function of twisted fields depending on the branch cuts defined by A is directly related (via Eq. (4.32)) to $S_A^{(n)}$. One recovers S_A in the limit $n \to 1$. Moreover, twisted fields are primary fields with scaling dimension d_n and conformal weights h_{T_n} , $h_{\tilde{\mathrm{T}}_n}$ given by:

$$h_{\mathrm{T}_n} = h_{\tilde{\mathrm{T}}_n} = \frac{c}{24}(n - \frac{1}{n}) \quad , \quad d_n = \frac{c}{12}(n - \frac{1}{n}) \tag{4.39}$$

The detailed proof for this can be found at [102].

4.2 Universal Out-of-Equilibrium Dynamics, Perturbed by Noise Coupled to Energy

I would like to inform the reader that this section deals with the theory presented in [46]. We first introduce the model and give a brief review of the main results. The technicalities and notions mentioned in this part will be explained in detail in the sections after.

4.2.1 Model and Results

We investigate a one-dimensional model that undergoes a second-order quantum phase transition, initially prepared in the ground state $|\Psi_0\rangle$ of its gapless and homogeneous Hamiltonian $\hat{H}_0$. For simplicity, we denote ground state averages as $\langle \ldots \rangle = \langle \Psi_0 | \ldots | \Psi_0 \rangle$. Although we assume continuous space, this treatment can be readily extended to lattice systems, for which a scaling limit is applied (as we will see in the free fermion case) and recovers the continuous theory. This will become clear later. At time $t = 0$, a perturbation $\hat{H}_1$ is introduced by coupling a space-dependent white noise term with the system's energy density. The total Hamiltonian is expressed as:

$$\hat{H} = \hat{H}_0 + \hat{H}_1 = \int dx (1 + \eta(x,t)) \hat{h}(x), \tag{4.40}$$

where $\hat{h}(x)$ is the Hamiltonian density and $\eta(x,t)$ represents the noise perturbation. Examples of such Hamiltonians with experimental counterparts include tight-binding non-interacting fermions with noisy hopping (see Sec. 4.2.8). Here, we characterize the noise by the spacetime correlation $\overline{\eta(x,t)\eta(x',t')} = \delta(t-t') f(x-x')$ and $\overline{\eta(x,t)} = 0$. The function $f(x)$, controlling the noise correlation, has the dimension of time; it is even, positive, and is chosen to be smooth, monotonically decreasing for $x > 0$, with rapid decay for large x. This criterion restricts the Fourier transform of $f(x)$ to be real, even and non-negative.

Throughout this work, we denote quantum operators with a hat $\hat{O}$ and use $\overline{Q}$ to indicate the average of any quantity Q over noise realizations. The low-energy behaviour of $\hat{H}_0$ is effectively described by conformal field theory (CFT).

When a Hamiltonian is both homogeneous and gapless, the low-energy spectrum becomes largely independent of the microscopic details of the system. This independence arises, due to the universality at critical points, where the macroscopic

behaviour of the system is dictated by symmetries and dimensionality rather than specific interactions at the microscopic level. This concept is encapsulated in the renormalisation group theory, where irrelevant short-range details are averaged out, leaving a universal description that applies to a wide range of systems [115].

In the absence of noise, the Heisenberg evolution of chiral primary fields under $\hat{H}_0$ reduces to translation in time at the light velocity v: $\hat{\phi}^{\pm}(y,t) = \hat{\phi}^{\pm}(y \pm vt)$. The coupling in Eq. (4.40) ensures that the time evolution of chiral primary fields remains equivalent to a flow but along a random stochastic trajectory (see Eq. (4.47)). In [116], the focus was on quench protocols resulting in an initial state with short spatial correlation length, whereas here the initial state is gapless with quasi-long-range order. This implies that for primary fields $\hat{\Phi}(x,t) = \hat{\phi}_+(x,t) \times \hat{\phi}_-(x,t)$ with scaling dimension $\Delta = \Delta_+ + \Delta_-$, the time evolution of the two-point correlation function can be parametrized by $\kappa^{\pm}$, two random functions of spatial separation ℓ and time t:

$$C(\ell,t) \equiv a_0^{2\Delta}\langle\hat{\Phi}(0,t)\hat{\Phi}(\ell,t)\rangle \tag{4.41}$$

$$= C(\ell,t=0)e^{-\Delta_+\kappa^+ - \Delta_-\kappa^-}, \tag{4.42}$$

where a_0 is an ultraviolet cut-off, that limits the highest energy (or the smallest length scale) that is considered in a discrete space theory. As discussed in Sect. 4.2.3, the statistics of the random variable $\kappa^{\pm}$ can be related to the joint distribution of four stochastic trajectories in the same noisy environment. By studying this stochastic process in detail, we demonstrate that the time-dependent distribution of each $\kappa = \kappa^{\pm}$ can be reduced to solving two coupled ordinary stochastic differential equations, as shown in Eq. (4.61). Surprisingly, this leads to a stationary state as $t \to \infty$, characterized by broad distributions of the variable $\kappa^{\pm}$ for all values of separation ℓ. This distribution takes a simple universal form in the limits of small and large ℓ, compared to the correlation length of the noise, chosen to be of order unity here.

For large ℓ, we set $\kappa = \theta\ell^2\chi/f(0) + O(\ell)$ and find that the random variable χ follows the stable one-sided Lévy distribution with index $1/2$:

$$\mathcal{L}(\chi) \equiv \frac{1}{\sqrt{2\pi}}\frac{e^{-\frac{1}{2\chi}}}{\chi^{3/2}}\Theta(\chi). \tag{4.43}$$

For small ℓ, we set $\kappa^{\pm} = \ell^2\tilde{\kappa}_0\left[(\omega/\omega_0) - 1\right]$, where $\tilde{\kappa}_0$ and ω_0 are constants derived from derivatives of $f(x)$ around $x = 0$ (see Eq. (4.73)). This yields the following

stationary distribution for the random variable ω:

$$\mathcal{B}(\omega) \equiv \frac{\Gamma(3/4)}{\Gamma(1/4)} \frac{1}{\sqrt{\pi}(1+\omega^2)^{3/4}}. \tag{4.44}$$

As explained in Sect. 4.2.5, in the small limit ℓ, the proportionality $\langle \hat{T}^{\pm} \rangle \propto \lim_{\ell \to 0} \kappa^{\pm}/\ell^2$ holds, where $T^{\pm}$ are the chiral components of the stress-energy tensors. Consequently, we can infer the stationary distribution of the local energy density, given by $h(x,t) = \langle \hat{h}(x,t) \rangle = v(\langle \hat{T}^{+} \rangle + \langle \hat{T}^{-} \rangle)$:

$$\lim_{t \to \infty} h(x,t) \overset{\text{in law}}{\sim} \frac{vc\tilde{\kappa}_0}{4\pi}(\Omega/\omega_0 - 2), \tag{4.45}$$

where c is the central charge of the underlying CFT and $\Omega = \omega^{+} + \omega^{-}$. At large times, the two chiral components are expected to be only weakly correlated, as they depend on increasingly distant regions. Thus, ω^{+} and ω^{-} can be assumed to be two independent random variables, both distributed according to $\mathcal{B}(\omega)$. Therefore, the stationary distribution of the local energy density reaches a universal form, still displaying a fat tail with a $3/2$ decay exponent and no finite integer moments. This aligns with our finding in Eq. (4.98), where we compute the first moment over time and show that, due to conformal invariance, it diverges exponentially fast in time. This highlights that the average over noise is not indicative of the typical behaviour of the full distribution. Interestingly, we extend this result to the steady distribution of the local energy density even when the initial state is prepared at a finite temperature. Remarkably, the initial temperature only affects the transient dynamics, while the stationary distribution remains unchanged, preserving the $3/2$ tail even at finite temperatures.

Equations (4.43) and (4.44) characterise the asymptotic behaviour of the stationary distribution for κ at small and large ℓ, respectively. For intermediate values of ℓ, a stationary distribution for $\kappa^{\pm}$ is still reached, but its explicit form depends on the function $f(x)$. However, we prove that the $3/2$ exponent for the right tail is consistently present for any ℓ with a sufficiently smooth $f(x)$ (see Appendix C.3.3). In Appendix C.3.6, we provide a general method to determine the stationary distribution, along with analytical formulas for some specific solvable choices of $f(x)$.

A direct manifestation of these results can be observed in bipartite entanglement

Rényi entropies. Indeed, one can express entanglement entropies in terms of correlators of twist fields [113], which leads to the relation (see Sec. 4.2.7):

$$\mathcal{S}_t^{(n)} = \frac{1}{1-n} \ln \mathrm{Tr}\left[\rho_{\ell,t}^n\right] = \mathcal{S}_{t=0}^{(n)} + \frac{(n+1)c}{24n}(\kappa^+ + \kappa^-), \tag{4.46}$$

where $\rho_{\ell,t}$ is the reduced density matrix at time t for an interval of length ℓ and $\mathcal{S}_{t=0}^{(n)}$ is the initial entropy of the ground state. Assuming that at large times κ^+ and κ^- are only weakly correlated, the corresponding stationary distribution can be extracted by convolution. Generally, the 3/2 right tail emerges for all interval sizes ℓ.

To test the validity of the field theory description, in Sec. 4.2.8, we study analytically and numerically a chain of non-interacting spinless fermions at half-filling with noisy hopping. At low energy, these fermions are well described by Dirac fermions corresponding to a $c = 1$ CFT. We identify a scaling for time and the energy density where the noise correlation length on the lattice ξ diverges and the CFT predictions are exactly recovered, as confirmed numerically by computing the local energy and entanglement entropy on the lattice.

4.2.2 Solution of the Dynamics via CFT

In this section, we establish the mathematical framework that we used to obtain the results presented in Sec. 4.2.1. We start by summarising some key results from [116], which allow for the computation of dynamical correlation functions in the presence of the noise term (4.40) within the framework of CFT. As mentioned in Sec. 4.1.2, CFT allows local operators to be decomposed over the primary fields. Moreover, in the same section we established that the Hamiltonian density is related to the stress-energy tensor and depends on both the holomorphic and antiholomorphic component $\hat{T}^+, \hat{T}^-$ (previously denoted as $T(z), \bar{T}(\bar{z})$) of the tensor and in $1+1$ dimensions one can write $\hat{h}(x) = v(\hat{T}^+(x) + \hat{T}^-(x))$, where v is a model dependent velocity. According to Sec. 4.1.2, this implies that there can be two types of primary fields in $1+1$ dimensions, the right and left chiral primary fields [117, 101]. So a primary field can be written as $\hat{\Phi}(x,t) = \hat{\phi}_+(x,t) \times \hat{\phi}_-(x,t)$, with $\hat{\phi}_\pm(x,t)$ being the two different chiral components. In principle, these chiral components are primary fields with conformal weights of $\Delta_+, 0$ and, $0, \Delta_-$ respectively. Consequently, $\hat{\phi}_\pm(x,t)$, have the property of changing only by the holomorphic/antiholomorphic part (see Eq. (4.11)) of the conformal transformation. All local operators, then, can

be decomposed into these chiral (right/left moving) components as mentioned in Sec. 4.1.2. An example is the Hamiltonian density, as well as the momentum density $\hat{p}(x)$ which, is related to the two different chiralities as $\hat{p}(x) = \hat{T}^{+}(x) - \hat{T}^{-}(x)$. This is the result of Eqs. (4.27), (4.28), where we restrict from the complex plane to the coordinate system of $(t, x) \equiv (x^0, x^1)$ and in particular over the spatial coordinate.

In [116], it was demonstrated that the time evolution of primary fields under $\hat{H}$ can be interpreted as a conformal transformation, which is briefly presented in the next paragraph. This is a very significant result that we use for the derivation of our results.

Time evolution as a conformal transformation: In practice, one introduces the stochastic trajectories $q^{\pm}(s)$ as solutions of the Langevin equation:

$$\frac{dq^{\pm}(s)}{ds} = \pm v(1 + \eta(q^{\pm}(s), s)) \tag{4.47}$$

where the Îto convention is assumed [118]. We assume that these are trajectories of some quasiparticles, just for a more intuitive picture of the problem. The Langevin equation describes the stochastic trajectories generated by a velocity field of $\pm v(1 + \eta(q^{\pm}(s), s))$ and the $\pm$ is related to the two different chiralities in our problem, as we will see later. Then, we define the functions $X_t^{\pm}(y)$ as the initial condition for Eq. (4.47) at $t = 0$ (i.e., $q^{\pm}(0) = X_t^{\pm}(y)$) such that $q^{\pm}(t) = y$. By definition $X_0^{\pm}(y) = y$. The functions $X_t^{\pm}(y)$ represent what we call backward trajectories and one can think of them as the backward in-time motion of the stochastic trajectories $q^{\pm}(t)$. The time evolution of the two different chiral primary fields is related to the backward trajectories and more explicitly the exact relation is:

$$\hat{\phi}^{\pm}(y, t) = (X_t^{\pm\prime}(y))^{\Delta^{\pm}} \hat{\phi}(X_t^{\pm}(y), 0) \tag{4.48}$$

where $X_t^{\pm\prime}(y) = \partial X_t^{\pm}(y)/\partial y$. This result can be proven with the use of Îto Calculus and Heisenberg time evolution. It is important to mention, that Eq. (4.48) indicates that the time evolution of $\hat{\phi}^{\pm}(y, t)$ under $\hat{H}$, reduces to being the Conformal transformation $(x, t = 0) \to (X_t^{\pm(x)}, t)$, which in turn introduces some Jacobian factors like $(X_t^{\pm\prime}(y))^{\Delta^{\pm}}$. This property introduces a graphical representation of time evolution as left/right moving quasiparticles, which follow the stochastic backward trajectories. Following, Eq. (4.48), arbitrary $n-$point correlation functions of primary fields, at

time t can be expressed as:

$$\left\langle \prod_{i=1}^{n} \hat{\phi}_i^+(y_i,t) \right\rangle = \mathcal{J}(y_1,\ldots,y_n) \left\langle \prod_{i=1}^{n} \hat{\phi}_i^+(X_t^+(y_i)) \right\rangle \tag{4.49}$$

where the factor $\mathcal{J}(y_1,\ldots,y_n) = \prod_i (X_t^{+\prime}(y_i))^{\Delta_i^+}$ accounts for the Jacobian of the conformal transformation. An analogous equation applies to the other chiral component, with $X_t^+ \to X_t^-$ and $\Delta_i^+ \to \Delta_i^-$.

A simple example of the above is the case of noiseless dynamics. The absence of noise in Eq. (4.47), implies that the quasiparticles travel in straight lines, with a constant velocity of $\pm v$, and their backward trajectories become $X_t^\pm(y) = y \mp vt$. It is straightforward then to see that the chiral primary fields evolve as $\hat{\phi}^\pm(y,t) = \hat{\phi}(y \mp vt, 0)$. The time evolution is nothing more than a space translation of the initial state of the field.

At this point it starts to become more obvious, that the stochasticity in our theory is introduced via $X_t^\pm$ and the statistics of these backward trajectories are the ones that are going to define the statistics of the physical quantities. This will become more evident in the following parts.

To analyse the correlation functions in Eq. (4.49) and their sample-to-sample fluctuations, we need the joint probability distribution function (jpdf) of the set of $2n$ random variables $X_t^\pm(y_j)$, $j = 1,\ldots,n$. Let us first focus on the jpdf of the backward trajectories and denote them from now on as, $X_t^\pm(y_j) = x_j$ for a fixed chirality, choosing either $\pm$, denoted $P_t^\pm(\mathbf{x}|\mathbf{y})$. Given n trajectories $q_j^\pm(s)$ satisfying Eq. (4.47) with endpoints $q_j^\pm(0) = x_j$ and $q_j^\pm(t) = y_j$, $P_t^\pm(\mathbf{x}|\mathbf{y})$ represents the jpdf of the initial positions $\mathbf{x} = (x_1,\ldots,x_n)$ of these n trajectories conditioned on their final positions $\mathbf{y} = (y_1,\ldots,y_n)$. The Langevin equation can be used to derive the equation for the probability distribution $P_t^\pm(\mathbf{x}|\mathbf{y})$, which is known as the Fokker-Planck (FP) equation. In particular, $P_t^\pm(\mathbf{x}|\mathbf{y})$ satisfies:

$$\partial_t P_t^\pm(\mathbf{x}|\mathbf{y}) = (\pm v \sum_{i=1}^{n} \partial_i + \frac{v^2}{2} \sum_{i,j=1}^{n} \partial_i \partial_j f(x_i - x_j)) P_t^\pm(\mathbf{x}|\mathbf{y}) \tag{4.50}$$

where $\partial_i = \partial/\partial x_i$ and f is the space correlation function of the noise defined in Sec. 4.2.2. The detailed derivation is being demonstrated in App. C.1. In order to understand how correlations exist between the different chiralities $X_t^\pm(y_j)$, let us assume a specific realization of the velocity field in Eq. (4.47) for all the points in

space-time up to time t. Then all trajectories $x_j = X_t^{\pm}(y_j)$ evolve under this same realization of the velocity field and thus the space correlation of $\eta(x,t)$, correlates x_j as well. This appears as the second term in Eq. (4.50), which represents a two quasiparticle interaction that decays over large distances. By taking the average over Eq. (4.47), one recovers the martingale property from the initial time:

$$\overline{x_i} = y_i \mp vt \tag{4.51}$$

Additionally, the trajectories y_j are solutions to a well-posed Cauchy problem and cannot cross each other, ensuring that the coordinates of $\mathbf{y}$ and $\mathbf{x}$ remain ordered in the same way.

4.2.3 Two-Point Correlations

In this section, we proceed with finding the exact relation between the two-point correlations and the backward trajectories and also the stochastic differential equations (SDE) that define the statistics of the correlations.

Consider a primary field $\hat{\Phi}(x,t) = \hat{\phi}_+(x,t) \times \hat{\phi}_-(x,t)$, which it has two chiral components and a scaling dimension $\Delta = \Delta_+ + \Delta_-$. We are interested in the two-point correlator, $C(y_1,y_2,t) = a_0^{2\Delta}\langle\hat{\Phi}(y_1,t)\hat{\Phi}(y_2,t)\rangle$. The parameter a_0 is called the ultraviolet cut-off and is a theoretical limit imposed on the maximum energy or the smallest length scale in a field theory. It acts as a boundary beyond which the theory does not apply.

At $t = 0$ since x_1, x_2 are the initial conditions we recover:

$$C(y_1,y_2,t=0) = a_0^{2\Delta}\langle\hat{\Phi}(y_1,0)\hat{\Phi}(y_2,)\rangle = \left(\frac{a_0}{y_1-y_2}\right)^{2(\Delta_+ + \Delta_-)} \tag{4.52}$$

where we used the known 2-point functions (see Sec. 4.1.1) from CFT in $d = 1+1$ dimensions. Using Eq. (4.49), we can relate the correlator at time t to the one at the initial time, leading to:

$$C(y_1,y_2,t) = C(y_1,y_2,0)e^{-\Delta_+\kappa^+ - \Delta_-\kappa^-} \tag{4.53}$$

where we assume $y_1 > y_2$ and define:

$$\kappa^{\pm}(y_1,y_2,t) = \ln\left|\frac{(X_t^{\pm}(y_1) - X_t^{\pm}(y_2))^2}{(y_1-y_2)^2 X_t^{\pm\prime}(y_1) X_t^{\pm\prime}(y_2)}\right| \tag{4.54}$$

The order of the final points y_1, y_2 fixes as well the order of the backward trajectories $X_t^{\pm}(y_1) > X_t^{\pm}(y_2)$ as we mentioned for Eq. (4.51). The stochastic variable $\kappa^{\pm}$, encodes the full statistics of the correlation function and that is why, we first focus on either κ^+ or κ^-. The variables κ^+, κ^- depend only on a single chiral trajectory X_t^+, X_t^- respectively and in principle, they are correlated. However, at large enough times, they become uncorrelated. Let us try to understand this.

Typically, the trajectories $X_t^{\pm}(y)$ corresponding to the two chiral components are separated by a distance, $\sim 2vt$ as we can see from Eq. (4.51). The stochastic trajectories of different chiralities have typical velocities, $\pm v$ and thus their spatial separation is growing in time. As we already mentioned, these trajectories take place under the same noise realization, which induces spatial correlations of $f(.)$. Therefore, for large times when $2vt \gg 1$, the noise they experience becomes uncorrelated, suggesting that the two components have little statistical correlation and $X_t^{\pm}(y)$ and eventually, become independent stochastic variables.

Let us define $\ell \equiv y_1 - y_2 > 0$ and the dimensionless ratio $r \equiv (X_t^{\pm}(y_1) - X_t^{\pm}(y_2))/\ell$. We are interested in studying the stochastic variable κ, but since it satisfies $\kappa = \kappa^{\pm}(y_1, y_2, t) = \ln\left|\frac{r^2}{X_t^{\pm\prime}(y_1) X_t^{\pm\prime}(y_2)}\right|$, it is coupled to the stochastic variable r, implying that we should consider the joint pdf (jpdf) $P_t(r, \kappa)$ of κ and r. Finding this distribution is essential to study the statistics of the correlations $C(y_1, y_2, t)$ and the physical properties of our theory. As we shall see later, $P_t(r, \kappa)$ is related to the distributions of the entanglement entropy and energy density.

4.2.4 jpdf $P_t(r, \kappa)$ and SDE of κ, r

This part is devoted to finding the FP equation for $P_t(\kappa, r)$ and the SDEs of κ& r. We first perform a point splitting in the derivatives in Eq. (4.54):

$$X_t^{\pm\prime}(y) = \lim_{h\to 0} \frac{X_t^{\pm}(y+h) - X_t^{\pm}(y)}{h} \tag{4.55}$$

This is important to our proof since it showcases that the derivatives introduce two backward trajectories, with the ending points (t, y) and $(t, y+h)$ being infinitesimal close. Thus, Eq. (4.54), and the definition of ℓ suggests that, both $\kappa^{\pm}(y_1, y_2, t)$ and r depend only on the initial points x_1, x_2, x_3, x_4 of four trajectories ending at $y_1, y_2, y_1 + \epsilon, y_2 + h$, whose jpdf is given by Eq. (4.50) for $n = 4$ (see Fig. 4.3). We mention that y_1 and y_2 are kept fixed while two additional variables are taken infinitesimally away

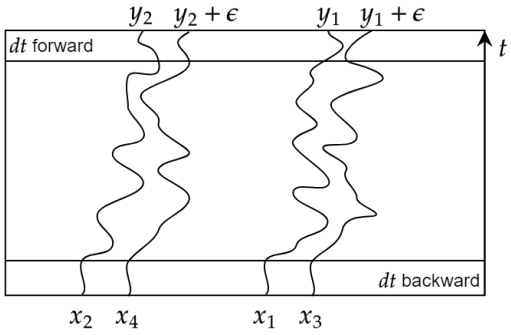

FIGURE 4.3: Sketch of the four trajectories required to access the full pdf of two-point correlation functions in the limit $\epsilon \to 0$.

from y_1 and y_2. More explicitly:

$$x_1 = X_t^{\pm}(y_1), \;\; x_2 = X_t^{\pm}(y_2), \;\; x_3 = X_t^{\pm}(y_1+\epsilon), \;\; x_4 = X_t^{\pm}(y_2+\epsilon) \tag{4.56}$$

We then perform the change of variables $x_1, x_2, x_1' = (x_3 - x_1)/\epsilon, x_2' = (x_4 - x_2)/\epsilon$ together with the limit $h \to 0$, so we can recover $X_t^{\pm'}(y_1), X_t^{\pm'}(y_2)$. By applying this change of variables in the Fokker-Planck equation Eq. (4.50) (n=4) and taking the limit $h \to 0$, one obtains the following equation for $P_t = P_t(x_1, x_2, x_1', x_2')$:

$$\begin{aligned}\partial_t P_t =& v\Big((\partial_{x_1} + \partial_{x_2}) + \frac{v}{2} f(0)(\partial_{x_1}^2 + \partial_{x_2}^2) + v\partial_{x_1}\partial_{x_2} f(x_1 - x_2) - \frac{v}{2} f''(0)(\partial_{x_1'}^2 (x_1')^2 + \partial_{x_2'}^2 (x_2')^2) \\ &+ v\partial_{x_2}\partial_{x_1'} x_1' f'(x_1 - x_2) - v\partial_{x_1}\partial_{x_2'} x_2' f'(x_1 - x_2) - v\partial_{x_1'}\partial_{x_2'} x_1' x_2' f''(x_1 - x_2)\Big) P_t\end{aligned} \tag{4.57}$$

Then, we exploit the invariance under the translation of the PDE by making the change of variables from (x_1, x_2, x_1', x_2') to $(R = \frac{x_1+x_2}{2}, r = (x_1 - x_2)/\ell, x_1', x_2')$. Finally, integrating out the centre of mass variable R, we obtain the FP equation for the jpdf $\Pi_t(r, x_1', x_2') = \int dR P_t(x_1, x_2, x_1', x_2')$

$$\begin{aligned}\partial_t \Pi_t = v^2 \Big(&\frac{1}{\ell^2}\partial_r^2 (f(0) - f(r\ell)) - \frac{f''(0)}{2}(\partial_{x_1'}^2 (x_2')^2 + \partial_{x_1'}^2 (x_2')^2) - f''(r\ell)\partial_{x_1'}\partial_{x_2'} x_1' x_2' - \\ &- \frac{1}{\ell}\partial_r f'(r\ell)(\partial_{x_1'} x_1' + \partial_{x_2'} x_2')\Big)\Pi_t\end{aligned} \tag{4.58}$$

From this result, we now obtain the Fokker-Planck equation for the joint distribution $P_t(\kappa, r)$ of the variable κ and the variable r. Using the explicit relation between, κ& r, it is defined as:

$$P_t(\kappa, r) \equiv \int dx_1' dx_2' \, \Pi_t(r, x_1', x_2') \delta \left(\kappa - \ln\left(\frac{r^2}{x_1' x_2'} \right) \right) \tag{4.59}$$

Interestingly, $P_t(\kappa, r)$ satisfies a closed evolution equation. To obtain it, we compute the time derivative of Eq. (4.59) using Eq. (4.58), then we integrate by part and obtain

$$\begin{aligned} \frac{\ell^2}{v^2} \partial_t P_t(\kappa, r) = \Big[& \partial_r^2 (f(0) - f(\ell r)) + 4 \frac{f(0) - f(\ell r) + \ell r f'(\ell r)}{r^2} \partial_\kappa^2 + \ell^2 f''(0)(\partial_\kappa - \partial_\kappa^2) - \\ & - \ell^2 f''(\ell r) \partial_\kappa^2 + 2\ell \partial_r \partial_\kappa f'(\ell r) + 4 \partial_r (f(0) - f(\ell r)) \frac{1}{r} \partial_\kappa + 2 \frac{f(0) - f(\ell r)}{r^2} \partial_\kappa \Big] P_t(\kappa, r) \end{aligned} \tag{4.60}$$

We, finally, deduced the FP for the probability distribution of κ, r. This equation has a complex form and is not as easy to handle directly to obtain results. For this purpose, it is more convenient to reformulate the problem in terms of equivalent SDEs of κ, r in Îto's form. To deduce them, we employ the same method as the one used in App. C.1, where we demonstrate the relation between an SDE like the Langevin equation Eq. (4.47) and its respective FP equation. Then, the FP equation in Eq. (4.60) is equivalent to the stochastic equations for r and κ (in Îto convention) given by:

$$dr = v \, dW_1(t) \quad , \quad d\kappa = v^2 g(r) dt + v \, dW_2(t) \tag{4.61}$$

where $v^2 g(r)$ is a drift term and $dW_1(t), dW_2(t)$ are two centred Gaussian white noises in time with r-dependent variances $\overline{dW_1(t)^2} = 2A(r)dt$, $\overline{dW_2(t)^2} = 2C(r)dt$, and cross-correlation $\overline{dW_1(t) dW_2(t)} = B(r)dt$. To simplify the notation, we introduced:

$$\begin{aligned} A(r) = \frac{f(0) - f(\ell r)}{\ell^2}, \; B(r) = \frac{2f'(\ell r)}{\ell} + \frac{4(f(0) - f(\ell r))}{\ell^2 r}, \\ C(r) = \frac{4(f(0) - f(\ell r) + \ell r f'(\ell r))}{\ell^2 r^2} - f''(0) - f''(\ell r), \\ g(r) = -f''(0) - \frac{2(f(0) - f(\ell r))}{\ell^2 r^2}. \end{aligned} \tag{4.62}$$

At $t = 0$ by definition $r = (y_1 - y_2)/\ell = 1$ and $\kappa = 0$. Eqs. (4.61) must be solved

with the initial condition $r = 1$ and $\kappa = 0$ at $t = 0$. The SDEs that we found are the main object of the study, as they define the statistics of κ, r, which in turn are related to the physical quantities of our problem, as it will be more clear later.

Since the equation for r does not involve κ, one may first solve for $r(t)$ and then insert the solution for $r(t)$ into the equation for $\kappa(t)$. For finite ℓ, Eq. (4.61) cannot be solved explicitly for an arbitrary $f(x)$. Nevertheless, one can understand its behaviour at finite time in two regimes $\ell = y_1 - y_2 \gg 1$ and $\ell = y_1 - y_2 \ll 1$, as well as in the large time limit. The following sections are devoted to extracting the analytical results in the aforementioned limits.

4.2.5 Small and Large Separation ℓ

Case of $\ell \ll 1$

For small $\ell \ll 1$, we can Taylor expand the function f in Eq. (4.62). The leading behaviour at small ℓ of each function is:

$$A(r) \simeq -\frac{1}{2} f''(0) r^2, \quad B(r) \simeq \frac{\ell^2}{6} f^{(4)}(0) r^3, \tag{4.63}$$

$$C(r) \simeq -\frac{\ell^4}{72} f^{(6)}(0) r^4, \quad g(r) \simeq \frac{\ell^2}{12} r^2 f^{(4)}(0) \tag{4.64}$$

The positivity of the Fourier transform of $f(x)$ implies alternating signs of the even derivatives $\text{sign}(f^{(2n)}(0)) = (-1)^n$, ensuring all variables above are positive. We can rewrite Eq. (4.61) after redefining the noises $dW_1(t) = r dB_1(t)$ and $dW_2(t) = -\frac{\ell^2}{6} r^2 dB_2(t)$:

$$dr = rv dB_1(t), \quad d\kappa = \frac{\ell^2 r^2 v}{6} \left(\frac{v f^{(4)}(0) dt}{2} - dB_2(t) \right) \tag{4.65}$$

where $dB_1(t), dB_2(t)$ are r-independent Gaussian white noises with fixed correlation matrix:

$$\overline{dB_1(t)^2} = -f''(0) dt, \quad \overline{dB_2(t)^2} = -f^{(6)}(0) dt, \quad \overline{dB_1(t) dB_2(t)} = -f^{(4)}(0) dt. \tag{4.66}$$

At this point, we should mention that $dB_1(t), dB_2(t)$ are scaled Wiener processes [119], since a typical Wiener process has a variance of dt. Thus, the stochastic variables $B_1(t), B_2(t)$ are Gaussian random variables $B_1(t) \sim \sqrt{-f''(0)}\mathcal{N}(0,t), B_2(t) \sim \sqrt{-f^{(6)}(0)}\mathcal{N}(0,t)$. Let us first discuss the marginal distribution $P_t(r)$ of r in this

regime ($\ell \ll 1$). One can solve the stochastic equation for r and obtain, after applying Ito's lemma [119]:

$$r(t) = e^{-\theta t + vB_1(t)} \tag{4.67}$$

We define $\theta = -v^2 f''(0)/2 > 0$. Since $B_1(t) \sim \sqrt{-f''(0)}\mathcal{N}(0,t)$, the exponent in the equation above $-\theta t + vB_1(t)$ follows the normal distribution $\mathcal{N}(-\theta t, 2\theta t)$. Alternatively, one can find the SDE of $\log r$ by using Ito's lemma, which suggests that we should keep up to second order in dr. More explicitly, we find that $\log r$ should satisfy:

$$d(\log r) = \frac{1}{r}dr - \frac{1}{2r^2}(dr)^2 = -\theta dt + vdB_1(t) \tag{4.68}$$

where we used Eq. (4.65). In either ways we find out that $\log r$ is a Brownian motion with a drift (of velocity $-v$), implying $P_t(r)$ is a log-normal distribution for r, with mean and variance:

$$\overline{\ln r} = -\theta t, \quad \mathrm{Var}[\ln r] = 2\theta t \tag{4.69}$$

We remind the reader, that $r = (x_1 - x_2)/\ell$ and taking into account that $r(t=0) = 1$, the positive θ leads to a decrease in time for the typical value of $\log r$. Therefore, the initial separation of the trajectories is smaller than ℓ and this implies that, trajectories x_1, x_2 or equivalently $X_t(y_1), X_t(y_2)$ tend to converge over time, illustrating the sticky particle phenomenon observed in turbulent fluids [120]. Additionally, the absence of a drift term for r in Eq. (4.65), leads to $d\bar{r}/dt = 0$ (this is due to the vanishing of the Ito integral under averaging [119] e.g $\overline{\int dB_1(t) r(B_1(t), t) v} = 0$). Hence, $\bar{r} = 1$ independently of time, showing that although the typical value $r_{\mathrm{typ}} = e^{\overline{\log r}}$ decreases to zero, the distribution of r broadens over time. The higher moments of r can be found by the standard moments of log-normal distribution as $\overline{r^n} = e^{n(n-1)\theta t}$ and demonstrate an exponential growth in time, in the regime of small ℓ.

Using this result, we can calculate the noise average of $\kappa = \kappa^{\pm}$ by integrating Eq. (4.65) over time and averaging:

$$\kappa(t) = \frac{v^2 f^{(4)}(0)\ell^2}{12} \int_0^t dt' r(t')^2 \tag{4.70}$$

using the already known moments of r, we finally obtain:

$$\overline{\kappa}(t) = \frac{v^2 f^{(4)}(0)\ell^2}{24\theta}(e^{2\theta t} - 1) \tag{4.71}$$

Using that $r(t)$ is uncorrelated in time $\overline{r(t)r(t')} = \overline{r(t)}\,\overline{r(t')}$ we can find the higher integer moments of κ as $\overline{\kappa^n} = \overline{\kappa}^n$. The moments grow exponentially with time in the small ℓ regime. However, $\overline{\kappa}$ has an exact upper bound. In order to see that, we use that the space correlation $f(x)$, is a decaying function of x and thus Eq. (4.62) leads to $g(r) \leq g(\infty) = -f''(0)$. This upper bound establishes in Eq. (4.61) that $d\overline{\kappa} \leq 2\theta dt$ and finally the bound $\overline{\kappa} \leq 2\theta t$. This limit is exact for an arbitrary ℓ and not just in the regime of small ℓ. Thus, going back to the small ℓ regime, the moments diverge at large times, but the exponential growth, established before, is valid only for times that satisfy $\ell^2 e^{2\theta t} \lesssim 1$.

Remarkably, the pdf of κ converge to a stationary distribution at large times, which is broad and lacks finite integer moments for $n \geq 1$. We now proceed with the proof for this. To obtain the pdf of κ, we proceed in two steps: first, solve for $r(t)$ using Eq. (4.67); second, reparameterize the Wiener processes $B_1(t), B_2(t)$ by looking at them from their final point, setting $\tilde{B}_{1,2}(s) = B_{1,2}(t) - B_{1,2}(t-s)$ The detailed calculations are being demonstrated in App. C.2. This recasts the resulting stochastic equation in a form studied by Bougerol [121]:

$$d\omega = 2\theta\omega dt + \sqrt{8\theta}\sqrt{1+\omega^2}d\tilde{B}, \quad \omega(t=0) = \omega_0 \tag{4.72}$$

where $\tilde{B}(t)$ is a standard Wiener process. The stochastic variables ω is related to κ, based on $\kappa = \kappa_0(\omega/\omega_0 - 1)$ where:

$$\kappa_0 = -\frac{\ell^2}{12}\frac{f^{(4)}(0)}{f''(0)}, \qquad \omega_0 = \frac{1}{\sqrt{\frac{f^{(6)}(0)f''(0)}{f^{(4)}(0)^2} - 1}} \tag{4.73}$$

Note that the positivity of the Fourier transform $\hat{f}(k) > 0$ of $f(x)$ ensures ω_0 being real and positive. This is a direct result of the Cauchy-Schwartz inequality in the case of:

$$f^{(6)}(0)f''(0) - f^{(4)}(0)^2 = \int k^2\hat{f}(k)\int k^6\hat{f}(k) - \left(\int k^4\hat{f}(k)\right)^2 > 0 \tag{4.74}$$

Performing another change of variable $\omega = \sinh(Y)$ for Eq. (4.72), the random variable Y satisfies:

$$dY = -2\theta\tanh Y dt + \sqrt{8\theta}d\tilde{B}, \quad \sinh(Y(0)) = \omega_0 \tag{4.75}$$

Eq. (4.75) describes Langevin motion for Y, which reaches an equilibrium stationary measure at large times, $P_{\text{stat}}(Y) = C/\sqrt{\cosh(Y)}$ with $C = \sqrt{2\pi}/\Gamma(1/4)^2$. The details for this derivation are in App. C.2. Finally, using the relation $\omega = \sinh Y$, we recover the corresponding to the stationary distribution for ω and thus κ:

$$\mathcal{B}(\omega) \equiv \frac{\Gamma(3/4)}{\Gamma(1/4)} \frac{1}{\sqrt{\pi}(1+\omega^2)^{3/4}}, \quad P_{\text{stat}\,\ell\ll 1}(\kappa) = \frac{\Gamma(3/4)\omega_0}{\Gamma(1/4)\kappa_0} \frac{1}{\sqrt{\pi}\left(1+\omega_0^2(\kappa/\kappa_0+1)^2\right)^{3/4}} \tag{4.76}$$

The stationary distribution has tails of, $\propto |\kappa|^{-3/2}$ indicating that ω and κ do not have finite integer moments, as we expected by the exponential growth of the moments.

Case of $\ell \gg 1$ at Short Times

The leading behaviour at large ℓ of each function in Eq. (4.62) up to $O(1/\ell^2)$ is:

$$\begin{aligned} A(r) &\simeq \frac{f(0)}{\ell^2}, \quad B(r) \simeq 4\frac{f(0)}{\ell^2 r}, \\ C(r) \simeq -f''(0) + 4\frac{f(0)}{\ell^2 r^2}, &\quad g(r) \simeq -f''(0) - \frac{2f(0)}{\ell^2 r^2} \end{aligned} \tag{4.77}$$

assuming $f(x)$ decays faster than a power law. In leading order, setting $B_\ell(r) \simeq 0$ implies that the equation for κ becomes independent of r. Using $g(r) \simeq -f''(0)$ and $C(r) \simeq -f''(0)$ in leading order, we obtain the following SDEs from Eq. (4.61):

$$dr = v dW_1(t), \quad d\kappa = 2\theta dt + v dW_2(t) \tag{4.78}$$

with $\overline{dW_1(t)^2} = 2f(0)/\ell^2 dt$, $\overline{dW_2(t)^2} = -2f''(0)dt$. In the large ℓ limit the two Gaussian white noises have cross-correlation $\overline{dW_1(t)dW_2(t)} = 0$, of leading order, and can be considered uncorrelated. At this point, we rescale the Gaussian noises as $W_1(t) = v\sqrt{2f(0)}/\ell \bar{W}(t), W_2(t) = 2\sqrt{\theta}W(t)$, with $W(t), \bar{W}(t)$ being two independent Brownian motions $\overline{dW(t)^2} = \overline{d\bar{W}(t)^2} = dt$. The time integration of leads, finally, to

$$\kappa = 2\theta t + 2\sqrt{\theta}W(t), \quad r = 1 + \frac{\sqrt{2f(0)}v}{\ell}\bar{W}(t) \tag{4.79}$$

note that the growth $\bar{\kappa} = 2\theta t$ saturates the exact bound $\bar{\kappa} \leq 2\theta t$ for κ. We remind the reader, that $\bar{W}(t) \sim \mathcal{N}(0,t)$ and hence the equation above suggests that r is a stochastic variable with fluctuations around 1 of the order of $\frac{\sqrt{2tf(0)}v}{\ell}$. At times $t \sim v^2\ell^2/f(0)$, the fluctuations are large enough to bring $r(t)$ close to zero, and thus

the expansion done in Eq. (4.77) stops being valid and according to Eq. (4.62), the expansion at small enough $r \ll 1$ brings us back to the theory demonstrated in the regime $\ell \ll 1$. This large ℓ expansion only holds for short times $t \lesssim v^2\ell^2/f(0)$. To access the large time limit, a different approach is needed, and that is what will be presented in the next section.

4.2.6 Large-Time at arbitrary ℓ

In this section, we investigate the stationary distribution of κ at arbitrary ℓ and showcase the appearance of non-trivial stationary distribution, with divergent integer moments. The calculations are quite technical, and for this reason, we present briefly the procedure, and the interested reader can refer to the appendix section for all the details.

We start by denoting the characteristic function of the distribution of κ, as:

$$Q_k(r_0, t) = \overline{e^{-ik\kappa}}^{r_0} = \int d\kappa P_{t,r_0}(\kappa) e^{-ik\kappa} \tag{4.80}$$

, where the superscript $r_0 = r(t = 0)$ signifies the initial condition for the variable r in Eq. (4.61), eventually setting $r_0 = 1$ and $P_{t,r_0}(\kappa)$ is the probability distribution of κ at t, given the initial condition r_0. The characteristic function is important since it is the Fourier transform of $P_{t,r_0}(\kappa)$ and if it can be found, then the probability distribution is an inversion of the Fourier transform. In the following part of this section, we are going to denote the initial condition r_0 as r.

Ito's calculus can help us find a PDE for the evolution of Q_k, and, as demonstrated in App. C.3, one finds out the following equation:

$$\partial_t Q_k = v^2 \left(A(r)\partial_r^2 - ikB(r)\partial_r - k^2 C(r) - ikg(r) \right) Q_k(r, t) \tag{4.81}$$

The coefficients A, B, C, g appear due to the use of the SDEs of κ, r that we saw in the previous sections. We are seeking a time-independent solution in the large time limit $Q_k(r, t) \to Q_k(r)$ and thus the stationary solution of Eq. (4.81), which is governed by:

$$\left(A(r)\partial_r^2 - ikB(r)\partial_r - k^2 C(r) - ikg(r) \right) Q_k(r) = 0 \tag{4.82}$$

By definition the stationary distribution that we are interested in is:

$$P_{\text{stat}}(\kappa) = \int dk e^{ik\kappa} Q_k(r=1) \tag{4.83}$$

For practical purposes, we perform a shift by extracting an exponential factor $Q_k(r) = e^{ik\kappa_0(\ell r)} G_k(r)$, with:

$$\kappa_0(x) = -\log\Big(\frac{2(f(x)-f(0))}{x^2 f''(0)}\Big) \,. \tag{4.84}$$

which in turn helps us recover a simpler equation satisfied by $G_k(r)$:

$$-G_k''(r) - k(k+i)V(r)G_k(r) = 0 \tag{4.85}$$

(more details in App. C.3) with boundary conditions $G_k(0) = 1$ and $\lim_{r\to+\infty} G_k(r) = 0$. In this formulation, the function $G_k(r)$ satisfies the Schrödinger-like equation for $r \geq 0$ with a potential which is given by:

$$V(r) = -\frac{d^2}{dr^2}\log[f(0) - f(\ell r)] + \frac{\ell^2 f''(0)}{f(0) - f(\ell r)} \,. \tag{4.86}$$

The aforementioned boundary conditions come from the boundary conditions of $Q_k(r)$ which are explicitly:

$$Q_k(r=0) = 1 \quad , \quad Q_k(r\to+\infty) = 0 \tag{4.87}$$

The first one is a result of the "sticky" behaviour of the stochastic trajectories found in Sec. 4.2.5. When we start at small r our theory is described by the $\ell \ll 1$ regime, and as we can see from Eq. (4.65), $dr = d\kappa = 0$ for $r = 0$, implying no time evolution for κ, r and thus their stationary probability distributions are just Dirac deltas around their initial conditions. The second one comes from observing that in the limit $r \to +\infty$ is described by the $\ell \gg 1$ regime, which was studied in Sec. 4.2.6. It was found in Eq. (4.79) that $\kappa \sim \mathcal{N}(2\theta t, 4\theta t)$ follows a Normal distribution, and one can easily see that the characteristic function of this Normal distribution vanishes at large times.

By analysing Eq. (4.85) (see Appendix C.3), one can not find an explicit solution for the stationary distribution for an arbitrary function $f(x)$ but we can prove the existence of fat $-3/2$ tails. In Appendix C.3.3, we prove that for sufficiently smooth $f(x)$, $Q_k(r) = 1 + O(\sqrt{k})$ at small k, regardless of ℓ. This leads to a $-3/2$ power-law

tail on the positive κ side $P_{\text{stat}}(\kappa) \propto \kappa^{-3/2}$.

To provide intuition on why the $-3/2$ tail appears: the random variable r is attracted to $r = 0$ since for $r < 1$, $\log r$ behaves approximately like a Brownian motion with a negative drift (see (4.69)). In this regime, the typical value of r will get smaller and smaller in time, and thus at large times, our theory is eventually described by the $\ell \ll 1$ regime, where it was shown (in Sec. 4.2.5), that the stationary distribution is Eq. (4.76). However, starting from 1, r has a finite probability of moving towards $r > 1$; in this case, if the stochastic variable passes from 1 after some later time t^*, then we enter again the case just described with $r < 1$, which at large times lead to the expected fat tails. So the distribution of the first passage time from 1 is essential for this case. More explicitly, when $r > 1$ the variable r follows approximately a drifted Brownian motion as already mentioned in Eq. (4.79), for which is known that the first passage time from $r = 1$ has a distribution of $\propto t^{*-3/2}$ [122]. Based on the same equation (Eq. (4.79)), κ increases by $\sim t^*$, showcasing a distribution with the same tails as the one of t^*.

The previous formulation with the characteristic function can be used to recover the stationary distributions of the already studied regimes of $\ell \ll 1, \ell \gg 1$. In the limit of small ℓ, as a consistency check (in Appendix C.3.4), we re-derive the asymptotic solution at small ℓ (Eq. (4.76)), obtained in Sec. 4.2.5 via a completely different approach.

In the opposite limit of large ℓ, it is observed that the potential approaches a constant value $V(r) \to \ell^2 f''(0)/f(0)$, leading to the simple solution of Eq. (4.85) in the form $G_k(r) \sim e^{-\sqrt{2k(k+i)\theta/f(0)}r\ell}$. For the full proof, see App. C.3.5. Consequently, setting $\kappa = \theta\ell^2\chi/f(0)$, one finds that in the limit $\ell \to \infty$, the variable χ is distributed according to:

$$\mathcal{L}(\chi) \equiv \frac{1}{\sqrt{2\pi}} \frac{e^{-\frac{1}{2\chi}}}{\chi^{3/2}} \Theta(\chi) \tag{4.88}$$

i.e., the stable one-sided Lévy distribution of index $1/2$.

Equations (4.44) and (4.88) describe the asymptotic behaviour of the stationary distribution for κ at small and large ℓ, respectively. For intermediate values of ℓ, an explicit expression is not available for generic $f(x)$. Finally, note that for time $t \gg 1/(2v)$, as already mentioned in Sec. 4.2.3, the two chiral components κ^+ and κ^- are expected to decorrelate, and their joint distribution reaches a factorized form $P_{\text{stat}}(\kappa^+)P_{\text{stat}}(\kappa^-)$. This will be useful later for finding the stationary distribution of

entanglement entropy.

4.2.7 Distribution of Entanglement Entropy and Energy Density

Entanglement Entropy

In the previous section, we talked about how CFT allows us to derive the stochastic trajectories/quasiparticle picture, which is crucial for understanding the dynamics of primary fields and thus correlations in our theory, as well as the statistics of these objects. Now we showcase, an intriguing application of the preceding results on the computation of entanglement entropies. Let $\rho_{A,t}$ represent the reduced density matrix for the interval $A = [y_1, y_2]$ at time t. The Rényi entropies are then defined as $S_t^{(n)} = \frac{1}{1-n} \ln \mathrm{Tr}\, \rho_{A,t}^n$ .By introducing the twist fields $\mathcal{T}_n(y,t)$, one can identify $\mathrm{Tr}\, \rho_{A,t}^n \propto \langle \mathcal{T}_n(y_1,t)\mathcal{T}_n(y_2,t)\rangle$. This is a result of the replica trick explained in Sec. 4.1.3. In the same section, we saw that the twist fields are primary fields with the scaling dimension of each chirality as $\Delta_\pm = c/24(n - 1/n)$. Therefore, if we consider the time evolution of their 2-point function under Hamiltonian in Eq. (4.40), we get the same description as the one that was introduced in Sec. 4.2.2. Thus, if we denote the entropy production as $\Delta S_t^{(n)} \equiv \mathcal{S}_t^{(n)} - \mathcal{S}_{t=0}^{(n)}$ and then use (4.53), one obtains:

$$\Delta S_t^{(n)} = \frac{(n+1)c}{24n}(\kappa^+ + \kappa^-) \tag{4.89}$$

where c is the central charge of CFT and depends on the specific model of interest [102] .The Von Neumann entropy production corresponds to the case $n = 1$ and is denoted simply as ΔS_t. Equation (4.89) demonstrates the explicit relation between a physical quantity like entanglement entropy and the random variables. Moreover, it is important to note that, all the Rényi entropies' production are governed by the same random variable, and that the specifics of the model enter only through the prefactor involving the central charge, indicating the universality of the theory.

Using the noise average:

$$\overline{\Delta S_t^{(n)}} = \frac{(n+1)c}{12n}\overline{\kappa} \tag{4.90}$$

based on the results that we found for $\kappa_\pm$ in Secs. 4.2.5,4.2.6 we observe that at the beginning of the study, there are two distinct growth regimes: for large intervals ($\ell \gg 1$), the average entropy production grows linearly with time as from (4.79), while for small intervals, it grows exponentially in time as from (4.71). Finally, at

large times, we find that the entropy production (4.89) attains a stationary distribution, up to a scale, given by the convolution $P_{\text{stat}} * P_{\text{stat}}$ determined previously, which still exhibits a $-3/2$ power law tail and lacks finite integer moments.

Distribution of Energy Density

A noteworthy physical quantity to examine is the dynamics of the energy density, which, in the context of conformal field theory (CFT), is represented via the stress-energy tensor and more explicitly as $\hat{h}(x) = v\left(\hat{T}^{+}(x) + \hat{T}^{-}(x)\right)$. The time evolution of $\hat{h}(x)$ can be directly calculated with the help of CFT. Specifically, one can use the fact that time evolution can be viewed as a conformal mapping and the corresponding transformation of the stress-energy tensor is:

$$\hat{T}(y,t) = |X_t'(y)|^2 \hat{T}(X_t(y), t=0) - \frac{c}{24\pi}(\mathcal{S}\cdot X_t)(y) \tag{4.91}$$

where we used the known way that the stress-energy tensor transforms under a conformal map. The reader can find the relevant proof in Ch.5 of [100]. For simplicity, we omit the $\pm$ superscript, since each component of the tensor is related to the respective backward trajectory out of $X_t^{\pm}(y)$. The second term in the equation above is proportional to the central charge c and the Schwarzian derivative $(\mathcal{S}\cdot X_t)(y)$. The Schwarzian derivative $(\mathcal{S}\cdot\zeta)(z)$ for two arbitrary variables ζ, z such that $\zeta = \zeta(z)$, is defined as follows:

$$(\mathcal{S}\cdot\zeta)(z) = \frac{\zeta'''}{\zeta'} - \frac{3}{2}\left(\frac{\zeta''}{\zeta'}\right)^2 \tag{4.92}$$

with $\zeta' = d\zeta/dz$ e.t.c for higher order derivatives. At this point we focus on the expectation value over the quantum state of the system at time t for which, one has:

$$\langle \hat{T}(y,t)\rangle = -\frac{c}{24\pi}(\mathcal{S}\cdot X_t)(y) \tag{4.93}$$

where we assume zero expectation value for the energy density in the initial ground state, meaning that $\langle \hat{T}(y,0)\rangle = 0$.

The time evolution of this quantity can be directly obtained from the previous analysis of $\kappa^{\pm}$ in the regime $\ell \to 0$. Specifically, by expanding Eq. (4.54) at small $\ell = y_1 - y_2$, we obtain:

$$\lim_{\ell\to 0}\frac{1}{\ell^2}\kappa(y_2+\ell, y_2, t) = -\frac{1}{6}(\mathcal{S}\cdot X_t)(y_2) \tag{4.94}$$

where this is valid for each chirality. This equation showcases the direct connection between the random variable κ and the physical quantity of $\langle \hat{T}(y,t) \rangle$ of our problem. More explicitly:

$$\langle \hat{T}(y,t) \rangle = \frac{c}{4\pi} \lim_{\ell \to 0} \kappa(y+\ell, y) \tag{4.95}$$

It is important to mention, that this equation implies that the statistics of the distribution of $\langle \hat{T}^{\pm}(y,t) \rangle$ can be derived from that of $\kappa^{\pm}$ in the limit of small ℓ. Following the derivation in Sec. 4.2.5, the full distribution over the noise can be expressed as:

$$\langle \hat{T}(y,t) \rangle \overset{\text{in law}}{=} \frac{c\tilde{\kappa}_0}{4\pi} \left(\frac{\omega}{\omega_0} - 1 \right) \tag{4.96}$$

where the random variable ω is a solution of Eq. (4.72) and the constants κ_0, ω_0 were defined in Eq. (4.73). We observe a remarkable correlation between the entanglement of an infinitesimal interval and the local energy density. Specifically, by using $\langle \hat{h}(x,t) \rangle = v(\langle \hat{T}^{+} \rangle + \langle \hat{T}^{-} \rangle)$ and the equation above, we find:

$$\langle \hat{h}(y,t) \rangle \overset{\text{in law}}{=} \frac{vc\tilde{\kappa}_0}{4\pi} \left(\frac{\omega^{+} + \omega^{-}}{\omega_0} - 1 \right) \tag{4.97}$$

The random variable of ω is space independent, making $\langle \hat{h}(y,t) \rangle$ space independent as well. The expectation value of the energy density demonstrates the same statistical behaviour at any point in space. Now if we compare with the Von Neumann entropy production from Eq. (4.89) we find $\langle \hat{h}(y,t) \rangle = \lim_{\ell \to 0} v \Delta S_t / (\pi \ell^2)$. The expectation value of the energy density in our theory is directly defined by the entanglement entropy of small subsystems. Additionally, defining the noise average (which is space-independent) as we have from (4.71):

$$\overline{\langle \hat{h}(y,t) \rangle} = \frac{cv^3 f^{(4)}(0)}{48\pi\theta} \left(e^{2\theta t} - 1 \right) \tag{4.98}$$

The noise average $\langle \hat{h}(y,t) \rangle$ demonstrates only an exponential increase in time, in contrast to the entanglement entropy production, which in the $\ell \gg 1$ limit, increases linearly, as shown in the previous section. The higher moments of $\langle \hat{h}(y,t) \rangle$ exhibit an exponential increase in time as well. This is understood from Sec. 4.2.5, where we saw the same exponential behaviour for the moments of κ.

For $t \gg 1/(2v)$, we expect $\kappa^{\pm}$ and therefore $\omega^{\pm}$ to decorrelate; thus from (4.45), we derive that the stationary distribution of the one-point energy density is coming from the convolution $\mathcal{B} * \mathcal{B}$, with $\mathcal{B}(\omega)$ being the stationary distribution in (4.44).

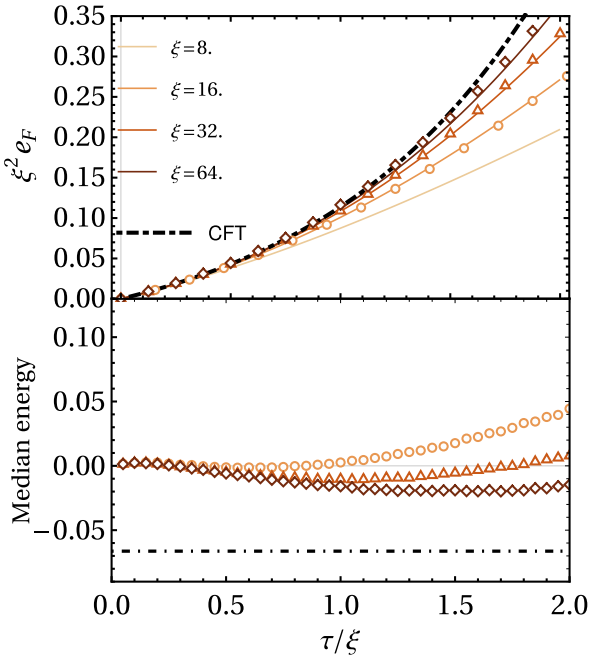

FIGURE 4.4: Top: The average energy $e_F(\tau)$ vs $t = \tau/\xi$, the scaled time, for different values of the noise correlation length ξ. Continuous lines are obtained from the numerical solution of the Wigner function equation (4.100), while the markers correspond to the exact dynamics of (4.99) for $L = 2048$. The dotted dashed line is the CFT result (4.98), which is predicted to hold for large ξ according to the scaling limit in Sec. 4.2.8. Bottom: The median of the distribution of $\xi^2(\langle \hat{h}_i \rangle_\tau - \langle \hat{h}_i \rangle_0)$ vs the scaled time τ/ξ. In the limit of $\xi \to \infty$, the median is expected to decrease towards the negative asymptotic value predicted by CFT (dot-dashed horizontal line). For finite ξ, the median starts to grow at large times, suggesting that heating may eventually dominate the lattice.

At this time scale, one can also find that the median value for the energy density is $\langle \hat{h}(y,t) \rangle = -c\tilde{\kappa}_0/2\pi$. Consequently, at large times, the one-point energy density has a distribution with fat $-3/2$ tails and all integer moments diverging.

4.2.8 Benchmarking with a Free Fermion model

Here we give a brief description of the analysis done to the free fermion model, that we used in order to confirm our theory both analytically and experimentally. The reader can refer to [46] for more technical details.

A. Tight-binding model

We examine a model of N non-interacting spinless fermions, where τ represents the time and space is discrete with L sites. The system is perturbed by noise coupled

to the energy density and its Hamiltonian will be:

$$\begin{aligned} \hat{H}_F &= \sum_i \left(1+\eta_i(\tau)\right)\hat{h}_i, \\ \hat{h}_i &= -J\left(\hat{a}_i^\dagger \hat{a}_{i+1} + \hat{a}_{i+1}^\dagger \hat{a}_i\right). \end{aligned} \tag{4.99}$$

where $\hat{a}_i, \hat{a}_i^\dagger$ are annihilation and creation fermionic operations at site i. The terms in $\hat{h}_i$ include the hopping terms of the fermions from the site i to $i+1$ and vice versa. J controls the probability for the fermion to hop on to the nearest neighbour e.g $J=0$ implies no hopping. It is generally negative, indicating that fermions tend to lower their energy by delocalizing over multiple sites. The noise is coupled to the energy density, inducing some random hopping rates to our problem. Without noise, $\hat{H}_F$ can be diagonalised by a Fourier transform of the operators, $\hat{a}_i$ in the momentum space and this leads to a dispersion relation $\epsilon(k) = -2J\cos(k)$. where k is the momentum with values $k = -\pi + 2\pi m/L,\ m = 1,2,\ldots,L$. The details of the diagonalization can be found in [123]. For the noise, we select the correlation

$$\overline{\eta_i(\tau)\eta_j(\tau')} = \tau_0 \delta\left(\tau-\tau'\right) F(i-j), \quad F(j) = f(j/\xi)$$

where ξ is the characteristic correlation length of the discrete model. Numerically, we choose $f(x) = 1/\cosh(x)$, as it corresponds to an analytically solvable case in the CFT limit. The dynamics induced by $\hat{H}_F$ are better studied using the noise-averaged Wigner function $n_\tau(k) = \sum_{j'} \overline{\left\langle \hat{a}_{j+j'}^\dagger \hat{a}_j \right\rangle_\tau} e^{ikj'}$, where $\langle \ldots \rangle_\tau$ denotes the quantum average at time τ. We choose the initial state as the ground state so that $n_\tau(k)$ does not depend on the lattice site j. The ground state of the noiseless tight binding model is a Fermi sea, with fermions occupying all the momentum states between $-k_F$ and k_F, with k_F being the Fermi point. The initial Wigner function with that ground state is then, $n_{\tau=0}(k) = \Theta\left(k+k_F\right) - \Theta\left(k-k_F\right)$, where $\Theta(z)$ is the Heaviside function and k_F is such that $\epsilon\left(k_F\right) = 0$ and $k_F = \pi/2$, corresponding to half filling. Half filling implies that we have to occupy $N = L/2$ k states of the system, starting from the one with the smallest $\epsilon(k)$. We are interested in this specific setup because the system is critical and can be described by a conformal field theory with central charge $c = 1$ [124], making it a good candidate for benchmarking out theory.

B. Scaling limit

Now we demonstrate the scaling limit of interest, but before we start we should

mention that we consider a continuous space description, by taking $L \to \infty$ and keeping the half filling. In continuous space the momentum becomes continuous and one can replace $\sum_k$ with, $\int_{-\pi}^{\pi} dk/2\pi$ based on the discrete values of k described in the beginning of this section. Using the Wigner function, we can express the noise-averaged energy density relative to the ground state as

$$\mathrm{e}_F(\tau) \equiv \overline{\left\langle \hat{h}_i \right\rangle_\tau - \left\langle \hat{h}_i \right\rangle_0} = \int \frac{dk}{2\pi} \epsilon(k) \left(n_\tau(k) - n_0(k) \right)$$

One can derive (see Appendix G in [46]) an exact evolution equation, for $n_\tau(k)$ which reads:

$$\partial_\tau n_\tau(k) = \tau_0 \int \frac{dk'}{2\pi} \tilde{F}\left(k'\right) \epsilon \left(k + k'/2\right)^2 \left(n_\tau\left(k + k'\right) - n_\tau(k) \right) \tag{4.100}$$

By analysing this equation (see Appendix G in [46]), we demonstrate that around the Fermi points, $n_\tau(k)$ takes the scaling form:

$$n_\tau(k) \simeq \mathfrak{n}\left(\xi\left(k_F - k\right), \tau/\xi\right) + \mathfrak{n}\left(\xi\left(k + k_F\right), \tau/\xi\right). \tag{4.101}$$

This leads to the result for fixed t as $\xi \to +\infty$:

$$\lim_{\xi \to \infty} \xi^2 \mathrm{e}_F(t\xi) = \tilde{\mathrm{e}}^+(t) + \tilde{\mathrm{e}}^-(t) \tag{4.102}$$

where we separate the energy contributions from the two Fermi points $\pm k_F$ by expanding $k = \pm\left(k_F - p/\xi\right)$. Introducing the Fermi velocity as $\epsilon'\left(\pm k_F\right) = \pm v$, we find for both chiral components:

$$\tilde{\mathrm{e}}^{\pm}(t) = -v \int_{-\infty}^{\infty} \frac{dp}{2\pi} p[\mathrm{n}(p,t) - \mathrm{n}(p,0)] = \mathrm{e}(t)/2. \tag{4.103}$$

and thus $\lim_{\xi\to\infty} \xi^2 \mathrm{e}_F(t\xi) = \mathrm{e}(t)$. The last equality is proven in Appendix G of [46], with $\mathbf{e}(t) = \overline{\langle \hat{h}(y,t) \rangle}$ given in Eq. (4.98) at $c = 1$. Thus, the CFT predicts, upon rescaling, the mean energy for the fermion system, confirming the exponential growth from a first-principles lattice calculation. This result suggests that in the scaling limit of large ξ, the noisy dynamics from $\hat{H}_F$ is fully described by the universal description provided by the CFT, with space and time rescaled as $j = x\xi, \tau = t\xi$, and setting $\tau_0 = \xi$.

To validate this hypothesis, we numerically computed the two-point correlation matrix $C_{ij}(\tau) \equiv \langle a_i^\dagger a_j \rangle_\tau$. Since the model of $\hat{H}_F$ is non-interacting and the initial ground state is Gaussian, all quantities for each noise realization can be expressed via the Wick theorem in terms of the coefficients C_{ij} [125]. However, despite the Gaussianity of the quantum state, the distribution of quantum expectations over different noise realizations remains analytically challenging. In Fig. 4.6 (top), we show the convergence of the noise-averaged energy density $e_F(\tau)$ to its CFT prediction as $\xi \to \infty$, consistent with Eqs. (4.102),(4.103). The correlation matrix $C(\tau)$ can also be used to compute the Renyi entropies for any interval I of size ℓ_F. For the Von Neumann entropy of the interval I (denoted as $\mathcal{S}_F$), setting C_I as the $\ell_F \times \ell_F$ submatrix obtained by restricting the indices of $C(\tau)$ to I, we have $\mathcal{S}_F(\tau) \equiv -\operatorname{Tr}[C_I \ln C_I + (1-C_I)\ln(1-C_I)]$. In Fig. 4.5 (upper right), we show the noise-averaged entanglement entropy production $S_F(\tau) \equiv \mathcal{S}_F(\tau) - \mathcal{S}_F(0)$ for the fermion system for intervals of various sizes ℓ_F on the lattice. Our prediction is that at large ξ, it should equal the CFT value $\overline{S_t^{(1)}}$ (without any prefactor) with $\ell = \ell_F/\xi$.

We also predict that the CFT describes the distribution of these quantities over the noise. In Fig. 4.5 (top right), we show the one-point PDF for the local energy density $\xi^2 \left\langle \hat{h}_i \right\rangle_\tau$ at the largest available time τ. It compares reasonably well, with no free parameters, to the CFT prediction, i.e., the convolution $P_{\text{stat}} * P_{\text{stat}}$ where P_{stat} was obtained in Eq. (4.76). This confirms that with the chosen $f(x)$, at this observation time, $2v_F\tau/\xi$ is sufficiently large, so that the two chiral components are only weakly correlated. v_F is the Fermi velocity satisfying $\epsilon'(k_F)$ and is equivalent to v the average velocity of the quasiparticles over the stochastic trajectories in our CFT theory. As seen in Fig. 4.6 (top), the average energy increases over time, consistent with P_{stat} having an infinite first moment. Therefore, the median of the energy distribution, shown in Fig. 4.5 (bottom), is a better indicator of the typical behaviour. Remarkably, it is found to decrease over time, approaching a stationary value at large ξ compatible with the CFT prediction $e_{\text{stat}}^{\text{median}} = -\frac{c}{2\pi}\tilde{\kappa}_0 < 0$ as mentioned in Sec. 4.2.7. Finally, in Fig. 4.5 (bottom), as a representative of finite ℓ behaviour, we compare the entanglement entropy distribution at different times for intervals of size $\ell_F = \ell\xi$ and $\ell = 1/2$, with the analytic prediction obtained from CFT.

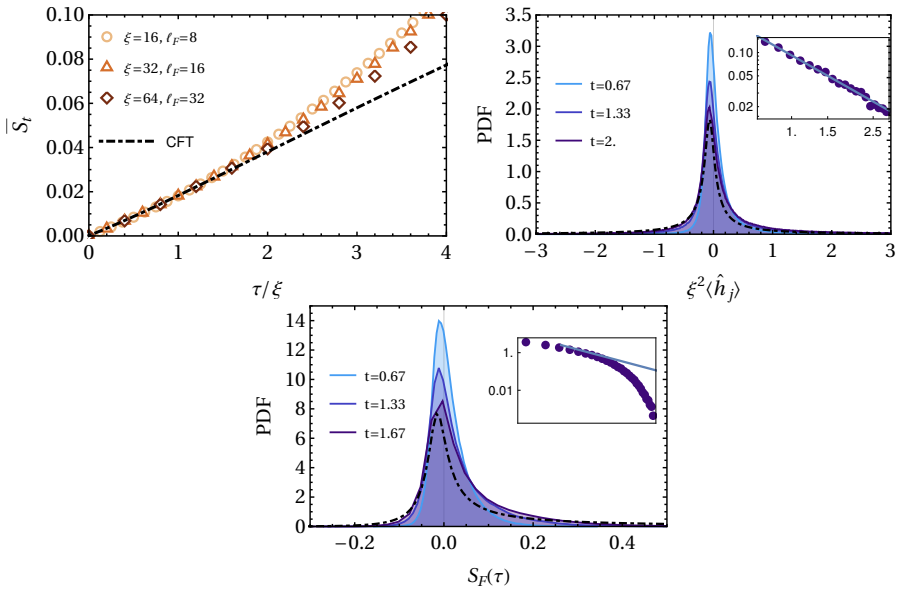

FIGURE 4.5: Upper left: Noise–averaged Von Neumann entanglement entropy production $\overline{S^{(1)}(\tau)}$ vs $t = \tau/\xi$ evolving in time under (4.99), for increasing values of ξ and fixed ratio $\ell_F/\xi = \ell = 1/2$. The dotted line is obtained from the numerical solution of Eqs. (4.61) and using (4.89) for $n \to 1$, i.e. $\overline{S_F(\tau)} = c\overline{\kappa}/6$ with $c = 1$. Upper right: Distribution of the scaled energy density $\xi^2\langle\hat{h}_i(\tau)\rangle$ at $\xi = 64$.. For the analytical prediction, we used that in the scaling limit $\xi^2\langle\hat{h}_j\rangle \to h(x,t)$ and at large time $h(x,t)$ is distributed as (4.45), which in the present case reduces to $h \overset{\text{in law}}{=} (3\Omega - 5)/(24\pi)$. In the inset, the right tail of the distribution is shown in log-log scale, showing the predicted $\propto h^{-3/2}$ tail. Lower centre: Distribution of the entanglement entropy $S_F(\tau)$ at $\xi = 64$. for an interval of size $\ell_F = 32$. For the analytical prediction, we used that in the stationary limit $\lim_{\tau\to\infty} S_F(\tau) \overset{\text{in law}}{=} c(\kappa^+ + \kappa^-)/12$, with $\kappa^\pm$ independently distributed according to $P_{\text{stat}}(\kappa)$. The stationary distribution $P_{\text{stat}}(\kappa)$ is obtained by numerically inverting the Fourier transform $Q_k(1)$ as a function of k, for $\ell = 1/2$, defined in (C.45) and (C.70) in Appendix C.3. All simulations are performed on systems of total length $L = 2048$ and are repeated for $N_{\text{sample}} = 800$ samples.

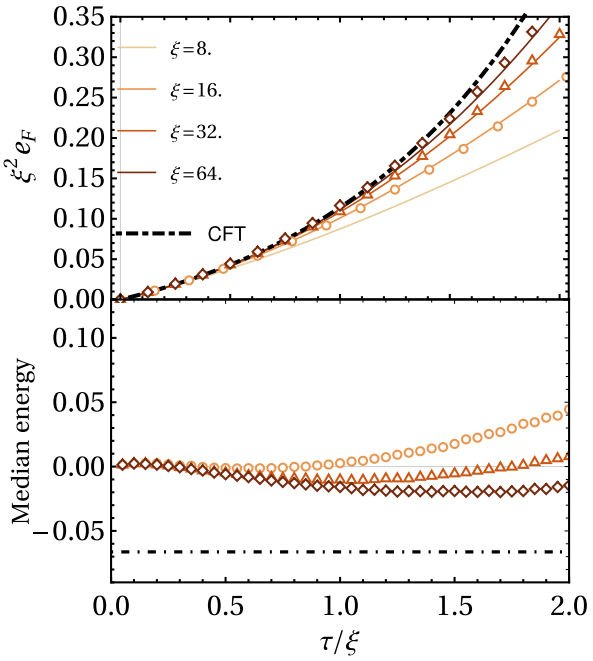

FIGURE 4.6: Top: The average energy $e_F(\tau)$ vs $t = \tau/\xi$, the scaled time, for different values of the noise correlation length ξ. Continuous lines are obtained from the numerical solution of the Wigner function equation (4.100), while the markers correspond to the exact dynamics of (4.99) for $L = 2048$. The dotted dashed line is the CFT result (4.98), which from (4.102) is predicted to hold for large ξ. Bottom: The median of the distribution of $\xi^2(\langle \hat{h}_i \rangle_\tau - \langle \hat{h}_i \rangle_0)$ vs the scaled time τ/ξ. In the limit of $\xi \to \infty$, the median is expected to decrease towards the negative asymptotic value predicted by CFT (dot-dashed horizontal line). For finite ξ, the median starts to grow at large times, suggesting that heating may eventually dominate the lattice.

Appendices

Appendix A

Correlations in dual Symplectic circuits

A.1 Change of variables in the dual picture

In this Appendix, we derive analytically an additional condition resulting from the requirement that the diagrammatic representations in both the original and dual frameworks are equivalent. We begin with the elementary scenario of two sites, hence our analysis is confined to the phase space M_2. Considering two arbitrary scalars $A, B \in L^2(M_2)$, we explore the Hermitian product $\langle B|\mathcal{P}_\Phi|A\rangle$, which is represented by the diagram below,

$\langle B|\mathcal{P}_\Phi|A\rangle \;=$ 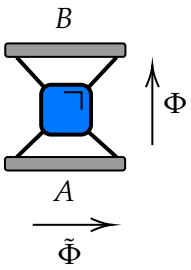

(A.1)

With the help of Eqs. (2.33),(2.34) on can write Eq. (A.1) as an integral

$$\langle B|\mathcal{P}_\Phi|A\rangle = \int d\vec{X}_1 d\vec{X}_2 d\vec{X}_1' d\vec{X}_2'\; A(\vec{X}_1,\vec{X}_2)B^*(\vec{X}_1',\vec{X}_2')\delta\big((\vec{X}_1',\vec{X}_2') - \Phi(\vec{X}_1,\vec{X}_2)\big) \quad \text{(A.2)}$$

in the time direction. In order for one to obtain the same analytic interpretation in the dual picture too, the following should be true

$$\langle B|\mathcal{P}_\Phi|A\rangle = \int d\vec{X}_1 d\vec{X}_2 d\vec{X}_1' d\vec{X}_2'\; A(\vec{X}_1,\vec{X}_2)B^*(\vec{X}_1',\vec{X}_2')\delta\big((\vec{X}_2,\vec{X}_2') - \tilde{\Phi}(\vec{X}_1,\vec{X}_1')\big), \quad \text{(A.3)}$$

where we used the definition of the dual map, as presented in Fig. 2.6, and exchanged the input from being the local states in space $(\vec{X}_1, \vec{X}_2)$ to local states in time $(\vec{X}_1, \vec{X}_1')$. In order for both Eqs. (A.2),(A.3) to be valid one has to demand that

$$\delta\big((\vec{X}_1', \vec{X}_2') - \Phi(\vec{X}_1, \vec{X}_2)\big) = \delta\big((\vec{X}_2, \vec{X}_2') - \tilde{\Phi}(\vec{X}_1, \vec{X}_1')\big) \tag{A.4}$$

The equivalence of the delta functions dictates the equivalence of the variable transformations between the two frameworks, thereby imposing a constraint on the Jacobian of this transformation. In particular, we define $g(\vec{X}_1, \vec{X}_2, \vec{X}_1', \vec{X}_2') = (\vec{X}_1', \vec{X}_2') - \Phi(\vec{X}_1, \vec{X}_2)$ and assume that we want to change variables with respect to $\vec{X}_2, \vec{X}_2'$. Then from Eq. (A.4), one obtains

$$\frac{\delta\big(g(\vec{X}_1, \vec{X}_2, \vec{X}_1', \vec{X}_2') = 0\big)}{|\det(Dg)|} = \delta\big((\vec{X}_2, \vec{X}_2') - \tilde{\Phi}(\vec{X}_1, \vec{X}_1')\big), \tag{A.5}$$

where Dg is the Jacobian matrix of the transformation g with respect to $\vec{X}_2, \vec{X}_2'$, and it is found as

$$Dg = \begin{bmatrix} -\frac{\partial \Phi^1(\vec{X}_1, \vec{X}_2)}{\partial \vec{X}_2} & 0 \\ -\frac{\partial \Phi^2(\vec{X}_1, \vec{X}_2)}{\partial \vec{X}_2} & \mathbb{1} \end{bmatrix} \tag{A.6}$$

where we decomposed Φ into single-site outputs

$$\Phi(\vec{X}_1, \vec{X}_2) = \big(\Phi^1(\vec{X}_1, \vec{X}_2), \Phi^2(\vec{X}_1, \vec{X}_2)\big) \tag{A.7}$$

The solutions of $g(\vec{X}_1, \vec{X}_2, \vec{X}_1', \vec{X}_2') = 0$ with respect to $\vec{X}_1, \vec{X}_1'$, are the points of the dual map $(\vec{X}_2, \vec{X}_2') = \tilde{\Phi}(\vec{X}_1, \vec{X}_1')$, and if we assume that Φ has a unique and bijective dual map then from Eq. (A.5) we obtain that

$$\frac{\delta\big((\vec{X}_2, \vec{X}_2') - \tilde{\Phi}(\vec{X}_1, \vec{X}_1')\big)}{|\det(Dg)|} = \delta\big((\vec{X}_2, \vec{X}_2') - \tilde{\Phi}(\vec{X}_1, \vec{X}_1')\big). \tag{A.8}$$

This is true in M_2 if $|\det(Dg)| = 1$, which according to Eq. (A.6) leads to

$$\left|\det\left(\frac{\partial \Phi^1(\vec{X}_1, \vec{X}_2)}{\partial \vec{X}_2}\right)\right| = 1 \quad \forall \vec{X}_1, \vec{X}_2 \in M \times M \tag{A.9}$$

This is an essential condition that the local gate Φ must fulfill to ensure the equivalence of diagrammatic representations in both the time picture and the dual picture.

We proceed by demonstrating that, as anticipated, Eq. (A.9) necessitates a corresponding condition for $\tilde{\Phi}$. This indicates that an equivalent outcome is achieved, even when the change of variables happens from the dual picture back to the original one. Firstly, if we denote the output of as $\Phi(\vec{X}_1, \vec{X}_2) = (\vec{X}_1', \vec{X}_2')$, from Eq. (A.7) we obtain:

$$\vec{X}_1' = \Phi^1(\vec{X}_1, \vec{X}_2) \tag{A.10}$$

$$\vec{X}_2' = \Phi^2(\vec{X}_1, \vec{X}_2) \tag{A.11}$$

Since, by the definition $(\vec{X}_2, \vec{X}_2') = \tilde{\Phi}(\vec{X}_1, \vec{X}_1')$ we need to find $\vec{X}_2, \vec{X}_2'$ as functions of $\vec{X}_1, \vec{X}_1'$ and thus we invert Eq. (A.10) with respect to $\vec{X}_2$ and replace it in Eq. (A.11),

$$\vec{X}_2 = (\Phi^1_{\vec{X}_1})^{-1}(\vec{X}_1')$$
$$\vec{X}_2' = \Phi^2\big(\vec{X}_1, (\Phi^1_{\vec{X}_1})^{-1}(\vec{X}_1')\big)$$

where we assume that the first output $\Phi^1(\vec{X}_1, \vec{X}_2) = \Phi^1_{\vec{X}_1}(\vec{X}_2)$ is a family of invertible maps $\Phi^1_{\vec{X}_1} : M \to M$ for every $\vec{X}_1 \in M$. Finally the dual map of Φ reads

$$\tilde{\Phi}(\vec{X}_1, \vec{X}_1') = \Big((\Phi^1_{\vec{X}_1})^{-1}(\vec{X}_1'), \Phi^2\big(\vec{X}_1, (\Phi^1_{\vec{X}_1})^{-1}(\vec{X}_1')\big)\Big) \tag{A.12}$$

Then, from Eq. (A.9), one can deduce that the inverse of $\Phi^1_{\vec{X}_1}(\vec{X}_2)$ has also a Jacobian equal to one,

$$\left|\det\left(\frac{\partial(\Phi^1_{\vec{X}_1})^{-1}(\vec{X}_1')}{\partial \vec{X}_1'}\right)\right| = 1, \tag{A.13}$$

which is exactly the respective condition Eq. (A.9) for the dual map $\tilde{\Phi}$, and thus making this condition consistent with the the dual operation, being an involution.

The same methodology can be applied to scenarios where diagrams are interpreted from right to left, leading to a respective change of variables in Eq. (A.4) is with respect to $\vec{X}_1', \vec{X}_1$. This is equivalent to defining a dual map as in Fig. 2.6, but with the swapping of the other diagonal of the legs of Φ. This dual map is the solution of $g(\vec{X}_1, \vec{X}_2, \vec{X}_1', \vec{X}_2') = 0$ with respect to $\vec{X}_1', \vec{X}_1$. Similarly, we demand that $\Phi^2(\vec{X}_1, \vec{X}_2) = \Phi^2_{\vec{X}_2}(\vec{X}_1)$ is a family of invertible maps $\Phi^2_{\vec{X}_2} : M \to M$ for every $\vec{X}_2 \in M$, and we obtain the extra condition

$$\left|\det\left(\frac{\partial \Phi^2(\vec{X}_1, \vec{X}_2)}{\partial \vec{X}_1}\right)\right| = 1 \quad \forall \vec{X}_1, \vec{X}_2 \in M \times M. \tag{A.14}$$

In addition, one can prove, in the same manner as for Eq. (A.13), that Eq. (A.14) is consistent with the dual map being an involution.

A.2 Weak contractivity and positivity of $\mathcal{F}_{\pm}$

In this Appendix, we demonstrate that the single-site transfer operator $\mathcal{F}$ (also denoted as $\mathcal{F}_+$) acts as a weak contraction and is a positive operator. Initially, as highlighted in the main text, the map $\mathcal{P}_\Phi$ is unitary within $L^2(M \times M)$, preserving the L^2-norm. Consequently, using Eq. (A.20), we derive the following for any $\rho_1, \rho_2 \in L^2(M)$:

$$\begin{aligned} |\langle \rho_1 | \mathcal{F} | \rho_2 \rangle| = |(\langle \circ | \otimes \langle \rho_1 |)\, \mathcal{P}_\Phi\, (|\rho_2\rangle \otimes |\circ\rangle)| &\leq \| \, |\circ\rangle \otimes |\rho_1\rangle \|_2 \, \| \mathcal{P}_\Phi \, (|\rho_2\rangle \otimes |\circ\rangle) \|_2 \\ &= \| \, |\circ\rangle \otimes |\rho_1\rangle | \|_2 \, \| \, |\rho_2\rangle \otimes |\circ\rangle \|_2 = \|\rho_1\|_2 \, \|\rho_2\|_2 \end{aligned} \tag{A.15}$$

Here, we apply the Cauchy-Schwarz inequality and note that the state $|\circ\rangle$ is normalized. By setting $|\rho_1\rangle = \mathcal{F}|\rho_2\rangle$, we can confirm

$$\|\mathcal{F}|\rho_2\rangle\|_2 \leq \|\rho_2\|_2 \tag{A.16}$$

for every $\rho_2 \in L^2(M)$. This implies that the single-site transfer operator acts as a weak contraction.

The operator's positivity is directly linked to the characteristics of the Frobenius-Perron operator. Consider $\rho \in L^2(M)$ and $\vec{X} \in M$. We focus on the scalar value $\langle \vec{X} | \mathcal{F} | \rho \rangle$. It is sufficient to prove, that it is always positive if $\rho \geq 0$. The calculation is based on the use of Eq. (A.20), from which we get

$$\langle \vec{X} | \mathcal{F} | \rho \rangle = (\langle \circ | \otimes \langle \vec{X} |)\, \mathcal{P}_\Phi\, (|\rho\rangle \otimes |\circ\rangle). \tag{A.17}$$

The scalar $|\circ\rangle \to u_\circ(\vec{X}) = 1/\sqrt{|M|}$ is positive. Therefore, assuming $\rho \geq 0$, the product $|\rho\rangle \otimes |\circ\rangle \to (\rho u_\circ)(\vec{X}_1, \vec{X}_2) = \rho(\vec{X}_1) u_\circ(\vec{X}_2)$ also yields a non-negative scalar. In the final step, it is important to recognize that $\mathcal{P}_\Phi$ acts as a Frobenius-Perron operator, which is inherently positive. This confirms that $\mathcal{P}_\Phi(|\rho\rangle \otimes |\circ\rangle) \geq 0$. . As a consequence the value Eq. (A.17), is non-negative for every $\vec{X} \in M$ meaning that

$$\mathcal{F}|\rho\rangle \geq 0 \quad \text{for any } \rho \geq 0 \in L^2(M).$$

In the same manner, one can prove these properties for $\mathcal{F}_-$ as well.

A.3 Diagrammatic equivalence

In this section, we demonstrate that our Ising Swap model meets the requirements set forth in Eq. (2.42) for classical spin variables in $\mathcal{S}^2$. We begin by breaking down Eq. (2.49) into its single-site components $\Phi_{\alpha,\beta,\gamma}(\vec{S}_1,\vec{S}_2) = \big(\Phi^1_{\alpha,\beta,\gamma}(\vec{S}_1,\vec{S}_2), \Phi^2_{\alpha,\beta,\gamma}(\vec{S}_1,\vec{S}_2)\big) = (\vec{S}'_1,\vec{S}'_2)$ with

$$\vec{S}'_1 = R_x(\beta)R_z\big(\alpha(R_x(\gamma)\vec{S}_1)^z\big)R_x(\beta)\vec{S}_2 \tag{A.18}$$

$$\vec{S}'_2 = R_x(\gamma)R_z\big(\alpha(R_x(\beta)\vec{S}_2)^z\big)R_x(\gamma)\vec{S}_1 \tag{A.19}$$

First, we observe that, $\Phi^1_{\alpha,\beta,\gamma}(\vec{S}_1,\vec{S}_2) = R_x(\beta)R_z\big(\alpha(R_x(\gamma)\vec{S}_1)^z\big)R_x(\beta)\vec{S}_2$ and $\Phi^2_{\alpha,\beta,\gamma}(\vec{S}_1,\vec{S}_2) = R_x(\gamma)R_z\big(\alpha(R_x(\beta)\vec{S}_2)^z\big)R_x(\gamma)\vec{S}_1$, which makes its Jacobian matrix over $\vec{S}_2$ and $\vec{S}_1$ respectively, a composition of rotations and implies that

$$\left|\det\Big(\frac{\partial\Phi^1_{\alpha,\beta,\gamma}(\vec{S}_1,\vec{S}_2)}{\partial\vec{S}_2}\Big)\right| = |\det\big(R_x(\beta)R_z\big(\alpha(R_x(\gamma)\vec{S}_1)^z\big)R_x(\beta)\big)| = 1 \quad ,\forall\vec{S}_1,\vec{S}_2\in\mathcal{S}^2\times\mathcal{S}^2$$

$$\left|\det\Big(\frac{\partial\Phi^2_{\alpha,\beta,\gamma}(\vec{S}_1,\vec{S}_2)}{\partial\vec{S}_1}\Big)\right| = |\det\big(R_x(\gamma)R_z\big(\alpha(R_x(\beta)\vec{S}_2)^z\big)R_x(\gamma)\big)| = 1 \quad ,\forall\vec{S}_1,\vec{S}_2\in\mathcal{S}^2\times\mathcal{S}^2$$

where we used that the determinant of rotations is 1 since they belong to $SO(3)$ group.

A.4 The operator $\mathcal{F}_\pm$ in block-diagonal form

In this Appendix, we compute the matrix representation of the one-site transfer operator using spherical harmonics and demonstrate that it exhibits a block-diagonal structure in terms of the angular momentum quantum number ℓ. This analysis is grounded in the diagram depicted in Fig. 2.7. Specifically, the general local gate $\mathcal{F}_\pm$ can be understood either in terms of temporal dynamics governed by Φ, or spatially via the dual representation with $\tilde{\Phi}$. Although these perspectives are equivalent, we opt for the former for this discussion. Consistent with the main text, we focus solely on the right-moving chirality $\mathcal{F}_+ \equiv \mathcal{F}$ and do not consider the $\pm$ notation further. As illustrated in Fig. 2.7, the transition amplitudes of $\mathcal{F}$ between any two functions

ρ_1, ρ_2 from $L^2(M)$ are described as follows:

$$\langle \rho_1 | \mathcal{F} | \rho_2 \rangle = \left(\langle \circ | \otimes \langle \rho_1 | \right) \mathcal{P}_\Phi \left(| \rho_2 \rangle \otimes | \circ \rangle \right). \tag{A.20}$$

We note that this holds for any dual-symplectic gate. We focus on the Ising Swap model, where since $|\circ\rangle = |00\rangle$ in the basis spherical harmonics one can use Eqs. (A.20),(A.31),(A.32) to obtain

$$\langle \ell m | \mathcal{F} | \ell' m' \rangle = \langle 00, \ell m | \mathcal{P}_{\Phi_{\alpha,\beta,\gamma}} | \ell' m', 00 \rangle = \delta_{\ell,\ell'} \sum_{q_2=-\ell}^{\ell} \langle \ell m | \mathcal{P}_{R_x(\gamma)} | \ell q_2 \rangle \frac{\sin(\alpha q_2)}{a q_2} \langle \ell q_2 | \mathcal{P}_{R_x(\gamma)} | \ell m' \rangle, \tag{A.21}$$

where we used that $T(0) = \mathbb{1}$, $C^{0,0,0}_{0,0,0} = 1$ and $j_0(x) = \sin(x)/x$, and the fact that a constant scalar is invariant under rotations, thus $\langle 00 | \mathcal{P}_{R_x(\beta)} | 00 \rangle = 1$. This expression can be further simplified by defining the map $Q(\alpha) : M \to M$

$$Q(\alpha) = \frac{1}{2} \int_{-1}^{1} dz' R_z(\alpha z') \tag{A.22}$$

Spherical harmonics serve as the eigenbasis for the Frobenius-Perron operator associated with rotations about the z-axis. Specifically, the matrix element $\langle \ell_1 m_1 | \mathcal{P}_{R_z(\theta)} | \ell_2 m_2 \rangle$ equals $e^{-i m_1 \theta} \delta_{\ell_1,\ell_2} \delta_{m_1,m_2}$ for a rotation by an angle $\theta \in [0, 2\pi)$. By applying this result in Eq. (A.22) and carrying out the necessary integrations, we obtain the representation of $\mathcal{P}_{Q(\alpha)} : D(M) \to D(M)$.

$$\langle \ell_1 m_1 | \mathcal{P}_{Q(\alpha)} | \ell_2 m_2 \rangle = \frac{\sin(\alpha m_1)}{\alpha m_1} \, \delta_{\ell_1,\ell_2} \delta_{m_1,m_2} \tag{A.23}$$

and we finally obtain the exact form of the transfer operator

$$\mathcal{F} = \mathcal{P}_{R_x(\gamma)} \mathcal{P}_{Q(\alpha)} \mathcal{P}_{R_x(\gamma)} \tag{A.24}$$

This result confirms that the operator in question is the Frobenius-Perron operator corresponding to the local phase-space map $f : M \to M$:

$$f = R_x(\gamma) Q(\alpha) R_x(\gamma) \quad , \quad \mathcal{F} \equiv \mathcal{P}_f \tag{A.25}$$

We have accurately derived the form of the transfer operator for both the density representation and the pointwise phase-space map. As illustrated in Eq. (A.21), the operator is block-diagonal with respect to the total angular momentum ℓ. The

derivations for $\mathcal{F}_-$ are analogous, employing the middle point reflection $\beta, \gamma \to \gamma, \beta$.

A.5 The spherical harmonics representation of $\mathcal{P}_{\Phi_{(\alpha,\beta,\gamma)}}$

In this Appendix, we detail the calculation of the matrix elements of the Frobenius-Perron operator $\mathcal{P}_{\Phi_{(\alpha,\beta,\gamma)}}$ for the local gate, using the spherical harmonics basis, denoted as $|\ell, m\rangle \to Y_{\ell,m}$. This basis, where $\ell = 0, \ldots, \infty$ and $|m| \leq \ell$, is orthonormal under the inner product defined in Eq. (2.33):

$$\langle \ell_1 m_1 | \ell_2 m_2 \rangle = \int_{\mathcal{S}^2} d\vec{X}\, Y^*_{\ell_1 m_1}(\vec{X}) Y_{\ell_2 m_2}(\vec{X}) = \delta_{\ell_1,\ell_2}\delta_{m_1,m_2} \tag{A.26}$$

According to Eq. (2.49), the local gate incorporates single-site rotations $R_x(\theta)$ for $\theta \in [0, 2\pi)$ and the Ising Swap gate I_α. The rotations about the x-axis are conveniently described in the spherical harmonics basis by $\mathcal{P}_{R_x(\theta)} = D(-\pi/2, \theta, \pi/2)$, where D represents the Wigner-D matrix [126] and is block diagonal in ℓ (implying $\langle \ell_1 m_1 | D | \ell_2 m_2 \rangle = 0$ for $\ell_1 \neq \ell_2$). The next step involves characterizing the representation of I_α, which we approach by deriving the kernel of the Ising gate on $\mathcal{S}^2 \times \mathcal{S}^2$ and subsequently determining its action on $|\ell, m\rangle$.

We already know from Eq. (2.50), how I_α acts on two spins and this leads to the following kernel

$$\mathcal{P}_{I_\alpha}(\vec{X}_1, \vec{X}_2, \vec{X}_3, \vec{X}_4) = \delta\big(\vec{X}_1 - R_z(\alpha z_3)\vec{X}_4\big)\, \delta\big(\vec{X}_2 - R_z(\alpha z_4)\vec{X}_3\big). \tag{A.27}$$

(one should mention that we choose polar coordinates $\vec{X}_i = (z_i, \varphi_i) \quad i = 1, \ldots, 4$ for the parametrization of the unit sphere). This operation couples two spins and thus by using Eq. (2.33) in the basis of two-spherical harmonics we obtain

$$\begin{aligned}\langle \ell_1 m_1, \ell_2 m_2 | \mathcal{P}_{I_\alpha} | \ell_3 m_3, \ell_4 m_4 \rangle = \; & \delta_{m_1,m_4}\delta_{m_2,m_3} \\ & \int_{\mathcal{S}^2} d\vec{X}_3 d\vec{X}_4\, Y^*_{\ell_1 m_1}(R_z(\alpha z_3)\vec{X}_4) Y_{\ell_4 m_4}(\vec{X}_4)\; Y^*_{\ell_2 m_2}(R_z(\alpha z_4)\vec{X}_3) Y_{\ell_3 m_3}(\vec{X}_3).\end{aligned} \tag{A.28}$$

The Kronecker deltas arise from the integration over the variables φ_3 and φ_4, reflecting the interaction of the rotations through the z-components of each vector. To advance our analysis, we recognize that a rotation around the z-axis translates into a shift in the azimuthal angle, thus for spherical harmonics, we have $Y_{\ell,m}(R_z(\theta)\vec{X}) = Y_{\ell,m}(\vec{x})e^{im\theta}$. Leveraging this property allows us to decouple the z-components as

follows:

$$\langle \ell_1 m_1, \ell_2 m_2 | \mathcal{P}_{I_\alpha} | \ell_3 m_3, \ell_4 m_4 \rangle = \int_{\mathcal{S}^2} d\vec{X}_3 d\vec{X}_4 \; Y^*_{\ell_1 m_1}(R_z(\alpha \frac{m_2}{m_1} z_4)\vec{X}_4) Y_{\ell_4 m_4}(\vec{X}_4) \; Y^*_{\ell_2 m_2}(R_z(\alpha \frac{m_1}{m_2} z_3)\vec{X}_3) Y_{\ell_3 m_3}(\vec{X}_3) \quad \text{(A.29)}$$

This formula demonstrates the coupling of the rotations R_z of one spin to its own z-component. Such nonlinear rotational dynamics are termed 'torsion', where $T(a)\vec{X} = R_z(az)\vec{X}$ (with a representing the coupling constant and $T(0) = \mathbb{1}$). The representation of torsion in spherical harmonics is detailed in [127]. In particular, it was found that

$$\langle \ell m | \mathcal{P}_{T(a)} | \ell' m' \rangle = \delta_{m,m'} (-1)^m \sqrt{(2\ell+1)\,(2\ell'+1)} \sum_{p=|\ell-\ell'|}^{\ell+\ell'} (-i)^p j_p(-ma) C^{\ell\ell' p}_{000} C^{\ell\ell' p}_{-mm0}. \quad \text{(A.30)}$$

where j_p is the spherical Bessel function and $C^{\ell_1,\ell_2,\ell_3}_{m_1,m_2,m_3}$ are the Clebsch-Gordan coefficients. Finally, we obtain the representation of the Ising Swap gate

$$\langle \ell_1 m_1, \ell_2 m_2 | \mathcal{P}_{I_\alpha} | \ell_3 m_3, \ell_4 m_4 \rangle = \langle \ell_1 m_1 | \mathcal{P}_{T(\alpha \frac{m_2}{m_1})} | \ell_4 m_1 \rangle \; \langle \ell_2 m_2 | \mathcal{P}_{T(\alpha \frac{m_1}{m_2})} | \ell_3 m_3 \rangle \; \delta_{m_1,m_4} \delta_{m_2,m_3} \quad \text{(A.31)}$$

This expression remains applicable even when $m_1, m_2 = 0$, as it can be seen from Eq. (A.30) that the denominators in the argument of j_p cancel out. With this understanding, we now proceed to integrate all the discussed components, culminating in the following representation:

$$\langle \ell_1 m_1, \ell_2 m_2 | \mathcal{P}_{\Phi_{\alpha,\beta,\gamma}} | \ell_3 m_3, \ell_4 m_4 \rangle = \sum_{q_1,q_2=-\ell_1,-\ell_2}^{\ell_1,\ell_2} \langle \ell_1 m_1 | \mathcal{P}_{R_x(\beta)} | \ell_1 q_1 \rangle \langle \ell_4 q_1 | \mathcal{P}_{R_x(\beta)} | \ell_4 m_4 \rangle \langle \ell_2 m_2 | \mathcal{P}_{R_x(\gamma)} | \ell_2 q_2 \rangle \langle \ell_3 q_2 | \mathcal{P}_{R_x(\gamma)} | \ell_3 m_3 \rangle \times \times \langle \ell_1 q_1 | \mathcal{P}_{T(\alpha \frac{q_2}{q_1})} | \ell_4 q_1 \rangle \; \langle \ell_2 q_2 | \mathcal{P}_{T(\alpha \frac{q_1}{q_2})} | \ell_3 q_2 \rangle \quad \text{(A.32)}$$

A.6 The modes which contribute to the correlations

In this Appendix, we establish that the only relevant ℓ-subspaces contributing to the correlations are those common to the expansions of the observables using spherical

harmonics. These subspaces, denoted as $V^\ell = span(\{|\ell, m\rangle\}_{m=-\ell}^{\ell})$, are crucial for our analysis. The proof stems from the block diagonal structure of the transfer operator $\mathcal{F}$ (denoted as $\mathcal{F}_+$), which implies that it can be expressed as a direct sum $\mathcal{F} = \bigoplus_{\ell=0}^{\infty} \mathcal{F}^\ell$, where $\mathcal{F}^\ell$ represents the blocks associated with each total angular momentum subspace. Thus, it's advantageous to work in a picture where the Hilbert space $L^2(\mathcal{S}^2) = \bigoplus_{\ell=0}^{\infty} V^\ell$ is a direct sum of these subspaces. In this context, the two local observables mentioned in the main text can also be decomposed as $|a\rangle = \bigoplus_{\ell=0}^{\infty} |a^\ell\rangle$ and $|b\rangle = \bigoplus_{\ell=0}^{\infty} |b^\ell\rangle$. We assume that their expansions using spherical harmonics overlap only with a finite number of V^ℓ spaces, denoted as ℓ_i^a for $i = 1, \ldots, n_a$ and ℓ_j^b for $j = 1, \ldots, n_b$, respectively. Here, n_a and n_b represent the total number of overlapping V^ℓ subspaces of the observables. Consequently, this implies that the components $|a^\ell\rangle$ and $|b^\ell\rangle$ trivially vanish in the remaining total angular momentum subspaces:

$$\begin{aligned} |a^\ell\rangle &= \vec{0}_\ell \text{ for } \ell \neq \ell_i^a \\ |b^\ell\rangle &= \vec{0}_\ell \text{ for } \ell \neq \ell_j^b \end{aligned} \tag{A.33}$$

where $\vec{0}_\ell$ is the zero vector in V^ℓ. Moreover, in this picture, the Hermitian product splits into a sum of Hermitian products over V^ℓ and by using $|\circ\rangle = |1\rangle/2\sqrt{\pi}$, we obtain from Eq. (2.46)

$$C_{a,b}(t,t) = \frac{1}{4\pi}\Big(\sum_{\ell=0}^{\infty} \langle a^\ell|(\mathcal{F}^\ell)^{2t}|b^\ell\rangle - \frac{1}{4\pi}\langle 1|b\rangle\langle 1|a\rangle\Big) = \frac{1}{4\pi}\sum_{\ell_c\neq 0} \langle a^{\ell_c}|(\mathcal{F}^{\ell_c})^{2t}|b^{\ell_c}\rangle, \tag{A.34}$$

where we applied Eq. (A.33) and now, one can observe, that the only non-vanishing terms are the ones of the common subspaces ℓ_c between ℓ_i^a and ℓ_j^b. The space V^0 of the constant on $\mathcal{S}^2$ scalars, does not contribute to the correlations since it is being cancelled out from the second term in Eq. (A.34). In addition, our result automatically implies, that only the eigenvalues of $\mathcal{F}^{\ell_c}$ contribute and thus the exact 2-point function is defined by a finite set of exponentials. One can obtain the results for the other chirality of correlations by using the middle point reflection $\beta, \gamma \to \gamma, \beta$.

Appendix B

Unitary designs and distributions of overlaps

B.1 $\mathbb{E}_{\text{GinUE}}$ and Isserlis' theorem

In this part, we provide an analytic proof of Eq. 3.59, in the main text. We use the compact way of representing the vectors on the basis of $\mathcal{H}_{2k}$, shown in Sec. 3.1.2. We start by focusing on the average of an arbitrary element of the tensor in Eq. (3.59):

$$\mathbb{E}_{\text{GinUE}}\left[\langle \boldsymbol{i},\boldsymbol{a}|\tilde{G}\otimes\cdots\otimes\tilde{G}\otimes\tilde{G}^*\otimes\cdots\otimes\tilde{G}^*|\boldsymbol{j},\boldsymbol{b}\rangle\right] = \mathbb{E}_{\text{GinUE}}[(\tilde{G})_{i_1,j_1}\ldots(\tilde{G})_{i_k,j_k}(\tilde{G}^*)_{a_1,b_1}\ldots(\tilde{G}^*)_{a_k,b_k}] \quad \text{(B.1)}$$

where we omit the index a since the result does not depend on it. So the average is being performed over $2k$ complex Gaussian variables, k coming from matrix elements of $\tilde{G}$ and k from $\tilde{G}^*$. Now, we apply Isserlis' theorem, which when applied to a product of $2k$ complex Gaussian variables, is supposed to simplify it to products of averages of pairings among these $2k$ random variables. However, in our case, we know that $\mathbb{E}[(\tilde{G}_\alpha)_{b,c}(\tilde{G}^*_\alpha)_{b',c'}] = \nu^2\delta_{b,b'}\delta_{c,c'}$, $\mathbb{E}[(\tilde{G}_\alpha)_{b,c}(\tilde{G}_\alpha)_{b',c'}] = 0$. Consequently, the only pairings that contribute are the ones where each of the k copies of $\tilde{G}$ is paired to a copy of $\tilde{G}^*$. This pairing is nothing more than a permutation of S_k.Based on that, the application of Wick's theorem at the equation above leads to:

$$\mathbb{E}_{\text{GinUE}}\left[\langle \boldsymbol{i},\boldsymbol{a}|\tilde{G}\otimes\cdots\otimes\tilde{G}\otimes\tilde{G}^*\otimes\cdots\otimes\tilde{G}^*|\boldsymbol{j},\boldsymbol{b}\rangle\right] = \sum_{\sigma\in S_k}\prod_{m=1}^{k}\mathbb{E}_{\text{GinUE}}[(\tilde{G}_\alpha)_{i_m,a_{\sigma(m)}}(\tilde{G}^*_\alpha)_{j_m,b_{\sigma(m)}}] =$$

$$\sum_{\sigma\in S_k}\nu^{2k}\prod_m\delta_{i_m,a_{\sigma(m)}}\delta_{j_m,b_{\sigma(m)}} = \sum_{\sigma\in S_k}\nu^{2k}\delta_{\boldsymbol{i},\sigma(\boldsymbol{a})}\delta_{\boldsymbol{j},\sigma(\boldsymbol{b})} \quad \text{(B.2)}$$

where for practical reasons we compacted all the Kronecker-δ, with our vector notation for the indices. By the definition of, $|\sigma\rangle\rangle$ in Sec. 3.1.2 we get that $\langle \boldsymbol{i}, \boldsymbol{a}|\, \sigma\rangle\rangle = \delta_{\boldsymbol{i},\sigma(\boldsymbol{a})}$ and $\langle\langle \sigma\, |\boldsymbol{j}, \boldsymbol{b}\rangle = \delta_{\boldsymbol{j},\sigma(\boldsymbol{b})}$, where the second equality comes from the fact that $|\sigma\rangle\rangle$ has real components. Finally, by applying these relations to Eq. B.2, we obtain that

$$\mathbb{E}_{\text{GinUE}}\left[\langle \boldsymbol{i}, \boldsymbol{a}|\tilde{G}\otimes\cdots\otimes\tilde{G}\otimes\tilde{G}^*\otimes\cdots\otimes\tilde{G}^*|\boldsymbol{j}, \boldsymbol{b}\rangle\right] = \sum_{\sigma\in S_k} \nu^{2k}\, \langle \boldsymbol{i}, \boldsymbol{a}|\, \sigma\rangle\rangle\langle\langle \sigma\, |\boldsymbol{j}, \boldsymbol{b}\rangle = \langle \boldsymbol{i}, \boldsymbol{a}|\left(\sum_{\sigma\in S_k} \nu^{2k}|\sigma\rangle\rangle\langle\langle\sigma|\right)|\boldsymbol{j}, \boldsymbol{b}\rangle$$

Since this is true for every, $\boldsymbol{i}, \boldsymbol{a}, \boldsymbol{j}, \boldsymbol{b}$ we finally recover the equation Eq. 3.59 in the main text.

B.2 Adjacency matrices

In the main text, we focused more on the adjacency matrix A of a single transposition, defined as $A_{\sigma,\sigma'} = \delta_{D(\sigma\sigma'^{-1}),1}$. However, in the expansion in Eq. (3.65), we can see that the adjacency matrices of multiple transpositions are appearing. In particular, we define the family of adjacency matrices $(A_i)_{\sigma,\sigma'} = \delta_{D(\sigma\sigma'^{-1}),i}$ with $i = 0, 1, 2, \ldots$. By its definition, A_i expresses which pairs of permutations differ by a minimal of i transpositions. The group structure of S_k actually connects all the adjacency matrices to $A_1 = A$. We are going to prove that one needs to know only A and the rest adjacency matrices can be recovered from it.

We start with the definition of $(A_i)_{\sigma,\sigma'} = \delta_{D(\sigma\sigma'^{-1}),i}$, which expresses that if $(A_i)_{\sigma,\sigma'} = 1$ then there exists a specific minimal number of i transpositions $\{\tau_1, \tau_2, \ldots, \tau_i\}$ such that $\sigma = \tau_1\tau_2\ldots\tau_i\sigma'$. In the main text for the purpose of studying our statistical model in Sec. 3.2.3, we explained that $(A^i)_{\sigma,\sigma'}$ is the total number of ways that σ, σ' can differ by i transpositions, but not minimally. To understand this, let's denote $\pi_1, \pi_2, \ldots, \pi_i$, i transpositions and each of them can be any of the $\binom{k}{2}$ transpositions in S_k. Then $(A^i)_{\sigma,\sigma'}$, will be the total number of possible ways that $\sigma = \pi_1\pi_2\ldots\pi_i\sigma'$. Among this possible combinations of transpositions and there should be as well the specific minimal one given by $\tau_1, \tau_2, \ldots, \tau_i$. If $(A^i)_{\sigma,\sigma'} = 0$ then there is no way of σ, σ' differing by i transpositions and thus no minimal way either $(A_i)_{\sigma,\sigma'} = 0$. There is only one thing left and that is related to the identity e permutation. When $\sigma = \sigma' \implies D(\sigma\sigma'^{-1}) = D(e) = 0$, where we consider that the identity element has

no minimal expression with transpositions. Taking this into account we can then deduce that $(A_i)_{\sigma,\sigma} = 0$. To conclude, all of the above can be expressed with the following relation for $i \geq 1$

$$(A_i)_{\sigma,\sigma'} = \begin{cases} 0, \text{ when } \sigma = \sigma' \\ \Theta\left((A^i)_{\sigma,\sigma'} - 1\right), \text{ otherwise} \end{cases} \tag{B.3}$$

with $\Theta(x)$ being the Heaviside function such that $\Theta(0) = 1$. The equation above demonstrates that the knowledge of A determines the rest of the adjacency matrices A_i.

B.3 Distribution of g for pbc

We start using the standard results of [98] about the spectrum of a random matrix with an external deterministic source. Consider a matrix M distributed according to

$$\text{Pro}(M) = \exp[-n \,\text{Tr}[V(M) - AM]]\,, \tag{B.4}$$

where V is the potential and A is a deterministic matrix that we can assume to be diagonal without loss of generality $A = \text{diag}(a_1, \ldots, a_n)$. Then, the eigenvalues $\{w_1, \ldots, w_n\}$ of M follow the joint probability distribution

$$\text{Pro}(w_1, \ldots, w_n) = \frac{1}{Z_n} \det\left(w_\alpha^{k-1}\right)_{\alpha,k=1}^{n} \det(e^{n a_k w_\alpha})_{\alpha,k=1}^{n} \prod_{\alpha=1}^{n} e^{-nV(w_\alpha)}\,, \tag{B.5}$$

where the constant Z_n enforces normalisation. For Eq. (3.166), one sets

$$M = \sqrt{xn} H + xB\,, \tag{B.6}$$

where H and B are as defined in the main text, which is equivalent to choosing in Eq. (B.5)

$$V(M) = \frac{M^2}{2xn}\,, \qquad A = \frac{B}{n}\,, \tag{B.7}$$

leading to

$$\text{Pro}(w_1, \ldots, w_n) = \frac{1}{Z_n} \det\left(w_\alpha^{k-1}\right)_{\alpha,k=1}^{n} \det\left(e^{-(k-1/2)w_\alpha}\right)_{\alpha,k=1}^{n} e^{-\sum_{\alpha=1}^{n} \frac{w_\alpha^2}{2x}}\,. \tag{B.8}$$

We are interested in computing the moments of $\mathrm{Tr}\left[e^{M}\right]$, i.e.

$$\Omega_k(x) := \left\langle \left(\sum_\alpha e^{w_\alpha}\right)^k \right\rangle = \int dw_1 \dots dw_n \, \mathrm{Pro}(w_1,\dots,w_n) \left(\sum_\alpha e^{w_\alpha}\right)^k . \tag{B.9}$$

The calculation will be analogous to [97], but we report it here with the appropriate notation and normalisations for convenience. As a proxy for the calculation of $\Omega_k(x)$, we first introduce Schur's polynomials. To an integer partition $\rho = (\rho_1,\dots,\rho_n)$ of the integer $k = \sum_{j=1}^n \rho_j$, with $\rho_1 \geq \rho_2 \geq \dots \geq \rho_n \geq 0$, one associates the corresponding Schur polynomial in n variables $y_1,\dots,y_n$ via [128]

$$s_\rho(y) := \frac{\det\left(y_\alpha^{\rho_j+n-j}\right)_{j,\alpha=1}^n}{\det\left(y_\alpha^{k-1}\right)_{k,\alpha=1}^n} = \frac{\det\left(y_\alpha^{h_j}\right)_{j,\alpha=1}^n}{\det\left(y_\alpha^{k-1}\right)_{k,\alpha=1}^n} , \tag{B.10}$$

where we denote $h_j \equiv \rho_j + n - j$. Schur polynomials are symmetric and homogeneous of degree k. Setting $y_\alpha = e^{w_\alpha}$ and using the Vandermonde determinant formula

$$\det\left(y_\alpha^{k-1}\right)_{\alpha,k=1}^n = \prod_{\alpha<\beta}(y_\beta - y_\alpha) , \tag{B.11}$$

we can deduce

$$(-1)^{n(n-1)/2} e^{(n-1/2)\sum_\alpha w_\alpha} \det\left(e^{-(k-1/2)w_\alpha}\right)_{\alpha,k=1}^n = \det\left(e^{(k-1)w_\alpha}\right)_{\alpha,k=1}^n , \tag{B.12}$$

which allows us to express the average as

$$\langle s_\rho(y=e^w)\rangle = \frac{(-1)^{n(n-1)/2}}{Z_n} \int dw_1 \dots dw_n \det\left(w_\alpha^{k-1}\right)_{\alpha,k=1}^n \det\left(e^{w_\alpha(h_j-n+1/2)}\right)_{j,\alpha=1}^n e^{-\sum_{\alpha=1}^n \frac{w_\alpha^2}{2x}} . \tag{B.13}$$

We can use Andreief identity [129] to express it in terms of a single determinant

$$\langle s_\rho(y)\rangle = \frac{(-1)^{n(n-1)/2}(2\pi x)^{n/2} n!}{Z_n} \det\left(I_{k,\rho_j-j+1/2}\right)_{k,j=1}^n , \tag{B.14}$$

where we defined

$$I_{k,\ell} = \int_{-\infty}^{\infty} \frac{dw}{\sqrt{2\pi x}} w^{k-1} e^{\ell w - \frac{w^2}{2x}} = \partial_\mu^{k-1}\left[e^{x\mu^2/2}\right]\Big|_{\mu=\ell} = \left(-i\sqrt{\frac{x}{2}}\right)^{k-1} e^{\ell^2 x/2} H_{k-1}\left(i\ell\sqrt{x/2}\right) , \tag{B.15}$$

and in the last equality we used the Hermite polynomials $H_p(z) = (-1)^p e^{z^2}\partial_z^p[e^{-z^2}]$. Note that in these conventions, the leading coefficient is $H_p(z) = 2^p z^p + O(z^{p-1})$.

Thus, by using the properties of determinants, we can combine the rows to extract only the leading coefficient out of each Hermite polynomials, obtaining

$$\det\left[I_{k,\rho_j-j+1/2}\right]_{k,j=1}^{n} = x^{n(n-1)/2}\exp\left[\frac{x}{2}\sum_j(\rho_j-j+1/2)^2\right]\det\left[(\rho_j-j+1/2)^{k-1}\right]. \tag{B.16}$$

This last determinant is once again a Vandermonde one which can be expressed via Eq. (B.11). We can now plug this back in Eq. (B.14) and fix the normalization Z_n using that for the trivial partition of 0, $\rho_1 = \rho_2 = \ldots \rho_n = 0$, so that $s_{\rho=0}(y) = 1$ identically. We finally obtain

$$\langle s_\rho(y)\rangle = \exp\left[\frac{x}{2}\sum_j(\rho_j-j+1/2)^2-(j+1/2)^2\right]s_\rho(1)\,, \tag{B.17}$$

where we recognized the equality

$$\prod_{1\le j<j'\le n}\frac{\rho_j-\rho_{j'}-j+j'}{j'-j} = s_\rho(y_1=1,\ldots,y_n=1)\,, \tag{B.18}$$

which expresses the number of semistandard Young diagram of shape ρ and n entries [128]. Eq. (B.17) is consistent with the fact that for $x = 0$, the distribution Eq. (B.8) reduces to $\mathrm{Pro}(w_1,\ldots,w_n) = \prod_\alpha \delta(w_\alpha)$ as the matrix M vanishes identically. Then, using the identity [128]

$$\sum_j(j-1)\rho_j = \frac{1}{2}\sum_i\rho_j^{\mathrm{t}}(\rho_j^{\mathrm{t}}-1)\,, \tag{B.19}$$

with ρ^{t} the dual partition of ρ, we obtain that

$$\frac{1}{2}\sum_j(\rho_j-j+1/2)^2-(j+1/2)^2 = \nu(\rho)\,, \tag{B.20}$$

as defined in Eq. (3.147). Now, we can relate the average of Schur polynomials to $M_k(x)$ using (see Eq. 3.10 in [130])

$$\Big(\sum_\alpha y_\alpha\Big)^k = \sum_{\rho\vdash k}\dim(\rho)s_\rho(y) \quad\Rightarrow\quad M_k(x) = \sum_{\rho\vdash k}\dim(\rho)e^{x\nu(\rho)}s_\rho(1)\,. \tag{B.21}$$

Finally, we consider the limit of large n. We have the standard identity (see Example 5, page 46 in [128])

$$\lim_{n\to\infty}\frac{s_\rho(1)}{n^k} = \frac{\dim(\rho)}{k!}\,, \tag{B.22}$$

which leads to the final result employed in the main text

$$\mathbb{E}(g^k) = \lim_{n\to\infty} \frac{M_k(x)}{n^k} = \frac{1}{k!} \sum_{\rho\vdash k} \dim(\rho)^2 e^{x\nu(\rho)} \,. \tag{B.23}$$

B.4 Numerical Simulations

In this section, we present additional numerical results related to the temporal-random and Floquet variations of the two models, RPM and BWM.

B.4.1 Temporal-Random Circuits

In this part we present the models with the local gates of the dynamics being chosen randomly in time and space. In Sec. 3.2.4, we established the convergence to the theory of the RPM and BWM under periodic (pbc) and open (obc) boundary conditions. Here, we further support our findings by demonstrating consistency with theoretical predictions under complementary boundary conditions, as illustrated in Fig. B.1. Figure B.2 explicitly confirms the universality of the Thouless scaling limit, as predicted by our theoretical framework. The numerical results presented in this paper were obtained as follows:

- *RPM*: Simulations were performed in the time direction for systems with a maximum size of $L_{\max} = 20$ and up to a maximum time of $t_{\max} = 20$, with an effective coupling strength $\epsilon = 1$ and $q = 2$. The system's dynamics were computed using the transfer matrix in the time direction. The single-time step transfer matrix at time t' consists of two layers, $\mathcal{U}(t') = \mathcal{U}_2(t')\mathcal{U}_1(t')$, where $\mathcal{U}_1(t'), \mathcal{U}_1(t')$ represent the layer of single site and two site gates respectively (as detailed in Sec. 3.2.4), applied iteratively for t steps. The resulting states, $|\Psi(t)\rangle = \left(\prod_{t'\le t} \mathcal{U}(t')\right) |\Psi_0\rangle \equiv |\Psi\rangle$, were then used to produce the overlap of two statistically independent states and thus generate the ensemble of $w' = \mathcal{N} |\langle\Psi|\Psi'\rangle|^2$ for a sample size of $N_{\text{sample}} = 1.5 \times 10^6$.

- *BWM*: The ensemble w was generated using the same approach as for RPM, with $q = 2$, $L_{\max} = 20$, $t_{\max} = 20$, but the local gate $u_{j,j+1}(t)$ acting on site j at time t is drawn from the circular unitary ensemble (CUE). The single time step dynamics are created by two layers of $u_{j,j+1}$, an even and an odd one as indicated in Fig. 3.3(a). The BWM model presents a greater numerical challenge due to the rapid growth of $L_{\text{Th}}(t)$ overtime, as shown in Fig. B.1 and Fig. 3.6 (in

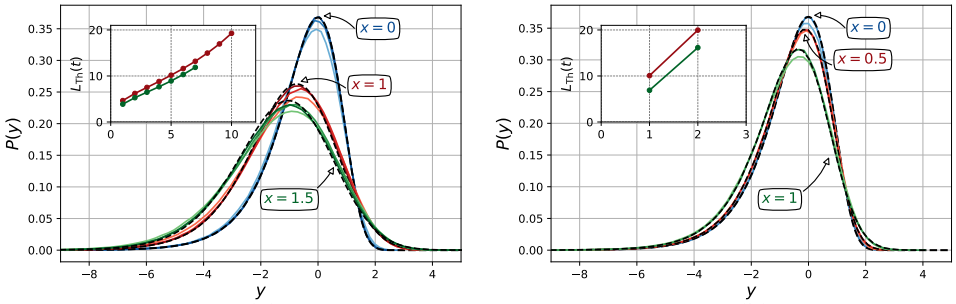

FIGURE B.1: Convergence of the numerical distributions (colored lines) to the theoretical ones (black-dashed line). (a): The obc numerical simulations of the RPM. For $x = 0$, we provide data for $(t, L) \in \{(10,6),(15,6),(20,6)\}$; for $x = 1$, $(t, L) \in \{(3,8),(5,10),(10,19)\}$; and for $x = 1.5$, $(t, L) \in \{(3,10),(5,13),(7,18)\}$. (b): pbc numerical simulations for the BWM at $q = 2$ and up to $L_{\max} = 20$, $t_{\max} = 20$. We provide data for $x = 0$ at $(t, L) \in \{(3,15),(5,15)\}$; for $x = 0.5$ at $(t, L) \in \{(1,5),(2,10)\}$; for $x = 1$ at $(t, L) \in \{(1,7),(2,16)\}$. Figure taken by [37].

the main text). To manage this, we used the spatial transfer matrix method for simulating $\langle \Psi | \Psi' \rangle$ with $L_{\max} = 120$ and $t_{\max} = 5$. This method was specifically applied to the obc case, as the pbc scenario requires even more computational resources, reaching up to $t_{\max} = 2$.

The theoretical distributions of the random variable $y = \log w'$ were obtained using equations Eq. (3.164) and Eq. (3.166) (in the main text) for obc and pbc, respectively. This analysis was conducted for $N_{\text{sample}} = 10^6$ at $x = 0, 0.5, 1, 1.5$. Figure B.3(a) illustrates that in the obc scenario, the theoretical distribution exhibits robust n-convergence at $n = 300$, which was used for numerical comparison. In Fig. B.3(b), we highlight the differences between the distributions for different boundary conditions. The Thouless length $L_{\text{Th}}(t)$ in our simulations was determined as $L_{\text{Th}}(t) = L_{\text{int}}(t)/x$, where $L_{\text{int}}(t)$ denotes the system size at which the numerical estimate of $\mathbb{E}[y]_{\text{sim}}(L = L_{\text{int}}(t), t)$ aligns with the theoretical prediction $\mathbb{E}[y]_{\text{RPM/BWM}}$ for a given time t and value of x. The consistency of $L_{\text{Th}}(t)$ estimates across different values of x reinforces the robustness of our approach.

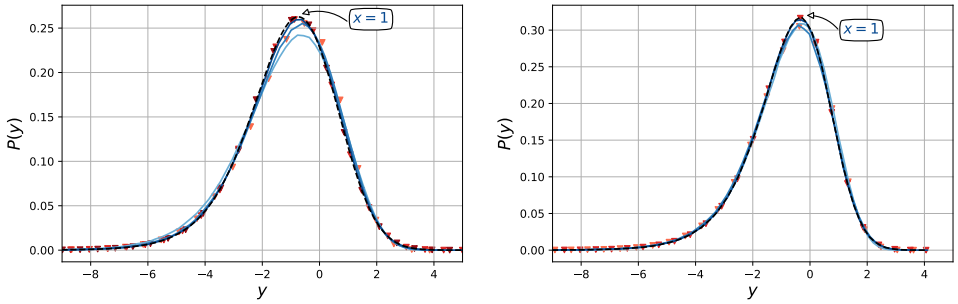

(a) (b)

FIGURE B.2: Convergence of the RPM (blue curves) and BWM (coloured triangles) models to the same scaling limit (black dashed curve) for $x = 1$. (a) The obc numerical simulations of RPM at $(t, L) \in \{(3,8), (5,10), (10,19)\}$ and of BWM at $(t, L) \in \{(1,8), (3,40), (4,88)\}$; (b) The pbc numerical simulations of RPM at $(t, L) \in \{(3,6), (5,9), (10,17)\}$ and of BWM at $(t, L) \in \{(1,7), (2,16)\}$. Figure taken by [37]

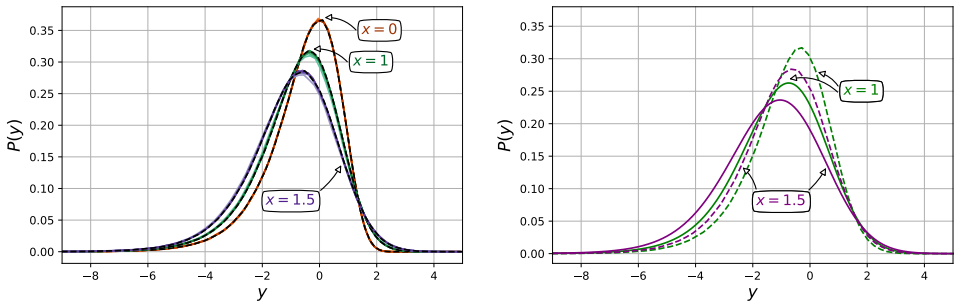

(a) (b)

FIGURE B.3: (a) The convergence in n for the pbc theoretical prediction of $P(y)$, which was found via Eq. (3.166) (in the main text). The lines of the same colour correspond to $n = \{10, 25, 50, 100, 150\}$ from lighter to darker shades, with the black dashed line corresponding to $n = 300$. (b) Comparison of the theoretical distributions for obc (solid curves) and pbc (dashed curves) at $x = 1, 1.5$. Figure taken from [37].

B.4.2 Floquet Circuits

Here, we present our numerical results for Floquet circuits, where the local gate $u_{j,j+1}(t) = u_{j,j+1}$ and the layers $\mathcal{U}_1, \mathcal{U}_2$ remains common across time steps t and is drawn randomly for both RPM and BWM models for different sites. Figure B.4 shows the convergence of the Floquet BWM model to our theoretical predictions, while the Floquet RPM at $q = 2$ does not exhibit convergence to the theoretical expectations. This observation is consistent with previous studies [39, 131], which suggest that the $q = 2$ Floquet RPM may display characteristics of a many-body localized (MBL) phase, except at large effective coupling ϵ. In the MBL phase, the quasi local conserved charges hinder scrambling, invalidating the coarse-grained picture

$\tilde{G}_a$ of the transfer matrix in the spatial direction. Moreover, the complete scrambled regions in the coarse grained picture are not expected to grow unbounded and thus the same behaviour is expected for the Thouless length, as well as hindering of the exponential its growth (see inset of Fig. B.4(a)).

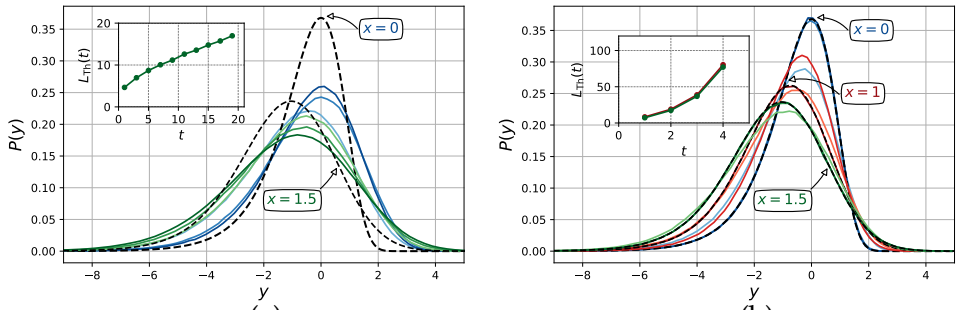

FIGURE B.4: The numerical distributions for the Floquet circuits (a): RPM with obc, $q = 2, \epsilon = 1, L_{\max} = 20$, and $t_{\max} = 20$. We present the distributions for $x = 0$ at $(t, L) \in \{(5,8), (10,8), (20,8)\}$; for $x = 1.5$ at $(t, L) \in \{(11,11), (13,14), (15,17)\}$. (b) BWM with obc, $q = 2$ for $x = 0$ at $(t, L) \in \{(1,6), (3,6), (5,6)\}$; for $x = 1$ at $(t, L) \in \{(1,8), (3,19), (4,80)\}$; for $x = 1.5$ at $(t, L) \in \{(1,11), (3,55), (4,116)\}$. Figure taken by [37].

Appendix C

Universal out of equilibrium dynamics

C.1 Fokker-Planck equation

In this section we derive the Fokker-Planck equation (4.50) of the text, for the joint PDF of the backward stochastic trajectories $x_1 = X_t^+(y_1), \dots, x_n = X_t^+(y_n)$ associated to the Langevin equation (4.47). We thus consider only a given chirality, here we choose $+$, but the same Fokker-Planck equation holds for the chirality $-$, with $v \to -v$. We do not consider here the joint PDF of both chiralities. So here we denote simply $X_t^+ \to X_t$.

One can show that Eq. (4.47) translates into a stochastic equation for the variable $X_t(y_i)$ as a function of t which takes the form (see Eq. (58-59) in Supp. Mat. of [116])

$$dX_t(y_i) = \frac{v^2}{2} X_t''(y_i) f(0) dt - X_t'(y_i) v \big(dt + d\mathsf{W}_t(y_i)\big) \tag{C.1}$$

where $dX_t(y_i) = X_{t+dt}(y_i) - X_t(y_i)$. The $\mathsf{W}_t(y_i)$ are mutually correlated Wiener processes in time t, which relates to the noise in Eq. (4.40) and Eq. (4.47) via

$$\mathsf{W}_t(y) = \int_0^t ds\, \eta(y,s)\,, \quad \overline{d\mathsf{W}_t(y) d\mathsf{W}_t(y')} = dt f(y-y') \tag{C.2}$$

Here $d\mathsf{W}_t(y) = \mathsf{W}_{t+dt}(y) - \mathsf{W}_t(y)$ and $f(y)$ is the noise correlation function defined in the text.

Consider an arbitrary smooth function of n-variables $G(x_1, \dots, x_n)$. In the case of these variables being the backward stochastic trajectories $x_i = X_t(y_i)$ of Eq. (4.47), we define:

$$g_t(y_1 \dots y_n) = G\big(X_t(y_1) \dots X_t(y_n)\big) \tag{C.3}$$

By Ito calculus the time variation $dg_t = g_{t+dt} - g_t$ of this observable is obtained by expanding up to second order.

$$dg_t = \sum_{j=1}^{n} \partial_j G\big(X_t(y_1), \dots, X_t(y_n)\big) dX_t(y_j) + \frac{1}{2} \sum_{j,m=1}^{n} \partial_j \partial_m G\big(X_t(y_1), \dots, X_t(y_n)\big) dX_t(y_j) dX_t(y_m) \tag{C.4}$$

Here we shortened the notation setting $\partial_{x_j} \dots \partial_{x_m} G(x_1 \dots x_n) = \partial_j \dots \partial_m G(x_1 \dots x_n)$. Using Eq. (C.1) and Eq. (C.2), we derive

$$dX_t(y_i)\, dX_t(y_j) = v^2 X_t'(y_i) X_t'(y_j) f(y_i - y_j) dt + O(dt^{3/2}) \,. \tag{C.5}$$

Averaging over the noise we obtain

$$\frac{d\overline{g_t}}{dt} = -v \sum_{j=1}^{n} \overline{\partial_j G\big(X_t(y_1), \dots, X_t(y_n)\big) X_t'(y_j)} + \frac{v^2 f(0)}{2} \sum_{j=1}^{n} \overline{\partial_j G\big(X_t(y_1), \dots, X_t(y_n)\big) X_t''(y_j)} + \\ + \frac{v^2}{2} \sum_{j,m=1}^{n} f(y_j - y_m) \overline{\partial_j \partial_m G\big(X_t(y_1), \dots, X_t(y_n)\big) X_t'(y_j) X_t'(y_m)} \tag{C.6}$$

From the chain rule for the derivation with respect to the variables $\{y_i\}$ it is easy to check that

$$\partial_{y_j} \partial_{y_m} g_t = X_t'(y_j) X_t'(y_m) \partial_j \partial_m G + \delta_{j,m} X_t''(y_j) \partial_j G \tag{C.7}$$

which finally leads to:

$$\frac{d\overline{g_t}}{dt} = \Big[-v \sum_{j=1}^{n} \partial_{y_j} + \frac{v^2}{2} \sum_{j,m=1}^{n} f(y_j - y_m) \partial_{y_j} \partial_{y_m} \Big] \overline{g_t} \,. \tag{C.8}$$

It is useful to re-express Eq. (C.8) in terms of the Fokker-Planck Hamiltonian (and its hermitian adjoint). In order to do so, we introduce the operators q_j and p_j, defined by their action on any smooth function $\omega(\mathbf{y})$ as $q_j \cdot \omega(\mathbf{y}) = y_j \omega(\mathbf{y})$ and $p_j \cdot \omega(\mathbf{y}) = -\imath \partial_j \omega(\mathbf{y})$. For these conjugate variables the canonical quantization holds $[q_i, p_j] = \imath \delta_{i,j}$. We can then define

$$\mathcal{H}_{\mathrm{FP}} \equiv -\mathrm{i}v \sum_{i=1}^{n} p_i + \frac{v^2}{2} \sum_{ij} p_i p_j f(q_i - q_j) \,, \tag{C.9}$$

so that we can rewrite

$$\frac{d\overline{g_t}}{dt} = -\mathcal{H}_{\mathrm{FP}}^{\dagger} \cdot \overline{g_t} \,, \qquad \mathcal{H}_{\mathrm{FP}}^{\dagger} \equiv \mathrm{i}v \sum_{i=1}^{n} p_i + \frac{v^2}{2} \sum_{ij} f(q_i - q_j) p_i p_j \,. \tag{C.10}$$

To deduce the Fokker-Planck equation for $P(\mathbf{x}|\mathbf{y})$, defined in the text, we need one more step. From the definition of $P(\mathbf{x}|\mathbf{y})$, we have

$$\overline{g_t(\mathbf{y})} = \int d\mathbf{x}' \; G(\mathbf{x}') P_t(\mathbf{x}'|\mathbf{y}) \tag{C.11}$$

We can choose $G(\mathbf{x}') = \delta_\epsilon(\mathbf{x}' - \mathbf{x})$, where $\delta_\epsilon(\mathbf{x})$ is a mollifier of the Dirac delta function. In the limit $\epsilon \to 0$, we recover $\overline{g_t(\mathbf{y})} \to P_t(\mathbf{x}|\mathbf{y})$ the jpdf for the initial points $\mathbf{x} = (x_1, \ldots, x_n)$ of the stochastic trajectories and finally deduce from Eq. (C.10)

$$\partial_t P_t(\mathbf{x}|\mathbf{y}) = -\mathcal{H}^T_{\rm FP}[\mathbf{y}] \cdot P_t(\mathbf{x}|\mathbf{y}) \tag{C.12}$$

This equation can be formally solved starting from the initial condition at $t = 0$ is $P_{t=0}(\mathbf{x}|\mathbf{y}) = \delta(\mathbf{x} - \mathbf{y})$. It is useful to employ the bra $\langle \mathbf{y}|$ and ket $|\mathbf{x}\rangle$ notation for the eigenstates of the position operators $\hat{q}_j$. Then, we can represent the probability distribution as:

$$P_t(\mathbf{x}|\mathbf{y}) \equiv \left\langle \mathbf{y}|e^{-t\mathcal{H}^\dagger_{\rm FP}}|\mathbf{x}\right|\left.\mathbf{y}|e^{-t\mathcal{H}^\dagger_{\rm FP}}|\mathbf{x}\right\rangle = \left\langle \mathbf{x}|e^{-t\mathcal{H}_{\rm FP}}|\mathbf{y}\right|\left.\mathbf{x}|e^{-t\mathcal{H}_{\rm FP}}|\mathbf{y}\right\rangle \tag{C.13}$$

where the last equality follows from the hermitian conjugation. Therefore, the following equation must also holds:

$$\partial_t P_t(\mathbf{x}|\mathbf{y}) = -\mathcal{H}_{\rm FP}[\mathbf{x}] \cdot P_t(\mathbf{x}|\mathbf{y}) \tag{C.14}$$

where the action of the differential operator $\mathcal{H}_{\rm FP}[\mathbf{x}]$ is now over the variables $\mathbf{x}$. More explicitly using Eq. (C.9), we arrive at

$$\partial_t P_t(\mathbf{x}|\mathbf{y}) = v\left(\sum_{i=1}^n \partial_i + \frac{v}{2}\sum_{i,j=1}^n \partial_i\partial_j f(x_i - x_j)\right) P_t(\mathbf{x}|\mathbf{y}) \; . \tag{C.15}$$

which coincides with Eq. (4.50) given in the main text.

C.2 Analysis of the short distance regime for κ

In the limit $\ell \ll 1$, one has Eq. (4.65) in the main text that we report for convenience

$$dr = rvdB_1 \quad , \quad d\kappa = -\frac{\ell^2}{6} r^2 v(-\frac{v}{2} f^{(4)}(0)dt + dB_2) \tag{C.16}$$

$$\overline{dB_1 dB_1} = -f''(0)dt \quad , \quad \overline{dB_2 dB_2} = -f^{(6)}(0)dt \quad , \quad \overline{dB_1 dB_2} = -f^{(4)}(0)dt \tag{C.17}$$

We will now show from these equations, that κ satisfies a closed SDE which leads to the stationary measure given in the main text. We first of all solve the equation for the variable r, which takes the form

$$r(t) = \exp\left[vB_1(t) + \frac{1}{2}v^2 f''(0)t\right] \tag{C.18}$$

Injecting this solution in the equation for κ and integrating in time we arrive at

$$\kappa(t) = -\frac{\ell^2}{6}\int_0^t e^{2vB_1(s)+v^2 f''(0)s} v\left(-\frac{v}{2} f^{(4)}(0)ds + dB_2(s)\right) \tag{C.19}$$

This equation gives already a closed representation for $\kappa(t)$.

We can further simplify Eq. (C.19) by making use of the following reparametrization: for each t, we define for $i = 1, 2$, $\tilde{B}_i(s') = B_i(t) - B_i(t - s')$, $s' \in [0, t]$, which is thus an equivalent Brownian process which measures the deviation from the final point $B_i(t)$ (which is kept fixed) of the original one. One clearly has $\tilde{B}_i(0) = B_i(0) = 0$, $\tilde{B}_i(t) = B_i(t)$ and $d\tilde{B}_i(s') = dB_i(t - s')$. We want now to rewrite Eq. (C.19) in terms of the processes $\tilde{B}_i$. A little bit of care is needed for the stochastic integral. Indeed, writing explicitly the Ito integral, we have

$$\begin{aligned}\int_0^t e^{2vB_1(s)+v^2 f''(0)s} dB_2(s) &= \lim_{n\to\infty} \sum_{i=0}^{n-1} e^{2vB_1(s_i)+v^2 f''(0)s_i}(B_2(s_{i+1}) - B_2(s_i)) = \\ &= e^{2v\tilde{B}_1(t)+v^2 f''(0)t} \lim_{n\to\infty} \sum_{j=1}^{n} e^{-2v\tilde{B}_1(\tilde{s}_j)-v^2 f''(0)\tilde{s}_j}(\tilde{B}_2(\tilde{s}_j) - \tilde{B}_2(\tilde{s}_{j-1}))\end{aligned} \tag{C.20}$$

where the s_i's are a partition of n elements of $[0, t]$, with $s_0 = 0$ and $s_n = t$. We have defined $\tilde{s}_j = t - s_i$ with $j = n - i$, which is an equivalent partition. Clearly, the last expression does not converge to a stochastic integral in the Ito form. We thus rewrite in the last term as

$$e^{-2v\tilde{B}_1(\tilde{s}_j)} = e^{-2v\tilde{B}_1(\tilde{s}_{j-1})} e^{-2v(\tilde{B}_1(\tilde{s}_j) - \tilde{B}_1(\tilde{s}_{j-1}))} \tag{C.21}$$

and then expand the second exponential, using $(\tilde{B}_1(\tilde{s}_j) - \tilde{B}_1(\tilde{s}_{j-1}))(\tilde{B}_2(\tilde{s}_j) - \tilde{B}_2(\tilde{s}_{j-1})) = -f^{(4)}(0)(\tilde{s}_j - \tilde{s}_{j-1})$. We then arrive at

$$\int_0^t e^{2vB_1(s)+v^2f''(0)s}dB_2(s) = e^{2v\tilde{B}_1(t)+v^2f''(0)t}\left[\int_0^t e^{-2v\tilde{B}_1(s)-v^2f''(0)s}d\tilde{B}_2(s) + 2vf^{(4)}(0)\int_0^t e^{-2v\tilde{B}_1(s)-v^2f''(0)s}ds\right] \tag{C.22}$$

Applying these transformations to Eq. (C.19) we obtain

$$\kappa(t) = \underbrace{-\frac{\ell^2}{6}e^{2v\tilde{B}_1(t)+v^2f''(0)t}}_{\kappa_1}\underbrace{\int_0^t e^{-2v\tilde{B}_1(s)-v^2f''(0)s}v\left(\frac{3v}{2}f^{(4)}(0)ds + d\tilde{B}_2(s)\right)}_{\kappa_2} \tag{C.23}$$

Using Ito's lemma, $d\kappa = \kappa_2 d\kappa_1 + \kappa_1 d\kappa_2 + d\kappa_1 d\kappa_2$, which, after collecting different contributions, leads to

$$d\kappa = v^2\left(\frac{\ell^2}{12}f^{(4)}(0) - f''(0)\kappa\right)dt - \frac{\ell^2 v}{6}d\tilde{B}_2(t) + 2vd\tilde{B}_1(t)\kappa \tag{C.24}$$

The correlations of the $d\tilde{B}_j(t)$ are the same as the ones of the $dB_j(t)$ in Eq. (C.17). However, $\kappa(t)$ defined by Eq. (C.23) is a *different process* in t than $\kappa(t)$ defined by Eq. (C.19). At fixed t the two random variables have the same law, but as t is varied the trajectories are different (since the relation between $\tilde{B}_i$ and B_i involves t explicitly). As a consequence, the two stochastic equations Eq. (C.24) and Eq. (C.19) are inequivalent although they lead to the same single-time distribution for $\kappa(t)$. One illustration of that is that while the second process converges, i.e. $\kappa(t) \to \kappa_\infty$, where the distribution of κ_∞ is given below, the first process is ergodic (with the same law). A simpler example, which allows to understand better this point (using more explicit notations) is worked out in the remark below.

We can recast Eq. (C.24) as an equation with a single Brownian process dB (we are using that $a_1dB_1 + a_2dB_2 = \sqrt{-a_1^2f''(0) - a_2^2f^{(6)}(0) - 2a_1a_2f^{(4)}(0)}d\tilde{B}$, where $d\tilde{B}$ is a new Wiener process with standard normalization, $d\tilde{B}^2 = dt$)

$$d\kappa = v^2\left(\frac{\ell^2}{12}f^{(4)}(0) - f''(0)\kappa\right)dt + \frac{vd\tilde{B}}{6}\sqrt{-\left(\ell^4f^{(6)}(0) - 24\ell^2f^{(4)}(0)\kappa + 144f''(0)\kappa^2\right)} \tag{C.25}$$

With the change of variable $\kappa = \kappa_0(\omega/\omega_0 - 1)$ where we defined as in the main text

$$\kappa_0 = -\frac{\ell^2}{12}\frac{f^{(4)}(0)}{f''(0)}, \qquad \omega_0 = \frac{1}{\sqrt{\frac{f^{(6)}(0)f''(0)}{f^{(4)}(0)^2} - 1}} \tag{C.26}$$

Note that ω_0 is real and positive as it is guaranteed by the positivity of the Fourier transform $\hat{f}(k) > 0$ of $f(x)$. Indeed,

$$f^{(6)}(0)f''(0) - f^{(4)}(0)^2 = \int k^2 \hat{f}(k) \int k^6 \hat{f}(k) - \left(\int k^4 \hat{f}(k) \right)^2 > 0 \tag{C.27}$$

which is a consequence of the Cauchy-Schwartz inequality.

The SDE for ω becomes Eq. (4.72), which is solved by

$$\omega(t) = e^{\sqrt{8\theta}B(t) - 2\theta t} \left(\omega_0 + \sqrt{8\theta} \int_0^t e^{-\sqrt{8\theta}B(s) + 2\theta s} d\gamma_s \right) . \tag{C.28}$$

One recognises a Bougerol variable with drifted Brownian motion in the exponent [121]. It is useful to do the change of variable (4.72)

$$\omega = \sinh Y \quad , \quad Y = Y(\omega) = \text{argsinh}\omega \tag{C.29}$$

One has

$$Y'(\omega) = \frac{1}{\sqrt{1+\omega^2}} = \frac{1}{\cosh Y} \quad , \quad Y''(\omega) = -\frac{\omega}{(1+\omega^2)^{3/2}} \tag{C.30}$$

and from Ito's rule, it follows Eq. (4.75) in the main text.

Remark We presented a method to transform the random variable Eq. (C.19) expressed as an integral into the solution of the stochastic process (C.25). As mentioned above, the two describe random variables having the same single-time distribution, but they differ as stochastic processes, i.e. in the way the realisation at time t and $t + dt$ are connected. In particular, Eq. (C.19) almost surely has a fixed limit $\kappa(t \to \infty)$ for each realisation, while the latter is ergodic (being equivalent to a Langevin equation Eq. (4.72)). Nevertheless, the distribution of $\kappa(t \to \infty)$ over the noise realisations is the same in the two cases. To further clarify the aspect, we have included a self-contained minimal example of this mechanism where we make the notation more explicit. Consider the process

$$Z_t = \int_0^t ds e^{B(s) - s/2} \tag{C.31}$$

where $B(s)$ is a standard Wiener process with $B(0) = 0$. Since $B(s)$ is almost surely subleading with respect to $s/2$, for each realisation of $B(s)$ the limit $Z_\infty = \lim_{t \to +\infty} Z_t$ exists almost surely. The value of Z_∞ changes from realisation to realisation and is

thus a random variable. On the other end, as in the previous discussion, we define at fixed t $\tilde{B}_t(s) = B(t) - B(t-s)$, which is also a standard Wiener process. Here t denotes the time around which the Brownian has been reflected, is indicated for clarity as a subscript. One can now write

$$Z(t) = \int_0^t ds' e^{B(t-s')-t/2+s'/2} = e^{-t/2+\tilde{B}_t(t)} \int_0^t ds' e^{-\tilde{B}_t(s')+s'/2} = \tilde{Z}_t(s)|_{s=t} \tag{C.32}$$

where we have defined

$$\tilde{Z}_t(s) = e^{-s/2+\tilde{B}_t(s)} \int_0^s ds' e^{-\tilde{B}_t(s')+s'/2} \tag{C.33}$$

This is a new process for $s \in [0,t]$ which obeys the following stochastic equation

$$d\tilde{Z}_t(s) := \tilde{Z}_t(s+ds) - \tilde{Z}_t(s) = ds + \tilde{Z}_t(s) d\tilde{B}_t(s) \tag{C.34}$$

where $\tilde{Z}_t(0) = 0$. By running this equation until $s = t$, we can recover $Z(t)$ via Eq. (C.32). We can solve this stochastic equation setting $Q_t(s) = \ln Z_t(s)$. One has

$$dQ_t(s) = d\tilde{B}_t(s) + \left(e^{-Q_t(s)} - \frac{1}{2}\right) dt = -V'(Q_t(s))ds + d\tilde{B}_t(s) \tag{C.35}$$

with $V(Q) = e^{-Q} + Q/2$. This last equation is of Langevin type and it implies a stationary distribution at large $s = t \to \infty$ for Q_∞ and Z_∞

$$P(Q_\infty) = Ce^{-2V(Q_\infty)} \quad \Rightarrow \quad P(Z_\infty) = \frac{C}{Z^2} e^{-2/Z} \tag{C.36}$$

which leads to the known inverse gamma distribution for Z_∞. Note that we have chosen t sufficiently large so that the stationary measure has been reached when $s = t$.

C.3 Stationary measure for κ for any finite ℓ

C.3.1 Backward method

We now apply the backward method to the full stochastic equation for $r(t), \kappa(t)$ in Eq. (4.61). As explained in the main text, we define

$$Q_k(r_0, t) \equiv \overline{e^{-ik\kappa(t)}}^{r_0} \tag{C.37}$$

where the superscript $r_0 = r(t=0)$ indicates the initial condition for the variable r. In the end we will set $r_0 = 1$ as it is required in our case, but it is useful to keep it free. One has

$$Q_k(r_0, t+dt) = \overline{e^{-ik(v^2 g(r_0)dt + v\, dW_2(0))} Q(r_0 + v dW_1(0), t)}^{r_0} \tag{C.38}$$

expanding with Ito's lemma and averaging we arrive at

$$\partial_t Q_k = v^2 \left(A_\ell(r)\partial_r^2 - ikB_\ell(r)\partial_r - k^2 C_\ell(r) - ikg_\ell(r) \right) Q_k(r,t) \, . \tag{C.39}$$

with the boundary conditions

$$Q_k(r_0, 0) = 1 \quad , \quad Q_k(r_0 = 0, t) = 1 \quad , \quad \lim_{r_0 \to +\infty} Q_k(r_0, t) = e^{-2\theta(k^2 + ik)t} \tag{C.40}$$

and we recall that

$$\begin{aligned} A_\ell(r) = \frac{f(0) - f(\ell r)}{\ell^2} \, , \, B_\ell(r) = 2\frac{f'(\ell r)}{\ell} + 4\frac{f(0) - f(\ell r)}{\ell^2 r} \\ C_\ell(r) = 4\frac{f(0) - f(\ell r) + \ell r f'(\ell r)}{\ell^2 r^2} - f''(0) - f''(\ell r) \\ g_\ell(r) = -f''(0) - 2\frac{f(0) - f(\ell r)}{\ell^2 r^2} \end{aligned} \tag{C.41}$$

The second condition in Eq. (C.40) comes from the fact that $d\kappa = 0$ and $dr = 0$ for $r = 0$ since $g(0) = 0$ and $C(0) = 0$. The third condition is obtained using the fact that the dynamics of κ is pure diffusion at large r_0.

Let us denote $Q_k(r)$ the stationary solution of Eq. (C.39). It thus satisfies

$$A_\ell(r) Q_k''(r) - ikB_\ell(r) Q_k'(r) - (k^2 C_\ell(r) + ikg_\ell(r)) Q_k(r) = 0 \tag{C.42}$$

with the boundary conditions

$$Q_k(r_0 = 0) = 1 \quad , \quad Q_k(r_0 \to +\infty) = 0 \tag{C.43}$$

From this stationary solution one obtains the stationary measure $P_{\text{stat}}(\kappa)$ for κ by Fourier inversion

$$P_{\text{stat}}(\kappa) = \int_{-\infty}^{+\infty} \frac{dk}{2\pi} e^{ik\kappa} Q_k(r=1) \tag{C.44}$$

C.3.2 Schrodinger equation for the stationary measure

We can further simplify Eqs. (C.40) and Eq. (C.42) by removing the first derivative term. This can be achieved setting

$$Q_k(r) = \phi_k(r) G_k(r) \, . \tag{C.45}$$

We choose $\phi_k(r)$ so that

$$\frac{\phi_k'(r)}{\phi_k(r)} = ik \frac{B(r)}{2A(r)} \quad , \quad \phi_k(r) = e^{ik \int_0^r dr' \frac{B(r')}{2A(r')}} = \left(\frac{\ell^2 r^2 f''(0)}{2(f(\ell r) - f(0))} \right)^{ik} = e^{ik\kappa_0(\ell r)} \tag{C.46}$$

where $\kappa_0(x)$ is defined in Eq. (4.84) of the main text. Then, one finds that $G_k(r)$ satisfies the Schrodinger equation

$$-G_k''(r) - k(k+i) V(r) G_k(r) = 0 \tag{C.47}$$

with the potential

$$V(r) = \frac{\ell^2 \left(f'(\ell r)^2 + (f(0) - f(\ell r)) \left(f''(\ell r) + f''(0) \right) \right)}{(f(0) - f(\ell r))^2} = -\frac{d^2}{dr^2} \log[f(0) - f(\ell r)] + \frac{\ell^2 f''(0)}{f(0) - f(\ell r)} \tag{C.48}$$

on the positive half-space $r \geq 0$ with the boundary condition inherited from Eq. (C.43)

$$G_k(0) = 1 \, , \qquad \lim_{r \to \infty} G_k(r) = 0 \, . \tag{C.49}$$

C.3.3 Proof of the right $3/2$–tail

Here, we show that for a smooth noise correlation $f(x)$, the right tail of the stationary distribution is always a power-law $P_{\rm stat}(\kappa) \propto \kappa^{-3/2}$ for $\kappa \to +\infty$, independently of ℓ. Thanks to Eq. (C.37), it is enough to prove the following expansion at small k for its Fourier transform

$$Q_k(r = 1) = 1 + C\sqrt{k} + O(k). \tag{C.50}$$

where C is a constant (see below). To prove Eq. (C.50), we proceed as follow. First of all, since $\phi_k(r)$ is analytic in k, using Eq. (C.45), we can focus on the small k expansion of $G_k(r)$. The small k behavior of the solution of Eq. (C.47) can be obtained setting $x = r\sqrt{\gamma}$, with $\gamma = k(k+i)$. Then, setting $G_k(r) = g(r\sqrt{\gamma})$, we can rewrite Eq.

(C.47) in the limit $k \to 0$ as

$$-g'(x) - V_\infty g(x) = 0 \quad \Rightarrow \quad g(x) = e^{-\sqrt{-V_\infty}x} \tag{C.51}$$

where we set $V_\infty = \lim_{r\to\infty} V(r)$ and enforced the boundary conditions Eq. (C.49). This implies

$$G_k(r) \sim g(r\sqrt{\gamma}) = e^{-\sqrt{-V_\infty \gamma}r}\,, \quad \forall r = O(\gamma^{-1/2}) \tag{C.52}$$

This is still not enough because we require the expansion Eq. (C.50) for $r = 1$. However, fixing $\delta > 0$ and r, we can write

$$|G_k'(r) - G_k'(\delta/\sqrt{\gamma})| = \left|\int_{\delta/\sqrt{\gamma}}^{r} dr' G_k''(r')\right| \leq \gamma \int_{\delta/\sqrt{\gamma}}^{r} dr' |V(r')G_k(r')| \leq K\gamma(r - \delta/\sqrt{\gamma}) \tag{C.53}$$

where we set $K = \sup_r |V(r)G_k(r)|$, which is finite for a sufficiently smooth $f(x) \in C^6$ fastly decaying at infinity. As a consequence, at small γ,

$$G_k'(r) = G_k'(\delta/\sqrt{\gamma}) + O(\delta\sqrt{\gamma}) = -\sqrt{-V_\infty\gamma}\,(g(\delta) + O(\delta)) \xrightarrow{\delta\to 0} -\sqrt{-V_\infty\gamma} + O(\gamma) \tag{C.54}$$

Finally, integrating over r

$$G_k(1) = 1 + \int_0^1 dr\; G_k'(r) = 1 - \sqrt{-V_\infty\gamma} + O(\gamma) \tag{C.55}$$

which proves Eq. (C.50) with $C = \sqrt{-V_\infty}$.

C.3.4 Small ℓ limit

At small ℓ one finds that the potential is a harmonic oscillator

$$V(r) = \frac{\ell^4 r^2 \left(f^{(4)}(0)^2 - f^{(6)}(0) f''(0)\right)}{36 f''(0)^2} + O(\ell^6 r^4) \tag{C.56}$$

and

$$\kappa_0 = \tilde{\kappa}_0 \ell^2 + O(\ell^4) \quad , \quad \tilde{\kappa}_0 = -\frac{f^{(4)}(0)}{12 f''(0)} \tag{C.57}$$

We see that κ_0 is $O(\ell^2)$ as $\ell \to 0$, so the random variable $\kappa = O(\ell^2)$ in this limit. Therefore, we can obtain a ℓ independent limit by scaling $k = \tilde{k}/\ell^2$. In terms of this

variable the potential term in the Schrodinger equation has a finite limit

$$-k(k+i)V(r) \simeq \frac{4\tilde{k}^2 r^2 \tilde{\kappa}_0^2}{\omega_0^2} \tag{C.58}$$

where we have defined as in the text

$$\omega_0 = \frac{1}{\sqrt{\frac{f''(0)f^{(6)}(0)}{f^{(4)}(0)^2} - 1}} \tag{C.59}$$

A solution of Eq. (C.47) with the potential Eq. (C.56) and the boundary conditions Eq. (C.49) can be expressed in terms of Bessel function as

$$G_k(r) = \frac{2^{3/4}}{\Gamma(1/4)} \left(\frac{\tilde{\kappa}_0|\tilde{k}|}{\omega_0}\right)^{1/4} \sqrt{r} K_{\frac{1}{4}}\left(\frac{|\tilde{k}| r^2 \tilde{\kappa}_0}{\omega_0}\right) \tag{C.60}$$

and the prefactor has been fixed imposing that $G_k(r=0) = 1$. This leads to

$$Q_k(r=1) = \frac{2^{3/4}}{\Gamma(1/4)} \left(\frac{\tilde{\kappa}_0|\tilde{k}|}{\omega_0}\right)^{1/4} e^{i\tilde{k}\tilde{\kappa}_0} K_{\frac{1}{4}}\left(\frac{|\tilde{k}|\tilde{\kappa}_0}{\omega_0}\right) \tag{C.61}$$

which allows to determine $P_{\text{stat}}(\kappa)$ by Fourier inversion from Eq. (C.44).

One can check that this coincides with the result in the text, identifying $\tilde{\kappa} = \tilde{\kappa}_0 \left(\frac{\omega}{\omega_0} - 1\right)$. Equivalently, we obtain the scaling form

$$P_{\text{stat}}(\kappa) \overset{\ell \ll 1}{\simeq} \frac{1}{\ell^2} \tilde{P}\left(\frac{\kappa}{\ell^2}\right), \qquad \tilde{P}(\tilde{\kappa}) \equiv \frac{C\omega_0}{\tilde{\kappa}_0} \left[1 + \omega_0^2 \left(\frac{\tilde{\kappa} + \tilde{\kappa}_0}{\tilde{\kappa}_0}\right)^2\right]^{-3/4} \tag{C.62}$$

and one can check that the Fourier transform of $\tilde{P}$

$$\int \frac{d\tilde{k}}{2\pi} e^{i\tilde{k}\tilde{\kappa}} \tilde{P}(\tilde{\kappa}) = Q_k(r=1) \tag{C.63}$$

as given in Eq. (C.61). This can be seen using the identity

$$\int dx e^{ikx} \frac{1}{(1+x^2)^{3/4}} = \sqrt{2\pi} \frac{(2|k|)^{1/4} K_{\frac{1}{4}}(|k|)}{\Gamma\left(\frac{3}{4}\right)} \tag{C.64}$$

$f(x)$	$V(r)/\ell^2$	$\hat{f}(k)$	Smoothness
$e^{-\lvert x\rvert}$	$\frac{1}{(1-e^{-r\ell})^2}$	$\frac{2}{1+k^2}$	C^0
$2e^{-\lvert x\rvert} - e^{-2\lvert x\rvert}$	$-\frac{2}{1-e^{-\ell r}}$	$\frac{12}{k^4+5k^2+4}$	C^2
$\frac{1}{\cosh x}$	$-\tanh(\ell r)^2$	$\frac{\pi}{\cosh(k\pi/2)}$	C^∞
$\frac{1}{(\cosh x)^2}$	$-2\tanh(\ell r)^2$	$\frac{\pi k}{\sinh(k\pi/2)}$	C^∞

TABLE C.1: A few examples of noise correlation functions $f(x)$ leading to Schrödinger equations with a solvable potential $V(r)$.

C.3.5 Large ℓ limit

At large ℓ, under the hypothesis that $f(x)$ and its derivatives decay at infinity, the potential term reaches a constant value

$$-k(k+i)V(r) \simeq -k(k+i)\ell^2\frac{f''(0)}{f(0)} \sim \frac{2i\tilde{k}\theta}{f(0)} \,. \tag{C.65}$$

where we used once again the scaling $k = \tilde{k}/\ell^2$, which implies again $\kappa = O(\ell^2)$, but with $\ell \to \infty$ in this case. From this potential, we immediately derive the solution respecting the boundary conditions Eq. (C.49) in the form

$$G_k(r) = e^{-\sqrt{2i\tilde{k}\theta/f(0)}r} \tag{C.66}$$

Note that at large ℓ

$$\kappa_0(\ell) \overset{\ell\to\infty}{=} \log\big(\ell^2(-f''(0))/2f(0)\big) \tag{C.67}$$

so that $k\kappa_0 \overset{\ell\to\infty}{\longrightarrow} 0$ and therefore $Q_k(r) = G_k(r)$. Inverting the Fourier transform Eq. (C.44), we obtain once again the stationary distribution

$$P_{\text{stat}}(\kappa) \overset{\ell\gg 1}{\simeq} \frac{1}{\ell^2}\tilde{p}\big(\frac{\kappa}{\ell^2}\big) \,, \qquad \tilde{p}(\tilde{\kappa}) \equiv \sqrt{\frac{\theta}{2\pi f(0)}}\frac{e^{-\frac{\theta}{2f(0)\tilde{\kappa}}}}{\tilde{\kappa}^{3/2}}\Theta(\tilde{\kappa}) \tag{C.68}$$

Equivalently, denoting $\kappa = \theta\ell^2\chi/f(0)$ one finds that χ is distributed according to $\mathcal{L}(\chi)$ in Eq. (4.88) in the text, i.e. the stable one sided Levy distribution of index $1/2$.

C.3.6 Solvable cases for $f(x)$

For some particular choice of the noise correlation function $f(x)$, the potential $V_k(r)$ takes a form which is explicitly integrable. In Table C.1, we list a few interesting cases. Here, we focus on the case

$$f(x) = 1/\cosh(x) \tag{C.69}$$

which is analytic and fastly decaying. Setting $\gamma = k(k+i)$, the solution $G_k(r)$ respecting the boundary conditions Eq. (C.49) can be expressed in terms of hypergeometric function

$$G_k(r) = e^{-\sqrt{\gamma}\ell r}(1+\tanh(\ell r))^{\sqrt{\gamma}} \frac{{}_2F_1\left(\frac{\sqrt{\gamma}}{2} - \frac{1}{2}\sqrt{\gamma+\frac{1}{4}} + \frac{1}{4}, \frac{\sqrt{\gamma}}{2} + \frac{1}{2}\sqrt{\gamma+\frac{1}{4}} + \frac{1}{4}; \sqrt{\gamma}+1; \frac{1}{\cosh(\ell r)^2}\right)}{{}_2F_1\left(\frac{\sqrt{\gamma}}{2} - \frac{1}{2}\sqrt{\gamma+\frac{1}{4}} + \frac{1}{4}, \frac{\sqrt{\gamma}}{2} + \frac{1}{2}\sqrt{\gamma+\frac{1}{4}} + \frac{1}{4}; \sqrt{\gamma}+1; 1\right)} \tag{C.70}$$

Equivalently, this expression can be represented in terms of generalised Legendre functions

$$G_k(r) = \frac{P^{-\sqrt{\gamma}}_{\frac{1}{2}\left(\sqrt{1+4\gamma}-1\right)}(\tanh(\ell r))}{P^{-\sqrt{\gamma}}_{\frac{1}{2}\left(\sqrt{1+4\gamma}-1\right)}(0)} \tag{C.71}$$

As a first check, we verify that the solution Eq. (C.70) reproduces the known solutions in the small/large ℓ limits.

C.3.6.1 Asymptotic limits $\ell \to \infty$

At large ℓ, we simply have

$$\lim_{\ell\to\infty} Q_{k'/\ell^2}(r) = \lim_{\ell\to\infty} G_{k'/\ell^2}(r) = e^{-r\sqrt{ik'}} \tag{C.72}$$

in agreement with Eq. (C.66) ($\theta = 1/2$ for Eq. (C.69)). The limit in Eq. (C.72) can be easily obtained using Eq. (C.70) using that

$$\lim_{\gamma\to 0} {}_2F_1\left(\frac{\sqrt{\gamma}}{2} - \frac{1}{2}\sqrt{\gamma+\frac{1}{4}} + \frac{1}{4}, \frac{\sqrt{\gamma}}{2} + \frac{1}{2}\sqrt{\gamma+\frac{1}{4}} + \frac{1}{4}; \sqrt{\gamma}+1; x\right) = {}_2F_1(0, \frac{1}{2}, 1; x) = 1 \tag{C.73}$$

irrespectively of x.

C.3.6.2 Small ℓ check

In this case, the limit is less trivial as $k = k'/\ell^2$ becomes large in the limit of small ℓ. So that simultaneously the parameters of the hypergeometric are diverging, while

its argument is going to 1. Thus, we first apply the transformation between hypergeometric functions

$$ {}_2F_1(a,b,c;z) = \frac{(1-z)^{-a-b+c}\Gamma(c)\Gamma(a+b-c)\,{}_2F_1(c-a,c-b;-a-b+c+1;1-z)}{\Gamma(a)\Gamma(b)} + \\ + \frac{\Gamma(c)\Gamma(-a-b+c)\,{}_2F_1(a,b;a+b-c+1;1-z)}{\Gamma(c-a)\Gamma(c-b)} \tag{C.74} $$

Then, we use that

$$ \lim_{\ell\to 0} {}_2F_1\left(\frac{1}{4}\left(2\sqrt{\gamma}-\sqrt{1+4\gamma}+1\right),\frac{1}{4}\left(2\sqrt{\gamma}+\sqrt{1+4\gamma}+1\right);\frac{1}{2};\tanh(\ell)^2\right) = \\ \frac{e^{k'/2}(k')^{1/4}\Gamma\left(\frac{3}{4}\right) I_{-\frac{1}{4}}(k'/2)}{\sqrt{2}} \tag{C.75} $$

to recover, after some manipulations, Eq. (C.61).

Bibliography

[1] Robert Hilborn. "Sea Gulls, Butterflies, and Grasshoppers: A Brief History of the Butterfly Effect in Nonlinear Dynamics". In: *American Journal of Physics - AMER J PHYS* 72 (Apr. 2004). DOI: 10.1119/1.1636492.

[2] Steven H. Strogatz. *Nonlinear Dynamics and Chaos: With Applications to Physics, Biology, Chemistry, and Engineering*. 2nd. CRC Press, 2015. DOI: 10.1201/9780429492563. URL: https://doi.org/10.1201/9780429492563.

[3] Edward Ott. *Chaos in Dynamical Systems*. 2nd ed. Cambridge University Press, 2002. ISBN: 9780511803260. DOI: 10.1017/CBO9780511803260.

[4] Philip Holmes. "Poincaré, celestial mechanics, dynamical-systems theory and "chaos"". In: *Physics Reports* 193.3 (1990), pp. 137–163. ISSN: 0370-1573. DOI: https://doi.org/10.1016/0370-1573(90)90012-Q. URL: https://www.sciencedirect.com/science/article/pii/037015739090012Q.

[5] Christophe Abraham, Gérard Biau, and Benoıt Cadre. "On Lyapunov exponent and sensitivity". In: *Journal of Mathematical Analysis and Applications* 290.2 (2004), pp. 395–404. ISSN: 0022-247X. DOI: https://doi.org/10.1016/j.jmaa.2003.10.029. URL: https://www.sciencedirect.com/science/article/pii/S0022247X03007601.

[6] Boris Chirikov and Dima Shepelyansky. "Chirikov standard map". In: *Scholarpedia* 3 (Jan. 2008), p. 3550. DOI: 10.4249/scholarpedia.3550.

[7] J A G Roberts and C J Tompson. "Dynamics of the classical Heisenberg spin chain". In: *Journal of Physics A: Mathematical and General* 21.8 (1988), p. 1769. DOI: 10.1088/0305-4470/21/8/013. URL: https://dx.doi.org/10.1088/0305-4470/21/8/013.

[8] L Kavitha and M Daniel. "Integrability and soliton in a classical one-dimensional site-dependent biquadratic Heisenberg spin chain and the effect of nonlinear inhomogeneity". In: *Journal of Physics A: Mathematical and General* 36.42 (2003),

p. 10471. DOI: 10.1088/0305-4470/36/42/005. URL: https://dx.doi.org/10.1088/0305-4470/36/42/005.

[9] J. V. Sengers Cannell J. M. Ortiz de Zárate. *Hydrodynamic Fluctuations in Fluids and Fluid Mixtures*. Vol. 30. 2. 2009, pp. 734–735. DOI: 10.1007/s10765-008-0517-7. URL: https://doi.org/10.1007/s10765-008-0517-7.

[10] Avijit Das et al. "Nonlinear Fluctuating Hydrodynamics for the Classical XXZ Spin Chain". In: *Journal of Statistical Physics* 180.1 (2020), pp. 238–262. DOI: 10.1007/s10955-019-02397-y. URL: https://doi.org/10.1007/s10955-019-02397-y.

[11] Herbert Spohn. "Nonlinear Fluctuating Hydrodynamics for Anharmonic Chains". In: *Journal of Statistical Physics* 154.5 (2014), pp. 1191–1227.

[12] Herbert Spohn. *Fluctuating hydrodynamics approach to equilibrium time correlations for anharmonic chains*. 2016. arXiv: 1505.05987 [cond-mat.stat-mech].

[13] Christian B. Mendl and Herbert Spohn. "Dynamic Correlators of Fermi-Pasta-Ulam Chains and Nonlinear Fluctuating Hydrodynamics". In: *Phys. Rev. Lett.* 111 (23 2013), p. 230601. DOI: 10.1103/PhysRevLett.111.230601. URL: https://link.aps.org/doi/10.1103/PhysRevLett.111.230601.

[14] Dennis Schubert et al. "Quantum versus classical dynamics in spin models: Chains, ladders, and square lattices". In: *Phys. Rev. B* 104 (5 2021), p. 054415. DOI: 10.1103/PhysRevB.104.054415. URL: https://link.aps.org/doi/10.1103/PhysRevB.104.054415.

[15] Ziga Krajnik and T. Prosen. "Kardar–Parisi–Zhang Physics in Integrable Rotationally Symmetric Dynamics on Discrete Space–Time Lattice". In: *Journal of Statistical Physics* 179.1 (Mar. 2020), pp. 110–130. DOI: 10.1007/s10955-020-02523-1. URL: https://doi.org/10.1007/s10955-020-02523-1.

[16] Alexios Christopoulos et al. "Dual symplectic classical circuits: An exactly solvable model of many-body chaos". In: *SciPost Phys.* 16 (2024), p. 049. DOI: 10.21468/SciPostPhys.16.2.049. URL: https://scipost.org/10.21468/SciPostPhys.16.2.049.

[17] M. Gromov. "Pseudo holomorphic curves in symplectic manifolds". In: *Inventiones mathematicae* 82.2 (1985), pp. 307–347. ISSN: 1432-1297. DOI: 10.1007/BF01388806. URL: https://doi.org/10.1007/BF01388806.

[18] Lorenzo Piroli et al. "Exact dynamics in dual-unitary quantum circuits". In: *Phys. Rev. B* 101 (9 2020), p. 094304. DOI: 10.1103/PhysRevB.101.094304. URL: https://link.aps.org/doi/10.1103/PhysRevB.101.094304.

[19] Pavel Kos, Bruno Bertini, and Tomaz Prosen. "Correlations in Perturbed Dual-Unitary Circuits: Efficient Path-Integral Formula". In: *Physical Review X* 11.1 (2021). DOI: 10.1103/physrevx.11.011022. URL: https://doi.org/10.1103%2Fphysrevx.11.011022.

[20] Bruno Bertini, Pavel Kos, and Tomaz Prosen. "Exact Spectral Form Factor in a Minimal Model of Many-Body Quantum Chaos". In: *Phys. Rev. Lett.* 121 (26 2018), p. 264101. DOI: 10.1103/PhysRevLett.121.264101. URL: https://link.aps.org/doi/10.1103/PhysRevLett.121.264101.

[21] Bruno Bertini, Pavel Kos, and Tomaz Prosen. "Random Matrix Spectral Form Factor of Dual-Unitary Quantum Circuits". In: *Commun. Math. Phys.* 387.1 (2021), pp. 597–620. DOI: 10.1007/s00220-021-04139-2. arXiv: 2012.12254 [math-ph].

[22] Márton Borsi and Balázs Pozsgay. "Construction and the ergodicity properties of dual unitary quantum circuits". In: *Phys. Rev. B* 106.1 (2022), p. 014302. DOI: 10.1103/PhysRevB.106.014302. arXiv: 2201.07768 [quant-ph].

[23] Jonas Haferkamp et al. "Linear growth of quantum circuit complexity". In: *Nature Physics* 18.5 (2022), pp. 528–532. ISSN: 1745-2481. DOI: 10.1038/s41567-022-01539-6. URL: https://doi.org/10.1038/s41567-022-01539-6.

[24] Stefan Sorg et al. "Relaxation and thermalization in the one-dimensional Bose-Hubbard model: A case study for the interaction quantum quench from the atomic limit". In: *Physical Review A* 90 (May 2014). DOI: 10.1103/PhysRevA.90.033606.

[25] F. Borgonovi et al. "Quantum chaos and thermalization in isolated systems of interacting particles". In: *Physics Reports* 626 (2016). Quantum chaos and thermalization in isolated systems of interacting particles, pp. 1–58. ISSN: 0370-1573. DOI: https://doi.org/10.1016/j.physrep.2016.02.005. URL: https://www.sciencedirect.com/science/article/pii/S0370157316000831.

[26] Shenglong Xu and Brian Swingle. "Scrambling Dynamics and Out-of-Time-Ordered Correlators in Quantum Many-Body Systems". In: *PRX Quantum*

5 (1 2024), p. 010201. DOI: 10.1103/PRXQuantum.5.010201. URL: https://link.aps.org/doi/10.1103/PRXQuantum.5.010201.

[27] Patrick Hayden and John Preskill. "Black holes as mirrors: quantum information in random subsystems". In: *Journal of High Energy Physics* 2007.09 (2007), p. 120. DOI: 10.1088/1126-6708/2007/09/120. URL: https://dx.doi.org/10.1088/1126-6708/2007/09/120.

[28] Akhilesh Pandey, Avanish Kumar, and Sanjay Puri. *Quantum Chaotic Systems and Random Matrix Theory*. 2019. arXiv: 1905.10596 [cond-mat.stat-mech]. URL: https://arxiv.org/abs/1905.10596.

[29] Michael Victor Berry, M. Tabor, and John Michael Ziman. "Level clustering in the regular spectrum". In: *Proceedings of the Royal Society of London. A. Mathematical and Physical Sciences* 356.1686 (1977), pp. 375–394. DOI: 10.1098/rspa.1977.0140. eprint: https://royalsocietypublishing.org/doi/pdf/10.1098/rspa.1977.0140. URL: https://royalsocietypublishing.org/doi/abs/10.1098/rspa.1977.0140.

[30] O. Bohigas, M. J. Giannoni, and C. Schmit. "Characterization of Chaotic Quantum Spectra and Universality of Level Fluctuation Laws". In: *Phys. Rev. Lett.* 52 (1 1984), pp. 1–4. DOI: 10.1103/PhysRevLett.52.1. URL: https://link.aps.org/doi/10.1103/PhysRevLett.52.1.

[31] Jonas Haferkamp. "Random quantum circuits are approximate unitary t-designs in depth $O\left(nt^{5+o(1)}\right)$". In: *Quantum* 6 (Sept. 2022), p. 795. ISSN: 2521-327X. DOI: 10.22331/q-2022-09-08-795. URL: https://doi.org/10.22331/q-2022-09-08-795.

[32] E. Knill. "Approximation by Quantum Circuits". In: (Aug. 2000).

[33] Pavan Hosur et al. "Chaos in quantum channels". In: *Journal of High Energy Physics* 2016.2 (2016), p. 4. ISSN: 1029-8479. DOI: 10.1007/JHEP02(2016)004. URL: https://doi.org/10.1007/JHEP02(2016)004.

[34] Daniel A. Roberts and Beni Yoshida. "Chaos and complexity by design". In: *Journal of High Energy Physics* 2017.4 (Apr. 2017). ISSN: 1029-8479. DOI: 10.1007/jhep04(2017)121. URL: http://dx.doi.org/10.1007/JHEP04(2017)121.

[35] E. Knill et al. "Randomized benchmarking of quantum gates". In: *Phys. Rev. A* 77 (1 2008), p. 012307. DOI: 10.1103/PhysRevA.77.012307. URL: https://link.aps.org/doi/10.1103/PhysRevA.77.012307.

[36] Sean Mullane. *Sampling random quantum circuits: a pedestrian's guide*. 2020. eprint: arXiv:2007.07872.

[37] Alexios Christopoulos, Amos Chan, and Andrea De Luca. *Universal distributions of overlaps from unitary dynamics in generic quantum many-body systems*. 2024. arXiv: 2404.10057 [cond-mat.stat-mech]. URL: https://arxiv.org/abs/2404.10057.

[38] Saumya Shivam et al. "Many-Body Quantum Chaos and Emergence of Ginibre Ensemble". In: *Phys. Rev. Lett.* 130 (14 2023), p. 140403. DOI: 10.1103/PhysRevLett.130.140403. URL: https://link.aps.org/doi/10.1103/PhysRevLett.130.140403.

[39] Amos Chan, Andrea De Luca, and J. T. Chalker. "Spectral Statistics in Spatially Extended Chaotic Quantum Many-Body Systems". In: *Phys. Rev. Lett.* 121 (6 2018), p. 060601. DOI: 10.1103/PhysRevLett.121.060601. URL: https://link.aps.org/doi/10.1103/PhysRevLett.121.060601.

[40] Robert M. Gray. "Toeplitz and Circulant Matrices: A Review". In: *Foundations and Trends® in Communications and Information Theory* 2.3 (2006), pp. 155–239. ISSN: 1567-2190. DOI: 10.1561/0100000006. URL: http://dx.doi.org/10.1561/0100000006.

[41] Amos Chan, Andrea De Luca, and J. T. Chalker. "Solution of a Minimal Model for Many-Body Quantum Chaos". In: *Phys. Rev. X* 8 (4 2018), p. 041019. DOI: 10.1103/PhysRevX.8.041019. URL: https://link.aps.org/doi/10.1103/PhysRevX.8.041019.

[42] Dmitry A. Abanin and Zlatko Papić. "Recent progress in many-body localization". In: *Annalen der Physik* 529.7 (), p. 1700169. DOI: https://doi.org/10.1002/andp.201700169. eprint: https://onlinelibrary.wiley.com/doi/pdf/10.1002/andp.201700169. URL: https://onlinelibrary.wiley.com/doi/abs/10.1002/andp.201700169.

[43] Rahul Nandkishore and David A. Huse. "Many-Body Localization and Thermalization in Quantum Statistical Mechanics". In: *Annual Review of Condensed Matter Physics* 6.Volume 6, 2015 (2015), pp. 15–38. ISSN: 1947-5462. DOI: https:

//doi.org/10.1146/annurev-conmatphys-031214-014726. URL: https://www.annualreviews.org/content/journals/10.1146/annurev-conmatphys-031214-014726.

[44] F. Arute et al. "Quantum supremacy using a programmable superconducting processor". In: *Nature* 574.7779 (2019), pp. 505–510. DOI: 10.1038/s41586-019-1666-5. URL: https://doi.org/10.1038/s41586-019-1666-5.

[45] S. Boixo, S. V. Isakov, V. N. Smelyanskiy, et al. "Characterizing quantum supremacy in near-term devices". In: *Nature Physics* 14 (2018), pp. 595–600. DOI: 10.1038/s41567-018-0124-x. URL: https://doi.org/10.1038/s41567-018-0124-x.

[46] Alexios Christopoulos et al. "Universal Out-of-Equilibrium Dynamics of 1D Critical Quantum Systems Perturbed by Noise Coupled to Energy". In: *Phys. Rev. X* 13 (1 2023), p. 011043. DOI: 10.1103/PhysRevX.13.011043. URL: https://link.aps.org/doi/10.1103/PhysRevX.13.011043.

[47] Kenneth G. Wilson. "Renormalization Group and Critical Phenomena. I. Renormalization Group and the Kadanoff Scaling Picture". In: *Phys. Rev. B* 4 (9 1971), pp. 3174–3183. DOI: 10.1103/PhysRevB.4.3174. URL: https://link.aps.org/doi/10.1103/PhysRevB.4.3174.

[48] A.A. Belavin, A.M. Polyakov, and A.B. Zamolodchikov. "Infinite conformal symmetry in two-dimensional quantum field theory". In: *Nuclear Physics B* 241.2 (1984), pp. 333 –380. ISSN: 0550-3213. DOI: https://doi.org/10.1016/0550-3213(84)90052-X. URL: http://www.sciencedirect.com/science/article/pii/055032138490052X.

[49] Vincenzo Alba and Pasquale Calabrese. "The quench action approach in finite integrable spin chains". In: (2015). DOI: 10.1088/1742-5468/2016/04/043105. eprint: arXiv:1512.02213.

[50] Vincenzo Alba, Luca Tagliacozzo, and Pasquale Calabrese. "Entanglement entropy of two disjoint blocks in critical Ising models". In: *Phys. Rev. B* 81 (6 2010), p. 060411. DOI: 10.1103/PhysRevB.81.060411. URL: https://link.aps.org/doi/10.1103/PhysRevB.81.060411.

[51] Ian Affleck. "Universal term in the free energy at a critical point and the conformal anomaly". In: *Phys. Rev. Lett.* 56 (7 1986), pp. 746–748. DOI: 10.

1103/PhysRevLett.56.746. URL: https://link.aps.org/doi/10.1103/PhysRevLett.56.746.

[52] H. W. J. Blöte, John L. Cardy, and M. P. Nightingale. "Conformal invariance, the central charge, and universal finite-size amplitudes at criticality". In: *Phys. Rev. Lett.* 56 (7 1986), pp. 742–745. DOI: 10.1103/PhysRevLett.56.742. URL: https://link.aps.org/doi/10.1103/PhysRevLett.56.742.

[53] Anatoli Polkovnikov Luca D'Alessio Yariv Kafri and Marcos Rigol. "From quantum chaos and eigenstate thermalization to statistical mechanics and thermodynamics". In: *Advances in Physics* 65.3 (2016), pp. 239–362. DOI: 10.1080/00018732.2016.1198134. eprint: https://doi.org/10.1080/00018732.2016.1198134. URL: https://doi.org/10.1080/00018732.2016.1198134.

[54] Fabien Alet and Nicolas Laflorencie. "Many-body localization: An introduction and selected topics". In: *Comptes Rendus Physique* 19.6 (2018). Quantum simulation / Simulation quantique, pp. 498–525. ISSN: 1631-0705. DOI: https://doi.org/10.1016/j.crhy.2018.03.003. URL: https://www.sciencedirect.com/science/article/pii/S163107051830032X.

[55] Pasquale Calabrese, Fabian H L Essler, and Giuseppe Mussardo. "Introduction to 'Quantum Integrability in Out of Equilibrium Systems'". In: *Journal of Statistical Mechanics: Theory and Experiment* 2016.6 (2016), p. 064001. DOI: 10.1088/1742-5468/2016/06/064001. URL: https://doi.org/10.1088/1742-5468/2016/06/064001.

[56] Christopher J Turner et al. "Weak ergodicity breaking from quantum many-body scars". In: *Nat. Phys.* 14.7 (2018), pp. 745–749. DOI: 10.1038/s41567-018-0137-5. URL: https://doi.org/10.1038/s41567-018-0137-5.

[57] Pablo Sala et al. "Ergodicity Breaking Arising from Hilbert Space Fragmentation in Dipole-Conserving Hamiltonians". In: *Phys. Rev. X* 10 (1 2020), p. 011047. DOI: 10.1103/PhysRevX.10.011047. URL: https://link.aps.org/doi/10.1103/PhysRevX.10.011047.

[58] Wojciech Hubert Zurek. "Decoherence, einselection, and the quantum origins of the classical". In: *Rev. Mod. Phys.* 75 (3 2003), pp. 715–775. DOI: 10.1103/RevModPhys.75.715. URL: https://link.aps.org/doi/10.1103/RevModPhys.75.715.

[59] Jamir Marino and Alessandro Silva. "Relaxation, prethermalization, and diffusion in a noisy quantum Ising chain". In: *Phys. Rev. B* 86 (6 2012), p. 060408. DOI: 10.1103/PhysRevB.86.060408. URL: https://link.aps.org/doi/10.1103/PhysRevB.86.060408.

[60] Gu Zhang, E. Novais, and Harold U. Baranger. "Rescuing a Quantum Phase Transition with Quantum Noise". In: *Phys. Rev. Lett.* 118 (5 2017), p. 050402. DOI: 10.1103/PhysRevLett.118.050402. URL: https://link.aps.org/doi/10.1103/PhysRevLett.118.050402.

[61] Rohit Prasad Bhatt et al. "Stochastic dynamics of a few sodium atoms in presence of a cold potassium cloud". In: *Scientific Reports* 12.1 (2022), p. 2422. ISSN: 2045-2322. DOI: 10.1038/s41598-022-05778-8. URL: https://doi.org/10.1038/s41598-022-05778-8.

[62] A Bermudez, M A Martin-Delgado, and D Porras. "The localization of phonons in ion traps with controlled quantum disorder". In: *New Journal of Physics* 12.12 (2010), p. 123016. DOI: 10.1088/1367-2630/12/12/123016. URL: https://doi.org/10.1088/1367-2630/12/12/123016.

[63] Brian Skinner, Jonathan Ruhman, and Adam Nahum. "Measurement-Induced Phase Transitions in the Dynamics of Entanglement". In: *Phys. Rev. X* 9 (3 2019), p. 031009. DOI: 10.1103/PhysRevX.9.031009. URL: https://link.aps.org/doi/10.1103/PhysRevX.9.031009.

[64] Zhi-Cheng Yang et al. "Entanglement phase transitions in random stabilizer tensor networks". In: *Phys. Rev. B* 105 (10 2022), p. 104306. DOI: 10.1103/PhysRevB.105.104306. URL: https://link.aps.org/doi/10.1103/PhysRevB.105.104306.

[65] Soonwon Choi et al. "Quantum Error Correction in Scrambling Dynamics and Measurement-Induced Phase Transition". In: *Phys. Rev. Lett.* 125 (3 2020), p. 030505. DOI: 10.1103/PhysRevLett.125.030505. URL: https://link.aps.org/doi/10.1103/PhysRevLett.125.030505.

[66] Bin Chen et al. "On the mutual information in conformal field theory". In: *Journal of High Energy Physics* 2017.6 (2017), p. 96. ISSN: 1029-8479. DOI: 10.1007/JHEP06(2017)096. URL: https://doi.org/10.1007/JHEP06(2017)096.

[67] Federica M. Surace et al. "Lattice Gauge Theories and String Dynamics in Rydberg Atom Quantum Simulators". In: *Phys. Rev. X* 10 (2 2020), p. 021041. DOI: 10.1103/PhysRevX.10.021041. URL: https://link.aps.org/doi/10.1103/PhysRevX.10.021041.

[68] J. D. Meiss. "Symplectic maps, variational principles, and transport". In: *Rev. Mod. Phys.* 64 (3 1992), pp. 795–848. DOI: 10.1103/RevModPhys.64.795. URL: https://link.aps.org/doi/10.1103/RevModPhys.64.795.

[69] Alexei Deriglazov. "Integral Invariants". In: *Classical Mechanics: Hamiltonian and Lagrangian Formalism*. Berlin, Heidelberg: Springer Berlin Heidelberg, 2010, pp. 155–166. ISBN: 978-3-642-14037-2. DOI: 10.1007/978-3-642-14037-2_5. URL: https://doi.org/10.1007/978-3-642-14037-2_5.

[70] "The Symplectic Group". In: *Symplectic Geometry and Quantum Mechanics*. Basel: Birkhäuser Basel, 2006, pp. 27–63. ISBN: 978-3-7643-7575-1. DOI: 10.1007/3-7643-7575-2_2. URL: https://doi.org/10.1007/3-7643-7575-2_2.

[71] Hyung tae Kook and James D. Meiss. "Periodic orbits for reversible, symplectic mappings". In: *Physica D: Nonlinear Phenomena* 35.1 (1989), pp. 65–86. ISSN: 0167-2789. DOI: https://doi.org/10.1016/0167-2789(89)90096-1. URL: https://www.sciencedirect.com/science/article/pii/0167278989900961.

[72] Arnd Bäcker and James D. Meiss. "Moser's Quadratic, Symplectic Map". In: *Regular and Chaotic Dynamics* 23.6 (2018), pp. 654–664. ISSN: 1468-4845. DOI: 10.1134/S1560354718060023. URL: https://doi.org/10.1134/S1560354718060023.

[73] J. E. Howard and R. S. MacKay. "Linear stability of symplectic maps". In: *Journal of Mathematical Physics* 28.5 (May 1987), pp. 1036–1051. ISSN: 0022-2488. DOI: 10.1063/1.527544. eprint: https://pubs.aip.org/aip/jmp/article-pdf/28/5/1036/19124301/1036_1_online.pdf. URL: https://doi.org/10.1063/1.527544.

[74] Maurice A. de Gosson. "The Symplectic Camel and the Uncertainty Principle: The Tip of an Iceberg?" In: *Foundations of Physics* 39.2 (2009), pp. 194–214. ISSN: 1572-9516. DOI: 10.1007/s10701-009-9272-2. URL: https://doi.org/10.1007/s10701-009-9272-2.

[75] Dusa Mcduff and Dietmar A. Salamon. "Introduction to Symplectic Topology". In: 1995. URL: https://api.semanticscholar.org/CorpusID:116966560.

[76] G. C. Layek. *An Introduction to Dynamical Systems and Chaos*. New York: Springer, 2015. ISBN: 978-81-322-2503-6.

[77] Pavel Kos, Bruno Bertini, and Toma ž Prosen. "Correlations in Perturbed Dual-Unitary Circuits: Efficient Path-Integral Formula". In: *Phys. Rev. X* 11 (1 2021), p. 011022. DOI: 10.1103/PhysRevX.11.011022. URL: https://link.aps.org/doi/10.1103/PhysRevX.11.011022.

[78] Bruno Bertini, Pavel Kos, and Tomaž Prosen. "Operator Entanglement in Local Quantum Circuits I: Chaotic Dual-Unitary Circuits". In: *SciPost Phys.* 8 (2020), p. 067. DOI: 10.21468/SciPostPhys.8.4.067. URL: https://scipost.org/10.21468/SciPostPhys.8.4.067.

[79] Bruno Bertini, Pavel Kos, and T. Prosen. "Exact Correlation Functions for Dual-Unitary Lattice Models in 1+1 Dimensions". In: *Phys. Rev. Lett.* 123.21 (2019), p. 210601. DOI: 10.1103/PhysRevLett.123.210601. arXiv: 1904.02140 [cond-mat.stat-mech].

[80] Hans-Dieter Meyer. "Theory of the Liapunov exponents of Hamiltonian systems and a numerical study on the transition from regular to irregular classical motion". In: *The Journal of Chemical Physics* 84.6 (Mar. 1986), pp. 3147–3161. DOI: 10.1063/1.450296. URL: https://doi.org/10.1063/1.450296.

[81] Ignacio GarcÃÂa-Mata, Rodolfo Jalabert, and Diego Wisniacki. "Out-of-time-order correlations and quantum chaos". In: *Scholarpedia* 18.4 (2023), p. 55237. ISSN: 1941-6016. DOI: 10.4249/scholarpedia.55237. URL: http://dx.doi.org/10.4249/scholarpedia.55237.

[82] D. Gross, K. Audenaert, and J. Eisert. "Evenly distributed unitaries: On the structure of unitary designs". In: *Journal of Mathematical Physics* 48.5 (May 2007), p. 052104.

[83] Benoît Collins and Piotr Śniady. "Integration with Respect to the Haar Measure on Unitary, Orthogonal and Symplectic Group". In: *Communications in Mathematical Physics* 264.3 (2006), pp. 773–795. DOI: 10.1007/s00220-006-1554-3. URL: https://doi.org/10.1007/s00220-006-1554-3.

[84] M. S. Anwar et al. "Practical implementations of twirl operations". In: *Phys. Rev. A* 71 (3 2005), p. 032327. DOI: 10.1103/PhysRevA.71.032327. URL: https://link.aps.org/doi/10.1103/PhysRevA.71.032327.

[85] David Gross, Sepehr Nezami, and Michael Walter. "Schurâ€"Weyl Duality for the Clifford Group with Applications: Property Testing, a Robust Hudson Theorem, and de Finetti Representations". In: *Communications in Mathematical Physics* 385.3 (2021), pp. 1325–1393. ISSN: 1432-0916. DOI: 10.1007/s00220-021-04118-7. URL: https://doi.org/10.1007/s00220-021-04118-7.

[86] Alessio Lerose, Michael Sonner, and Dmitry A. Abanin. "Influence Matrix Approach to Many-Body Floquet Dynamics". In: *Physical Review X* 11.2 (May 2021). ISSN: 2160-3308. DOI: 10.1103/physrevx.11.021040. URL: http://dx.doi.org/10.1103/PhysRevX.11.021040.

[87] Matteo Ippoliti, Tibor Rakovszky, and Vedika Khemani. "Fractal, Logarithmic, and Volume-Law Entangled Nonthermal Steady States via Spacetime Duality". In: *Physical Review X* 12.1 (Mar. 2022). ISSN: 2160-3308. DOI: 10.1103/physrevx.12.011045. URL: http://dx.doi.org/10.1103/PhysRevX.12.011045.

[88] Gernot Akemann, Zdzislaw Burda, and Mario Kieburg. "Universality of local spectral statistics of products of random matrices". In: *Phys. Rev. E* 102 (5 2020), p. 052134. DOI: 10.1103/PhysRevE.102.052134. URL: https://link.aps.org/doi/10.1103/PhysRevE.102.052134.

[89] Dang-Zheng Liu, Dong Wang, and Yanhui Wang. *Lyapunov exponent, universality and phase transition for products of random matrices*. 2022. arXiv: 1810.00433 [math.PR].

[90] Andrea De Luca et al. *Universality classes for purification in nonunitary quantum processes*. 2023. arXiv: 2312.17744 [cond-mat.stat-mech].

[91] George Mackiw. "Permutations as Products of Transpositions". In: *The American Mathematical Monthly* 102.5 (1995), pp. 438–440. ISSN: 00029890, 19300972. URL: http://www.jstor.org/stable/2975036 (visited on 06/06/2024).

[92] Amos Chan et al. "Many-body quantum chaos and space-time translational invariance". In: *Nature Communications* 13.1 (2022), p. 7484. ISSN: 2041-1723. DOI: 10.1038/s41467-022-34318-1. URL: https://doi.org/10.1038/s41467-022-34318-1.

[93] Persi Diaconis. *Group representations in probability and statistics*.

[94] Noah Miller. "Representation Theory And Quantum Mechanics". In: 2018. URL: https://api.semanticscholar.org/CorpusID:145036233.

[95] Michel Lassalle. "An explicit formula for the characters of the symmetric group". In: *Mathematische Annalen* 340.2 (2008), pp. 383–405. ISSN: 1432-1807. DOI: 10.1007/s00208-007-0156-5. URL: https://doi.org/10.1007/s00208-007-0156-5.

[96] Michael Larsen and Aner Shalev. "Characters of symmetric groups: sharp bounds and applications". In: *Inventiones mathematicae* 174.3 (2008), pp. 645–687. ISSN: 1432-1297. DOI: 10.1007/s00222-008-0145-7. URL: https://doi.org/10.1007/s00222-008-0145-7.

[97] Federico Gerbino et al. "A Dyson Brownian Motion Model for Weak Measurements in Chaotic Quantum Systems". In: *Quantum Reports* 6.2 (May 2024), 200–230. ISSN: 2624-960X. DOI: 10.3390/quantum6020016. URL: http://dx.doi.org/10.3390/quantum6020016.

[98] E. Brézin and S. Hikami. "Level spacing of random matrices in an external source". In: *Phys. Rev. E* 58 (6 1998), pp. 7176–7185. DOI: 10.1103/PhysRevE.58.7176. URL: https://link.aps.org/doi/10.1103/PhysRevE.58.7176.

[99] V. E. Kravtsov. *Random matrix theory: Wigner-Dyson statistics and beyond. (Lecture notes of a course given at SISSA (Trieste, Italy))*. 2012. arXiv: 0911.0639 [cond-mat.dis-nn]. URL: https://arxiv.org/abs/0911.0639.

[100] Philippe Francesco, Pierre Mathieu, and David Sénéchal. *Conformal field theory*. Springer Science & Business Media, 2012.

[101] Pasquale Calabrese and John Cardy. "Entanglement entropy and conformal field theory". In: (2009). DOI: 10.1088/1751-8113/42/50/504005. eprint: arXiv:0905.4013.

[102] Paul Ginsparg. "Applied Conformal Field Theory". In: (1988). eprint: arXiv:hep-th/9108028.

[103] E.J. Schreier. "Conformal symmetry and three-point functions". In: *Phys. Rev. D* 3 (1971), pp. 980–988. DOI: 10.1103/PhysRevD.3.980.

[104] Giuseppe Mussardo. *Statistical field theory: an introduction to exactly solved models in statistical physics*. New York, NY: Oxford Univ. Press, 2010.

[105] Massimo Materassi. *Polyakov's string classical mechanics*. 1999. eprint: arXiv:hep-th/9905028.

[106] Máximo Bañados and Ignacio A. Reyes. "A short review on Noether's theorems, gauge symmetries and boundary terms". In: (2016). DOI: 10.1142/S0218271816300214. eprint: arXiv:1601.03616.

[107] "Continuous Symmetries and Conservation Laws.: Noether's Theorem". In: *Multivalued Fields*, pp. 71–110. DOI: 10.1142/9789812791726_0003. eprint: https://www.worldscientific.com/doi/pdf/10.1142/9789812791726_0003. URL: https://www.worldscientific.com/doi/abs/10.1142/9789812791726_0003.

[108] C. Holzhey, F. Larsen, and F. Wilczek. "Geometric and Renormalized Entropy in Conformal Field Theory". In: (1994). DOI: 10.1016/0550-3213(94)90402-2. eprint: arXiv:hep-th/9403108.

[109] Luigi Amico and Rosario Fazio. "Entanglement and magnetic order". In: (2009). DOI: 10.1088/1751-8113/42/50/504001. eprint: arXiv:0911.1930.

[110] Tatsuma Nishioka. "Entanglement entropy: holography and renormalization group". In: (2018). DOI: 10.1103/RevModPhys.90.035007. eprint: arXiv:1801.10352.

[111] Pasquale Calabrese and John Cardy. "Entanglement Entropy and Quantum Field Theory". In: (2004). DOI: 10.1088/1742-5468/2004/06/P06002. eprint: arXiv:hep-th/0405152.

[112] Andreas Wipf. *Statistical Approach to Quantum Field Theory*. Vol. 864. Jan. 2013. ISBN: 978-3-642-33104-6. DOI: 10.1007/978-3-642-33105-3.

[113] Pasquale Calabrese and John Cardy. "Entanglement entropy and conformal field theory". In: *Journal of Physics A: Mathematical and Theoretical* 42.50 (2009), p. 504005. URL: https://doi.org/10.1088/1751-8113/42/50/504005.

[114] Pasquale Calabrese, John Cardy, and Erik Tonni. "Entanglement entropy of two disjoint intervals in conformal field theory". In: (2009). DOI: 10.1088/1742-5468/2009/11/P11001. eprint: arXiv:0905.2069.

[115] Andrea Pelissetto and Ettore Vicari. "Critical phenomena and renormalization-group theory". In: *Physics Reports* 368.6 (Oct. 2002), 549–727. ISSN: 0370-1573.

DOI: 10.1016/s0370-1573(02)00219-3. URL: http://dx.doi.org/10.1016/S0370-1573(02)00219-3.

[116] Denis Bernard and Pierre Le Doussal. "Entanglement entropy growth in stochastic conformal field theory and the KPZ class". In: *EPL (Europhysics Letters)* 131.1 (2020), p. 10007. DOI: 10.1209/0295-5075/131/10007. URL: https://doi.org/10.1209/0295-5075/131/10007.

[117] Pasquale Calabrese and John Cardy. "Quantum quenches in 1 + 1 dimensional conformal field theories". In: 2016.6 (2016), p. 064003. DOI: 10.1088/1742-5468/2016/06/064003. URL: https://doi.org/10.1088/1742-5468/2016/06/064003.

[118] Marta Sanz-Sole. *An Introduction to Stochastic Calculus, publisher = Facultat de Matematiques i Informatica Universitat de Barcelona*. Barcelona, 2017. URL: https://people.emich.edu/ocalin/Teaching_files/D18N.pdf.

[119] Ovidiu Calin. *An Informal Introduction to Stochastic Calculus with Applications*. WORLD SCIENTIFIC, 2015. DOI: 10.1142/9620. eprint: https://www.worldscientific.com/doi/pdf/10.1142/9620. URL: https://www.worldscientific.com/doi/abs/10.1142/9620.

[120] Krzysztof Gawedzki and Péter Horvai. "Sticky behavior of fluid particles in the compressible Kraichnan model". In: *Journal of statistical physics* 116.5 (2004), pp. 1247–1300.

[121] Stavros Vakeroudis. *Bougerol's identity in law and extensions*. 2012. arXiv: 1201.5823 [math.PR].

[122] Alain Mazzolo. *First-passage time of a Brownian motion: two unexpected journeys*. 2024. arXiv: 2306.17656 [cond-mat.stat-mech]. URL: https://arxiv.org/abs/2306.17656.

[123] Franz Utermohlen. *Tight-Binding Model in the Second Quantization Formalism*. Accessed: 2024-08-29. 2018. URL: https://bpb-us-w2.wpmucdn.com/u.osu.edu/dist/3/67057/files/2018/09/tight-binding_model_in_the_second_quantization_formalism-1egl8n3.pdf.

[124] Thierry Giamarchi. *Quantum physics in one dimension*. Vol. 121. Clarendon press, 2003.

[125] Xiangyu Cao, Antoine Tilloy, and Andrea De Luca. "Entanglement in a fermion chain under continuous monitoring". In: *SciPost Phys.* 7 (2019), p. 024. DOI: 10.21468/SciPostPhys.7.2.024. URL: https://scipost.org/10.21468/SciPostPhys.7.2.024.

[126] D A Varshalovich, A N Moskalev, and V K Khersonskii. *Quantum Theory of Angular Momentum*. WORLD SCIENTIFIC, Oct. 1988. ISBN: 978-9814415491. DOI: 10.1142/0270. URL: https://doi.org/10.1142/0270.

[127] Joachim Weber et al. "Resonances of the Frobenius-Perron operator for a Hamiltonian map with a mixed phase space". In: *Journal of Physics A: Mathematical and General* 34.36 (2001), p. 7195. DOI: 10.1088/0305-4470/34/36/306. URL: https://dx.doi.org/10.1088/0305-4470/34/36/306.

[128] I G Macdonald. *Symmetric functions and hall polynomials*. en. 2nd ed. Oxford Classic Texts in the Physical Sciences. London, England: Oxford University Press, Oct. 1998.

[129] Peter J. Forrester. "Meet Andréief, Bordeaux 1886, and Andreev, Kharkov 1882–1883". In: *Random Matrices: Theory and Applications* 08.02 (2019), p. 1930001. DOI: 10.1142/S2010326319300018. eprint: https://doi.org/10.1142/S2010326319300018. URL: https://doi.org/10.1142/S2010326319300018.

[130] Bhargavi Jonnadula, Jonathan P. Keating, and Francesco Mezzadri. "Symmetric function theory and unitary invariant ensembles". In: *Journal of Mathematical Physics* 62.9 (Sept. 2021), p. 093512. ISSN: 0022-2488. DOI: 10.1063/5.0048364. eprint: https://pubs.aip.org/aip/jmp/article-pdf/doi/10.1063/5.0048364/16677277/093512_1_online.pdf. URL: https://doi.org/10.1063/5.0048364.

[131] Nicolas Macé. *Quantum circuit at criticality*. 2019. arXiv: 1912.09489 [cond-mat.dis-nn].